Crop mapping using high resolution optical and radar satellite data: case study of maize in Trans Nzoia County, Kenya

Dissertation

zur

Erlangung des Doktorgrades (Dr. rer. nat.)

der

Fakultät für Geowissenschaften

der

Ruhr Universität Bochum

vorgelegt von

Bartholomew Thiong'o Kuria

aus

Nairobi, Kenia

Bochum, May 2018

Crop mapping using high resolution optical and radar satellite data: case study of maize in Trans Nzoia County, Kenya

Angefertigt mit Genehmigung der Fakultät für Geowissenschaften der Ruhr Universität Bochum

1. Gutachter: Prof. Dr. Carsten Jürgens
2. Gutachter: Prof. Dr. Bernd Marschner

Tag der Promotion: 16.07.2018

Erscheinungsjahr: 2018

Eidesstattliche Erklärung

Ich versichere an Eides statt, dass ich die eingereichte Dissertation selbststän-dig und ohne unzulässige fremde Hilfe verfasst, andere als die in ihr angegebene Literatur nicht benutzt und dass ich alle ganz oder annähernd übernommenen Textstellen sowie verwendete Grafiken, Tabellen und Auswertungsprogramme kenntlich gemacht habe. Außerdem versichere ich, dass die vorgelegte elektroni-sche mit der schriftlichen Version der Dissertation übereinstimmt und die Ab-handlung in dieser oder ähnlicher Form noch nicht anderweitig als Promotions-leistung vorgelegt und bewertet wurde.

....

Place   Date   Signature

Acknowledgements

Abstract

Agriculture and food security are some of the main drivers of strong societies, essentially propelling countries' economies. However, the reality is that buffeted by climate change, urbanization and accompanying unsustainable human activities, crop yields have been on a monotonic decline. With the advent of freely available high resolution optical and radar images, a paradigm change in agriculture mapping and crop monitoring has been witnessed. The objective of this study was to map the maize fields in Trans Nzoia county and monitor the growth conditions from optical images (Landsat-8– L-8, RapidEye- RE, and Sentinel-2– S-2), and radar images (TerraSAR-X- TSX, and Sentinel-1- S-1) during the 2015 cropping season, and explore the integration of the results in policy advise. 18 large scale maize fields with existent field management data were selected, and their field leaf area index (LAI) modeled. The field areas were extracted from the satellite images and compared to the field areas reported by the farmers. Classification of various combined sets of the optical and radar images was carried out as well, for crop type mapping. Monitoring of the maize using the optical images involved relating the vegetation indices (VIs) (EVI2, SAVI, NDVI, NDVIre and gNDVI) from L-8 and RE images, whereas the 2016 S-2 LAI values validated the field modelled LAI. On the other hand, monitoring of the maize with radar images involved analysing the image backscatter (BS) values for the cropping season. This was threefold: the analysis of the TSX and S-1 BS values separately; comparison of TSX and S-1 BS values; comparison of the 2015 and 2016 S-1 BS values. The maize phenological growth stages were described by the **B**iologische **B**undesanstalt, **B**undessortenamt und **CH**emische Industrie (BBCH) scale. From the results, 38% of the maize fields reported similar areas between the satellites measured areas, and the reported areas recorded by the farmers, 33% of the fields' areas were overestimated while the remaining 29% were underestimated. Combining the TSX, RE, and RE-NDVIre images achieved the best classification results (user accuracy -72%, producer accuracy -89%). The line of best fit for modeled LAI against the VIs plots was linear with R^2 values of 0.88 (0.07 RMSE), 0.81 (0.09 RMSE), 0.8 (0.07 RMSE), and 0.82 (0.04 RMSE) for EVI2, SAVI, NDVI and gNDVI respectively. Due to unavailability of images during the cloudy early season, the conventional exponential LAI vs VIs model fits was not realized. Validation of the 2015 modeled LAI with 2016 S-2 LAI achieved an R^2 of 0.54 (RMSE 0.31). Fewer validation points were available during the early crop season due to cloud influence on the S-2 images. The fields S-1 BS values were grouped according to the cultivated maize varieties, the fields' orientation, and the planting dates. Of the three factors, the fields' orientation had the greatest influence on the BS curves. The backscatter values increased during the rapid growth stages, before saturating at BBCH 7, and later decreased towards senescence. The phenological stages were identifiable from the image backscatter values, with either a sudden increase or decrease in the backscatter values at the main growth stages. Comparing S-1 to TSX, similar BS curves were observed for the various

phenological stages, though TSX BS values were higher than the S-1 values. For the 2015 and 2016 S-1 BS values comparison, the VV ascending IW1 mode produced the best results in comparing the maize phenological characteristics from one year to the next. Estimation of the field sizes from satellite images provided a fast, accurate, and cost effective method of acreage estimation which would improve yields estimations. With the increase in the number of freely available high-resolution optical and radar satellite images, and with a high repeat cycle, crops can be monitored for the entire cropping season. The phenological analysis of the backscatter values provides a tool in the monitoring and evaluation of the maize fields for the entire season, independent of weather conditions. A reference baseline from S-1 backscatter values can be formulated for maize monitoring during subsequent years. The study provides evidence and results in support of the implementation of satellite data in the formulation of policy towards crop monitoring and food security. Policy areas include: elimination of fraud in the provision of government subsidies occasioned by the overestimation of field sizes; making timely decisions on the need for maize importation in the event of a poor crop season; adoption of irrigation policies to complement the rains in cases of poor rain seasons.

Zusammenfassung

Landwirtschaft und Ernährungssicherung sind Grundpfeiler starker Gesellschaften, da sie nationale Wirtschaften wesentlich voran bringen. Trotzdem unterliegen die Ernteerträge jedoch starken Schwankungen aufgrund von Klimawandel, Urbanisierung und weiterer nicht nachhaltiger menschlicher Aktivitäten und erfahren einen stetigen Rückgang. Mit dem Aufkommen frei verfügbarer hochaufgelöster optischer und Radarbilder wurde ein Paradigmenwechsel in der Kartierung von Landwirtschaft und deren Erträgen. Ziel dieser Arbeit war die Kartierung von Maisfeldern im Trans Nzoia Bezirk, die Beschreibung der Wachstumsbedingungen im Jahre 2015 mit Hilfe von optischen Bildern (Landsat-8– L-8, RapidEye- RE und Sentinel-2– S-2) und Radarbildern (TerraSAR-X- TSX und Sentinel-1- S-1)und die Evaluierung von Möglichkeiten, die Ergebnisse in politische Empfehlungen aufzunehmen. Hierfür wurden 18 großflächige Maisfelder mit bekannten Feldmanagementinformationen ausgewählt und deren Blattflächenindex (leaf area index, LAI) modelliert. Anschließend wurden die Feldgrenzen aus Satellitenbildern entnommen und mit den Größenaussagen lokaler Bauern verglichen. Zusätzlich wurden unterschiedlich kombinierte Datensätze aus optischen und Radarbildern klassifiziert, um Feldfruchtarten zu kartieren. Die Überwachung des Mais mittels optischer Bilder beinhaltete die Vegetationsindizes (VIs) (EVI2, SAVI, NDVI, NDVIre und gNDVI) von L-8 und RE-Bildern miteinander zu verknüpfen, wohingegen 2016 S-2 LAI-Werte mit feldbasiert modellierten LAI validiert wurden. Das Monitoring des Mais mit Radarbildern wurde durch die Analyse von Rückstreuungswerten (backscatter, BS) von Bildern für die Anbauzeit erreicht. Dies erfolgte auf dreierlei Weise: durch getrennte Analyse der TSX und S-1 BS-Werte; durch Vergleich von TSX und S-1 BS-Werten; und durch Vergleich der 2015 und 2016 S-1 BS-Werte. Die phänologischen Wachstumsphasen des Mais wurden mit der Skala der **B**iologischen **B**undesanstalt, **B**undessortenamt und **CH**emischen Industrie (BBCH) beschrieben. In den Ergebnissen entsprachen 38% der satellitenbasierten Maisfeldgrößen denen der von Bauern angegebenen Feldgrößen, 33% der Felder wurden überschätzt, während die verbleibenden 29% unterschätzt wurden. TSX, RE und RE-NDVIre Bilder in Kombination erzielten die besten Klassifikationsergebnisse (Nutzergenauigkeit -72%, Herstellergenauigkeit -89%). Die R^2-Werte der Ausgleichsgerade für den modellierten Blattflächenindex und für die VIs waren linear mit 0,88 (0,07 RMSE), 0,81 (0,09 RMSE), 0,8 (0,07 RMSE) und 0,82 (0,04 RMSE) jeweils für EVI2, SAVI, NDVI und gNDVI. Aufgrund fehlender Bilder für die bewölkte Zeit der Wachstumsphase wurden Vergleiche von konventionellen LAI vs. modellierten VIs nicht durchgeführt. Die Validierung des modellierten 2015 LAI mit dem 2016 S-2 LAI erreichte ein R^2 von 0,54 (RMSE 0,31). Es waren weniger Validierungspunkte während der frühen Anbausaison wegen Wolkeneinflusses auf

S-2-Bilder vorhanden. Die S-1 BS-Werte der Felder wurden nach der angebauten Maissorte, nach der Ausrichtung des Feldes und nach dem Datum der Aussaat gruppiert. Von diesen drei Faktoren hatte die Ausrichtung den größten Einfluss auf die BS-Kurven. Die Rückstrahlungswerte stiegen während schneller Wachstumsphasen an, bevor sie in BBCH 7 den Sättigungspunkt erreichten und mit der Pflanzenalterung sanken. Die phänologischen Phasen waren in den Rückstrahlungswerten der Bilder erkennbar, entweder in plötzlichem Anstieg oder Abfall der Rückstrahlungswerte während der Hauptwachstumsphasen. Beim Vergleich von S-1 und TSX wurden ähnliche Kurven verschiedener phänologischer Stadien beobachtet, wobei TSX BS-Werte höher waren als S-1 Werte. Eine Gegenüberstellung der S-1 BS-Werte aus 2015 und 2016 ergab für den VV aufsteigenden IW1-Modus die besten Ergebnisse für einen annuellen Vergleich der phänologischen Charakteristika von Mais. Die Abschätzung der Feldgrößen anhand von Satellitenbildern erwies sich als eine schnelle, genaue und kosteneffektive Methode, welche Ertragsschätzungen verbessern würde. Mit zunehmender freier Verfügbarkeit hochaufgelöster optischer und Radarsatellitenbilder, mit einhergehenden hohen Wiederholraten, können Feldfrüchte über die ganze Anbausaison überwacht werden. Die phänologische Analyse der Rückstrahlungswerte liefert ein Werkzeug zum Monitoring und der Evaluierung von Maisfeldern über die ganze Saison hinweg, unabhängig von der Wetterlage. Eine Referenzgrundlage der S-1 Rückstrahlungswerte kann für das Maismonitoring während der nächsten Jahre erstellt werden. Die Studie liefert Beweise und Ergebnisse, die den Nutzen der Einbringung von Satellitendaten während des Entwurfs politischer Strategien für landwirtschaftliches Monitoring und für die Ernährungssicherung stützen. Die Bereiche politischer Handlungsfelder beinhalten hier: die Beseitigung des Erschleichens gesetzlicher Fördermittel durch Überschätzung von Feldgrößen; rechtzeitige Entscheidungen für Maisimporte im Falle einer schlechten Erntesaison; und die Umsetzung von Bewässerungsstrategien, um Regenfälle im Falle schlechter Regenzeiten zu ergänzen.

Table of contents

List of Figures

List of Tables

List of Abbreviations

ADC	Agricultural Development Corporation
BBCH	**B**iologische **B**undesanstalt, **B**undessortenamt und **CH**emische Industrie
DEM	Digital Elevation Model
EVI2	Enhanced Vegetation Index-2
gNDVI	Green Normalized Difference Vegetation Index
KSC	Kenya Seed Company
LAI	Leaf Area Index
L-8	Landsat-8
NDVI	Normalized Difference Vegetation Index
NDVIre	Normalized Difference Vegetation Index red edge
ppd	Plant Population Density
RE	RapidEye
SAR	Synthetic Aperture Radar
SAVI	Soil-Adjusted Vegetation Index
SDGs	Sustainable Development Goals
S-1	Sentinel-1
S-2	Sentinel-2
TSX	TerraSAR-X
$\sigma°$	Sigma nought
$\beta°$	Beta nought
$\beta°_{dB}$	Beta nought (decibels)
RS	Remote Sensing

1. Introduction

The introduction chapter highlights the background, motivation and problem statement of the study. The objectives of the study and a review of the previous research partaining the topic of this study are described as well.

1.1 Background

Agriculture sector remains the backbone of Kenya's economy contributing about 25 percent to the Gross Domestic Product (GDP) of the country, with maize remaining the main staple food despite reduced productivity over the years (Louwaars, 2005). With over 2 million hectares of Kenya's land being under small-and large-scale maize cultivation, a majority of Kenyans depend on maize as an income-generating crop (Renard & Storr, 2014). The sector accounts for 65 percent of the country's total exports and provides more than 60 percent of informal employment in rural areas (Kenya National Bureau of Statistics, 2016). About 63 percent of the Kenyan population lives in the rural areas and derives its livelihood directly or indirectly from agriculture. It is the source of livelihood for most of the rural population, inevitably making it key to food security and reduction of poverty. The performance of the agricultural sector in Kenya is an indicator of the performance of the country's economy as a whole, with a decline in the agricultural growth leading to a decline in the gross domestic product (GDP) and employment as well (Alila & Atieno, 2006). Agriculture is also the determinant of equity in development, fundamental to reducing poverty and hunger (Kenya National Bureau of Statistics, 2016). Despite this major role played by agriculture towards the country's economy, it remains highly dependent on rainfall, such that any disturbance in the rainfall distribution patterns not only affects the amount of yield production, but also exposes the maize crops to attacks by various pests and diseases, for example maize lethal necrosis disease (MLND) (Dixit et al., 2011). In 2014, for example, the maize production declined by 4.2 percent to 39.0 million bags (one bag of maize weighs 90 kilograms) in the country's central, eastern, and coastal maize production zones, attributed to the poor rains and attacks by MLND (Kenya National Bureau of Statistics, 2015). In 2015, the maize production increased by 9.0 percent to 42.5 million bags from 39.0 million bags in 2014 as a result of improved weather condition and reduced incidences of the MLND (Kenya National Bureau of Statistics, 2016). Again, in 2016, there was a decline from 42.5 million bags in 2015 to 37.1 million bags due to a persistent drought that impacted negatively on the agriculture sector, and incidences of the MLND (Kenya National Bureau of Statistics, 2017). MLND, which is a combination of two plant viruses can cause

nearly 100 percent crop loss, has been a persistent maize disease in Kenya since 2011 (Renard & Storr, 2014). With over 3.6 million tons of maize being required to feed the country's population annually, the yearly fluctuation in the yield amounts creates an unreliable food insecurity situation.

Over the years, the Kenyan government has continued to enact laws, legislation, and policies geared towards strengthening the agriculture sector in order to increase food security. These policies have been found to address the main goals of increasing productivity and income growth, and which revolve around: enhanced food security and equity; emphasis on irrigation to introduce stability in agricultural output; commercialisation and intensification of production especially among small-scale farmers; appropriate and participatory policy formulation and environmental sustainability (Alila & Atieno, 2006). Key among the policies is the Kenya Vision 2030 agenda (2008-2030) (Government of Kenya, 2007). This is the long-term development blueprint for the country aiming at transforming the country into a newly industrializing middle-income country, providing a high-quality life to its citizens by 2030. It comprises of three pillars: Economic, Social and Political. The agriculture sector is placed under the economic pillar, whose flagship projects include the preparation and passage of consolidated agricultural policy reform legislation and converting idle land into agricultural land (United Nations, 2017). Implementation of the Vision 2030 agenda would also be directly linked to the achievement of the Sustainable Development Goals (SDGs) for Kenya, and in this particular case, the second SDG that aims at ending hunger by achieving food security and improved nutrition and promoting sustainable agriculture (de Zoysa, 2015). This is through the promotion of the land area under productive and sustainable agriculture by ensuring sustainable food production systems and implementing resilient agricultural practices that increase productivity and production. However, despite the formulation of these numerous policies and legislation, food insecurity remains a perennial issue in the country, with notable delays in the implementation of the set time lines. One of the reasons attributed to delays in implementation is the lack of political goodwill and bureaucracy (Parry et al., 1988a; Waswa & Juma, 2012). Before the promulgation of the new Kenyan constitution in 2013, the country was divided into 8 administrative units called provinces. The central government was in charge all state organs and functions, for example, agriculture and health. Any decisions made would then be cascaded down to the respective administration units (Kenya, 1963). This resulted in a delay in implementation due to the levels of bureaucracy involved. With the promulgation of the new Kenyan constitution however, the provinces were abolished and in their place 47 county governments formed (Kenia, 2013). One of the objectives envisaged in this devolved system of government was the decentralization of some of the state organs, their functions, and services. Among the decentralized state organs was agriculture, with the national government being charged with the national

agricultural policy formulation, and the county governments being charged with the running of the agriculture organ (Kenia, 2013). This meant that the running and management of the agricultural sector in the country was now disaggregated to the county level, with counties having the mandate of running and reporting on the agriculture output (Kenya National Bureau of Statistics, 2016). The governments at both the national and county levels are therefore distinct and inter-dependent, expected to conduct their mutual relations based on consultation and cooperation. It was envisaged that the counties would hence formulate local policies tailored to addressing specific challenges facing agriculture in their areas of jurisdiction, in addition to faster implementation of policies since the bureaucracy chain was cut down (Kenia, 2013). Policy formulation process however also requires support by up-to-date data and information (Timmer et al., 1983). Remote sensing techniques provide a fast and cost effective data collection approach, compared to data acquisition from ground field visits (Waswa & Juma, 2012). The country's needs for remote sensing techniques was already realised in the 1970s when aerial photos were used in the ecological and agriculture monitoring (Mwidau, 1990). The lack of availability of high-resolution imagery however limited the application of remote sensing in field-scale agriculture mapping. This challenge was coupled with the unavailability of cloud free images covering the entire cropping season from planting to harvesting (Sabour et al., 2008). However, with the increased number of satellite sensors at various resolutions, and availability of radar images to complement the optical images, application of satellite images in the mapping of agriculture fields, at both large scale and small scale fields has increased (Burke & Lobell, 2017).

1.2   Motivation and Problem Statement

According to the (FAO, 2017) report, there has been an increase in maize production over the years in the country (**Figure 1.1**). However, this has translated neither to improved food security nor to decreased poverty rates due to the increase in the cost of production per hectare of land (**Figure 1.2**), coupled with both pre harvest and post harvest grain losses (FAO, 2017). In addition, the rural population in the country is on a steady increase (**Figure 1.3**). This population increase has led to a decrease in land sizes, occasioned by uncontrolled subdivision of the fertile agricultural land (Burke & Lobell, 2017). Visualizing the extent to which the subdivisions and the consequent land use changes have affected maize production at the county level remains a challenge due to the lack of up to date land use maps. Field-based investigations are hardly of sufficient length to establish robust relationships between factors influencing crop growth, (for example rainfall amounts, rainfall distribution, daily temperatures), and the resultant crop responses to contrasting management practices

(Dixit et al., 2011). This is mainly due to the expenses involved with carrying out physical field visits to monitor maize growth. There has therefore been a need to employ more inexpensive methods that supply data continuously with frequent revisit periods, that are operationally sustainable, timely and with a wide geographical coverage (Attema et al., 2009; Drusch et al., 2012; Kihara et al., 2012). Georeferenced high-resolution satellite images provide a convenient approach in extracting the land use information (Burke & Lobell, 2017). Thus, freely available high-resolution satellite images can be applied to identify maize fields within the study area. Furthermore, the field boundaries can be mapped, and the actual area size under cultivation estimated. Tapping into the potential of satellite data, both optical and radar in monitoring the crop growth and development, it would be possible to monitor the maize from germination to senescence (Sabour et al., 2008). This is by relating the amount of reflectance emitted from the maize crops' surface to the crops' structure at the different phenological stages. The maize phenological growth stages are described by the **B**iologische **B**undesanstalt, **B**undessortenamt und **CH**emische Industrie (BBCH) scale (Meier, 2001). Tropical regions like Kenya unfortunately have frequent cloud cover occurrences that hinder image acquisition with optical sensors (Castillejo-González et al., 2009; Devadas et al., 2012). This results in the lack of optical images covering the entire cropping season and therefore gaps in the data. Given that radar sensors are independent of weather conditions, and can therefore collect data for the entire cropping season (Baghdadi et al., 2009; Gao et al., 2013; Mróz & Mleczko, 2008; Sabour et al., 2008; Woodhouse, 2006), combining optical sensors with radar sensors ensures coverage of the entire cropping season. A regional adapted method should then be developed to routinely monitor the maize fields throughout the entire cropping season.
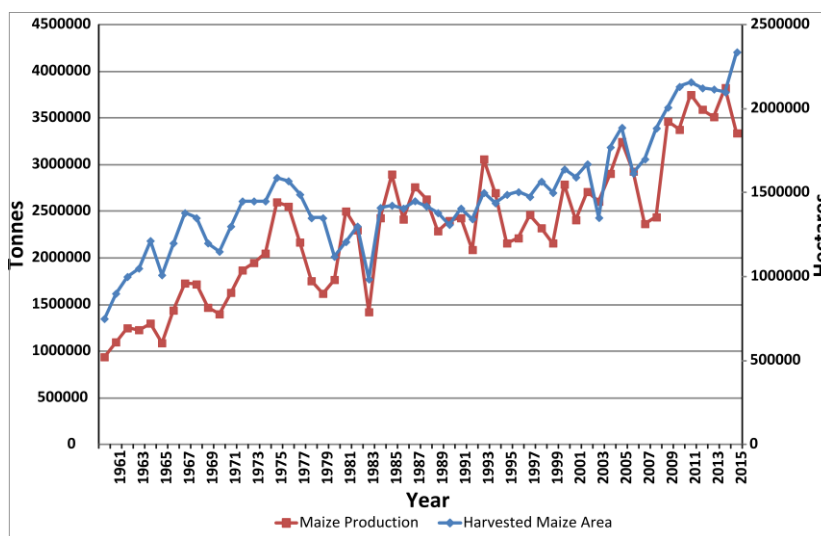
Figure 1.1: Linear graph showing Kenya's maize production estimate in Tonnes, and the harvested maize area estimate in Hectares, for the years 1961 to 2016. Source (FAO, 2017).
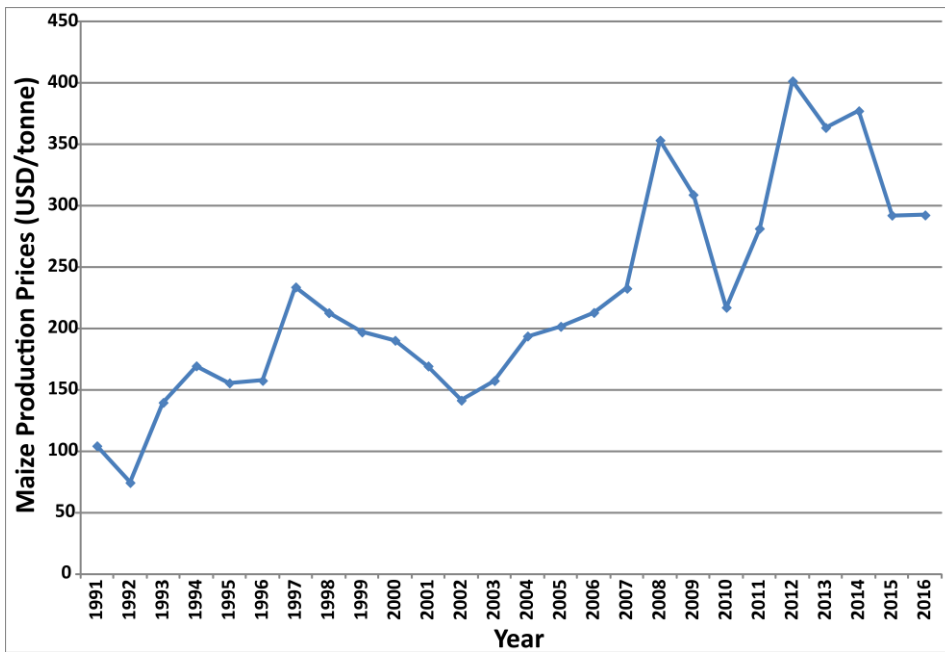
Figure 1.2: Linear graph showing Kenya's maize production cost in US dollars per tonne (USD/tonne) for the years 1961 to 2016. Source (FAO, 2017).
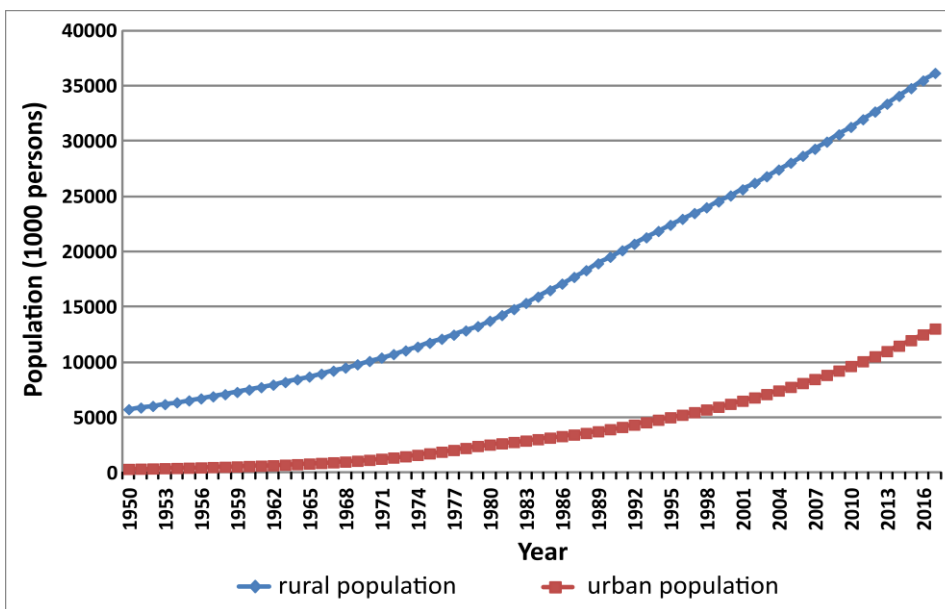
Figure 1.3: Linear graph showing the population growth change in Kenya from the 1950s to 2017, in both the rural and urban areas. The high increase in the rural population growth leads to the subdivision of agricultural land due to the population pressure, which is a major concern for the attainment of food security. Source (FAO, 2017).

Lack of data and information to support policy formulation in the agriculture sector in order to advise the policy decision makers in a timely and accurate manner has been noted as one of the challenges in Kenya (Timmer et al., 1983; Waswa & Juma, 2012). Despite the necessity of this agricultural data by a wide spectrum of stakeholders, ranging from decision-makers in government, the private sector, academia for research and teaching and the international community, a comprehensive census of agriculture has not been carried out in Kenya since independence in 1963 (Kenya National Bureau of Statistics, 2016). Production of agricultural indicators has been through sample surveys estimation, deeming them unverifiable due to lack of adequate benchmark indicators. The lack of a comprehensive census has been attributed to meagre allocation of resources, limited awareness in national and county governments on the importance of statistics, lack of a policy on agriculture, and lack of data availability for monitoring and evaluation purposes (Waswa & Juma, 2012). Previous research has highlighted the integration of remote sensing data in policy formulation (Soria-Ruiz et al., 2009; Juma, 2015). Thus, with an increase in the number of freely available high-resolution and high temporal optical and radar satellite images covering the country, data and information relating to maize crop mapping and monitoring will be collected on a regular and continuous basis. The output of the data analysis on the collected data would then form a basis upon which future policies formulation relating to maize farming and crop mapping in general shall be based.

1.3 Research Identification

1.3.1 Research Objectives

General objectives

The main objective of this research was to map the large-scale maize fields at field level using high-resolution radar and optical satellite images, to monitor the maize throughout the cropping season, and demonstrate possible policy areas into which these research findings can be integrated to advice the policy formulation process. Due to cloud cover that affects the optical images, combining of optical and radar images ensured that images are available for the entire cropping season (Guissard et al., 2005). The study focused mainly on the government owned large-scale farms that grow maize for commercial purposes and maintain crop management records for the monitoring of the crop during the cropping seasons. Maize fields owned and run by the government parastatals were selected since the top management of these parastatals are from time to time, either consulted before the implementation of agriculture policies, or are selected and appointed in committees that formulate the agriculture policies. They can therefore influence the policy decisions made by the government. Thus,

the results of this research will provide proof and evidence on the advantages of incorporating remote sensing data into agriculture mapping.

In order to achieve this general objective, three specific objectives were identified.

Specific objectives

- *Development of methods to map the areal coverage of selected large-scale parastatal fields under maize crops.* To date, the farms rely on over 40 years old sketch maps indicating the field boundaries as per the initial subdivisions following the incorporation of the Agriculture Development Corporation (ADC) (Government of Kenya, 1965). This however more often than not does not tally with the actual field size under cultivation. In some instances, for example, the edges around the fields are usually left unplanted, while in others, only a section of the field is cultivated. Despite this, the field size captured in the farm management records is usually the total field size. Carrying out ground surveys to map the maize fields is unfortunately an expensive exercise. With the aid of the high-resolution satellite images throughout the cropping season however, the actual planted area per field can be estimated (Carletto et al., 2015; Gallego et al., 2014). In this study therefore, the estimated planted maize area on the fields were derived from the acquired high resolution optical and radar images. The area estimation was done after germination and just before harvest to not only provide more accurate maize crop areas, but also provide an estimate of the maize loss by comparing the cropland change between planting and harvesting.

- *Establish phenology based maize assessment by assessing maize phenological conditions in the fields from SAR backscatter and optical vegetation indices.* The maize BBCH-scale phenological stages, from germination to senescence, are characterized by various physical changes in the maize plants. One of these changes is in the increase in the leaf sizes, from which the leaf area index (LAI) is derived. Radar backscatter values and the optical vegetation indices can be expressed as a function of phenology by establishing a relationship between the LAI and the backscatter values (Gao et al., 2013; Guissard et al., 2005), and between LAI and the vegetation indices (Kross et al., 2015). In this study therefore, a region specific LAI model for the maize varieties cultivated within the study area was developed based on the ground LAI collected during the fieldwork. A relationship between the model LAI and the images backscatter values and vegetation indices was derived. This relationship once established can serve as an indicator of the maize growth status in the field up until harvest. The farmers shall thus be equipped with

information to enable them undertake timely mitigation measures, if need be, before the crop is damaged. In addition, from the general BBCH-scale description (Meier et al., 2010), a locally modified BBCH-scale was derived based on the local growing conditions and the maize varieties grown within the study area.

- *Application of the remote sensing findings in supporting the formulation of policies affecting food production.* Policies for agriculture consist of government decisions that influence, directly or indirectly, the level and stability of input and output prices, public investments affecting agricultural production, costs and revenues and allocation of resources (Alila & Atieno, 2006). Policy formulation and review is a continuous process that needs to be advised and supported by new research findings, in order to address any shortcomings in the existing policies (Juma, 2015). The remote sensing research findings in this study sought to address policy gaps that were geared towards promoting food security and the attainment of SDGs. The target policies are those formulated at a local scale (farm level), at a regional scale (county level) and at a national scale (country level). At the local scale, the focus was at policies addressing mainly the farming practices. For example, farmers would be advised on the best cropping and management practices for optimal production, based on the crop monitoring results from the satellite images analysis. At the regional scale, the policies target the involvement of the county governments in supporting the farmers with local services and interventions when needed. For instance, in cases where the remote sensing results predict a good cropping season, policy guidelines on availing transport and storage facilities to the farmers can be formulated. At the national scale, the policies stipulating the involvement of the national government towards supporting agriculture, and specifically maize production, will be targeted. An example is, when the government decides to extend credit facilities and subsidies to the farmers. These facilities can be provided based on the estimated cultivated area. Thus, with the mapping results from the remote sensing data in this study, a database containing the maize cultivated area is created, against which the cultivated areas provided by the farmers can be verified. This in turn would reduce on the level of fraud especially in cases where farmers overestimate their planted areas.

1.3.2 Theoretical Basis for the Study

This section is based on the identified research objectives and the methodological approach applied in this study.

1.3.2.1 Improvement of crop production and the associated challenges

The ability to accurately estimate the expected crop yield, coupled with proper economic policies, is critical for any country's food security (Thornton et al., 1997). The agriculture sector plays a major role in Africa in as far as food security is concerned (Dixit et al., 2011). It however remains majorly rain fed hence making the production environment very sensitive to relatively small variations in climate (Kirimi, 2012; Parry et al., 1988b). Climatic aspects such as precipitation frequency and amplitude, length and moment of frost periods and daily sun hours influence crop development. Any shift in either of these aspects due to the lately notable changes in the global climate ultimately also lead to a shift in the crop development times and influences the choice of crops cultivated (Apfelbeck et al., 2007). Whereas climate change is a detectable and evidenced global phenomenon, its manifestation at the regional scale can be difficult to identify (Tadross et al., 2009). This is because of the low density of weather observations, especially in the rural agriculture areas. Changes in the rainfall pattern hugely impacts on maize cultivation with respect to the crop phenological cycle, which is critically dependent on the timing of the rains (Tadross et al., 2009). Failed rains, delayed rains, or scanty rainfall in crop growing areas have been identified as a major influence of food security (Dixit et al., 2011). Irrigation as a mitigation measure to the failed rains has been proposed. An example is the irrigation of maize fields during the hot weather season in France (Battude et al., 2016). Birch et al. (1998) applied irrigation as well to ensure that non-limiting conditions associated with crop water stress were avoided. Maize under irrigation has been established to have higher production and performance compared to non-irrigated maize (Nguy-Robertson et al., 2012). Irrigation is however, a capital-intensive practice that needs harvesting and storage of rainwater for use during the dry season. In instances where natural water sources such as rivers are to be used, polices and guidelines are necessary to control access and ensure non destruction of rainfall catchment areas, good management of government irrigation schemes, non-degradation of surface water, and controlled exploitation of underground water (Parry et al., 1988a).

In addition to the overreliance on rain fed agriculture, other factors attributed to reduced agricultural production and food availability include poor weather, crop disease, ecological degradation, failure of national input supply and marketing systems, poor farm management, market forces, resource

limitations, storage problems, import and distribution constraints, and political and economic marginality (Parry et al., 1988b). In order to mitigate these food insecurity factors, there has been a lot of research revolving around agriculture, and more specifically maize production in Kenya, since post-independence in 1963 (Alila & Atieno, 2006). A lot of research has been centered on increased food production, intensification and extensification of agriculture in the country. One of the outcomes of this research has been the development of new maize varieties that are suited for various climatic zones in the country (Allan & Allan, 1971). The influence of various environmental factors on maize growth and the expected yields has been investigated as well. For instance, Cooper (1979) explored the association between altitude, environmental variables, maize growth and yields in Kenya and concluded that yield decreased with a decrease in altitude due to the differences in the number of grains per plant. Law and Cooper (1976) and Cooper and Law (1977) examined the association between soil temperature and maize yield variations in the Kenyan highlands, concluding that a decline in yields associated with late planting was not due to water stress but rather to low soil temperatures during the growing season. Hawkins and Coooper (1981) investigated the influence of grain number and grain weight on the final grain yield. Incidences of infestation of the maize fields by weeds (Odhiambo et al., 2015), and attacks by pests like the army worms (Daily Nation, 2017) have also been reported. Maize has been found to be sensitive to farm management practices like plant population density (Sangoi, 2001) and soil nutrient composition (Ngome et al., 2012).

Given the great impact agricultural production has on Kenya's economy, coupled with environment, industrial and political effects, there is a need for increased complementarities among information, technology, and public intervention to monitor agricultural areas (Parry et al., 1988b; Sabour et al., 2008). This can be realised through improved information on agro climatic potential and improved use of new agricultural technologies to increase production potential in good years and reduce losses in poor years. Application of remote sensing is considered part of the improved technologies required to increase agriculture production (Parry et al., 1988b; Juma, 2015).

1.3.2.2 Application of remote sensing in crop production

Remote sensing techniques provide a very cost effective, reliable, and continuous means of monitoring cultivation activities by matching ground reference data collected from the fields to satellite information (Sabour et al., 2008). Satellite images provide non-contact and non-destructive observation methods of crops and their biophysical variables e.g. leaf area index (LAI) and biomass, with field observations being extrapolated to larger scales (Esch et al., 2014). There is however a challenge in

scaling local field observations crop conditions and yield monitoring to a regional scale using satellite imagery as some of the plant processes, for example gas exchange of single leaves, are difficult to upscale (Doraiswamy, 2004). Crops show highly variable seasonal characteristics as well, depending on the geographical region, local climate, sowing dates, weather conditions during the vegetation period, equipment and behavior of the farmer, or cultivation cycle and harvesting times (Esch et al., 2014). Availability of cloud-free images covering the entire cropping cycle, especially during the wet season, is a challenge (Esch et al., 2014). Thus, matching of collected ground reference data to the satellite images becomes difficult (Mohd Noor, 2013). To overcome this challenge, various approaches have been proposed. First is the approach of using a single image captured at an optimal time for the estimation of the yields (Wang et al., 2010). A second approach would be combining of image data from different sensors to not only provide for the continuous monitoring of crop seasonal development trends, but to shorten the revisit cycle as well (Vinciková et al., 2010; Shang et al., 2014a). Before combining images from different sensors however, factors like the images resolution, the preprocessing and evaluation requirement of the images, their price and format, and the time needed for the acquisition or delivery, are considered (Vinciková et al., 2010). The final approach is the integration of optical and radar satellite data (Guissard et al., 2005). Radar data is independent of weather conditions and therefore can capture information all year round, thus increasing the monitoring temporal frequency (Guissard et al., 2005; Sabour et al., 2008).

In order to analyze the satellite images, and retrieve the information pertaining to the crops, different strategies have been employed. One strategy involves extraction of vegetation indices (VIs) from the optical images and relating them to the crops biophysical parameters (LAI, biomass) or the estimated yield production (Schmidt et al., 2015). For instance, Ramoelo et al. (2012) estimated the leaf or canopy nitrogen content from space with RapidEye red-edge channel. Battude et al. (2016) estimated the maize biomass and yield using Sentinel-2 NDVI (R=0.92; RRMSE=3.5%). Lewis et al. (1998) estimated the maize production in Kenya using a spatial linear regression model in combination with NDVI data from the NOAA advanced very high-resolution radiometer (AVHRR) (r=0.75; p=0.05). Burke & Lobell (2017) coupled high-resolution 1-m Terra Bella images with intensive field sampling campaigns for monitoring and understanding agricultural productivity, and thus predict yield in western Kenya. An accuracy (R^2 up to 0.4) between satellite-based and traditional field survey-based yield estimates was achieved, especially on large fields. Ranson (1985) investigated the effects of the sun angle on maize reflectance and concluded that it was smaller for well-developed maize canopies with high LAI. With reference to radar images, Moran et al. (2012) concluded that there was a positive correlation between cross-polarized Radarsat C-band sigma nought (σ^0_{HV}) and NDVI in the monitoring of both crop and soil

conditions. Vegetation dominated the backscatter values for LAI values greater than 0.5, and saturating at LAI value 4.6. For the dual VV/VH polarized images, Blaes et al. (2006) concluded that vegetation for sparsely vegetated dense fields dominated the backscatter values for LAI values greater than 2.7, and saturating at around LAI value 4.6. Gao et al. (2013) established a relatively strong relationship between the HV cross-polarization and the volume scattering of the maize, which was largely determined by the crown structure. Apart from polarization, the incidence angles also influences the backscatter values. Inoue et al. (2002) concluded that the correlation between backscattering coefficient at X-band and the LAI values over rice fields was slightly better at 35° than at 55° for the HH polarization. Blaes et al. (2006) discriminated various crop conditions between fields of the same region using the co-polarized ratio (VV/HH) computed at low incidence angle (below 35°). Dual-polarizion ratios (VV/VH) computed at high incidence angles (35° to 45°) were found sensitive to maize growth and less sensitive to soil moisture variations. In some instances, both optical and radar satellites have been combined especially in yield estimation. For instance Fieuzal et al. (2017) combined optical and radar satellite images to forecast and estimate wheat and corn yields. Crop monitoring and yield estimation accuracies deteriorate with coarser image resolutions, with higher resolution images providing better accuracies. In addition to the image resolutions, noise in the ground data as well as in the satellite-based estimates may lead to imperfect agreement between satellite and ground-based yield measures (Burke & Lobell, 2017).

Apart from the VIs strategy, field mapping has been undertaken through the classification of the images. Classical classifiers like random forest, maximum likelihood, and support vector machine have been applied. The crops' phenological period was evaluated and then compared to classification results (Sabour et al., 2008). For instance, Lussem et al. (2016) combined Sentinel-1 and RapidEye data to provide a more reliable crop type mapping approach for monitoring and modelling purposes. Mohd Noor (2013) assessed the capability of integrating and analysing socio-biophysical (climate change, agriculture, and food security) and remote sensing information by classifying RapidEye, SPOT-VGT, and NOAA-AVHRR satellite images. Schuster et al. (2012) and Adam et al. (2014) used commercial satellite sensors for land use/cover classification and quantitative estimation of vegetation descriptors. Conrad et al. (2014) established that the overall classification accuracy increased with an increase in the number of acquisition dates selected during distinctive phases of the vegetation period. Kimanga (1986) created an inventory of the rural land use and land cover inventory for purposes of regional and national development planning by providing accurate crop hectarage estimates, and accurate crop cover zones using low-resolution satellite images (79m x 79m).

Estimation of the actual agriculture field sizes under crop cultivation is another area of remote sensing

application. Agricultural data, especially in many African countries, are subject to substantial reporting errors and when gross errors exist in the observations, the reliability of data diminishes which then leads to potentially biased estimates of the relationship between land and productivity (Lewis et al., 1998). For instance Burke & Lobell (2017) and Carletto et al. (2015) noted an average of 1.3% over reporting of field areas when self-reported land sizes were compared with GPS measured land sizes. De Groote & Traoré (2005) observed that large fields tend to be underestimated while small fields are overestimated (11%). Due to the high costs associated with the ground surveying of the fields, high resolution aerial photographs and satellite images are relied upon to provide estimates of field sizes by extracting the agricultural areas, and in effect estimating the land area under agriculture, at both regional and global scales (FAO, 2017). The extracted fields boundaries information is in vector data format, for example the German Official Topographic Cartographic Information System (ATKIS), which is then applied to create a mask of potential agricultural land on which analysis should be focused (Esch et al., 2014). Kimanga (1986) for example extracted accurate crop hectarage estimates and gave accurate crop cover zones using low altitude aerial photography.

Application of remote sensing data in maize phenological mapping involves coupling of the spectral signature that are derived from remote sensing data with corresponding phenological phases (Gerstmann et al., 2015). The daily phenological stages are interpolated from phenological data collected from the field (Moeller et al., 2011; Moran et al., 2012). More accurate results when mapping the maize phenology are achieved when images are selected within the cropping season to ensure that the spectral signatures from the fields represent the planted crops (Bargiel et al., 2010; Sabour et al., 2008). Ground reference data is however vital for the validation process since the spectral signatures of different crop types can be quite similar to each other in some growth stages, depending on their individual phenological stages (Esch et al., 2014).

1.3.2.3   Application of remote sensing in food security policies

Agricultural policies are formulated at several levels of government, with each level having a different analytical focus and need for policy. Most of the policies seeking to address enhanced food security are geared towards addressing food production and marketing issues (Kirimi, 2012; Timmer et al., 1983). For instance, (Alila & Atieno, 2006; Parry et al., 1988a) proposed policies that would intensify agricultural production through the increased use of improved inputs, diversification especially from low to high value crops, commercialisation and intensification of agriculture production, increased value addition through stronger linkages, and emphasis on irrigation to reduce over-reliance on rain-

fed agriculture. Kimanga (1986) proposed the formulation of policy that would address the current land tenure system that allows for uncontrolled subdivision of land parcels, especially for inheritance, and thus eliminating the economies of scale in agriculture production.

International laws and legal principles touching on remote sensing generally focus on three matters of concern. These are: the right to acquire remotely sensed imagery or to launch remote sensing satellites; the right to disseminate remotely sensed imagery without prior consent of the sensed country; and the right to obtain remotely sensed satellite imagery from a particular country (Khorram et al., 2012). Given that satellite observations transcend national boundaries and geophysical space, national laws and policies are rooted in similar fundamental principles allowing access to remotely sensed imagery for scientific, social, and economic benefit, and confining access to protect national security as long as the prerequisite licenses and permissions are obtained (Khorram et al., 2012). The African Union (2016) recognised that the successful implementation of its policy frameworks, which food security is part of, is highly reliant on space technologies and applications. A proposal to develop an African Space Policy was made to provide guiding framework for the development and operationalizing of an indigenous space programme on the continent-level. The proposal to establish the space sector envisaged some challenges. These challenges included: i) the lack of awareness by kenyan policy makers and other stakeholders of the capabilities offered by space-based technologies towards addressing national development challenges; ii) lack of necessary knowledge and skills required to establish and efficiently run a space sector from onset; iii) lack of scalable infrastructure; iv) limited capital to invest in the expensive, time involving and risky space technology despite the unquestionable returns on space investment; v) few willing partners from countries with established space sectors because of the investments involved, national security and fear of encouraging competition to their domestic space industry; vi) restrictions on transferable technology from the countries of origin may hamper the process of building space capability in Kenya; vii) undue conditional technology transfer from some technology transferring countries that may apply political and policy pressure on Kenya to buy space technology systems from them as a precondition to initiate cooperation or for continued technology transfer; viii) unfair competition from well-established countries that unfairly protect their industries; ix) poor leadership, retrogressive policies and lack of political support towards this initiative with some government policies in their present form working against the smooth establishment of a space sector (Waswa & Juma, 2012). Kenya adopted the Africa Space Policy framework through which its national development agenda in health, education, food security and natural resource management would be addressed, in line with the Kenya Vision 2030 agenda (Waswa & Juma, 2012). In terms of agriculture, the space technology would be applied in monitoring of crops and cropping systems with the aim of

improving food security. The implementation of space technology is to be carried out in 8 phases, spanning over a 30-year period. Phases 1 and 2 establish the necessary legal framework and political enabling environment. Phases 3 and 4 establish the space sector by building human, organisational and societal capacity, eventually launching the first experimental satellite in collaboration with its partners. In phases 5 and 6, the country would be capable of independently designing and fabricating space technology parts and subsystems. Finally, in phases 7and 8 the country would have achieved launch capability (Waswa & Juma, 2012).

Remote sensing data has been successfully applied to advise and inform formulation of policy in agriculture. Examples are in the united states through the United States Geological Survey (USGS), Germany through the European Space Agency (ESA), Canada through the Canadian Space Agency, and South Africa through the South African national Space Agency (SANSA) (Khorram et al., 2016). The European Union has used it to support annual land cover mapping for the Common Agriculutural Policy (CAP) (Tapsall et al., 2010). In Kenya, a number of agricultural policy areas and gaps have been identified where remote sensing data is applicable. For example, in the development of infrastructure (public utilities, public works, transportation, and research facilities), remote sensing data can be utilized to identify the inaccessible agricultural areas, on which development should focus on (Juma, 2015). The government provides credit facilities and subsidies to farmers to encourage production (Parry et al., 1988a; Sanchez et al., 2009). Hence, remote sensing data can be used to verify the farmers field sizes and eliminate fraud, in cases where the farmers provides false information. Lack of monitoring and evaluation of many agricultural interventions has been a challenge due to the difficulty and high cost of collecting outcome data (African Union, 2014). Remote sensing provides inexpensive field scale productivity measures from which baseline data for monitoring and evaluation could be established (Burke & Lobell, 2017). In addition, remote sensing data analysis provides data on most of the socio-economic aspects (Juma, 2015). Thus, different entities charged with policy making operations that were working in isolation can now work together (African Union, 2014; Dowman & Kufoniyi, 2010). Finally, government interventions and behaviour towards policy formulation and implementation have at times been unpredictable and uncertain, e.g. decision on import tariff rates, export bans, maize pricing, fertiliser subsidy, thus creating uncertainty in the agriculture sector (Kirimi, 2012). However, with the availability of more supporting data and information, timely and well thought through decisions can be made (Parry et al., 1988b; Stewart & Faught, 1984).

1.3.3   Research Novelty

Lack of up-to-date data and information continues to be one of the challenges influencing policymaking geared towards food security. However, with the availability of free high-resolution Sentinel-2 optical images and Sentinel-1 radar images, a new paradigm of application of remote sensing at the field level in Kenya emerges. The mapping of the cultivated maize fields with satellite images will provide both a more reliable and cost effective area estimation approach. By comparing the area estimates from satellite images with the farmers' reported areas, an approach of analyzing the net impact of overestimation or underestimation of field sizes on the predicted yields, and thus food security within the study area will be explored. On the other hand, the modeling of crop biophysical parameters like the LAI is specific to the dataset from a particular region and therefore cannot be generalized. In this study therefore, a novel LAI model is developed for the maize crops in the study area based on ground reference data, and supported by existing data from previous research. Given the planting date, and the plant population density, the LAI values can be simulated for any point in time within the cropping season, provided there are no drastic changes or alterations in the weather patterns. The Sentinel-2 LAI products then validate the modeling results. In addition a local BBCH-scale, customized from the universal BBCH-scale is developed. The local BBCH-scale describes the maize varieties cultivated in the study area, taking into account the duration taken by the maize from planting to maturity. In addition, a radar backscatter values baseline for the monitoring of the maize crops in the fields is established and tested for the 2015 and 2016 maize cropping seasons. Due to the frequent cloud cover presence during the cropping season, the radar satellite data provides an alternative for mapping and monitoring the crops during the entire growth cycle. The research findings will also serve to convince policy makers on the importance of integrating remote sensing data into the policy formulation process, and thus aid in filling the existing data gap in crop mapping and monitoring.

2. Description of the Study Area

This chapter gives a detailed description of the study area in terms of the geographical location, geology of the area, vegetation, soils and climate.
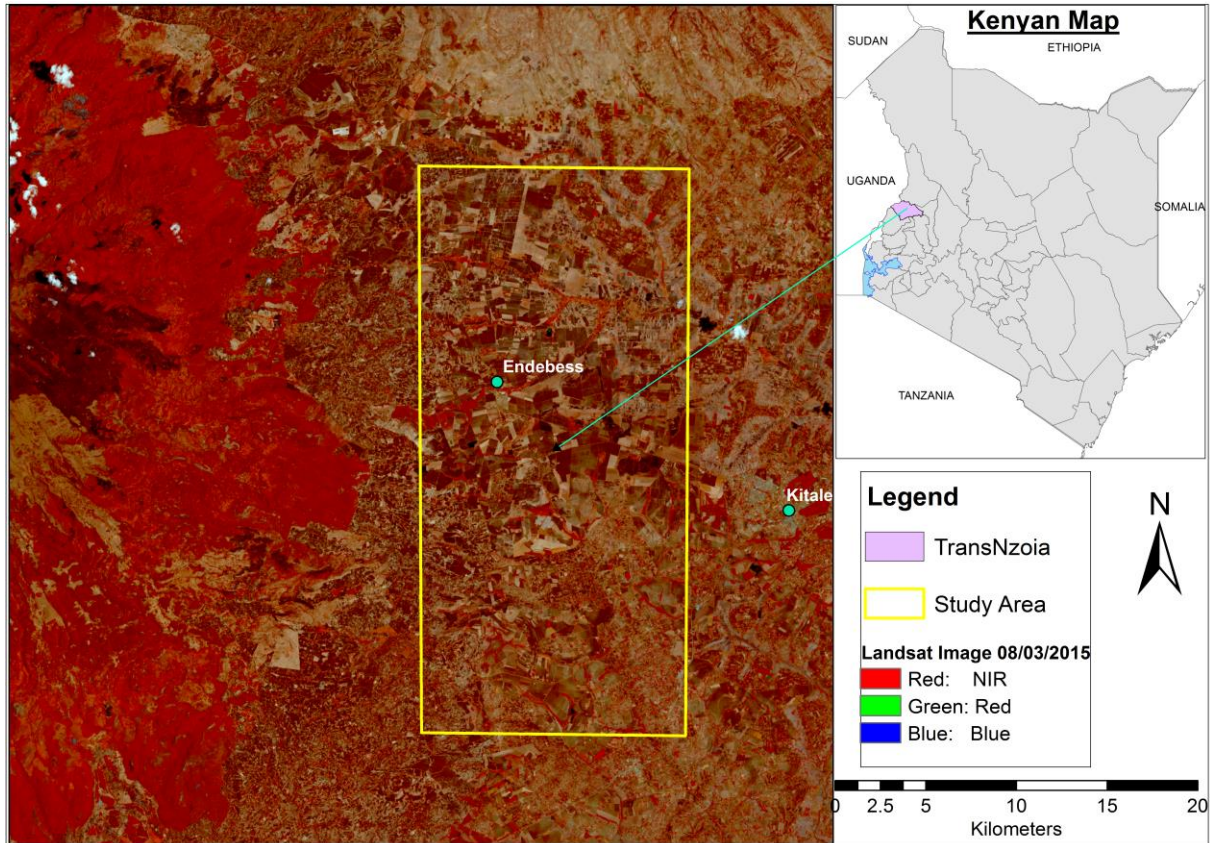
Figure 2.1: The study area in Trans Nzoia County overlaid on a false color composite Landsat 8 image Kenya.

2.1 Geographical Location

The study area (**Figure 2.1**) is located within Trans Nzoia County, Kenya, with center coordinates: latitude 1.067° N, longitude 34.867° E. It is characterized as a highland tropics area (Hassan, 1998) and as an LH3 agro-ecological zone (Ransom et al., 1997). The topography is gently undulating with an average elevation of 1900 meters above sea level that increases towards Mt. Elgon in the west (Dixit et al., 2011). The extent of the study area covers approximately 460 km^2.

The fields considered for this research were under the management of the Agricultural Development Corporation (ADC) Sabwani, ADC Olngatongo, and the Kenya Seed Company (KSC). These are Kenyan government parastatals, which fall under the ministry of agriculture, and are mandated with agricultural research and production in the country. Majority of the fields are more than 5 hectares in

size, which is the minimum size for medium-scale fields (Jayne et al., 2014, 2016; Nyoro et al., 2004). This was an important consideration for the selection of the study area site to avoid field sizes that were smaller in size than the largest pixel size of the remote sensing images that were used (description on the acquired remote sensing data is in **Chapter 3.1**). Another important consideration was the availability of reliable and up to date farm management records from the parastatals. These included information such as planting, weeding, fertilizer application, herbicide application, harvesting dates, and the estimated planting area. This data was necessary for the maize growth analysis step.

2.2   Geology

Due to the presence of the volcanic mountain Mt. Elgon, the area is characterized by igneous or magmatic rocks (Zech, 2016). These are rocks that are formed after solidification of the magma from the volcanic eruption and are widely distributed in the tropics. Depending on the site of the magma solidification, the rocks are subdivided into three, namely the plutonites, the volcanites and the intrusive or dyke rocks. The plutonites were formed following the slow solidification of the magma in deep geological strata, with coarse granitic structure; examples: granite, diorite, and gabbro. On the other hand, the volcanites were formed following the rapid solidification of the magma after eruption on the earth surface, with porphyric or basaltic structure; examples: rhyolite, andesite, porphyrite, basalt, diabase. Finally, we have the intrusive or dyke rocks which were formed after solidification of the magma in the dykes after volcanic eruption (Zech, 2016). Soils in mountainous areas are generally defined by their parent rock, with their minerals being strongly related with those of the parent material. These soils, described in detail in **section 2.3**, are the humic Nitisols which are developed on tertiary basic igneous rocks (basalts, nepheline phonolites; basic tuffs included) and the eutric nitosols which are developed on basic igneous rocks (basalts, etc) (Jaetzold & Schmidt, 1982).

2.3   Soils

The differences in soil properties (color, grain size, structure, etc.), allows for the distinction in soil horizons/layers. The soil horizons are a good indicator of the soil-forming processes, and their sequence along a vertical cut through soil profile is crucial for soil classification (Zech, 2016). The area around Endebess consists of humic and eutric Nitisols (Gachene & Kimaru, 2004). Nitisols, which are predominant in the slope position of volcanic landscapes and developed from volcanic rocks (**section 2.2**), are characteristically red, dark red or dark reddish brown in colour, with the organic matter

content, cation exchange capacity and percentage base saturation ranging from low to high (Jaetzold & Schmidt, 1982). These soils occur in the highlands and on volcanic foot slopes and are found extensively in the central highlands of Kenya, some areas of the Ethiopian highlands, and around Mts. Elgon and Kilimanjaro (Dewitte et al., 2013). The Nitisols soil, which has diffuse horizon boundaries, is about 150 cm deep or deeper, with evidence of clay movement within the profile. It is well drained with a favorable moisture-storage capacity and aeration. Most Nitisols are acidic (a low pH value of less than 5.5) due to the leaching of soluble bases (Onyatta & Huang, 1999). Their physical and chemical properties compare favorably to those of most other tropical soils and are some of the best agricultural soils found in the region (Muchena & Gachene, 1988).

2.4   Vegetation

The natural vegetation characterizing the study area is high moisture savannah, which is described as a savannah occurring under high rainfall and characterized by thickly scattered broad-leafed trees, and a herbage composed of tall grasses (150-240 cm) (Edwards, 1940). However, due to the conducive climate and soil conditions, the area is also characterized by both large scale and small scale agricultural farming activities (Moore et al., 2014). Some of the crops that are grown in the area for both commercial and subsistence farming include maize, wheat, sugarcane, coffee, beans, sunflower, potatoes, among others. Maize however remains the predominant crop and is grown either for silage, as seed maize or for commercial purposes.

2.5   Climate

The climate in the study area is characterized as tropical savanna climate (Kottek et al., 2006; Peel et al., 2007). The area is considered a high potential maize growing area, with long duration maize hybrids being widely grown (FURP, 1987). It receives an average annual rainfall ranging between 970 - 1300 mm and distributed in a uni-modal rainfall pattern largely between March and October (Government of Kenya, 2012; Kottek et al., 2006) with a mean annual temperature of 18.6°C (Jaetzold & Schmidt, 1982). This is shown in (**Figure 2.2**).
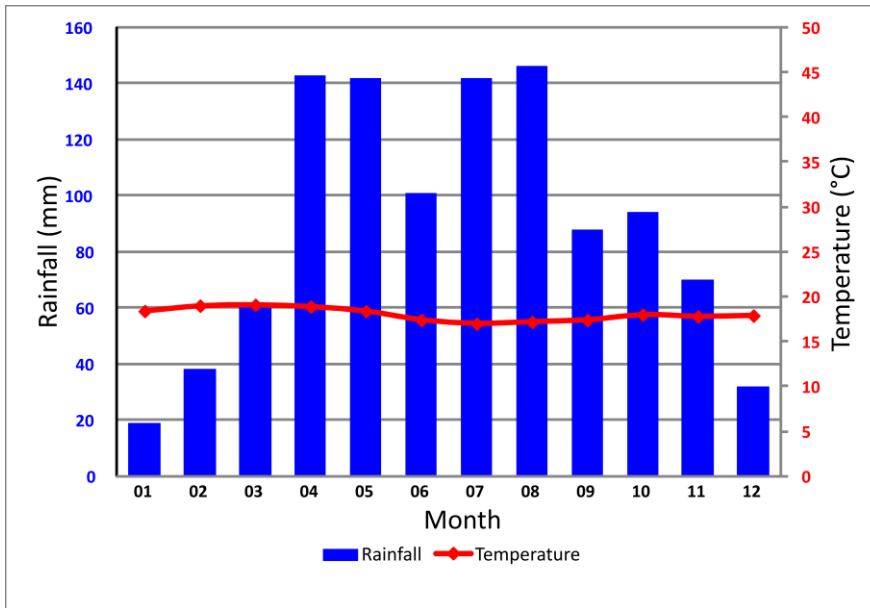
Figure 2.2: Average monthly rainfall and temperatures recorded in the study area. The figure has been modified after (Schwarz, 2015).
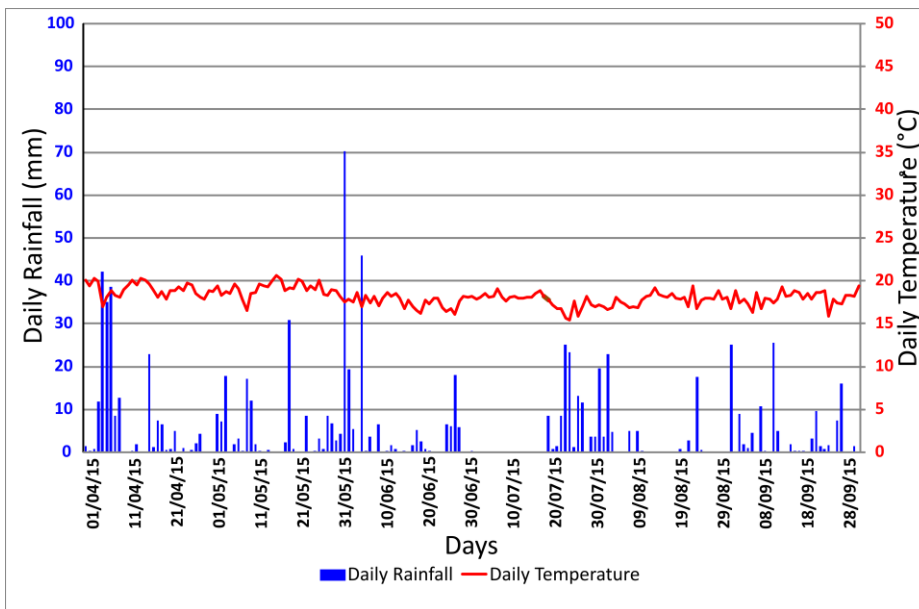
Figure 2.3: Daily rainfall and temperature amounts for the cropping season between April and September, 2015. The data was recorded at the Kenya Seed Company (KSC) weather station in Endebess.

The weather data was collected from a weather station located at the Kenya Seed Company (KSC) in Endebess. The station recorded the temperature, humidity, wind speed, radiation, and rainfall amounts on a daily basis. For the purpose of this study, the daily and cumulative rainfall amounts for the cropping season between April and September, was analyzed (**Figure 2.3**).

3. Geodata

This chapter describes the data acquired for this study. This includes the satellite images, digital elevation model, ancillary data (maps), and the ground reference data collected during the field visit. The general workflow through which the entire research was undertaken is illustrated in (**Figure 3.1**). it provides an overview of the data acquired, both satellite and fieldwork data; the data preprocessing steps carried out; the data analysis procedures, and the final results achieved.
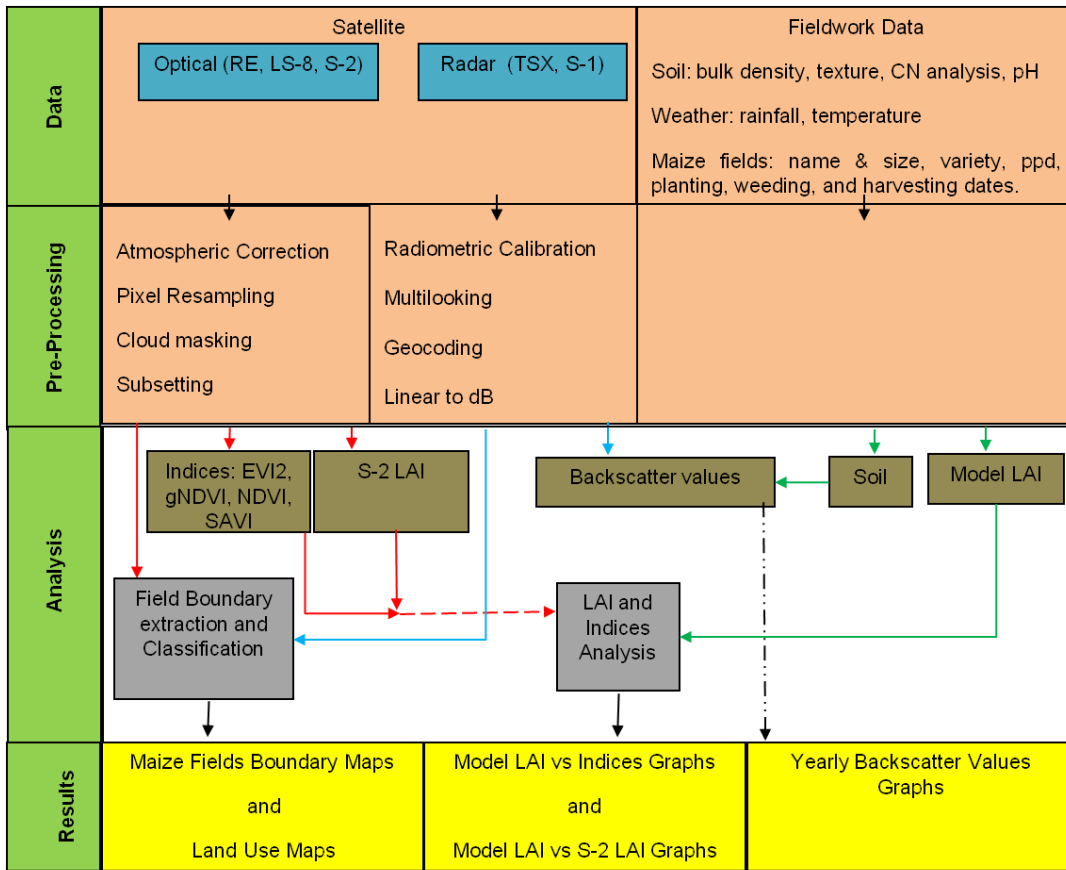
Figure 3.1: The general workflow approach implemented in the research. It highlights the satellite and fieldwork data acquired, the data preprocessing steps, the data analysis approach, and the achieved results.

3.1   Satellite Data

Satellites are platforms for imaging sensors that are revolving round the earth in space on an orbital platform, as they obtain information about the earth using remote sensing techniques (Jones & Vaughan, 2010). Remote sensing is defined as the science and art of obtaining information about an object, area, or phenomenon through the analysis of data acquired by a device that is not in contact with

the object (Lillesand et al., 2014). For satellite observations to be operationally sustainable, aspects of data supply continuity, frequent revisit, wide geographical coverage and timeliness have to be observed. The choice of satellite data to use depends on the application for which the data is intended, and is influenced by four major factors namely the spatial, spectral, radiometric and spectral resolutions of the images (Vinciková et al., 2010). The spatial resolution of a satellite refers to the minimum object size and the degree of detail identifiable from an image (Lillesand et al., 2014). It is related to the pixel size and the smaller the pixel sizes, the higher the spatial resolution. The spatial resolution ranges from high (1 meter and below), moderate (100-10m) to low (1000-100m). The spectral resolution refers to the ability of a satellite sensor to distinguish among different ground features, based on their spectral properties (Woodhouse, 2006). It is dependent upon the number of bands, their position on the electromagnetic spectrum, and the width of these spectral bands. The extent of the spectral bands in which any sensor collects data can be categorized according to the data recordings and remote sensing subject areas into: optical (including VIS $0.4 - 0.7\mu$ m, near IR $0.7 - 1.5\mu$ m and middle IR $1.5 - 3\mu$ m); thermal (3μ m $-$ 1mm); and microwave (radar) RS (1mm $-$ 1m) (Asrar, 1989). This is illustrated in (**Figure 3.2**).
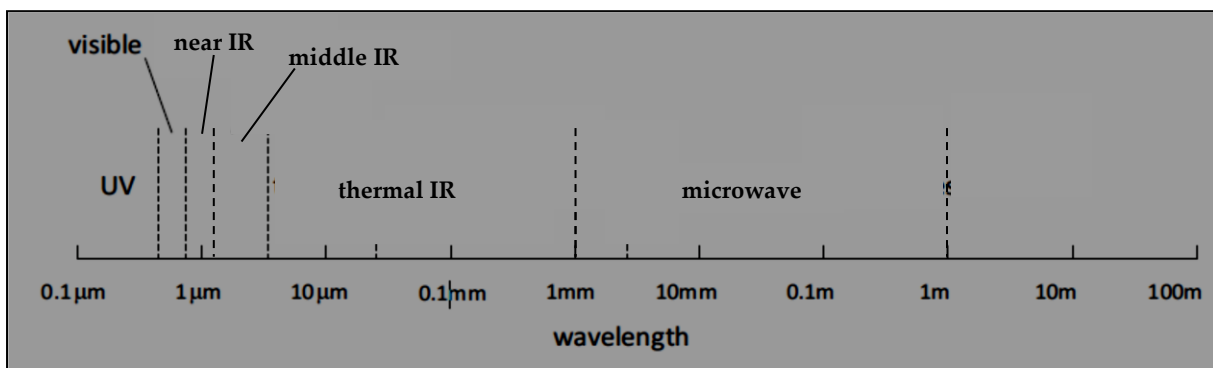
Figure 3.2: The electromagnetic spectrum showing the wavelength ranges of the ultra violet (UV) visible (VIS) near infrared (near IR), middle infrared (middle IR), thermal infrared (thermal IR) and the microwave spectral bands. The figure has been modified after (Richards, 2013).

Radiometric resolution is the ability of the sensor to differentiate among fine variations in brightness. It determines the value scale (gray shades) of each pixel in the scene, indicated in bits (bit/pixel) (Richards, 2013). It is defined by the sensitivity of the detector and the amount of incident radiation that is recorded. The finer the radiometric resolution is, the greater the quality and interpretability of an image, e.g. a 16bit image has a finer/higher radiometric resolution compared to an 8bit image. Temporal resolution refers to the time interval between two subsequent revisits of a sensor over an area on the

land's surface (Woodhouse, 2006). Changes over shorter or longer periods can be detected. It is given in terms of days.

Radar and optical satellite images have been used together in the field of agriculture for purposes of classification, crop mapping any yield prediction (Fieuzal & Baup, 2017; Guissard et al., 2005; Lussem et al., 2016) to complement each other and take advantage of their different characteristics. The radar and optical images used in this research are described in this section.

3.1.1   SAR Data

A radar wave can be considered, with a good approximation, as plane, coherent and monochromatic, emitted by an antenna towards a target (Nezry, 2014). The radar wave is partially backscattered in the direction of a receiving antenna. In the vast majority of spaceborne Synthetic Aperture Radars (SAR), a single antenna assumes the two functions of emission and reception (monostatic radar). They operate in the microwave portion of the spectrum that approximately extends from 1 mm to 1 m wavelength (Lillesand et al., 2014). SAR systems measure the ratio between the power, phase and amplitude of the pulse transmitted and that of the echo received. This ratio (referred to as backscatter) is projected into the slant range geometry. Geometric and radiometric calibration of the backscatter values are necessary for inter-comparison of radar images acquired with different sensors, or even of images obtained by the same sensor if acquired in different modes or processed with different processors. The removal of geometric distortions requires a high precision geocoding of the image formation. The geometric correction has to consider the sensor and processor characteristics and thus must be based on a rigorous range-Doppler approach (Lemp & Koch, 2009). The amount of radar backscattering from the terrain is primarily controlled by two sets of factors (Craig Dobson et al., 1995). These factors are: 1) geometrical factors related to structural attributes of the surface and any overlying vegetation cover relative to the sensor parameters of wavelength and viewing geometry; and 2) electrical factors determined by the relative dielectric constants of soil and vegetation at a given wavelength. These two factors may be time-variant in response to atmospheric forcing (i.e. precipitation, temperature and wind), phenological development of vegetation and disturbances (i.e. harvest, tillage and fire) (**Figure 3.3**). SAR is sensitive to incidence angle, soil moisture, and physical properties of soil, such as roughness, which may affect signatures and deteriorate the vegetation signal. However, its all-weather capability that enables high temporal resolution and regular data acquisition,   is an important advantage in the application of SAR images for agricultural monitoring purposes (Lohmann et al., 2010).
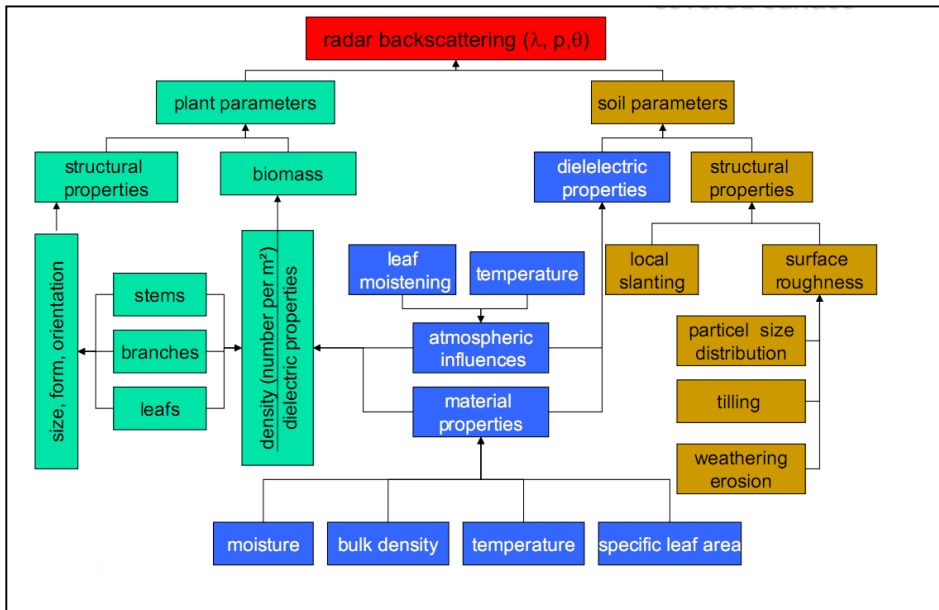
Figure 3.3: Primary factors controlling radar backscattering from terrain (Craig Dobson et al., 1995).

Sentinel-1 (S-1) and TerraSAR-X (TSX) radar images were acquired for this study (**Figure 3.4**). The S-1 images were acquired for 2015 and 2016 in single and dual polarization modes. The overpass was either ascending (asc) or descending (des) mode. The TSX images were available only for 2015 in dual polarization modes, and with both asc and des overpasses. Images were acquired for the cropping period between March and October. An overview of the acquired radar images is provided in (**Figure 3.5**), which gives a breakdown of all the images that were acquired.
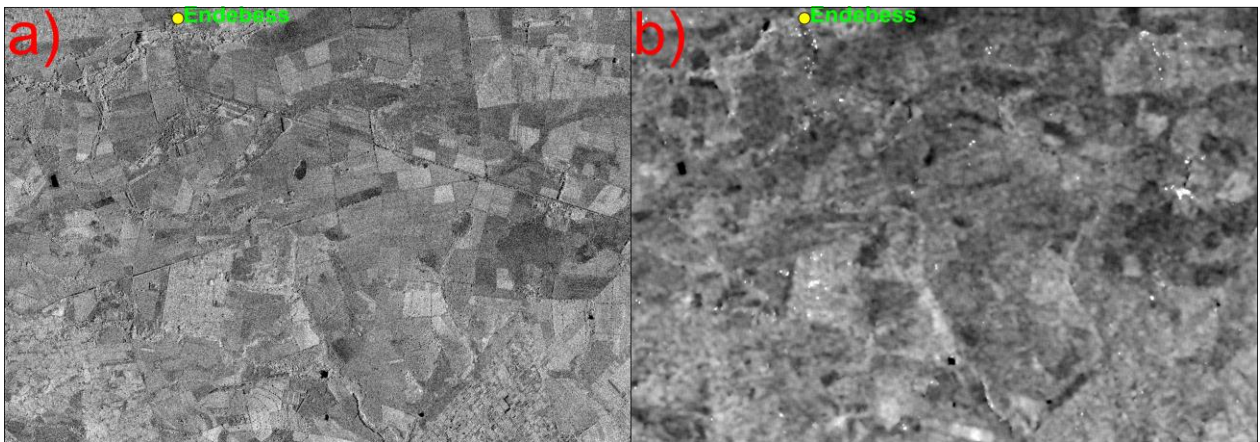
Figure 3.4: Examples of Radar images acquired for the study area: a) a TerraSAR-X scene (3 m pixel size); b) a Sentinel-1 scene (15m pixel size). Both images were acquired on the 8/5/2015.
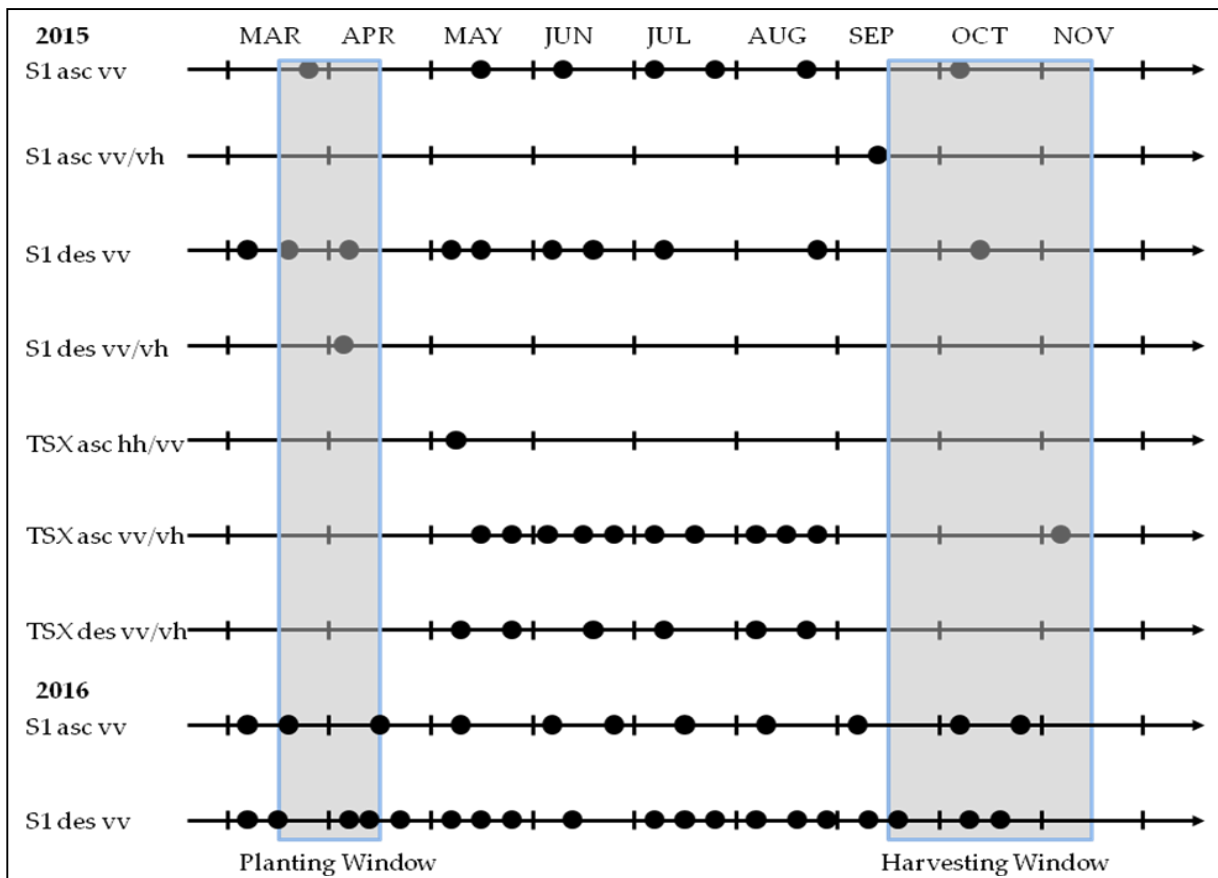
Figure 3.5: Chronogram of the Sentinel-1 (S-1) and TerraSAR-X (TSX) satellite radar images acquired during the cropping season between March and November for the years 2015 and 2016. The images were available in single polarization (vv) or dual polarization (vv/vh or hh/vv). The overpass was in both ascending (asc) and descending (des) modes. The planting window was between March and April and the harvesting period between September and November.

3.1.1.1 Sentinel-1

The Sentinel-1 (S-1) is a two satellites constellation, S-1A launched in 2014, and S-1B launched in 2016, and provides cloud free observations (Geudtner et al., 2014). Its launch was necessitated by the European Union and European Space Agency (EU-ESA) need for Global Monitoring for Environment and Security (GMES) programme that had identified marine core services, land monitoring and emergency services as the three priority areas (Malenovský et al., 2012). The S-1 operates in the C-band with a 5.6 cm wavelength, a revisit time of 12 days and images with up to 5 meters spatial resolution. On the other hand, S-1 has also been successfully used for crop mapping for food security (Attema et al., 2009a). It's increased number of acquisitions during the growing season (six day temporal resolution) enables the proper sampling of the crops' growth cycles even in situations where the

sowing dates may be different throughout the region (Torres et al., 2012; Veloso et al., 2017). The increased number of acquisitions by S-1 during the growing season (six-day temporal resolution) enables to properly sample the growth cycle and to limit the impact of geophysical noise (for example by identifying a date with no wind where the water surface is very smooth). With one S-1 acquisition every six days, it is expected that the performance of the multi-temporal algorithm will drastically improve compared to what was obtained with ASAR. In addition, in regions where multiple agricultural practices are common (e.g. different sowing dates throughout the region), a higher temporal sampling will be very beneficial (Torres et al., 2012).

The S-1 has an Interferometric Wide Swath Mode that operates for a maximum of 25 minutes per orbit (Attema et al., 2009a). The remaining time the instrument operates over the open ocean in the Wave Mode providing sampled images of 20 x 20 km at 100 km along the orbit with low data rate and 5 x 5 meter spatial resolution. To support on-demand emergency response, the system provides additional operational modes. A Strip Map Mode provides 5 x 5 meter spatial resolution within a minimum swath of 80 km wide that can be selected out of six across track positions within a 375 km wide access strip. The Extra-wide Swath Mode provides 400 km swath width and 20 x 40 meter spatial resolution. Sentinel-1 has selectable single polarization (VV or HH) for the Wave Mode and selectable dual polarization (VV+VH or HH+HV) for all other modes. The S-1 characteristics are displayed in (**Table 3.1**).

The S-1 images are available in three processing levels: level-0, level-1 and level-2 (Torres et al., 2012). Level-0 products consist of the compressed and unfocused SAR raw data which forms the basis from which the other level products are created. They are available only in the strip map (SM), interferometric wide swath (IW) and extra wide swath (EW) modes. The level-1 products are available in single look complex (SLC) and ground range detected (GRD) forms. SLC products consist of geo-referenced SAR data that is provided in slant-range geometry. The geo-referencing is performed using satellite orbit and attitude data. On the other hand, GRD products consist of S-1 images that have been detected, multi-looked and projected to ground range using an Earth ellipsoid model such as WGS84. Lastly, the level-2 products consist of geo-located geophysical products that have been derived from Level-1 products. They may contain the ocean wind field (OWI), ocean swell spectra (OSW), or the surface radial velocity (RVL) geophysical components.

Table 3.1: Sentinel 1 characteristics adopted after Attema et al. (2009b) and Torres et al. (2012).

Parameter	Strip-Map Mode – SM	Interferometric Wide Swath Mode-IW	Extra Wide Swath Mode-EW	Wave Mode-WV
Polarization	Dual (HH+HV or VV+VH)	Dual (HH+HV or VV+VH)	Dual (HH+HV or VV+VH)	Dual (HH or VV)
Minimum Incidence	20°-45° (access range)	25°	20°	23°+36.5°
Azimuth Resolution	<5m	<20m	<40m	<5m
Ground Range Resolution	<5m	<20m	<20m	<5m
Swath	>80km	>250km	>400km	Vignette 20x20km
For all Modes				
Point Target Ambiguity			-25 dB	
Distributed Target Ambiguity Ratio			-22 dB	
Noise Equivalent Sigma Zero			-22 dB	
Radiometric Stability			0.5 dB (3σ)	
Radiometric Accuracy			1 dB (3σ)	

The first S-1 images for the study area, and Kenya as a whole started in October 2014. The images were freely available for download from the European Space Agency (ESA) website: http://www.esa.int/spaceinimages/Missions/Sentinel-1. The S-1 images for the years 2015 and 2016 were downloaded for this study (**Table 3.2**). The images overpass was in both descending (des) and ascending (asc) modes. The incidence angle was 34°, and in single polarization VV. Only two acquisitions in 2015 were in dual polarization VV/VH. The images were level-1 SLC product, and in IW orbit precision mode.

Table 3.2: Sentinel 1 images acquired for the study area in 2015 and 2016. The images were all processing level L1, SLC product type and IW orbit precision.

Sentinel-1 DATA ACQUISITION DATES 2015 and 2016									
Date	Time UTC	Overpass	Mode	Incidence Min (°)	Date	Time UTC	Overpass	Mode	Incidence Min (°)
14/3/15	3:27	des	vv	34	01/3/16	15:56	asc	vv	34
21/3/15	3:19	des	vv	44	08/3/16	3:27	des	vv	34
31/3/15	15:56	asc	vv	34	15/3/16	3:27	des	vv	44
07/4/15	3:27	des	vv/vh	34	25/3/16	15:56	asc	vv	34
14/4/15	3:19	des	vv	44	01/4/16	3:27	des	vv	34
01/5/15	3:27	des	vv	34	08/4/16	3:27	des	vv	44
08/5/15	3:19	des	vv	44	18/4/16	15:56	asc	vv	34
18/5/15	15:56	asc	vv	34	25/4/16	3:27	des	vv	34
01/6/15	03:19	des	vv	44	02/5/16	3:27	des	vv	44
11/6/15	15:56	asc	vv	34	12/5/16	15:56	asc	vv	34
25/6/15	3:19	des	vv	44	19/5/16	3:27	des	vv	34
05/7/15	15:56	asc	vv	34	26/5/16	3:27	des	vv	44
12/7/15	3:27	des	vv	34	05/6/16	15:56	asc	vv	34
29/7/15	15:56	asc	vv	34	12/6/16	3:27	des	vv	34
22/8/15	15:56	asc	vv	34	29/6/16	15:56	asc	vv	34
29/8/15	3:27	des	vv	34	06/7/16	3:27	des	vv	34
15/9/15	15:56	asc	vv/vh	34	13/7/16	3:27	des	vv	44
09/10/15	15:56	asc	vv	34	23/7/16	15:56	asc	vv	34
16/10/15	0:27	des	vv	34	30/7/16	3:27	des	vv	34
					06/8/16	3:27	des	vv	44
					16/8/16	15:56	asc	vv	34
					23/8/16	3:27	des	vv	34
					30/8/16	3:27	des	vv	44
					09/9/16	15:56	asc	vv	34
					16/9/16	3:27	des	vv	34
					23/9/16	3:27	des	vv	44
					03/10/16	15:56	asc	vv	34
					10/10/16	3:27	des	vv	34
					17/10/16	3:27	des	vv	44
					27/10/16	15:56	asc	vv	34

3.1.1.2 TerraSAR-X

The radar satellite TerraSAR-X (TSX) was launched from Baikonur Cosmodrome in Kazakhstan on June 15, 2007. It is funded as a public/private partnership between the German Aerospace Center (DLR) and Airbus (formerly EADS Astrium) (Eineder et al., 2008). The satellite has a near-polar orbit

with an altitude of 514 km and an inclination of 97.5°. Time of circulation is 94.84 min and the orbit repetition time is 11 days with a radar carrier frequency of 9.65 GHz. The TSX operates in the X-band with a 3 cm wavelength (Santos et al., 2010). It is a side-looking synthetic aperture radar (SAR) based on active phased array antenna technology, able to produce high-resolution images (up to 1 meter). The active antenna allows not only the conventional Stripmap imaging mode but additionally Spotlight and ScanSAR mode with minimum resulting spatial resolutions of 3 meters, 1 meter and 16 meters respectively, and single (VV, HH) and dual (VH, HV) polarization (Fritz & Werninghaus, 2007) (**Table 3.3**). The DLR provides these images to the scientific community on demand as three differently processed radar products: (1) a radiometrically enhanced multilook ground range detected (MGD) image, (2) a spatially enhanced MGD image and (3) a spatially enhanced ellipsoid-corrected (EEC) backscatter image based on the spatially enhanced MGD image. The difference between the radiometrically enhanced product and the spatially enhanced product is the equivalent number of looks that have been selected during the SAR-processing. The number of looks is higher for the radiometrically enhanced product resulting in a higher radiometric accuracy at the cost of some reduction in geometric resolution, compared with the spatially enhanced product. Consequently, the speckle of the radiometrically enhanced image is reduced, resulting in a better radiometric resolution (Breidenbach et al., 2010).

Table 3.3: TerraSAR-X properties (Eineder et al., 2008)

Parameter	Strip-Map Mode (SM)	High Resolution Spotlight Mode (HS)	Spotlight Mode (SL)	ScanSAR Mode (SC)
Polarization	Single (HH, VV) Dual (HH/VV, HH/HV, VV/VH)	Single (HH, VV) Dual (HH/VV)	Single (HH, VV) Dual (HH/VV)	Dual (HH or VV)
Full performance Incidence angle range	20°-45°	20°-55°	20°-55°	20°-45°
Data access Incidence angle range	15°-60°	15°-60°	15°-60°	15°-60°
Azimuth Resolution	3.3 m single pol. 6.6 m dual pol.	1.1 m single pol. 2.2 m dual pol.	1.7 m single pol. 3.4 m dual pol.	18.5 m
Ground Range Resolution	1.70 m – 3.49 m	1.48 m – 3.49 m	1.48 m – 3.49 m	1.70 m – 3.49 m
Swath (ground range x azimuth)	30 x 50 km single pol. 15 x 50 km dual pol.	10 km x 5 km	10 km x 10 km	100 x 150 km

The X-band is usually scattered from the leaves and twigs of the crops. This is satisfactory for crop culture differentiation as different crop cultures have different leaf structures (Rowland et al., 2008). Its

signal has very low volume diffusion, meaning that the influence of the material to the backscatter intensity is not as large as it is in longer wavelengths like the L-band. There is also a high degree of mixture of analyzing phenological periods and characteristics of crops (Lohmann et al., 2009). For this reasons, the X-band data is classified via standard deviation (STD) and mean (MEAN) values within predefined cells (Lemp & Koch, 2009). The TSX provides a very detailed description of the land surface since the radar beam is reflected very close to the surface instead of penetrating the vegetation Lemp & Koch (2009) and Rowland et al. (2008), with previous studies showing its application in field-based agriculture mapping (Sonobe et al., 2014; Thiong'o et al., 2015). It has been successfully used in the separation of different agricultural land uses (Breidenbach et al., 2010), classification of crops in regions of small agricultural fields (Mróz & Mleczko, 2008), and even the mapping of crop height in the fields (Fieuzal et al., 2012). The short wavelength signal of the X-band however makes it more sensitive to soil roughness, especially at high incidence angles (Aubert et al., 2011).

The TSX images were acquired for the year 2015. They were dual polarized (HH/VV and VV/VH) L1B products, in both ascending (asc) and descending (des) overpasses (**Table 3.4**).

Table 3.4: TerraSAR-X images acquired for the study area in 2015. The images were all processing level L1, SSC product type and SCIENCE orbit precision.

TSX DATA ACQUISITION DATES 2015								
Acquisition Date	Time	Mode	Mode	Incidence min	Incidence max	Processing level	Product type	orbit precision
6/5/15	15:56	asc	hh/vv	42.65	43.71	1B	SSC	SCIENCE
8/5/15	03:29	desc	vv/vh	34.08	35.40	1B	SSC	SCIENCE
17/5/15	15:56	asc	vv/vh	42.65	43.71	1B	SSC	SCIENCE
28/5/15	15:56	asc	vv/vh	42.65	43.71	1B	SSC	SCIENCE
30/5/15	03:30	desc	vv/vh	34.08	35.40	1B	SSC	SCIENCE
8/6/15	15:56	asc	vv/vh	42.65	43.71	1B	SSC	SCIENCE
19/6/15	15:56	asc	vv/vh	42.65	43.71	1B	SSC	SCIENCE
21/6/15	03:30	desc	vv/vh	34.08	35.40	1B	SSC	SCIENCE
30/6/15	15:56	asc	vv/vh	42.65	43.71	1B	SSC	SCIENCE
11/7/15	15:56	asc	vv/vh	42.65	43.71	1B	SSC	SCIENCE
13/7/15	03:30	desc	vv/vh	34.08	35.40	1B	SSC	SCIENCE
22/7/15	15:56	asc	vv/vh	42.65	43.71	1B	SSC	SCIENCE
2/8/15	15:56	asc	vv/vh	42.65	43.71	1B	SSC	SCIENCE
4/8/15	03:30	desc	vv/vh	34.08	35.40	1B	SSC	SCIENCE
13/8/15	15:56	asc	vv/vh	42.65	43.71	1B	SSC	SCIENCE
24/8/15	15:56	asc	vv/vh	42.65	43.71	1B	SSC	SCIENCE
26/8/15	03:30	desc	vv/vh	42.65	43.71	1B	SSC	SCIENCE
9/11/15	15:56	asc	vv/vh	42.65	43.71	1B	SSC	RAPID

3.1.2 Optical Data

These are satellite systems that include UV, visible (red, green and blue), near-, mid-, and thermal IR wavelengths (Lillesand et al., 2014). They operate in the optical spectrum that extends from about 0.3 to 14 µm. This section looks at the Landsat-8 (L-8), RapidEye (RE) and Sentinel-2 (S-2) images acquired for 2015 and 2016. Whereas L-8 and S-2 are freely available, RE is commercial and its acquisition was supported with a data request proposal.

The major criteria for the selection of the optical images were that, cloud coverage had to be less than 20% (**Table 3.5**), and that the images selected were to be within the maize cropping season. There were 9 L-8, 3 RE, and 9 S-2 images fitting this criteria (**Figure 3.6**). L-8 and RE images were acquired for 2015 cropping season in order to complement the ground reference data collected during the field visits. The S-2 images were however not available for the 2015 cropping season. They were available for the 2016 cropping season and were therefore acquired in order to process the S-2 leaf area index (LAI) product necessary for the validation of the LAI model developed in (**Chapter 3.3.3.4.3**).

The L-8 and S-2 images were acquired as level-1 products, while RE images were acquired as level-3A products.
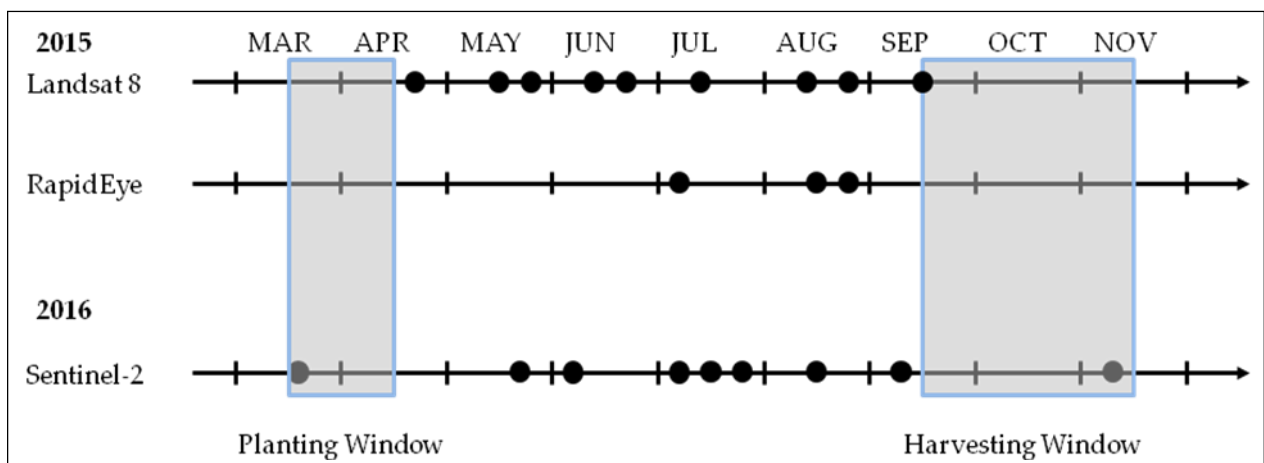
Figure 3.6: Chronogram of the Landsat 8 (L-8), RapidEye (RE) and Sentinel-2 (S-2) optical satellite images acquired during the cropping season between March and November for the years 2015 and 2016. The L-8 and RE images were acquired for the year 2015 while the S-2 images were acquired for the year 2016. The planting window was between March and April and the harvesting period between September and November.

Table 3.5: Landsat 8 (L-8), RapidEye (RE), and Sentinel-2 (S-2) images acquired in 2015 and 2016. The L-8 uses the Operational Land Imager (OLI) sensor while RE and S-2 use the Multispectral imager (MSI) sensor. The L-8 images are acquired in level L1T (terrain-corrected), the RE in level 3A (orthorectified products with radiometric, geometric and terrain corrections) and S-2 in level 1C (geo-coded top of atmosphere reflectance product).

Acquisition Date	Space craft	Sensor	Data type	Cloud cover (%)	Solar Zenith / sun elevation (°)	Solar Azimuth (°)
25/4/15	LS	OLI	L1T	5	61.36	64.69
11/5/15	LS	OLI	L1T	17	59.63	55.77
27/5/15	LS	OLI	L1T	9	57.68	50.32
12/6/15	LS	OLI	L1T	20	56.13	48.13
28/6/15	LS	OLI	L1T	7	55.42	48.69
4/7/15	RE	MSI	L3A	2	64.69	29.07
14/7/15	LS	OLI	L1T	3	55.82	51.58
15/8/15	LS	OLI	L1T	6	59.65	63.92
16/8/15	RE	MSI	L3A	11	72.38	42.79
24/8/15	RE	MSI	L3A	6	73.23	52.08
31/8/15	LS	OLI	L1T	16	62.31	73.86
16/9/15	LS	OLI	L1T	6	64.52	86.71
28/3/16	S2	MSI	L1C	12	31.75	45.90
27/5/16	S2	MSI	L1C	10	30.62	43.13
6/6/16	S2	MSI	L1C	1	30.82	44.33
6/7/16	S2	MSI	L1C	10	31.85	46.18
16/7/16	S2	MSI	L1C	11	31.25	48.59
26/7/16	S2	MSI	L1C	14	30.21	51.83
15/8/16	S2	MSI	L1C	4	27.08	61.19
4/9/16	S2	MSI	L1C	5	23.52	75.43
13/11/16	S2	MSI	L1C	11	27.13	136.58

3.1.2.1   Landsat-8

The Landsat program was the first formal civil research and development activity that aimed at using satellites for global monitoring of land resources (Lillesand et al., 2014). The Landsat series sensors have provided high-resolution Earth observation (EO) data since 1972. This long-term record is now continuously carried on by the Landsat Data Continuity Mission (LDCM) with the launch of the Landsat-8 (L-8) in February 2013 (Wulder et al., 2008). It was a collaboration between National Aeronautics and Space Administration (NASA), who were responsible for the space segment of the mission, and United States Geological Survey (USGS), who were responsible for the ground segment development (Lillesand et al., 2014). The main objectives for the mission were: collect and archive moderate resolution (30 m ground sampling distance - GSD) image data permitting seasonal coverage of the global land mass for a period of no less than five years; collect and archive moderate- to low-resolution (120 m) thermal image data permitting seasonal coverage of the global land mass for a period of no less than three years; ensure consistency of data with previous Landsat missions; distribute

standard data at affordable prices to the user (Lillesand et al., 2014). Due to the free-access policy, data acquired by the Landsat series satellites provide an essential resource for retrospective as well as prospective studies for a wide range of research and application users.

The L-8 was launched into a repetitive, near-circular, sun-synchronous, near polar orbit. It has a nominal altitude of 705 km at the equator. Due to the earth's rotation, the distance between ground tracks for consecutive orbits is approximately 2752 km at the equator. The revisit cycle is 16 days with the time interval between adjacent coverage tracks of the satellite being 7 days. The east-west swath width of each image scene is 185 km whereas the north-south dimension is 180 km (Irons et al., 2012). L-8 incorporates two sensors namely the Operational Land Imager (OLI) and the Thermal Infrared Sensor (TIRS) with similar fields of view and coincidental datasets of the same ground area that are subsequently merged during ground processing into a single data product for each scene (**Table 3.6**). Compared to its predecessors, the OLI sensor has a similar band-set configuration in the solar reflective range and two additional bands, one in the deep blue range designed for water resources and coastal zone studies, and another in the shortwave infrared range for cirrus cloud detection (Shang et al., 2014b).

An example of the L-8 true colour composite image of the study area is illustrated in (**Figure 3.7**).

Table 3.6: Landsat 8 (L-8) spectral bands (Lillesand et al., 2014).

Band	Nominal Spectral Location	Band Width (μm)	Spatial Resolution (m)	Sensor
1	Coastal/Aerosol	0.433-0.453	30	OLI
2	Blue	0.450-0.515	30	OLI
3	Green	0.525-0.600	30	OLI
4	Red	0.630-0.680	30	OLI
5	NIR	0.845-0.885	30	OLI
6	SWIR 1	1.560-1.660	30	OLI
7	SWIR 2	2.100-2.300	30	OLI
8	Panchromatic	0.500-0.680	15	OLI
9	Cirrus	1.360-1.390	30	OLI
10	TIR 1	10.6-11.2	100	TIRS
11	TIR 2	11.5-12.5	100	TIRS

3.1.2.2   RapidEye

The RapidEye (RE) is among the new generation high-resolution optical sensors, launched into orbit on August 29, 2008 (Naughton et al., 2011). It is a sun-synchronus orbit with a period of about 98 minutes, a swath width of around 77 km from a nominal altitude of 630 km, an inclination of 97.8° and a local time of 23:30 at the ascending node. It comprises of a constellation of five identical and cross-

calibrated satellites, established with about 19.5-minutes separations, and phased in such a way that ensures that at least one RE sensor is viewing the same point on the Earth within a 24-hour period. The constellation has daily global visibility with an off-nadir pointing angle below 20°, and a nadir revisit period of about 6.7 days (Chander et al., 2013). The RE image products are delivered in two different levels, depending on the customers' needs: 1) RE Basic (Level 1B) products that are radiometrically and sensor corrected, but without any geo-correction; and 2) RE Ortho (Level 3A) which are orthorectified products with radiometric, geometric and terrain corrections in a map projection (RapidEye, 2011).

The multispectral imager (MSI) is a push-broom imaging sensor operated onboard the RE. The pixel size is 6.5×6.5µ m, with the pixels arranged in a linear array, each containing 12×103 pixels. Images are acquired in five different spectral bands each with a 6.5 m ground sampling distance (GSD) at nadir (**Table 3.7**) (Weichelt et al., 2011). For purposes of radiometric calibration, each MSI in the RE constellation is viewed as a unique instrument even though the spectral transmission characteristics of the instruments are optically similar (Naughton et al., 2011).

RE satellites were designed to be used mainly for the monitoring of agriculture and natural resources, for example forests, at relatively large cartographic scale (Tapsall et al., 2010; Weichelt et al., 2011).

An example of the RE true colour composite image of the study area is illustrated in (**Figure 3.7**).

Table 3.7: RapidEye (RE) Spectral Bands (Weichelt et al., 2011).

Band	Nominal Spectral Location	Band Width (µm)	Spatial Resolution (m)	Sensor
1	Blue	0.440-0.510	6.5	MSI
2	Green	0.520-0.590	6.5	MSI
3	Red	0.630-0.685	6.5	MSI
4	Red Edge	0.690-0.730	6.5	MSI
5	NIR	0.760-0.850	6.5	MSI

3.1.2.3   Sentinel-2

The Sentinel-2 (S-2) mission was envisaged within the Global Monitoring for Environment and Security (GMES) Space component programme to provide land monitoring, emergency response, and security services (Drusch et al., 2012; Fletcher & European Space Agency, 2012). This was by: (1) providing systematic global acquisitions of high temporal and high-resolution multi-spectral imagery, (2) providing enhanced continuity of multi-spectral imagery provided by the SPOT (Satellite Pour l'Observation de la Terre) series of satellites, and (3) providing observations for the next generation of operational products such as land-cover maps, land change detection maps, and geophysical variables.

The S-2 mission comprises of two identical satellites, S-2A launched in 2015, and S-2B launched in 2017, each having a 7.25-year lifetime over a 15-year period. The satellites are maintained with a phase delay of 180°, in the same sun-synchronous orbit, at an altitude of 786 km, providing a revisit time of five days at the equator. The local overpass time at the equator is 10:30 a.m. descending node. This overpass time not only provides the best compromise between minimizing cloud cover and ensuring suitable sun illumination, but also matches SPOT's local overpass time and is also close to the Landsat local overpass time. This allows for the combination of S-2 data with other images from other satellites for time series analysis. The S-2 satellites systematically acquires observations over land and coastal areas from −56° to 84° latitude (Martimort et al., 2007).

The S-2 is a Multi Spectral Instrument (MSI) imager with 13 spectral bands spanning from the visible (VIS) and the near infrared (NIR) to the short wave infrared (SWIR) (Martimort et al., 2007). It has a unique combination of high spatial resolution ranging from 10 m to 60 m depending on the spectral band, wide field of view (290 km) and a wide spectral coverage (**Table 3.8**). The S-2 end-to-end system comprises two segments: the space segment with the two orbiting satellites including their payload instrument, and the ground segment (Drusch et al., 2012). The ground segment comprises of the Flight Operations Segment (FOS), which is responsible for all flight operations of the S-2 spacecraft including monitoring and control, execution of all platform activities and commanding of the pay-load schedules, and the payload data ground segment (PDGS), which is responsible for payload and downlink planning, data acquisition, processing, archiving and downstream distribution of the S-2 satellite data, while contributing to the overall monitoring of the payload and platform in coordination with the FOS.

The available image products are, the Level 0 and Level 1A products, which provide raw compressed and uncompressed data, respectively. The Level 1B data are radiometrically corrected radiances. The Level 1C product provides geo-coded top of atmosphere (TOA) reflectance with a sub-pixel multi-spectral and multi-date registration. The level 2A product provides the Bottom-Of Atmosphere (BOA) reflectance from the enhanced cloud masks generated from the TOA reflectance (Level-1C) (Martimort et al., 2007).

An example of the S-2 true colour composite image of the study area is illustrated in (**Figure 3.7**).

Table 3.8: Sentinel-2 (S2) Spectral Bands (Drusch et al., 2012).

Band	Name	Central wavelength (μm)	Spatial resolution (m)	Bandwidth (nm)	Sensor
1	Coastal aerosol	0.443	60	20	MSI
2	Blue	0.490	10	65	MSI
3	Green	0.560	10	35	MSI
4	Red	0.665	10	30	MSI
5	Vegetation Red Edge	0.705	20	15	MSI
6	Vegetation Red Edge	0.740	20	15	MSI
7	Vegetation Red Edge	0.783	20	20	MSI
8	NIR	0.842	10	115	MSI
8b	Narrow NIR	0.865	20	20	MSI
9	Water vapour	0.945	60	20	MSI
10	SWIR – Cirrus	0.1380	60	20	MSI
11	SWIR	0.1610	20	90	MSI
12	SWIR	0.2190	20	180	MSI
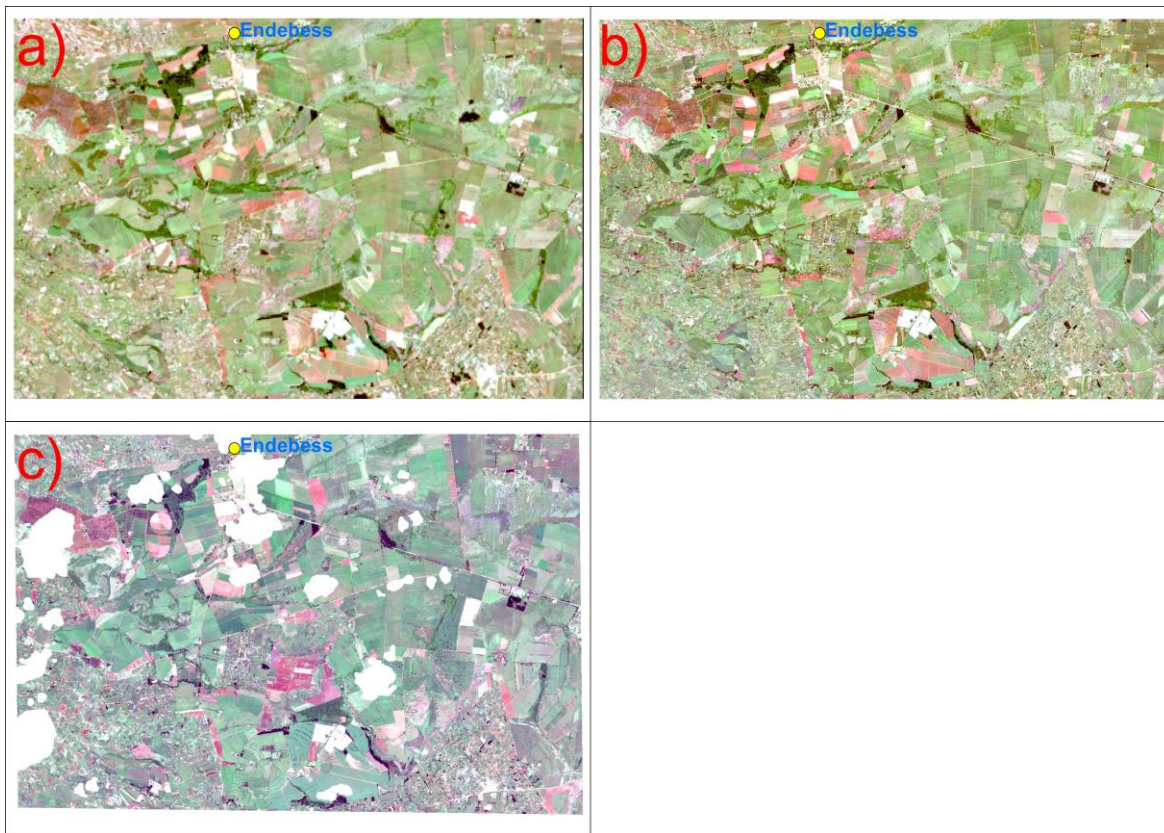
Figure 3.7: Examples of true color composite (RGB) optical images acquired for the study area: a) a Landsat-8 scene (30 m pixel size) acquired on 16/9/2015; b) a RapidEye scene (5m pixel size) acquired on 24/8/2015; and c) a Sentinel-2 scene (10m pixel size) acquired on 4/9/2016.

3.1.3   Digital Elevation Model

A digital elevation model (DEM) can be defined as any image where the pixel values represent the elevation coordinates (Lillesand et al., 2014). The Shuttle Radar Topography Mission (SRTM) with relative vertical accuracies of 12 m (slope less than 20%) and 15 m (slope greater than 20%), an absolute vertical accuracy of 18 m, a relative horizontal accuracy of 15 m, a horizontal accuracy of 23 m, and a spatial resolution of 30 m (1 arc sec at the equator), has been considered more reliable than other open source DEMs from an accuracy perspective because it uses radar techniques (Uddin et al., 2015). However, due to its inclined orbit of the space shuttle and its mapping geometry, the SRTM's coverage is limited to a latitude range from 56° S to 60° N (Krieger et al., 2007). This had the challenging goal of achieving a homogeneous, global DEM with a high spatial resolution, which led to the conception of the TanDEM-X (TDX) (Rossi et al., 2012).

TDX is a TSX add-on satellite for high-resolution single-pass SAR inter-ferometry launched on June 21, 2010, three years after TSX (Moreira et al., 2004). In their tandem configuration, TSX and TDX follow orbit tracks separated by approximately 200 to 500 m, with the interferometric data collected being used to develop a globally uniform topographic data set with 12.5-m-by-12.5-m pixel spacing. Elevations in this DEM have better than 2-m relative and 10-m absolute accuracy (Moreira et al., 2004).

The TDX mission concept is based on a coordinated operation of two spacecraft flying in close formation providing the highly flexible and reconfigurable imaging geometry required for the different mission objectives. The main differences to the TSX satellite are the more sophisticated propulsion system to allow for constellation control, the additional S-band receiver to enable for reception of status and GPS position information broadcast by TSX and the X-band inter-satellite link for phase referencing between the TSX and TDX (Zink et al., 2006). The two systems are operated in tandem, in a bistatic configuration where one system transmits radar signals and both record the amplitude and phase of the backscattered response, effectively forming large X-band single-pass inteferometric radar. This provides on-demand topographic mapping capability anywhere on earth at 2 m accuracy, significantly better than anything previously available from space (Lillesand et al., 2014).

For imaging purposes, each of the two satellites offers a variety of modes. In the standard stripmap mode, the imagery is collected at approximately 3-m resolution, over a swath width of 30 km (single polarization data) or 15 km (dual polarization). Several Spotlight modes provide 1- to 3-m resolution imagery over a 5-km to 10-km swath, again with the choice of single or dual polarization. Finally, in ScanSAR mode the instruments cover a 100-km-wide swath at a spatial resolution of 3 m in range by

18 m in azimuth (Lillesand et al., 2014).

The main goal of the TDX mission was the generation of world-wide, consistent, timely, high-precision DEMs corresponding to the digital terrain elevation data-3 (DTED-3) / high resolution terrain information-3 (HRTI-3) standard (relative vertical accuracy 2 m (90% linear point-to-point error), absolute vertical accuracy 10 m (90% linear error), absolute horizontal accuracy 10 m (90% circular error), post spacing 12 m x 12 m), as the basis for a wide range of scientific research, as well as for operational, commercial DEM production. The global DEM is derived by monitoring the earth at the northern hemisphere with ascending orbits and the southern hemisphere with descending orbits without TDX affecting the TSX operation (Zink et al., 2006). TDX performance is always better than the DTED-3 specification with the possibility of further improvement by a coherent combination of multiple interferograms from ascending and descending orbits (Krieger et al., 2007). Besides the primary goal of the mission, several other secondary mission objectives have been defined in line with commercial and scientific applications. The scientific applications can be summarized into three groups: 1) Across-Track Interferometry, for example: hydrology, geology, land environment, renewable resources, and oceanography; 2) Along-Track Interferometry, for example: Oceanography, Moving Target Detection, Glaciology; 3) New Techniques with Bi-Static SAR, for example: Super Resolution, Bi-static SAR, Moving Target Detection, Polarimetric SAR Interferometry (Moreira et al., 2004). Interferometric data acquisition with the TDX satellite formation can be achieved in three different operational modes: Bistatic, Monostatic, and Alternating Bistatic Mode (**Figure 3.8**). The bistatic mode is characterized by the illumination of a scene by one transmitter and the simultaneous measurement of the same scene with two receivers, thereby avoiding temporal decorrelation. In the mono-static InSAR mode, the two satellites are operated independently, avoiding the need for synchronization. The transmitter satellite in the alternating bistatic mode alternates between the two satellites. Operational DEM generation is performed using bistatic interferometry mode (Krieger et al., 2007), with studies demonstrating similarities in qualities between the various acquisition modes (Rodriguez-Cassola et al., 2012). The TDX satellite is designed for a nominal lifetime of 5 years and has a nominal overlap with TSX of 3 years.

In this research, the TDX DEM was used due to its high resolution.
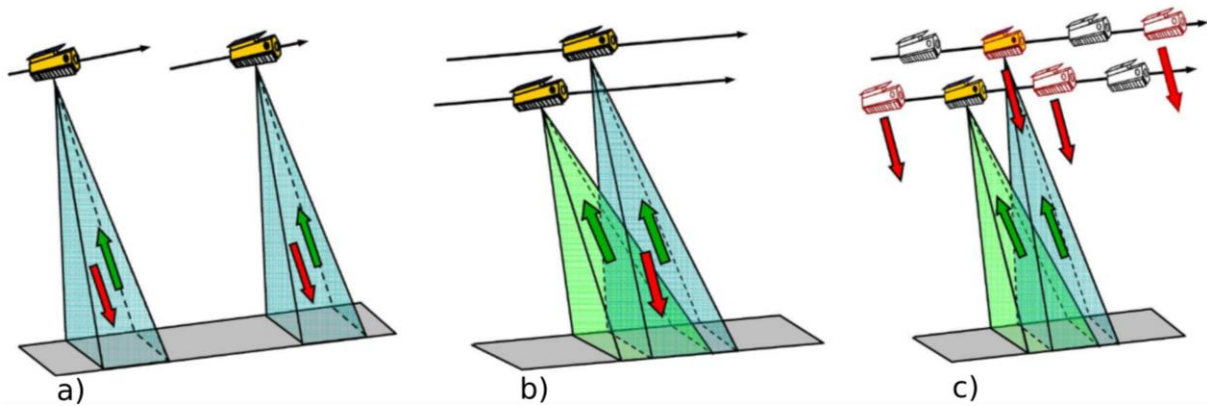
Figure 3.8: TanDEM-X data acquisition modes adopted from (Krieger et al., 2007). Figure a) shows the mono-static mode (two satellite operating independently), figure b) shows the bistatic mode (illumination of a scene by one transmitter and the simultaneous measurement of the same scene with two receivers), and figure c) shows the Alternating Bistatic Mode (similar to bistatic mode principle, with the difference being the alternating transmitting satellite).

3.2   Ancillary Geodata

The ADC Sabwani, ADC Olngatongo, and the Kenya Seed Company provided sketch maps of the existing land parcels under their management. These sketches showed field boundaries as they were demarcated during the colonial times. They showed the location of the various land parcels, their names and estimated acreages. Even though the maps had not being updated to reflect some of the developments on the ground, for example, settlements and buildings, it was a reliable reference, especially when identifying the various fields on the satellite images (**Figure 3.9 and 3.10**). Since field delineations is vital in crop growth monitoring and mapping (Guissard et al., 2005), the maize fields were identified and retrieved from the sketches.
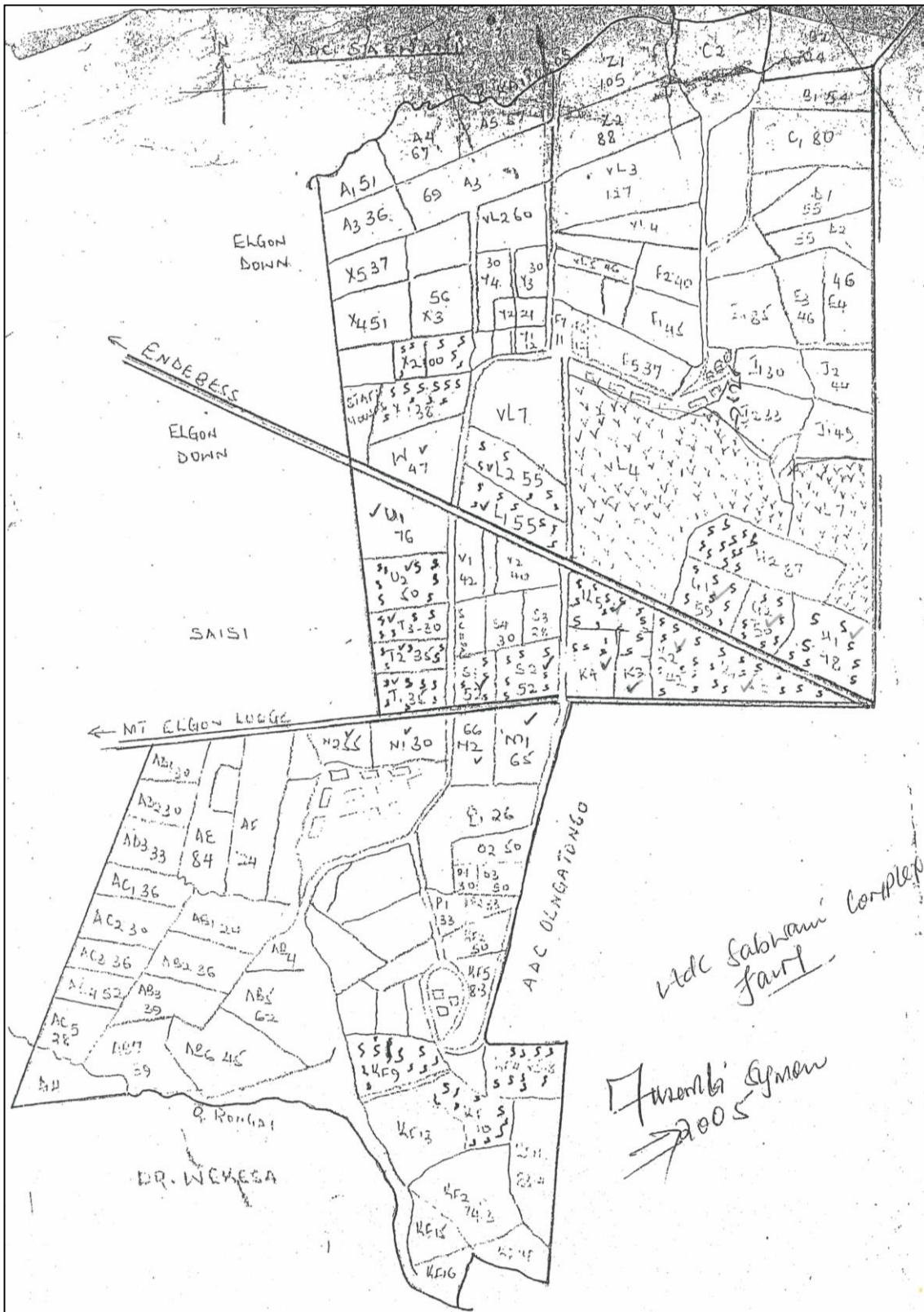
Figure 3.9: A sketch map showing the fields subdivisions in the ADC Sabwani.

Figure 3.10: A sketch map showing the fields subdivisions in the ADC Olngatongo.

3.3 Field Reference Data

3.3.1 Maize Growth and Development

3.3.1.1 Description of Maize Cultivation in the Study Area

Maize remains the main staple food of the country with Trans Nzoia area being considered as one of the country's grain basket (Kipkorir et al., 2007). Maize grows well on a range of soils, but thrives in deep, well drained, fertile soils that are slightly acid to neutral, (pH 5.5 to 7.0) (Gachene & Kimaru, 2004; Moore et al., 2014). The maize crop has a low tolerance to moisture stress especially if it occurs towards the end of the growing season (Moore et al., 2014; O'Callaghan et al., 1994). It is however highly responsive to plant population and plant uniformity. The study area has two maize seasons which are dependent on the rains (FAO, 2010; Jones, 2013). The long rains season runs from March to September, while the short rains season is from November to March (**Table 3.9).** The sowing time is governed by soil temperature, soil moisture and the targeted flowering date (Cooper, 1979; Moore et al., 2014). For example, at 12°C, emergence will occur in 14 days, whereas at 25°C emergence occurs in 4 to 5 days. Late planting (when weather is warmer) influences the maize maturity by reducing the days from planting to silking, but may increase the time between physiological maturity and harvest maturity where seasons are short as well (Moore et al., 2014).

Table 3.9: The Food and Agriculture Organization (FAO) Endebess maize crop calendar (FAO, 2010).

	J	F	M	A	M	J	J	A	S	O	N	D
Maize (long rains)			red	green	green	green	green	green	green/yellow	yellow	yellow	yellow
Maize (short rains)	green	green	green	green	yellow	yellow	yellow			red	green	green
Sowing	red											
Growing	green											
Harvesting	yellow											

For the farmers, the main planting window, which is between the 11th and 26th of March, is normally guided by their long term experiences, and the regional weather forecast provided by the Kenya Meteorological Department via public media (radio, television and newspapers) (Kipkorir et al., 2007). Any delays in planting of maize reduces the amount of expected yield, with a reduction of approximately 0.6 t/ha for every 1 week delay in planting of maize after the onset of the rains (Cooper & Law, 1977; Saseendran et al., 2005). For this reason, the farmers may choose to sow the maize seeds before the onset of the rains (dry sowing) or immediately after the onset of the rains (wet sowing) (Kipkorir et al., 2007). Dry sowing vis-à-vis wet sowing can result in a 9 days' difference in the

germination, which may increase to about 15 days for late sowing and hence cause discrepancies in the maize phenological stages, even in neighboring fields (Fieuzal et al., 2017). Sowing at a uniform depth ensures uniform emergence and achievement of the target plant stand (Moore et al., 2014).

Maize is a row crop and its population density is determined by the row and line spacing (Bisanda et al., 1998). This population density is governed by factors which include the soil moisture, climatic conditions, soil fertility, hybrid and end use (Moore et al., 2014). There are already pre-established and recommended plant population densities which are based on the maize row and plant spacing (Mokhtarpour et al., 2010; Jones, 2013; MacRobert et al., 2014). For example, a row and plant spacing of 75cm by 20 cm gives a plant population density of 50,000 plants per hectare whereas 75 cm by 30 cm gives a plant population of 44,000 plants per hectare. Decreasing of the row spacing can result in increased yields, which can be attributed to: increased plant population density; improved water use efficiency since evaporation losses are reduced as ground cover increases; formation of a dense crop canopy that smothers weeds thereby reducing resource competition (Moore et al., 2014; Sangoi, 2001; Sharifi & Namvar, 2016). However, a decrease in row spacing comes with socio economic implications which include: increased seed rate and fertilizer input; more labor and time needed during manual weeding; harvesting and agronomic maintenance operations (Onyango, 2009). The harvesting technology to be used (manual or mechanized), or the weed control measure to be applied (mechanical, manual or chemical) also influence the plant population density (Finke et al., 1999).

Determination of maize maturity is based on the time from planting to silking, planting to physiological maturity and planting to harvest maturity (Moore et al., 2014). The average time taken by a maize variety is already approximated during the development of any particular variety ("Improved Maize (Zea mays) Variety List From Kenya, Uganda and Tanzania," n.d.). However, the approximate maturity period is also subject to environmental variability, with temperature being the most important environmental factor influencing the rate of maize development (Cooper, 1979). An increase in the temperature decreases the phenological cycle while a decrease in the temperature increases it (Bassu et al., 2014). Though temperature is the most important environmental factor influencing the maize development rate, increase in the rainfall amounts may also prolong the maize period by up to 20 days (Tadross et al., 2009).

The common maize varieties grown in the area of study are H6213, H9401, H628, H614D, and H629, H624, KH600-23A, H6210, and KH6000-16A (J. Jones, 2013; Onyango, 2009; Rohrbach et al., 2003). These varieties are grown during the long rain season since they require approximately 6 months to mature (**Table 3.10**). This information was corroborated by the ground truth information collected from the maize fields during the fieldwork exercise.

Table 3.10: Maize varieties grown in the region, their year of release, the owner of the variety, the production zone (meters above sea level), the number of months required to reach maturity, and the expected amount of yields (in tons/ha). The owners of the varieties were either Kenya Agriculture Livestock Research Organization (KALRO) and/or the Kenya Seed Company (KSC) ("Improved Maize (Zea mays) Variety List From Kenya, Uganda and Tanzania," n.d.; Rohrbach et al., 2003).

Maize Variety	Year of release	Owner	Production zone (masl)	Maturity (months)	Yields (tons/ha)
H614D	1986	KALRO/KSC	1500-2100	6-9	8-10
H628	1999	KSC	1500-2100	6-8	9-12
H629	2000	KSC	1500-2100	6-8	9-11
KH600-16A	2001	KALRO-Kitale	1800-2500	6-8	7-8
H6213	2002	KSC	1600-2200	6-8	10-15
H6210	2002	KSC	1700-2100	6-8	11-15
H624	2004	KSC	1600-2100	6-7	6-8
KH600-23A	2008	KALRO	1800-2500	5-6	8.6-14.8

Whereas late maturing hybrids are favored for early sowings, quick maturing hybrids are favored for late sowings (Moore et al., 2014). This is because the early sowing balances the risk of frost soon after emergence and excessive heat at flowering while late sowing avoids excessive heat at flowering but increases the risks of insect attack, disease in the hot months, and slow dry down periods in cool, wet months.

Some of the reasons for which maize is grown within the study area include: human consumption; for seed crop; harvesting for fodder or silage (Moore et al., 2014). Whereas the maize planted for human consumption, fodder and silage has fewer controls, the maize grown for seed has more controls and restrictions.

3.3.1.2   Description of Maize BBCH Development Stages in the Study Area

3.3.1.2.1   BBCH-Scale Description

The Biologische **B**undesanstalt, **B**undessortenamt und **CH**emische Industrie (BBCH) scale is a universal system for a uniform coding of phenologically similar growth stages of all plant species (Meier, 2001). It was developed by scientists of the German Federal Biological Research Centre for Agriculture and Forestry (BBA), in conjunction with the Federal Office of Plant Varieties (BSA), the German Agrochemical Association (IVA) and the Institute for Vegetables and Ornamentals to aid in distinguishing between monocotyledons, dicotyledons, perennial plants, graminae and vegetatively propagated plants (Lancashire et al., 1991). Before the BBCH-scale was developed, there existed other scales , for example the Hanway scale (O'Keeffe et al., 2009). There was therefore need to ensure that its descriptions of developmental stages peculiar to particular crops, was synchronized with other scales already in existence (Harrell et al., 1998; Lancashire et al., 1991). The BBCH code uses a decimal code for

the description of agricultural crops growth stages and outlines the main growth/phenological stages as well as the secondary growth stages of the plant development (Odendo et al., 2001). The main growth stages are: germination, leaf development, formation of side shoots/tillering, stem elongation, booting, heading, flowering, development of fruit, ripening/maturity, and senescence/beginning of dormancy (**Table 3.11**).

Table 3.11: Principal growth stages (Meier, 2001).

PRINCIPAL GROWTH STAGES	
STAGE	DESCRIPTION
0	Germination/ sprouting/ bud development
1	Leaf development (main shoot)
2	Formation of side shoots/ tillering
3	Stem elongation or rosette growth/ shoot development (main shoot)
4	Development of harvestable vegetative plant parts or vegetatively propagated organs/ booting (main shoot)
5	Inflorescence emergence (main shoot)/ heading
6	Flowering (main shoot)
7	Development of fruit
8	Ripening or maturity of fruit and seed
9	Senescence, beginning of dormancy

The secondary growth stages are more specific and provide the details specific to groups of plants with similar growth patterns (Lancashire et al., 1991). The same scale using the same definitions generally covers species that develop similarly. The secondary growth stages 0 to 8 correspond to the respective ordinal numbers or percentage values indicating the degree of development within the principal stage (**Table 3.12**). For example, stage 3 could represent 3rd true leaf, 3rd tiller, 3rd node or 30% of the final length or size typical of the species or 30% of the flowers open.

Table 3.12: Phenological growth stages and BBCH-identification keys of cereals (Maize) (Lancashire et al., 1991).

Principal growth stage 0: Germination
00 Dry seed (caryopsis)
01 Beginning of seed imbibition
03 Seed imbibition complete
05 Radicle emerged from caryopsis
06 Radicle elongated, root hairs and/or side roots visible
07 Coleoptile emerged from caryopsis
09 Emergence: coleoptile penetrates soil surface (cracking stage)

Principal growth stage 1: Leaf development
10 First leaf through coleoptile
11 First leaf unfolded
12 2 leaves unfolded
13 3 leaves unfolded
1 . Stages continuous till . . .
19 9 or more leaves unfolded

Principal growth stage 3: Stem elongation
30 Beginning of stem elongation
31 First node detectable
32 2 nodes detectable
33 3 nodes detectable
3 . Stages continuous till . . .
39 9 or more nodes detectable

Principal growth stage 5: Inflorescence emergence, heading
51 Beginning of tassel emergence: tassel detectable at top of stem
53 Tip of tassel visible
55 Middle of tassel emergence: middle of tassel begins to separate
59 End of tassel emergence: tassel fully emerged and separated

Principal growth stage 6: Flowering, anthesis
61 Male: stamens in middle of tassel visible
    Female: tip of ear emerging from leaf sheath
63 Male: beginning of pollen shedding
    Female: tips of stigmata visible
65 Male: upper and lower parts of tassel in flower
    Female: stigmata fully emerged
67 Male: flowering completed
    Female: stigmata drying
69 End of flowering: stigmata completely dry

Principal growth stage 7: Development of fruit
71 Beginning of grain development: kernels at blister stage, about 16% dry matter
73 Early milk
75 Kernels in middle of cob yellowish-white (variety-dependent), content milky, about 40% dry matter
79 Nearly all kernels have reached final size

Principal growth stage 8: Ripening
83 Early dough: kernel content soft, about 45% dry matter
85 Dough stage: kernels yellowish to yellow (variety dependent), about 55% dry matter
87 Physiological maturity: black dot/layer visible at base of kernels, about 60% dry matter
89 Fully ripe: kernels hard and shiny, about 65% dry matter

Principal growth stage 9: Senescence
97 Plant dead and collapsing
99 Harvested product

In addition to the code description, drawings showing clear and easily recognizable (external) morphological characteristics for some important phenological stages are included (**Figure 3.11**).
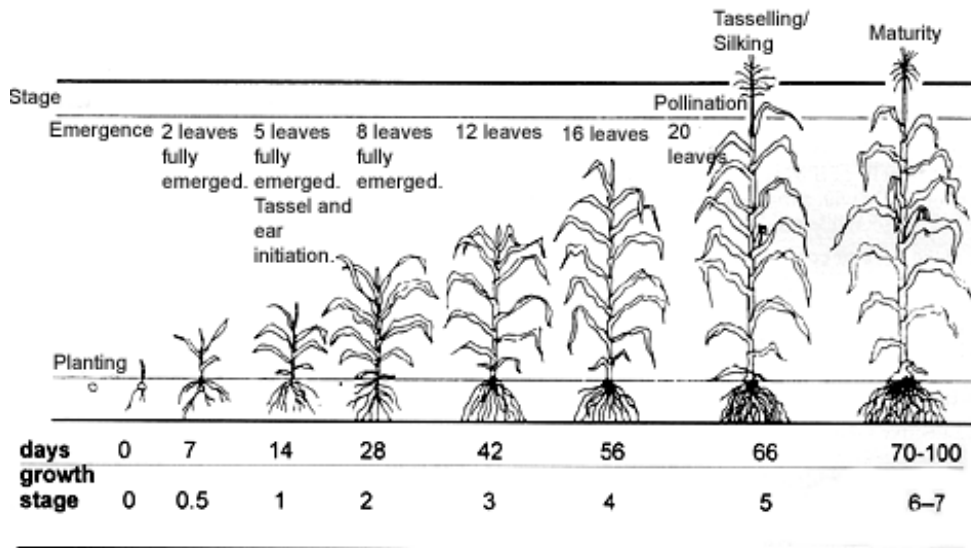
Figure 3.11: An example of the maize growth stages from planting to maturity ("NSW Department of Primary Industries," 2017) http://www.dpi.nsw.gov.au/__data/assets/image/0013/125212/sweet-corn-fig5.gif.

The design of the code is sufficiently flexible to describe the development of many important crops and weeds since it uses two decimal digits to represent the principal and secondary growth stages. Thus, it provides a framework within which more specific scales for individual crops may be constructed (Lancashire et al., 1991). The arithmetic difference between codes has no mathematical meaning, with an arithmetically greater code indicating a plant at a later growth stage (Meier et al., 2010). The uniformity of the scale on the other hand makes the code easy to remember and use in agricultural practice and simplifies storage and retrieval in a computer system.

An assumption by the BBCH coding programs is that the user-supplied information is correct. However, the BBCH-scale generally refers to stands or populations of plants rather than to individual plants (Lancashire et al., 1991). Thus, at times the user may be required to estimate the number of leaves produced at a certain growth stage in order to determine the average growth stage of the plants. In instances where there are notable differences in the different plants within a field, noting the period of the first principal growth stage occurrence may be particularly important (Lancashire et al., 1991).

3.3.1.2.2 BBCH-Stages Identifcation of Maize Varieties in the Study Area

The identification of the maize BBCH growth stages was an important aspect of this research. During the field campaign, some of the principal growth stages were identified (**Figure 3.12**). Since the planting days for the maize fields were varying, the photographs were acquired from different fields within the study area that were at different growth stages.
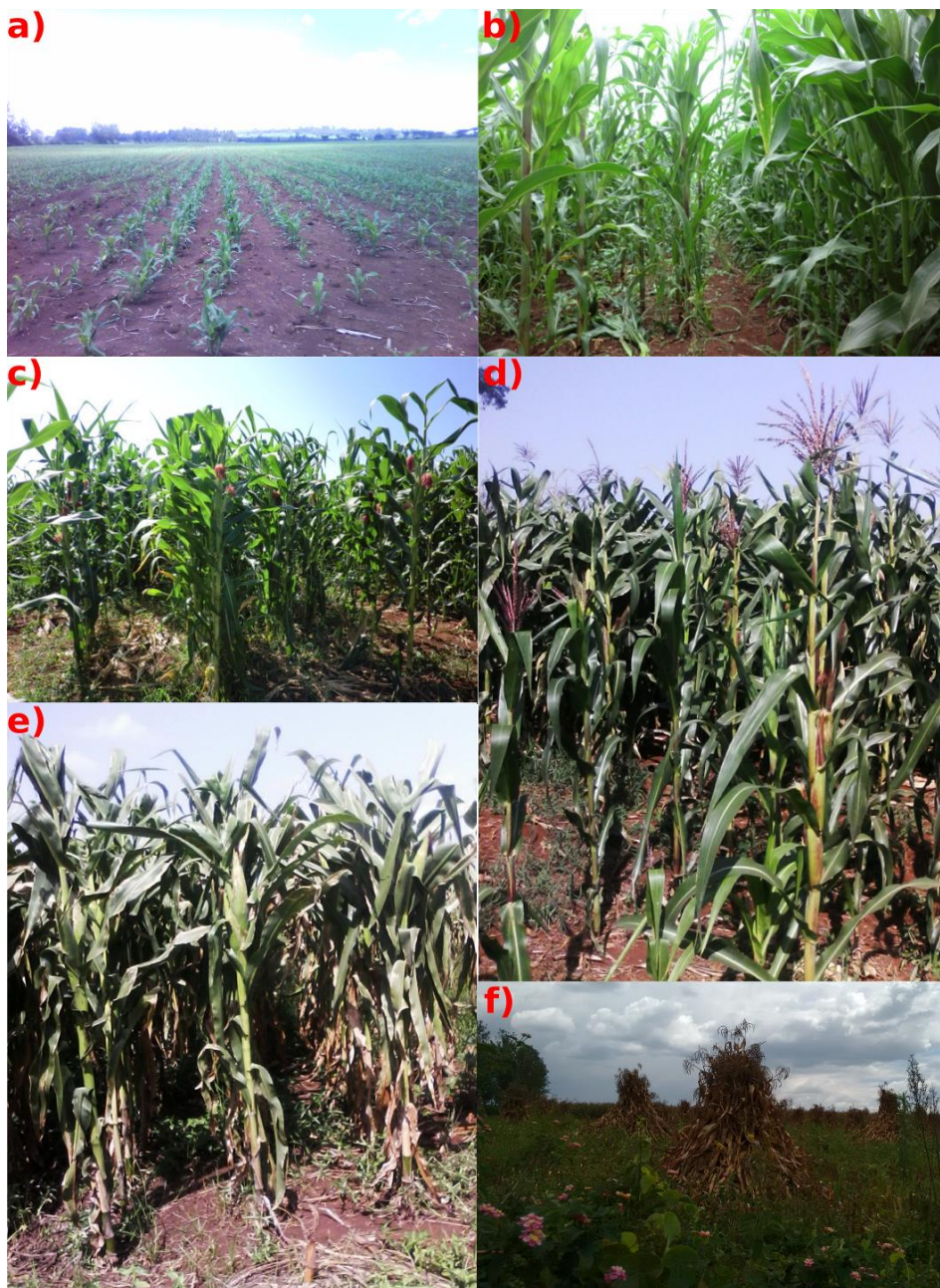
Figure 3.12: Photographs taken from the fields during the fieldwork campaign, showing the different BBCH growth stages. a) BBCH 1 (5/5/2015), b) BBCH 3 (24/6/2015), c) BBCH 5 16/7/2015, d) BBCH 6 11/8/2015, e) BBCH 7 (28/8/2015), f) BBCH 9 (15/9/2015).

The fieldwork exercise could not however exhaustively cover the whole six month maize growth duration. Information to identify all the BBCH growth stages was therefore inferred from the farm managers and farmers field information. Using their experiences and field knowledge, and coupled with the elaborate BBCH secondary stages description (**Table 3.12**), the number of days for the various BBCH stages could be deciphered. For example, the days taken from planting to germination were 7 days, from germination to flowering an average of 3 months, the fruit development stage started on the fourth month after germination, and continued for a period of 1 month to maturity. The period from maturity to senescence lasted 1 month. With this information the principal and secondary BBCH stages were deduced (**Table 3.13**). This information was also compared with a previous research study which had established that the full tassel emergence (BBCH: 59) usually occurs 50 days after germination (Earth Observation Research Branch Team & Agriculture and Agri-Food Canada, 2011).

Table 3.13: Principal and secondary BBCH maize growth stages inferred from the farmers and farm managers' information.

Principal Stage 0	Days After Germination	Principal Stage 5	Days After Germination
00	1	51	31-38
01	2	53	39-45
03	3	55	46-53
05	4	59	54-60
06	5	Principal Stage 6	Days After Germination
07	6	61	61-65
09	7	63	66-71
Principal Stage 1	Days After Germination	65	72-77
10	8	67	78-83
11	9	69	84-90
12	10	Principal Stage 7	Days After Germination
13/14	11	71	91-98
15/16	12	73	99-105
17/18	13	75	106-113
19	14	79	114-120
Principal Stage 3	Days After Germination	Principal Stage 8	Days After Germination
30	15	83	121-128
31	16	85	129-135
32	17/18	87	136-143
33	19/20	89	144-150
34	21/22	Principal Stage 9	Days After Germination
35	23/24	97	151-170
36	25/26	99	171-180
37	27/28		
38	29		
39	30		

3.3.2   Farm Management Records Information

Accurate identification of ground features captured on the satellite images is an important component of image interpretation. For this reason, field visit campaigns were conducted in order to collect the ground reference data. In addition to assisting in the interpretation of the satellite images, reference data serves the purposes of sensor calibration, analysis of the satellite images and the verification of information extracted from satellite images (Lillesand et al., 2014). Despite the process of reference data collection being very expensive and time-consuming, ground reference data points should be selected such that they are evenly distributed across the entire study area (Dusseux et al., 2014).

With the aid of the field maps of the ADC Sabwani and ADC Olngatongo fields, the sample fields from which the ground reference data was to be collected were selected such that they were spatially distributed across the extent of the entire study area, ensuring that the heterogeneity within the entire study area was captured. A total of nine fields were selected for this (**Figure 3.13**).
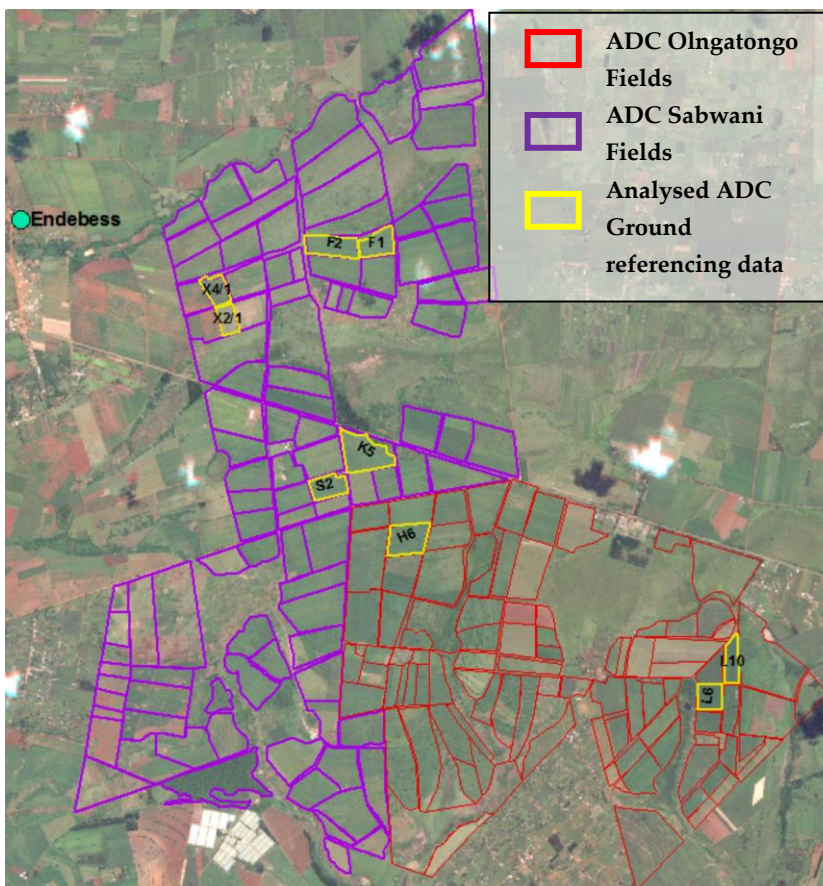
Figure 3.13: The location of the 9 selected ground-referencing fields from ADC Sabwani and ADC Olngatongo. The fields are overlaid on a true color composite Sentinel-2 image, acquired on 06/06/2016.

In addition to the 9 selected fields used for the collection of the ground referencing data, 15 ADC Olngatongo fields were selected for analysis (**Figure 3.14**). Information on all the 24 maize fields is provided in (**Table 3.14)**. The ADC Olngatongo maize fields were selected for further analysis since the farm management records were more accessible and the response by the management on follow up querries about the collected data was positive.
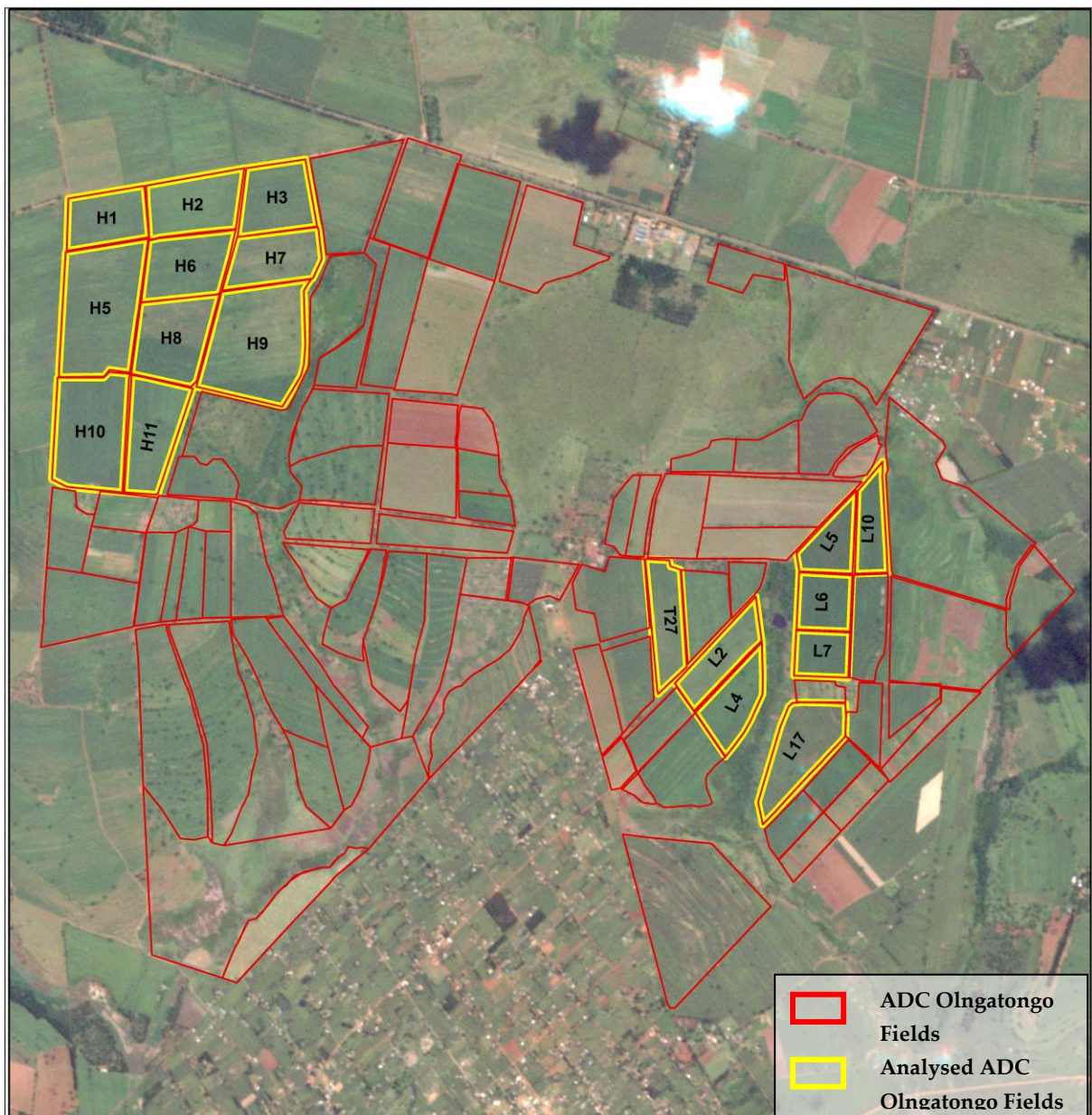
Figure 3.14: The ADC Olngatongo maize fields that were selected for further analysis, in addition to those that had been selected for the collection of the ground referencing data. The fields are overlaid on a true color composite Sentinel-2 image, acquired on 06/06/2016.

Table 3.14: Field information showing the field names and sizes, maize planting dates, planting direction (measured in degrees from the north direction) and the maize variety cultivated.

Field name	Size (Ha)	Planting date	Planting direction	Maize Variety
F1	16	28/03/2015	80°	H6213
F2	16	20/03/2015	80°	H6213
K5	18	07/03/2015	80°	H628
S2	14	28/03/2015	80°	H628
X2/1	15	02/04/2015	180°	H614
X4/1	15	28/04/2015	80°	H614
H1	14	03/03/2015	80°	H6213
H2	18	04/03/2015	80°	H6213
H3	24	25/03/2015	80°	H6213
H5	40	02/03/2015	80°	H6213
H6	16	22/03/2015	80°	H6213
H7	16	24/03/2015	80°	H6213
H8	18	14/03/2015	80°	H6213
H9	40	06/03/2015	80°	H6213
H10	24	04/03/2015	180°	H6213
H11	19	05/03/2015	180°	H6213
L2	13	03/04/2015	45°	H628
L4	12	26/04/2015	45°	H628
L5	11	26/04/2015	180°	H628
L6	10	24/04/2015	180°	H628
L7	10	24/04/2015	180°	H628
L10	10	25/04/2015	180°	H628
L17	18	23/04/2015	180°	H628
T27	12	14/04/2015	175°	H628

The field campaigns dates' were selected to coincide as much as possible with some of the TSX image acquisition dates (**Table 3.15**). This ensured that the ground reference information collected was a true reflectance of the image information and therefore minimized the error and distortions that would occur due to high crop development rates, rainfall or farm management practices (Dusseux et al., 2014; Zillmann et al., 2015).

Table 3.15: Comparison of the field visit dates to the TerraSAR-X image acquisition dates.

	Dates		
TerraSAR-X dates	8/06/2015 (Monday)	21/06/2015 (Sunday)	13/07/2015 (Monday)
Field visit dates	11/06/2015 (Thursday)	23/06/2015 (Tuesday)	16/07/2015 (Thursday)

The ground reference data collected from the fields included: the soil data- for the analysis of the bulk density, texture, carbon/nitrogen content, and pH; weather data- rainfall and temperature; maize crop data- variety type, plant population density (row and crop spacing), leaf length, leaf width, canopy height; farm management activities- reason for which the farmer grows the maize, the field sizes, the planting direction, the dates for the application of fertilizers, the top dressing, and herbicides, as well as, harvesting modes (**Table 3.16**). Additionally, questionnaires described in (**chapter 3.3.5**), were administered for the collection of the field information.

Table 3.16: Summary of the field data collected during the field visits.

Field	Soil Data	Weather Data	Maize Crop Data	Farm Management Activities Data
Sabwani F1	x	x	x	x
Sabwani F2	x	x	x	x
Sabwani K5	x	x	x	x
Sabwani S2	x	x	x	x
Olngatongo L6	x	x	x	x
Olngatongo L10	x	x	x	x
Olngatongo H6	x	x	x	x
Kenya Seed X2/1	x	x	x	x
Kenya Seed X4/1	x	x	x	x

Within each of the 9 selected ground referencing fields, namely F1, F2, K5, S2, L6, L10, H6, X2/1, and X4/1, a maximum of three sampling quadrats q1, q2 and q3 were selected, each measuring 6 m^2 x 6 m^2 (**Figure 3.15**). The number of sampling quadrats was dependent on the size of the field, soil variability within the field, and the slope of the field. After identifying the location of each of the quadrats within the field, the four corners of each quadrat were clearly marked using ropes and sticks for easy identification during the consequent field visits. The quadrats were then geo-located and mapped using a Juno Trimble handheld GPS with up to two meters accuracy. A longitudinal transection within each of the quadrat was selected, along which data collection and measurements would be undertaken. Three sub-quadrats (a, b, c) were identified, each for the three different field visits: on the first field visit (11/06/2015) sampling was done on sub-quadrat a; on the second field visit (23/06/2015) sampling was done on sub-quadrat b; and on the third field visit (16/07/2015) sampling done on the sub-quadrat c. The sampling operations that were undertaken in each of the quadrats were specific to the kind of data collected: leaf area index (LAI) data or soil data. The operations are elaborated in the sub chapters below, namely Leaf Area Index (LAI) Data and Soil data.
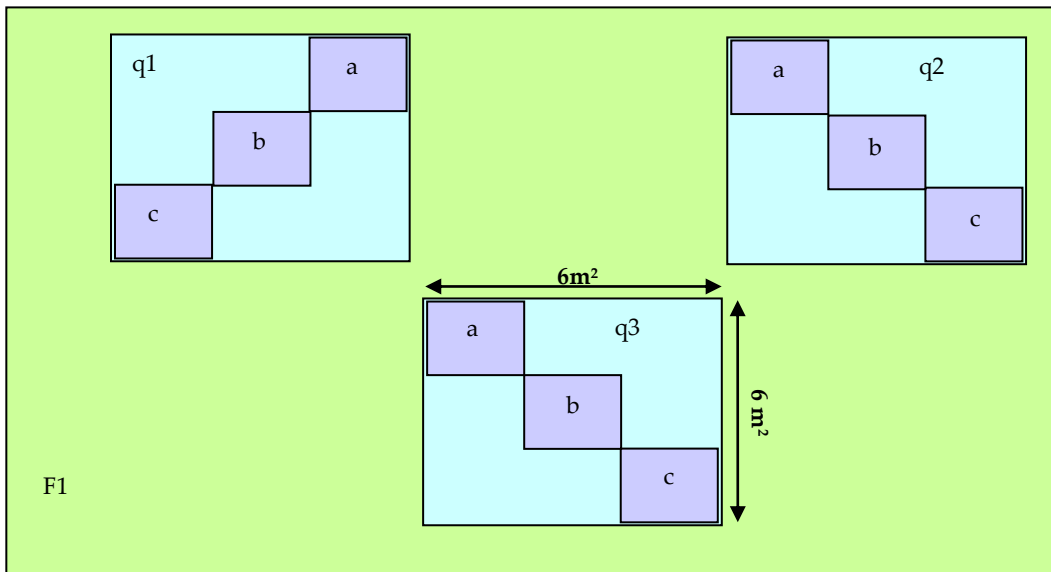
Figure 3.15: An example of the sampling quadrats q1, q2, and q3 that were taken in one of the fields, F1. The sub-quadrats a, b and c sampled on the 11/06/2015, 23/06/2015 and 16/07/2015 respectively, were taken along the longitudinal transection of each of the quadrat.

3.3.3   Leaf Area Index (LAI) Data

Leaf Area Index (LAI) is defined as half the developed area of photosynthetically active elements of the vegetation per unit horizontal ground area (Chen & Black, 1992; Demarez et al., 2008). It is a measure of leafiness per unit ground area and a strong indicator of crop productivity (Ranson, 1985). It is therefore an important parameter in predicting crop growth and yields (Yin et al., 2003). Being a fundamental canopy primary variable, LAI should be independent of observation conditions (Weiss & Baret, 2016). LAI determines the size of the interface for exchange of radiation energy and mass between the canopy and the atmosphere (Demarez et al., 2008). In crop growth models, LAI is one of the state parameter of crop growth models that controls processes such as photosynthesis, respiration and rain interception (Guissard et al., 2005) with the performance of the crop growth model being strongly influenced by the accuracy of the leaf area predictions (Keating & Wafula, 1992). Various methods and techniques are applied to measure LAI. These can be broadly categorized into two namely: indirect LAI measurement which is carried out using space-based observations; and in situ LAI measurement which entails destructive sampling of the leaves or the use of commercially available dedicated instruments (Baret et al., 2014). Even though various techniques are used to measure LAI, algorithms providing a good basis to monitor the seasonal variation of the LAI for crops at decametric resolution between field measurements, digital hemispherical cameras (DHPs), radiative transfer model results and satellite imagery has been developed (Li et al., 2015).

3.3.3.1   Indirect LAI Estimation

Vegetation LAI estimated from remote sensing techniques includes all green contributors (Weiss & Baret, 2016). However, except when using directional observations, LAI is not directly accessible from remote sensing observations. This is due to the possible heterogeneity in leaf distribution within the canopy volume (Chen et al. 2005). Therefore, remote sensing observations are rather sensitive to the 'effective' leaf area index (one-half of the total area of light intercepted by leaves per unit horizontal ground surface area, assuming random foliage spatial distribution) (Zheng & Moskal, 2009). In the visible and infrared spectral domains, the wavelength is very short compared to the size of the leaves and stems. The intensity of the reflected signal is mainly driven by the chemical composition of the target. In the microwave domain, the wavelength is on the order of the leaves and stem size and the intensity and phase of the wave backscattered are related to its geometry and to its dielectric properties (Ulaby et al., 1984). In both cases, the measured signal is the resultant of the plants and soil contributions. The relative importance of the plant and soil contributions varies with the crop type and phenological stage (Blaes et al., 2006). The reflectance/backscattering to LAI relationship is affected by a large number of external and internal factors that are subject to spatial and temporal variations. These factors include the canopy architecture (angular distribution of the stems, leaves, flowers, fruits), the fraction of visible soil, the soil mineral and organic composition, soil moisture and roughness (Royo & Villegas, 2011).

LAI has been established to be strongly non-linearly related to reflectance and therefore its estimation from remote sensing observations is strongly scale dependent (Garrigues et al., 2006; Weiss & Baret, 2016). Various studies to estimate and monitor LAI via remote sensing techniques have been undertaken. Laurent et al (2014) estimated the LAI from S-2 images whereas Korhonen et al. (2017) combined both S-2 and L-8 images. Radar has been used in estimating and relating of maize and other crops' LAI to backscatter coefficient, demonstrating its important all-weather capability advantage for operational crop growth monitoring (Dusseux et al., 2014; Hosseini et al., 2015; Inoue et al., 2002; Ulaby et al., 1984). LAI from SAR images was found to be significant at values of LAI greater than 0.5 (Ulaby et al., 1984). The C-band SAR signal in single polarization saturates at an LAI value of 4.6 m^2m^{-2}, above which changes in the crop growth and development cannot be sensed (Blaes et al., 2006). Soil moisture influences the signal for sparsely vegetated crop fields where the LAI was less than 2.7 thus making LAI the best vegetation descriptor for soil moisture and backscatter retrieval from microwave remote sensing (Blaes et al., 2006; Kumar et al., 2015). Optical and radar satellites have also been used in combination for the purposes of LAI estimation (Gao et al., 2013).

Available satellite LAI products, which are currently used over local (less than 10km^2), regional (less than 1000km^2) and global extents, exhibit significant differences (Baret et al., 2014). This can be attributed to the LAI spatial and temporal variation or the implemented processing technique in the LAI processing (Koetz et al., 2005). Acquisition conditions (the illumination and observation geometry, the state of the atmosphere, landscape fragmentation, landscape elements inherent contrasts and topography) and the sensor's technical characteristics design (band width and location, pixel footprint, image sensor technology, internal calibration algorithms, pre-processing algorithms, etc) may be attributed to the differences (Royo & Villegas, 2011).

Many indirect LAI estimates rely on statistical approaches that require a minimum spatial sample size equal to the images pixel size (Baret et al., 2014). Three kinds of approaches are used to retrieve LAI from remote sensing images: determinist modeling, semi-empirical modeling and empirical modeling (Laurent et al., 2014).

Determinist/physically-based approaches have higher transferability, making them better suited than empirically based approaches for estimating LAI even at global scales. They employ the inversion of radiative transfer models (plant canopy and underlying soil). Radiative transfer models are a good technique for describing the expected reflectances at different frequencies (usually, in the visible and infrared), based on the acquisition parameters (soil properties, leaf structure and composition, canopy structure and composition, illumination and observation geometry). The LAI being one of the input parameter of the models, would be possible to retrieve its value by inverting the model. However, in most of the cases, the complexity of the radiative transfer process does not allow an analytical inversion of the physical model. Consequently, a numerical optimisation process is generally required. Four regularization methods have been proposed, allowing for stable solutions: 1) model coupling, 2) using a priori information (e.g. Bayesian approaches), 3) spatial constraints (e.g. using objects), and 4) temporal constraints. For mono-temporal data, only the first three methods can be applied (Laurent et al., 2014). Radar physical models on the other hand are based on complex electromagnetic descriptions of all the canopy scatterers (stalks, leaves and ears) and of the underlying soil surface (Ulaby et al., 1984). Due to the large amount of parameters needed and to their complexity, they are not suitable for operational inversion purposes. Different approaches have been used to model the volume diffraction problems - the main electromagnetic phenomenon inside crop canopies. The two main approaches are the amplitude approach (based on the Maxwell equations) and the intensity or power approach (also refered to as the radiative transfer theory based on a power balance within an elementary volume). Each of them can consider the vegetation as a continuous medium or as a collection of discrete scatterers with randomly distributed losses (Ulaby et al., 1984).

Semi-empirical LAI retrieval techniques usually combine a physical model with an inversion method making use of empirical relationships (Laurent et al., 2014). The semi-empirical models utilize optical remote sensing of radiative transfer models in order to build a synthetic dataset. The synthetic dataset is then used to establish empirical statistical relationships between measured reflectances and LAI. The most popular approaches for building such an empirical relationship are the lookup table approach (LUT) and the artificial neural network (ANN) approaches. Both a LUT and ANN method needs a time-consuming initialisation phase, but after initialisation, the operational retrieval computations are almost instantaneous. On the other hand, radar semi-empirical models are based on simplified theoretical principles (Attema & Ulaby, 1978). They use only a few parameters and can be inverted to retrieve bio- or geophysical parameter from the backscattering coefficient. Semi-empirical models need calibration efforts for each crop species and for the most distinct phenological stages of the crop. Two approaches are mainly applied. The first approach is based on the radiative transfer theory formulated for a very simplified medium supposed to represent the canopy layer, for example the water cloud model, developed by (Attema & Ulaby, 1978). The vegetation canopy is modeled as a volumetric water cloud consisting of the volumetric moisture content of the soil, volumetric water content of the vegetation and the plant height as three target parameters. A second approach that was based on the simplification of the RT2 model was proposed by Cookmartin et al. (1998). RT2 is a theoretical model based on the radiative transfer theory applied to a layer composed of discrete scatterers. Only the relevant relationships are conserved, calibrated and finally validated.

The empirical models are based on statistical relationships built on remote sensing vegetations indices (VIs) and LAI ground measurements (Guissard et al., 2005). Most of the existing VIs are based on the large contrast existing between vegetation reflectance observed in the red wavebands and the infrared wavebands. This contrast is as an indicator of vegetation presence and status. VIs have been largely used to retrieve not only LAI, but also other vegetation descriptors like soil canopy coverage, and leaf density. A lot of different VIs were developed by many authors, in order to improve the sensibility of the indices to the parameter to retrieve, while minimising the interferences brought by external factors such as soil background, illumination and observation conditions, atmosphere diffusion. Radar empirical models on the other hand are based on a statistical analysis of experimental data set (Ulaby et al., 1984). These models consist in rather simple mathematical relationships between the backscattering coefficient and the bio- or geo-physical variables. The developed models are specific to the data set and cannot be generalised.

In summary, the major challenge in modeling remains the loss in the model's predictions quality when it is calibrated in more diverse conditions in comparison to when it is calibrated and run into the same acquisition conditions (Guissard et al., 2005).

3.3.3.2   In situ LAI Estimation

The in situ LAI estimation techniques are categorized into non-destructive and destructive techniques. Despite the in situ LAI estimation techniques being more time-consuming and labour-intensive compared to indirect LAI estimation techniques (Zheng & Moskal, 2009), they are still needed for the calibration and validation of indirect methods (Jonckheere et al., 2004).

3.3.3.2.1   Non Destructive LAI Estimation

The non-destructive LAI measurements involves the use of either Digital Hemispherical Photographs (DHPs), for example the Nikon D3200 camera and an EX Sigma 4.5 mm 1:2.8 DC HSM circular fisheye lens (Latorre, 2014; Martinez et al., 2004; Weiss et al., 2004; Zhang et al., 2005), or the use of Meters, for example AccuPAR, LAI-2000, SunScan (Wilhelm et al., 2000). Their non-destructive nature allows repetitive measurements to be taken over time on the same plot or plant, such that the grain produced on the measured plants is available at the end of their growth cycle. In addition, the method avoids the errors associated with destructive samplings of biomass, and is fairly quick (Royo & Villegas, 2011). However, the use of canopy spectra for biomass assessment requires a thorough knowledge of the conditions of use and the constraints imposed by the measurement-related noise caused by the sensor system, the canopy structure, and the environment, which should be carefully taken into consideration in order to obtain reliable results. In comparison to LAI from destructive sampling, the LAI from the meters is usually underestimated (Wilhelm et al., 2000). There is however a unique linear correlation between LAI estimated destructively and by each of the meters. Comparing the LAI estimated from the DHPs to the LAI estimated from the meters, Homolová et al., (2007) found that the LAI-2000 produces higher estimates of the effective leaf area index than DHP, whereas the DHP produced the higher "true" LAI estimates. In order to standardize the estimation of the LAI from the DHPs and the meters, protocols and manuals for example by Demarez et al., (2008), Pfeifer & Gonsamo (2015) and Shang et al., (2014a), have been provided.

The DHPs are usually processed using available digital processing softwares, for example the CAN_EYE V6.4.91 free software (Weiss & Baret, 2017). The softwares extract various canopy structure characteristics from the DHPs. These characteristics are: a) Plant Area Index (PAI), b) Average Leaf

inclination Angle (ALA), c) Fraction of Absorbed Photosynthetically Active Radiation (FAPAR), d) Vegetation cover fraction (FCOVER) and e) the Bidirectional & mono-directional gap fraction. The software's set of features are such that it provides an efficient, accurate, flexible, portable, and traceable approach.

The CAN_EYE software estimates the effective and true LAI from unidirectional gap fractions measured in crops (Demarez et al., 2008). Whereas the effective LAI is computed with the Poisson law, the true LAI is estimated by introducing a clumping index in the Poisson law. This clumping index estimation of the LAI is based on the averaging method proposed by Lang (1986). CAN_EYE includes an automatic image classification and allows the processing of a series of photographs which is mandatory to sample the spatial variability of the canopy (Demarez et al., 2008). The classification process is an iterative and interactive process where the user not only picks training pixels for vegetation class, but can also refine either the selection of the training pixels or the classification results if necessary. The remaining pixels are classified as "sky". An automatic classification is then performed by calculating the images gap fraction (Latorre, 2014). The processing time is short since a series of photographs can be processed at once. A look-up-table (LUT) is used to estimate the effective LAI and the true LAI (Weiss et al., 2004).

3.3.3.2.2   Destructive LAI Estimation

The methods used for the destructive measurement can be categorized into three: planimetric method; leaf area to weight ratios; and area from leaf dimensions (Norman & Campbell, 1989).

In the planimetric method, automatic planimeters, for example the LI-3000, or the LI-3100, are used to measure the area of the destructively sampled leaves.

The leaf area to weight ratios method involves taking a representative subsample of the collected sample, measuring the leaf area or the weight of this subsample, and then relating it to greater sample.

With the area from leaf dimensions method, the length and width of the individual leaves on any one sampled plant are measured, and then summed up (Odhiambo et al., 2015). The summed up leaf area is then multiplied by the plant population density (ppd) in order to derive the LAI (Amanullah et al., 2007). The ppd is the number of plants per unit ground area (**Equation 3.1**).

Leaf Area Index = Leaf area per plant × No of plants per m^2 … (**Equation 3.1**)

3.3.3.3   Procedure for the estimation of LAI from the field

The LAI estimations were done for the fields F1, F2, K5, S2, L6, L10, H6, X2/1 and X4/1(**Chapter 3.32, Figure 3.13**). The counting of the total number of maize plants in each of the sub quadrats was first done. The ppd was estimated by dividing the number of maize plants within the sub-quadrat with the area size of the sub quadrat. Applying the sampling procedure by Pearce et al.,(1975), three maize plants were randomly selected along the identified transect of each of the sub-quadrats, and cut. Once cut, the samples from the different quadrats, but still within a specific single field were mixed together. From this field sample, five maize plants were randomly selected (**Figure 3.16**). The length of the five randomly selected maize plants was measured and averaged. This was to establish the average maize canopy height. To get an average of the total number of leaves per maize plant, the number of leaves for each of the five selected plants was counted, and then averaged.

Figure 3.16: Destructive leaf area sampling in one of the fields in the study area. The photo was taken on 23/6/2015.

The next step was the measurement of the leaves' lengths (L) and widths (W) (**Figure 3.17**). These measurements were then averaged and the average total leaf area estimated using (**Equation 3.2**) (Keating & Wafula, 1992; Mokhtarpour et al., 2010).

LA = 0.75 × L × W   …**Equation 3.2**

Where:

LA is the leaf area

L is the leaf length along the main nerve

W is leaf width of the widest place

0.75 is a coefficient

The destructive LAI was then determined using Montgomery's formula (**Equation 3.3**) which has been quoted by Pearce et al., (1975), Borowiecki & Filipiak (1992), and Szulc et al., (2015):

LAI = (LA * PPD) / 10000   …**Equation 3.3**

Where:

 LAI is the leaf area index

LA is the leaf area of a single plant (cm^2)

PPD is plant density per 1 m^2 (plants·m^{-2})
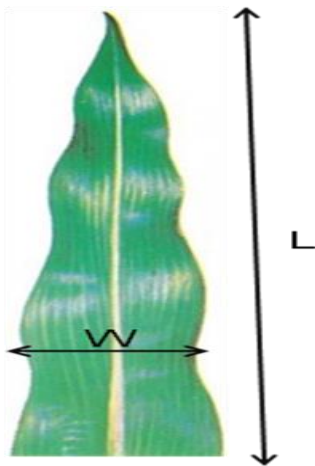
Figure 3.17: The leaf dimensions, Length (L) and Width (W) to calculate the leaf area.

The results from the field measurements are displayed in (**Table 3.17**). These measurements varied from one field to the other, and were indicative of the condition of the plant. In (**Figure 3.18**), fields F1 and X2/1 show a notable difference in the maize condition in the photo taken on the 16/07/2015.

Table 3.17: Field measurements taken in the field for the calculation of the LAI. The measurements are rounded up to the nearest whole number.

Field	Field Visit Date	Average Plant Height (cm)	Average Leaf Length (cm)	Average Leaf Width (cm)	Average Leaf Number (per plant)	Average Total Leaf Area per field (cm²)	Plant population density per field	LAI per field
F1	11/06/2015	182	75.5	8.5	17	8182.3	4.4	3.6
	23/06/2015	202	77	8.6	18	8939.7	4.4	3.93
	16/07/2015	216	78	9.2	23	12378.6	4.4	5.45
F2	11/06/2015	139	76	8.8	19	9530.4	4.4	4.19
	23/06/2015	161	77	9	20	10395.0	4.4	4.57
	16/07/2015	178	78	9	21	11056.5	4.4	4.86
K5	11/06/2015	189	76	8.7	18	8926.2	4.4	3.93
	23/06/2015	241	77	8.8	19	9655.8	4.4	4.25
	16/07/2015	253	79	9	21	11198.3	4.4	4.93
S2	11/06/2015	177	75.6	8.5	17	8193.2	4.4	3.6
	23/06/2015	250	75.8	8.7	18	8902.7	4.4	3.92
	16/07/2015	269	78.8	9	22	11701.8	4.4	5.15
H6	11/06/2015	214	75.7	8.5	17	8204.0	4.4	3.61
	23/06/2015	234	77	8.9	19	9765.5	4.4	4.3
	16/07/2015	286	77.5	9.1	23	12165.6	4.4	5.35
L6	11/06/2015	82	68	6.2	12	3794.4	4.4	1.67
	23/06/2015	137	74.8	8	16	7180.8	4.4	3.16
	16/07/2015	264	75.8	8.7	18	8902.7	4.4	3.92
L10	11/06/2015	64	72.1	6.6	12	4282.7	4.4	1.88
	23/06/2015	119	73	7.8	15	6405.8	4.4	2.82
	16/07/2015	240	78.7	8.7	18	9243.3	4.4	4.07
X2/1	11/06/2015	115	69.2	6.1	12	3799.1	4.4	1.67
	23/06/2015	158	71.3	7.9	15	6336.8	4.4	2.79
X4/1	11/06/2015	133	68.2	5.9	10	3017.9	4.4	1.33
	23/06/2015	190	69.1	7.1	13	4783.4	4.4	2.1
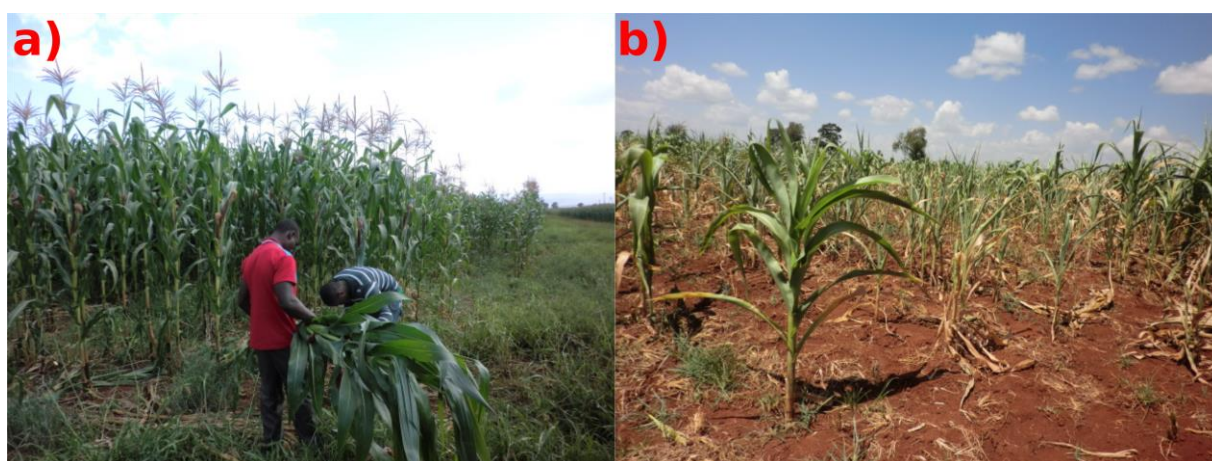
Figure 3.18: Photos showing two of the sample fields in the study area on 16/07/2015. a) field F1, b) field X2/1.

3.3.3.4 LAI Modeling Techniques

3.3.3.4.1 LAI Modeling Techniques in General

A model may be defined as a simplified schematic representation of a system behavioral concept using a set of equations for the purpose of explaining, understanding or improving the performance of a system (Murthy, 2004). A model simulation therefore reproduces the essential characteristics of a system, which are then studied in an abbreviated time scale.

Depending on their purpose, models can be classified into different groups (Murthy, 2004):

i. Statistical models (use statistical techniques to measure model relationships. e.g. step down regressions, correlation);

ii. mechanistic models (are based on physical selection and explain the relationship of influencing dependent variables);

iii. deterministic models (they have defined coefficients and estimate the exact value of the dependent variable);

iv. stochastic models (give different outputs for the various sets of inputs, along with the probabilities);

v. dynamic models (time is included as a variable and both dependent and independent variables are having values which remain constant over a given period of time);

vi. static (time is not included as a variables and both dependent and independent variables remain constant over a given period of time);

vii. simulation models (use one or more sets of differential equations, and calculate both rate and state variables over time);

viii. descriptive model (defines the behaviour of a system in a simple manner with little or no reflection of the mechanisms that are the causes of phenomena but, consists of one or more mathematical equations);

ix. Explanatory model (consists of quantitative description of the mechanisms and processes that cause the behaviour of the system, then integrating the descriptions into the system).

Despite models simplifying and offering a comprehensive description of a process, the simplification may turn out to be a great setback since the simulation may not be a true representation of the complex systems encountered in the real world (Murthy, 2004). The quality of the predictions is lost when the model is calibrated in more diverse conditions in comparison to when they are calibrated in the same acquisition conditions (Guissard et al., 2005). A minimum dataset of good quality (weather,

management and soil inputs) is required to ensure accurate comparison with observed field data (Nix, 1983).

Various maize modeling approaches have been implemented over the years. Most of the studies aimed at analyzing the various factors influencing final maize yield. Some of these factors include soil temperature (Cooper & Law, 1977, 1978; Law & Cooper, 1976), and climate (Araya et al., 2015; Bassu et al., 2014; Cairns et al., 2012; Dixit et al., 2011; Cooper et al., 2013). Two of the most used crop models are the Decision Support System for Agrotechnology Transfer (DSSAT) model and the Agricultural Production Systems sIMulator (APSIM) model. The DSSAT was implemented to make recommendations on improving soil fertility for maize growth (Kihara et al., 2012). Dixit et al. (2011) using the MARKsim weather generator module of the DSSAT model to demonstrate the value of models in complementing field research. The APSIM model was used for example by Kisaka et al. (2016) to integrate nitrogen management in maize under semi-arid conditions in Kenya. The calibration parameters were provided by Jones (2013). Besides the crop models, statistical models have also been used, for example by Kipkorir et al. (2007) to identify and quantify the risk of crop development failure caused by dry sowing of maize.

3.3.3.4.2   LAI modeling technique employed in the field

A statistical modeling approach was proposed for this study. Extensive studies and research on different aspects of maize farming in Kenya has been carried out by Allan & Allan (1971), Cooper (1979), Cooper et al. (2008), Cooper & Law (1977), Cooper & Law (1978), Law & Cooper (1976), Cooper et al. (2013) with most of their findings and recommendations being applied in the growing of maize in Kenya to this day. This observation was also made by Dixit et al., (2011) who applied recommendations by Allan and Allan (1971) to carry out a study on climate risk assessment on maize yields in Kenya. Based on this approach, the study proposed the adoption of the findings by Cooper (1979), that established how the number of leaves on a maize plant is related to the number of days after emergence occurs, and how maize leaf area is related to LAI. The Kitale simulation was adopted for this study given that the weather (temperature~19°C, rainfall~780mm) and altitude (~1890m) conditions were comparable to those of the study area. Since maize measurements had to cover the whole growing season and recorded at regular intervals within the maize growth and development stages in order to monitor the crop growth and development, (Keating & Wafula, 1992), the modeling approach was adopted to extrapolate the field measured LAI data (11/06/2015 - 16/07/2015) for the months for which no field LAI measurements were carried out (March-June and July-October). The modeled LAI values

would then be related to the field LAI measurements collected from the field. The relationship between the leaf number (LN) and days after emergence (DAE) (**Figure 3.19**) was described by the **Equation 3.4**.

LN = - (0.00001783*DAE^3) + (0.001575*DAE^2) + (0.2209*DAE) + 3.206   ... **Equation 3.4**

Where:

Leaf No. (Y-axis) is the leaf number

DAE (X-axis) is the days after emergence
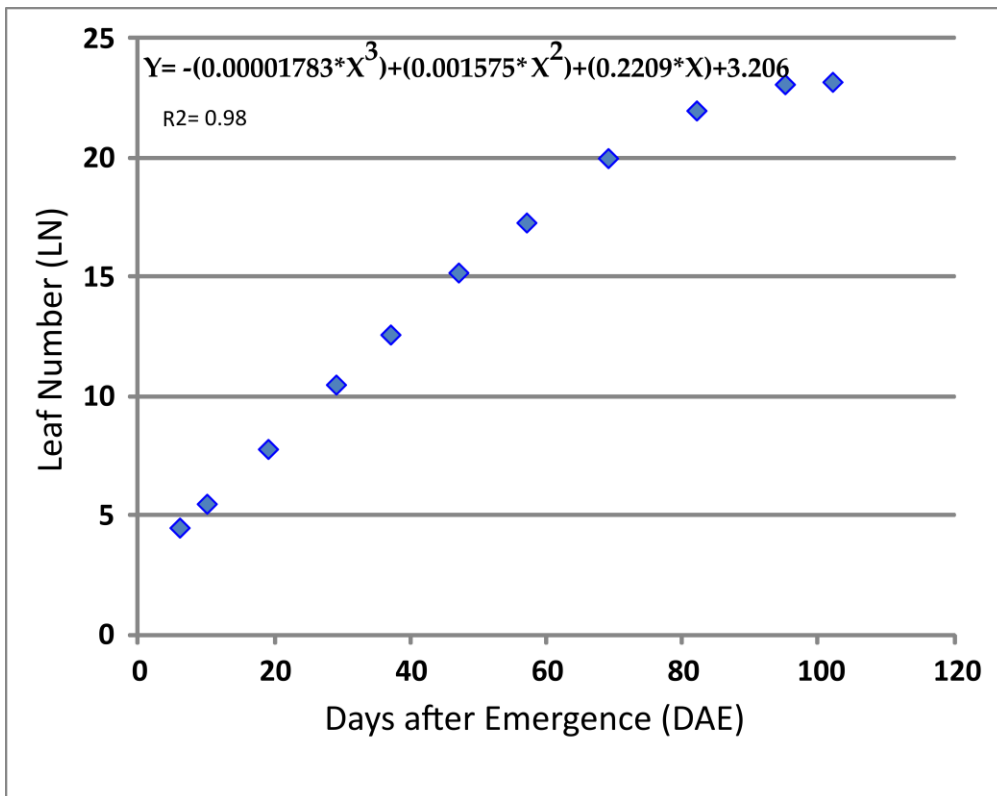
Figure 3.19: Leaf Number against days after emergence relationship from Cooper (1979).

Once the leaf number had been established, the LAI was determined using **Equation 3.5**.

LAI = - (0.0009*LN^3) + (0.0404*LN^2) - (0.2768*LN) + 0.4265   ... **Equation 3.5**

Where:

LAI (Y-axis) is the Leaf Area Index

LN (X-axis) is the Leaf Number

65
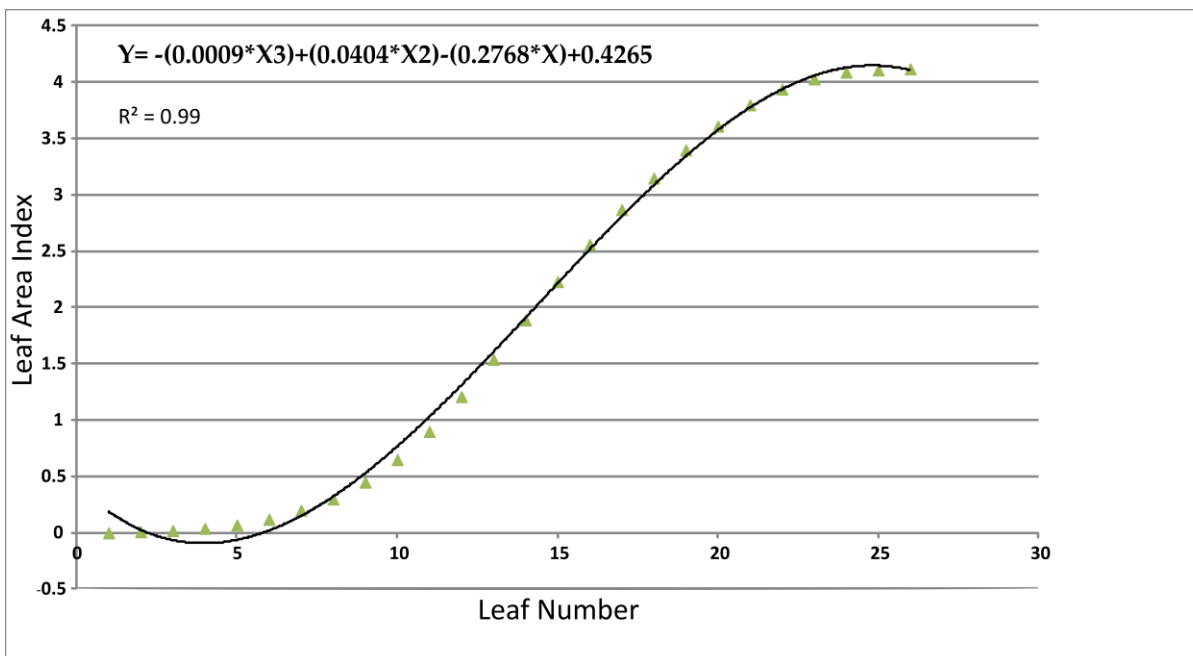
Figure 3.20: Leaf Area Index against Leaf Number relationship modeled after Cooper (1979).

The result of the modeled LAI is displayed in (**Figure 3.20**). The assumptions in the modeling were: the maize hybrids took 180 days to maturity; a plant population density (ppd) of 44000 plants ha^{-1}; weeding was undertaken five weeks post emergence; and N fertilizer used was 30 kg N ha^{-1} at sowing, plus 120 kg N ha^{-1} at five weeks post emergence. The simulation was performed until leaf number 26 (**Table 3.18**), past which no simulation research has been undertaken (Birch et al., 1998).

Table 3.18: Field simulated LAI values from the simulated leaf numbers (LN). The plant population density was assumed to be 44000 plants ha^{-1}.

Individual leaf number	Individual leaf area (cm²)	Summed up leaf area (cm²)	LAI
1	8.2	8.2	0
2	17.2	25.4	0.01
3	32	57.4	0.02
4	57.1	114.5	0.04
5	98.2	212.7	0.07
6	162	374.7	0.12
7	217	591.7	0.2
8	311	902.7	0.3
9	449	1351.7	0.45
10	609	1960.7	0.65
11	764	2724.7	0.9
12	936	3660.7	1.21
13	1015	4675.7	1.54
14	1055	5730.7	1.89
15	1031	6761.7	2.23
16	1004	7765.7	2.56
17	933	8698.7	2.87
18	843	9541.7	3.15
19	753	10294.7	3.4
20	656	10950.7	3.61
21	550	11500.7	3.8
22	430	11930.7	3.94
23	293	12223.7	4.03
24	163	12386.7	4.09
25	70	12456.7	4.11
26	16	12472.7	4.12

3.3.3.4.3   Results of the LAI Modeling in the Field

Once the simulated LAI had been determined using the model (**Figure 3.20**), the LAI measurements collected from the field were plotted against the simulated LAI values. This was done by picking out the LAI values from (**Table 3.17**) and (**Table 3.18**) that had identical leaf number values, and plotting these values (**Figure 3.21**).
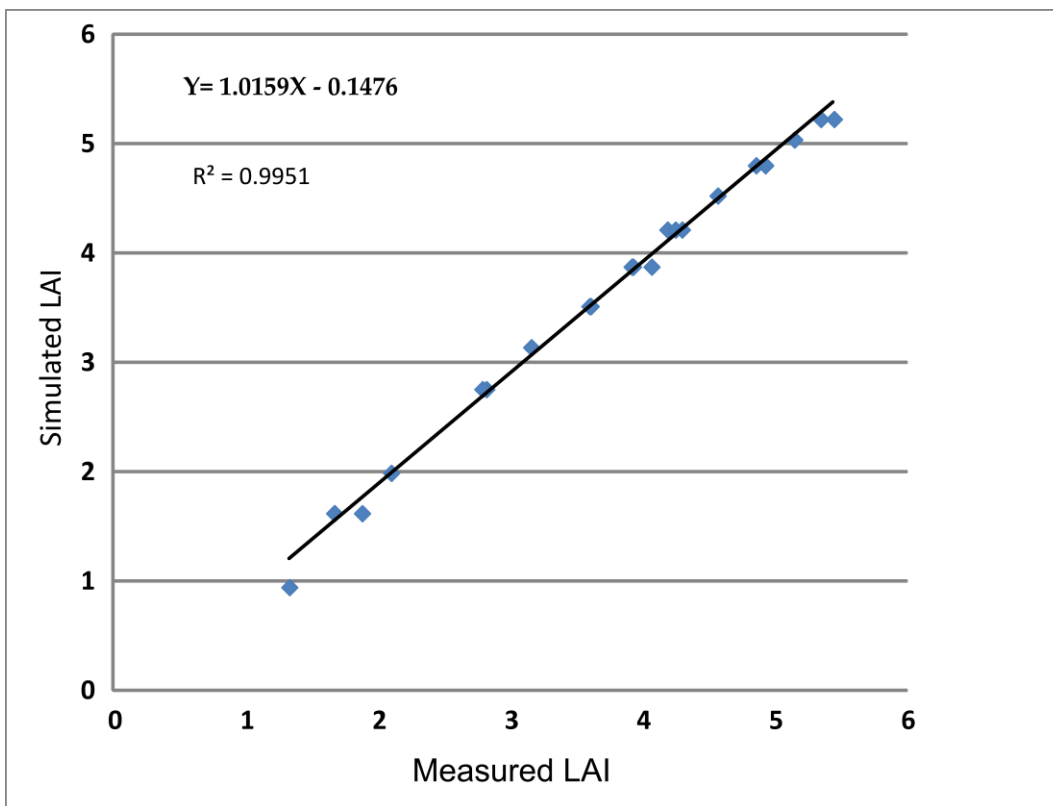
Figure 3.21: Simulated LAI against measured LAI.

The results indicated a high correlation between the simulated LAI values and the measured LAI values (**Table 3.19**). An R^2 value of 0.99 was achieved, with an RMSE value of 0.09. The results were corroborated by Birch et al. (1998) in his study on improved methods for predicting individual leaf area and leaf senescence in maize.

Table 3.19: Accuracy assessment results of the simulated LAI values against the measured LAI values. The coefficient of determination (R^2), the sample size (N), and the P-value are shown.

R^2	N	RMSE	P-Value
0.99	25	0.09	< 0.001

The results were further validated using LAI generated from S2 images for the following year 2016 (**Chapter 7.2.3**) to test on the robustness of the model and the transferability of the model from one year to another.

3.3.4 Soil Data

3.3.4.1   Soil Data Collection Procedure

The soil samples for the soil analysis were collected from the selected fields F1, F2, K5, S2, L6, L10, H6, and X4/1 (**Chapter 3.3.2, Figure 3.13**). These were taken within the same quadrats where the LAI information was collected (**Chapter 3.3.2, Figure 3.15**). Unlike the LAI measurements however, the soil samples were collected only once during the field visits. The samples were collected at two depths namely 0-20 cm and 20-40 cm, with the exception of X4/1 where the sample was collected at 0-20 cm depth. The soil samples were taken for the measurement of the bulk density, texture analysis, Carbon/Nitrogen (CN) analysis, and pH.

For the bulk density, a 10 cm core ring, with a volume of 50.91 cm^3 was driven into the soil using a hammer until its top side was flush to the soil surface. The core ring was then carefully pulled out ensuring that the soil sample is not disturbed. The sample was then placed in a soil bag for transportation back to the laboratory for drying and analysis processes. Two samples were collected for the bulk density analysis.

A soil auger was used to collect the samples for the texture, CN and pH analysis. The soil auger was driven into the ground to the 20 cm depth (**Figure 3.22 a**), then pulled out and the collected soil placed in a marked soil bag (**Figure 3.22 b**). This procedure was then performed for the 40 cm depth. This was repeated in all the selected quadrats. The soil samples were collected in different bags marked 0-20 cm, and 20-40 cm for each field. These soil samples were then mixed up into one 0-20 cm and one 20-40 cm sample for one entire maize field. The soil samples were then transported back to the laboratory for drying and analysis process.

Figure 3.22: Soil sampling using a soil auger: a) soil auger being driven into the ground; b) the soil sample from the ground is placed in a soil bag. Images accessed from http://www.tellus.ie/ on 1/2/2018.

3.3.4.2 Soil Analysis

The soil was analyzed for the carbon-nitrogen content, pH and texture.

The soil pH was measured both in distilled water and calcium chloride. The soil was air dried and later crushed gently in a mortar in order to achieve even distribution of soil particles (**Figure 3.23 a-c**). The soil was then passed through a 2 mm sieve in preparation for the pH analysis. For the pH measurement in distilled water, 25 ml of distilled water was added to 5 g of soil then measured after an hour. For the pH measurement in calcium chloride, 25 ml of calcium chloride was added to a mixture of 25 ml distilled water and 5 g soil (**Figure 3.23 e-f**). To ensure thorough mixing, a mechanical shaker was used and the measurements recorded after an hour (**Figure 3.23 d**).
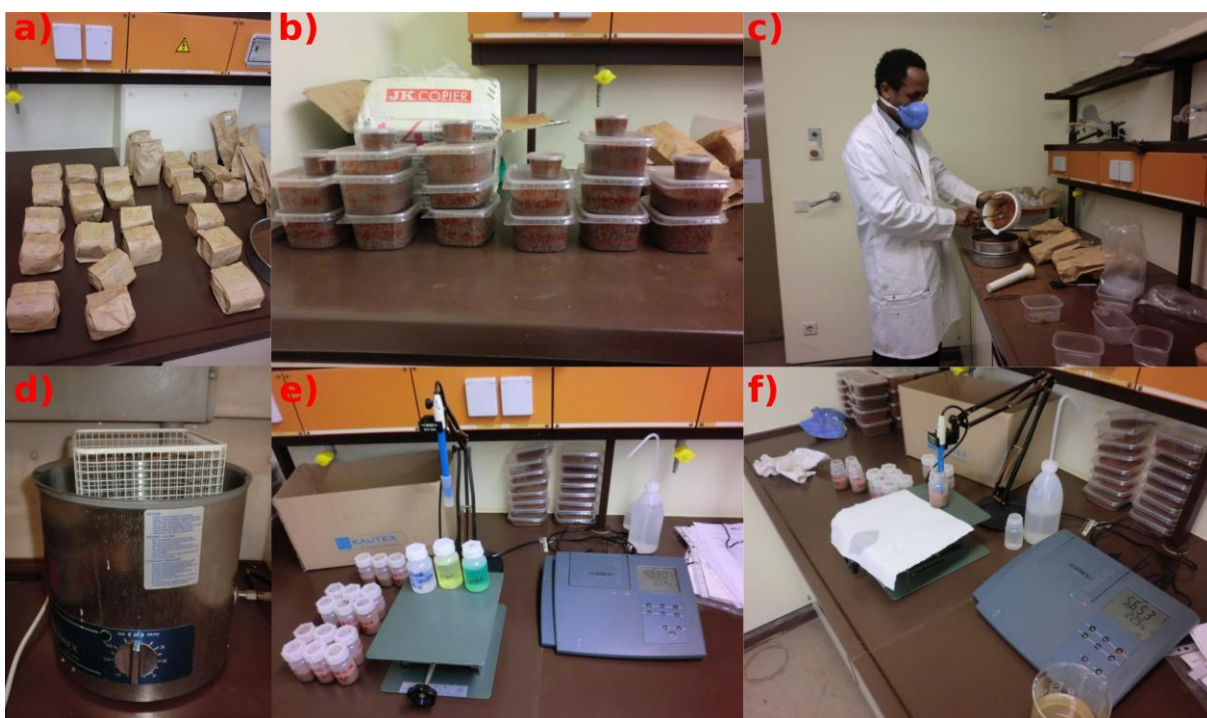
Figure 3.23: Soil pH analysis procedure. a) the soil samples in soil bags from the field; b) the air dried soil samples; c) crushing of the soil sample using a mortar, and then sieving it; d) mechanical shaker that ensured the soil samples were thoroughly mixed; e)-f) measuring of the soil pH content.

For the soil texture analysis, the laser diffractometry method was used (**Figure 3.24**). This was done using the "Streulichtspektrometer HORIBA LA-950" with the procedure described in Di Stefano et al. (2010). The soil samples were weighed before being placed in the centrifugal machine (**Figure 3.24 a**) to ensure that they had equal weights. The samples were then placed in a centrifugal machine (**Figure 3.24 b**) for thorough mixing before carrying out the texture analysis using the HORIBA LA-950 light-scattering spectrometer **(Figure 3.24 c and d)**.
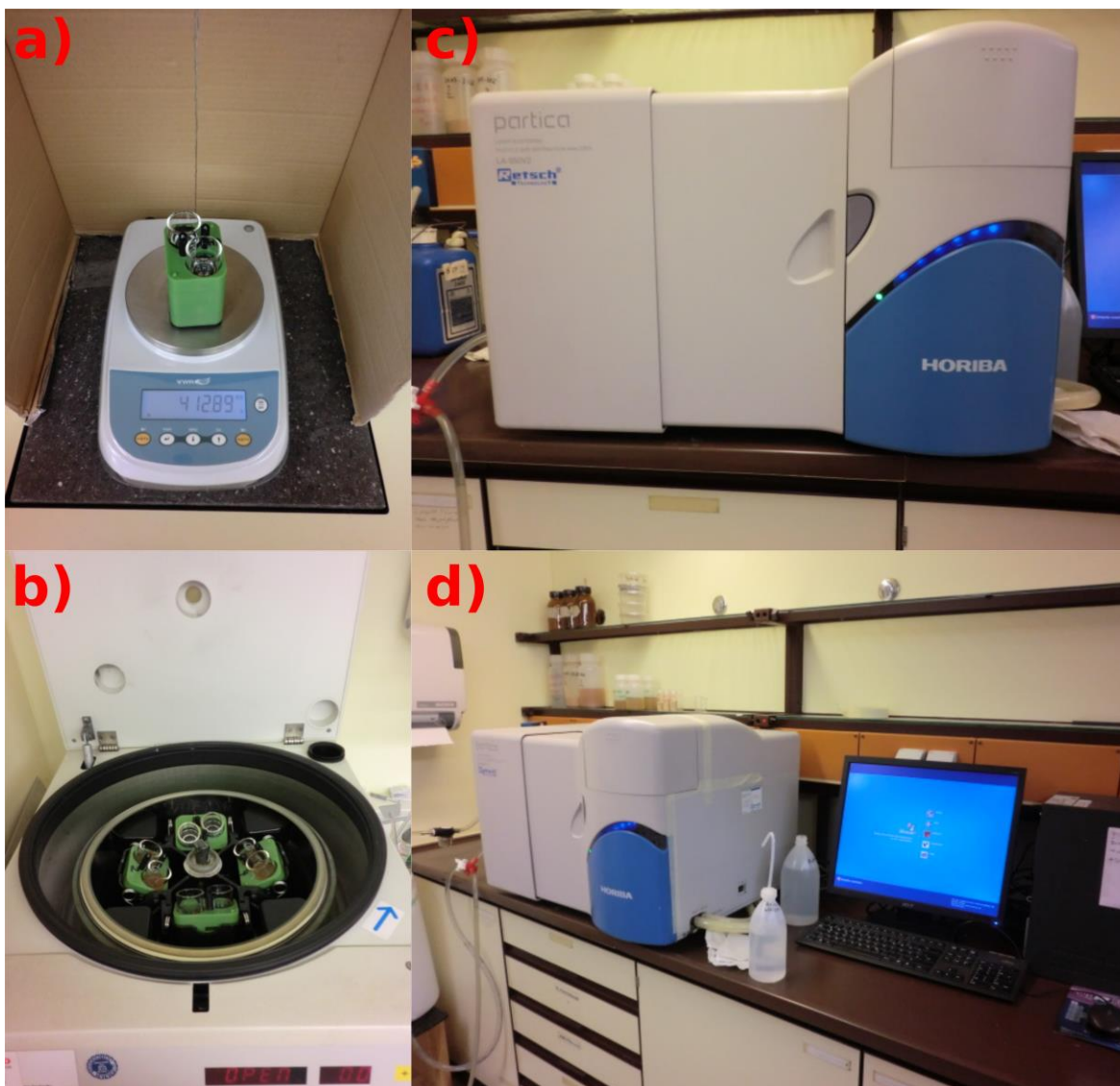
Figure 3.24: Soil texture analysis procedure using the laser diffractometry method. a) weighing of the soil samples to ensure they weighed the same, before placing them in the centrifugal machine; b) the soil samples placed in the centrifugal; c) a photo of the HORIBA LA-950 light-scattering spectrometer d) texture analysis using the HORIBA LA-950 light-scattering spectrometer.

Total carbon and total nitrogen (N tot) were determined for finely ground samples after dry combustion with an elemental analyzer (Fisons NA; ISO 10694: 1995; ISO 13878: 1998) (**Figure 3.25**). Very small grain particles of the soil were placed in two metal containers (**Figure 3.25 a**), before being placed in the Fisons elemental analyzer for the C/N analysis (**Figure 3.25 b**).
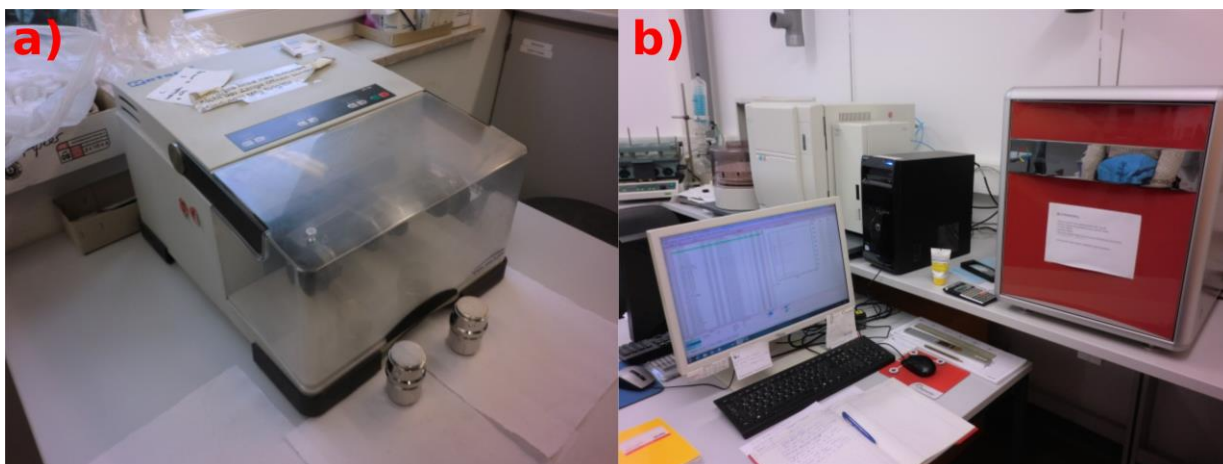
Figure 3.25: Soil Carbon/Nitrogen (CN) analysis procedure using an elementary analyzer. a) soil samples that were prepared and placed into the metal containers; b) CN analysis using the Fisons elemental analyzer.

3.3.4.3   Soil Analysis Results

The soil in the region has a clay content of up to 80%, a characteristic of nitisols (**Table 3.20**), as highlighted in **Chapter 2.3**. The pH was averagely 5.5 and 4.8 in water (H_2O) and calcium chloride ($CaCl_2$) respectively (**Table 3.21**), which is ideal for maize growing (**Chapter 3.31**). The soil bulk density was 1.16 gcm^{-3} on average (**Table 3.22**).

Table 3.20: Results of the soil texture analysis for the fields F1, F2, K5, S2, L6, L10, H6 and X4/1.

Depth (cm)	CLAY (%)	SILT (%)	SAND (%)
F1 0-20	67.32	24.84	7.85
F1 20-40	70.60	23.15	6.26
F2 0-20	67.83	26.03	6.15
F2 20-40	69.87	25.18	4.96
K5 0-20	72.22	22.51	5.27
K5 20-40	77.52	18.74	3.75
S2 0-20	74.38	19.86	5.77
S2 20-40	79.44	16.74	3.82
L6 0-20	76.01	17.72	6.28
L6 20-40	78.77	15.24	5.99
L10 0-20	78.14	18.80	3.06
L10 20-40	82.67	15.50	1.84
H6 0-20	66.65	25.19	8.16
H6 20-40	73.80	22.15	4.05
X4/1 0-20	75.26	20.78	3.97

Table 3.21: The average (AVG) carbon (C) nitrogen (N) ratio analysis and soil pH results for the fields F1, F2, K5, S2, L6, L10 & H6.

Field	Depth (cm)	N%	C%	C/N Ratio	AVG N%	AVG C%	AVG C/N Ratio	water	CaCl$_2$
								pH at 21.4°C	
F1	0-20	0.22	2.58	11.96	0.22	2.56	11.84	5.38	4.81
		0.22	2.55	11.72					
F1	20-40	0.15	1.72	11.73	0.15	1.72	11.58	5.58	4.76
		0.15	1.73	11.44					
F2	0-20	0.20	2.47	12.16	0.20	2.46	12.24	5.66	4.78
		0.20	2.44	12.32					
F2	20-40	0.18	2.17	12.31	0.18	2.16	12.36	5.69	4.79
		0.17	2.16	12.42					
K5	0-20	0.20	2.48	12.46	0.20	2.48	12.59	5.67	4.83
		0.19	2.47	12.71					
K5	20-40	0.14	1.59	11.69	0.14	1.58	11.44	5.78	4.88
		0.14	1.57	11.19					
S2	0-20	0.20	2.40	11.97	0.20	2.40	11.99	5.49	4.80
		0.20	2.39	12.00					
S2	20-40	0.14	1.63	11.46	0.15	1.64	11.36	5.71	4.82
		0.15	1.65	11.25					
L6	0-20	0.21	2.62	12.54	0.21	2.63	12.51	5.61	4.68
		0.21	2.65	12.49					
L6	20-40	0.17	2.05	12.06	0.17	2.05	12.03	5.26	4.73
		0.17	2.05	12.00					
L10	0-20	0.22	2.75	12.40	0.22	2.75	12.30	5.71	4.75
		0.23	2.75	12.19					
L10	20-40	0.17	2.10	12.37	0.17	2.08	12.11	5.31	4.79
		0.17	2.05	11.86					
H6	0-20	0.23	2.95	13.03	0.22	2.89	12.97	5.71	4.86
		0.22	2.83	12.91					
H6	20-40	0.17	2.05	12.46	0.16	2.03	12.39	5.59	4.82
		0.16	2.01	12.33					
X4/1	0-20	0.21	2.53	12.30	0.21	2.54	12.30	5.65	4.67
		0.21	2.54	12.30					

Table 3.22: Bulk density was done for two fields F1 (1.14 gcm^{-3}) and S2 (1.18 gcm^{-3}), at a depth of 0-10 cm. Volume of the core ring was 50.91cm^3.

Field Reference	Depth	Dry Soil + Bag Weight (g)	Bag Weight (g)	Dry Soil Weight (g)	Bulk Density (gcm^{-3})
Sample 1	0-10	70	12	58	1.14
Sample 2	0-10	72	12	60	1.18

3.3.5   Questionnaires

Crops tend to display varying seasonal characteristics that are dependent on the geographical region, local climate, sowing dates, weather conditions during the vegetation period, equipment and behavior of the farmer, cultivation cycle and harvesting times (Esch et al., 2014). Therefore, questionnaires administered aimed at collecting information pertaining to the maize crop management. The farmers and farm managers of the fields considered for this study maintained records for most of the activities that were being undertaken in the fields: from planting of the maize, to harvesting. However, the records for each field were kept separately since the fields were divided into blocks, each under a different sub manager. For example, the fields H1-H11 belonged to H block, while the fields L2-L10 belonged to the L block. Questionnaires were therefore structured in such a way that the information contained in the various documents could be consolidated into one.

The questionnaires were administered both in interview form (both face-to-face and via telephone) and self-administration form. Since the response to a questionnaire is influenced, by among other factors, the length and the readability of the questionnaire (Sapsford & Jupp, 2006), the one page questionnaire was structured in such a way that it captured as much necessary information as possible, without inconveniencing the farmers. The information collected included: Farm location and ownership details- the name of the farmer, his/her contact details, and the location of the farm; Reason for which the farmer grows the maize- either subsistence, commercial, fodder, or seed maize; Planting information- the maize variety grown, the acreage, the row and crop spacing, and the planting direction. Information on whether mixed cropping or mono cropping was practiced was collected; as wellas Management information- the dates for the application of fertilizers, the top dressing, and herbicides, and the amounts applied; Harvesting- manual or mechanized; Yield- expected yields and the actual yields, and in cases of a difference in the two, a reason for the same. This information was necessary in the discussion and analysis of the processed results in supporting the research findings.

A sample of the questionnaire is provided in the appendix.

4. Preprocessing of Remote Sensing Data

Image preprocessing can be described as the manipulation and transformation of the digital raw data received from a satellite or airborne imager into an interpretable form (Jones & Vaughan, 2010). Even though the received satellite images normally already have some of the basic geometric and radiometric errors corrected, further processing is required to correct errors and distortions that may have been introduced during acquisition (Lillesand et al., 2014). The distortions could be due to: 1) satellite motion; 2) earth's surface curvature; 3) non-linear scanning; 4) banding/striping caused by faulty detectors; 5) non-linear response of the detectors; 6) atmospheric effects; and 7) geometric distortions due to changes in the pixel size along the scan line and the rotation of the earth.

The preprocessing step involves a number of stages. **Chapters 4.1** to **4.3** describe the theory of the satellite images preprocessing process, while **Chapters 4.4** and **4.5** highlight the preprocessing steps and procedure undertaken on the images acquired for this research, for the radar and optical satellite images respectively.

4.1 Geometric Correction

The objective of geometric correction is to generate an image that is a true representation and depiction of the ground scene that can result in a one-to-one relationship between image and a map of the area (Lillesand et al., 2014). Satellite geometric errors are categorized as either being systematic or non-systematic and are as a result mainly of scale distortions caused by varying nadir angle, variations in the flying height (altitude), or platform instability (pitch, roll and yaw) (Bernstein, 1976). Systematic errors are predictable and their occurrence is present on all images. Correction parameters are therefore applicable to all the images to correct the errors, before the distribution of the data. On the other hand, non-systematic errors are unpredictable and usually apply only to a particular image. They need to be corrected on an individual basis, often by the user. The major sources of both systematic and non-systematic geometric errors are shown in (**Figure 4.1**).
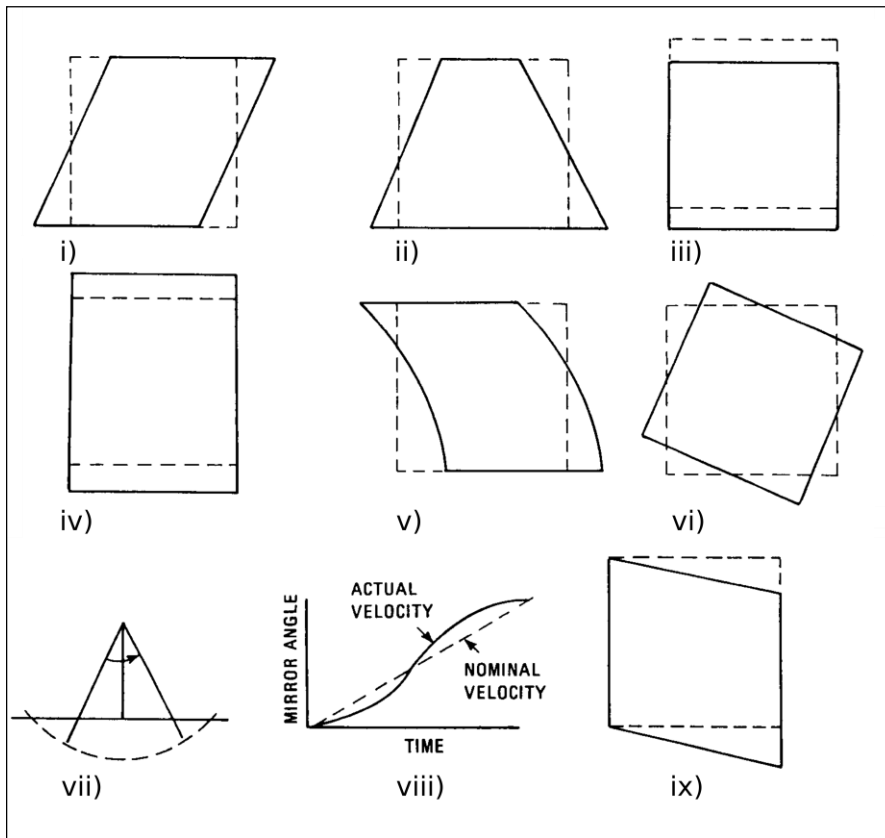
Figure 4.1: Geometric error sources affecting satellite images. The non-systematic geometric error sources include: i) earth rotation; ii) altitude variation; iii) pitch variation; iv) spacecraft velocity; v) roll variation; vi) yaw variation. The systematic error sources include: vii) cross-track scanner error; viii) mirror velocity variations; ix) scan skew. The broken lines indicate the distorted image whereas the solid lines indicate the shape of the corrected image. The figure has been modified after Bernstein (1976).

The major sources of systematic geometric errors include: a) the west-east rotation of the earth, which as the satellite orbits the earth, tends to skew the scanned images and give them a rhombus shape. b) Platform motion during the acquisition of successive pixels with scanning sensors causes a scan skew effect evidenced by a slight upward curve. c) non-linear scanning due to varying velocity of the scanning mirror during the sweep across the field of view. d) panoramic distortion due to increasing angle of view of the scanner from nadir outwards caused by the curvature of the earth's surface. e) aspect ratio as a result of resampling of the rectangular image pixels into square pixels.

The non-systematic errors resulting from the random variations in both the platform's altitude and attitude (yaw, roll and pitch) include: a) platform instability that causes image distortion since airborne imagery are sensitive to changes in attitude. b) the undulating terrain effects have an influence on the scale of the image since the area viewed in a single pixel depends on the angle of the surface relative to the view angle.

Whereas the first order of the systematic errors correction is usually undertaken by the producers before data distribution any extra systematic errors and non-systematic errors must be corrected on each individual image by the user (Bernstein, 1976). The correction takes place in two stages:

a. Reprojection

This is the registration of the image to the map by matching the image coordinates of the easily identifiable features e.g. road junctions for the corresponding map coordinates of the same features. The image is warped to the map coordinates, an operation that can be defined by **Equations 4.1** and **4.2**. The reprojection represents a first-order, six parameter, affine (linear) transformation. The six-parameters are: translation in x and y, scale changes in x and y, skew, and rotation (Bernstein, 1976).

$$x = a_0 + a_1 x' + a_2 y'$$ **…Equation 4.1**

$$y = b_0 + b_1 x' + b_2 y'$$ **…Equation 4.2**

Where:

x and y are the coordinates of the reprojected image.

x′ and y′ are the coordinates of the original image.

a_0, b_0, a_1, b_1, a_2, and b_2 represent the six distortions, namely: translation in x and y, scale changes in x and y, skew, and rotation.

In order to reproject the satellite images, identification and selection of ground control points (GCPs) of features easily identifiable on the image is done (Lillesand et al., 2014). The GCPs need to be sufficiently large in number and evenly distributed across the image, for the image to be accurately tied down. By applying any empirical method, the geometric transform is performed by comparing the differences between positions of common points that can be identified on both the image and on a map of suitable scale. The root-mean-square (RMSE) value of the differences between the calculated and actual positions of the GCPs is used as an accuracy check (**Table 4.1**) (Lillesand et al., 2014). RMSE values achieved for the L-8, S-2 and RE images were 5.25, 4.70, and 1.06 respectively. Though increasing the number of control points improves the accuracy of the adjusted satellite images, six control points are normally sufficient enough to adjust the satellite images using first order polynomial model (Yousif & Abdalla, 2011). An alternative to reprojection using GCPs is the relative georegistration technique whereby images are registered to one another.

Table 4.1: An example of some of the selected ground control points (GCPs) selected for reprojection. The x_image and y_image represent the points on the satellite images, x_map and y_map represent the corresponding GCPs selected from high resolution google maps, and the rmse is the root mean square error values achieved.

x_image	y_image	x_map	y_map	rmse
712836.7	116776.1	712840	116786	0.99
705647.2	114826.2	705650	114834	0.76
704201.5	118401.2	704204	118406	1.23
709505.6	111569.3	709508	111579	0.85
714639.8	110970.8	714642	110980	1.35
704200.2	118392.1	704223.3	118400.1	5.88
705623.5	114815.3	705650	114834	7.16
709481	111535.5	709522.1	111582	7.82
714635.7	110962.9	714629.3	110981.9	8.00
712833.3	116768.7	712840	116786	10.21

b. Resampling

Resampling calculates new pixel values from the original image pixel values associated with the points, thus forming a new image (Jones & Vaughan, 2010). The most commonly used resampling methods are nearest neighbor; bilinear interpolation; cubic convolution; bicubic spline interpolation.

The nearest neighbor method is an easy and fast resampling method that preserves the original values without averaging their values thus no data values are lost (Tanase et al., 2010). This makes it suitable for classification and discrimination of various vegetation types, and edge detection algorithms (Corbane et al., 2009). However, some data values may be dropped or duplicated thus giving linear features a stair stepped especially when resampling from a larger to a smaller grid size.

The bilinear interpolation method involves substituting the pixel values with those calculated from the four neighboring pixels based on the distance weightings of their centres from the centre of the new one using a linear function (Inglehart, 1997). Apart from generating a smoother output image compared to the nearest neighbor method, the method is also more spatially accurate making it preferred when changing image cell sizes. However, this method results in low-frequency convolution of the pixels since their values is averaged, leading to smoothing of the edges and loss of data values (Inglehart, 1997).

The cubic convolution method implements a cubic function to weigh the set of 16 input pixels in a 4 x 4 array, that are averaged to determine the pixel values (Reinartz et al., 2011). The mean and standard deviation of the output pixels match the mean and standard deviation of the input pixels more closely than any other resampling method in most cases. The effect is both the sharpening of the image and

smooth out noise, though the actual effects depend upon the data being used (Reinartz et al., 2011; Taubenböck et al., 2012). This method is recommended method when dramatically changing the cell size of the data even though it alters the data values, in addition to being an extremely slow method.

The bicubic spline Interpolation method is similar to the bilinear interpolation technique with the exception of the surface smoothness maximization technique (Shikin & Plis, 1995). It is based on fitting a cubic spline surface through the current block of points hence giving a more exact fit to the curve without the oscillations that other interpolation methods create. The result is the smoothest output images that are more spatially accurate than nearest neighbor. This method is often used when upsampling, though it is the most computationally intensive resampling method, and therefore the slowest.

4.2   Radiometric Correction

Radiometric correction reconstructs the physically calibrated brightness values of the image by correcting the spectral distortions caused by sensors, sun angle, topography and the atmosphere (Richards, 2013). The radiometry of an image is determined by analyzing the following image aspects:

   a.   Histograms

A histogram is a graph showing the frequency of occurrence of every digital value in the image (Jones & Vaughan, 2010). The distribution of the values within an image band will be characteristic of the ground cover in the image. The value is dependent on the illumination of the scene and on the reflectance of the surface. Analysis of the peaks of the histogram gives a good depiction of the ground features.

   b.   Noise

Noise from the image can be due to either electronic interference, scanning errors, data transmission/recording (random noise) or the malfunction of the detectors, which can occur as striping or banding whereby distinctive horizontal banding pattern or periodic variation in the brightness of lines of data appear (systematic noise) (Jones & Vaughan, 2010). The reduction of the random noise is usually done by smoothing the image using filters. The filters substitute the average value of the surrounding pixels for that of the rogue pixel value, while maintaining the legitimate variations in the pixel values (Richards, 2013). As for the systematic noise, analyzing of the histograms from each detector using destriping algorithms and suitably adjusting the response of the rogue detector(s) so that its input is similar to the others, reduces the effect. This improves the visualization of the image but does not replace the lost data.

c. Sun angle and viewing geometry

The magnitude of the received signal at the sensor depends upon both the angular properties of the illumination, and on the reflectance of the target, which itself varies with view angle (Jones & Vaughan, 2010). The amount of incoming irradiance is influenced by factors like: atmospheric effects, variations related to solar angle variation with time of day and time of year, variation of earth-sun distance during the year, and variation between the incidence beam and the surface. With the exception of sun-synchronous satellites, these factors have the consequence that two images of the same area taken on different dates or times look different even without a change having occurred in the spectral characteristics of the scene. On the other hand, the reflected radiation depends on the topography of the surface in relation to the solar beam. Variations in the angle between the surface and the solar beam cause topographical shading effects, and smaller-scale shading. This can result in large differences in vegetation reflected radiance, even where the true reflectance of the vegetation is constant over the scene (Jones & Vaughan, 2010). Measured radiances are usually converted to "at satellite" or "at surface" reflectances using satellite algorithms in order to estimate the true surface reflectance.

d. Atmospheric correction

A proportion of radiation received at the detector arises from the scattering of incident radiation by the atmosphere without having interacted with the surface and so needs to be removed. The calculation of the reflectance at the surface requires information on the incident radiation at the surface as well, which itself depends on the atmospheric attenuation of the incoming radiation (Jones & Vaughan, 2010). Atmospheric correction therefore eliminates the atmospheric effect on the incident solar irradiance and ensures that the radiance received at the satellite is from the ground surface (Richter & Schläpfer, 2005a). Inadequate atmospheric correction underlies the general lack of transferability of image analysis and interpretation, from one image to another, especially when using multispectral and multitemporal data (Jones & Vaughan, 2010).

The different approaches to atmospheric correction can be grouped as (Jones & Vaughan, 2010): a) Direct methods where the atmospheric parameters are obtained and used to correct the atmospheric effects to individual spectral bands. The parameters include: calibration with in situ measurements of geophysical parameters or with simultaneous meteorological data from the satellite or from ground stations; the evaluation (compensation or elimination) of the atmospheric effects on a pixel-by-pixel basis using image-derived information. b) Indirect methods whereby the atmospheric effects are overcome by avoiding or minimizing the effects instead of quantifying them as a problem. Direct methods are most effective and the most commonly used. They generally make use of radiative

transfer models for the assessment of the atmospheric contribution to the at-satellite measured signal by modeling the radiation pathway from source to sensor. Examples are the ATCOR, 6S or MODTRAN. They usually provide very accurate estimates of the atmospheric effects and of surface-atmosphere interactions as long as the correct input parameters are used. In order to calibrate the model, in situ measurements on ground targets that do not change significantly with time e.g. asphalt or concrete must be made in representative areas throughout the image, to cater for the varying atmospheric conditions over the image. The parameters used in the model atmospheres must be relevant to that geographical location as well. Differences in their reflectances can be assumed to be as a result of atmospheric interference and so a relative correction can be applied by subtracting the difference in reflectance on the rest of the images or by linearly empirically regressing the reflectance differences.

An alternative approach is the use of image-derived information to eliminate the effects of the atmosphere, referred to as the dark object subtraction (DOS) method. An assumption that within an image there are some pixels in complete shadow is made, so that any radiance measured for these pixels must be attributed to the atmosphere. This method has the advantage that it does not require information relating to the state of the atmosphere at the time of data collection. It however, has the disadvantage of performing subjective selection of dark values, which ignores effects of atmospheric absorption (Jones & Vaughan, 2010).

4.3   Spatial Filtering Techniques

A filter refers to a regular matrix of numbers, also referred to as a kernel, which operates successively on all the pixels in an image to produce new pixel values, hence modifying the image (Jones & Vaughan, 2010). The filters are used either to smooth an image or to identify and enhance features such as boundaries and edges. The kernel is centered on one pixel in the original image and all pixels within the box are multiplied by the corresponding value in the kernel and added together. This sum is then divided by the sum of the elements in the kernel, and the nearest integral value is used to replace the central pixel. The kernel passes along each row of pixels in the image, operating on them in turn, producing a new image.

The filters can be categorized into (Jones & Vaughan, 2010):

   a.   Low-Pass/ Smoothing filter

This suppresses the high-frequency variations between neighboring pixels while retaining the slowly varying, low-frequency background component. The net effect is the reduction of the range of values

in the image. This in turn blurs the image, removing the finer details. The blurring effect increases with an increase in the size of the filter as the average values become nearer to each other.

b.   Adaptive filter

An example of this is the gamma filter (**Figure 4.2**) which is used to suppress speckle in SAR images without too much reduction in the spatial resolution, while preserving the object edges (Dimov et al., 2016). The weight of the filter changes as the filter passes across the image depending on the variance in the grey level at that point.

c.   High-pass/ edge-detection/ edge-enhancement filters

They are used to enhance the high frequency variations by increasing the magnitude of the differences in values between the neighboring pixels, thus making steps in values more noticeable. Edges could be linear objects e.g. roads, field boundaries, hedges, rivers. Examples include laplacian filters, prewitt filters.

d.   Mean difference filter

It is formed by subtracting the weightings of a mean (smoothing) filter from the unit filter (all elements zero apart from the central one, which is unity), producing an image that is similar to the original except that edges and boundaries are more distinct. In addition to distinctly detecting the edges, it enhances them as well.
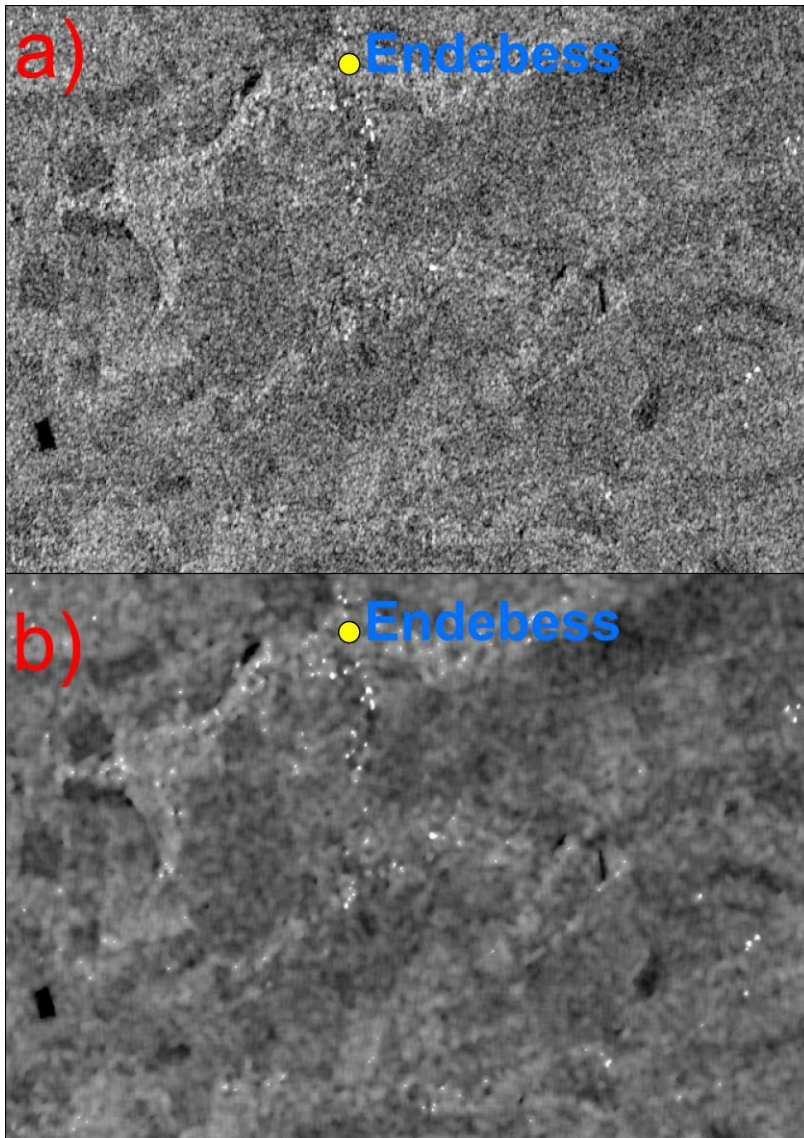
Figure 4.2: Effect of applying the gamma filter on a Sentinel-1 image scene acquired on 8/5/2015. a) before applying a filter, b) after filtering.

4.4 Preprocessing Workflow of Radar Satellite Images

Both the Sentinel-1 (S-1) and TerraSAR-X (TSX) images were subjected to similar preprocessing steps. This was to ensure that the original sensors' resolution was preserved and able to comparatively compare the acquired S-1 and TSX images (Mittermayer et al., 2010). The steps were: split; de-burst; multi-look; calibrate; speckle filtering; terrain correction; pixel resampling; linear to dB conversion for the S-1 images, and multi-look; calibrate; speckle filtering; terrain correction; pixel resampling; linear to dB conversion for the TSX images (**Figure 4.3**).
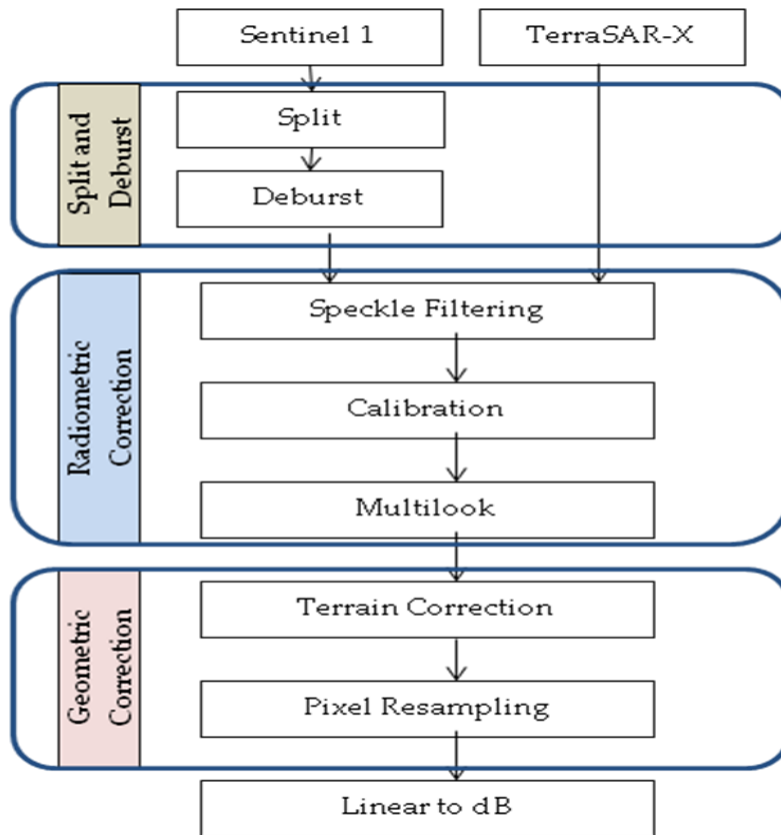
Figure 4.3: The preprocessing steps carried out on the Sentinel-1 (S-1) and the TerraSAR-X (TSX) radar images. Similar preprocessing steps were carried out on both sets of images to ensure preservation of the original sensors' resolution and to comparatively compare the images. The exceptions were the "split" and" deburst" steps, which were peculiar to S-1 images only.

The "split" and "de-burst" processing steps are peculiar to S-1 data since the S-1 IWs SLC products come as individual burst images comprising of three single sub-swath dataset, namely IW1, IW2 and IW3, for each polarization acquired (**section 3.1.1.1**) (Torres et al., 2012). Each sub-swath image consists of a series of bursts, with each burst having been processed as a separate SLC image (**Figure 4.4**). The individually focused complex burst images are included, in azimuth-time order, into a single sub-swath image, with black-fill demarcation in between. Due to the one natural azimuth look inherent in the data, the imaged ground area of adjacent bursts will only marginally overlap in azimuth—just enough to provide contiguous coverage of the ground. The images for all bursts in all sub-swaths of an IW SLC product are re-sampled to a common pixel spacing grid in range and azimuth. Burst synchronization is ensured for IW products. The processing is phase preserving (Torres et al., 2012).

The split process ensures the processing of each sub-swath individually. Since every burst within any single sub-swath is processed as a single image, the de-bursting step resolves the various bursts within any single sub-swath into one image (Torres et al., 2012).
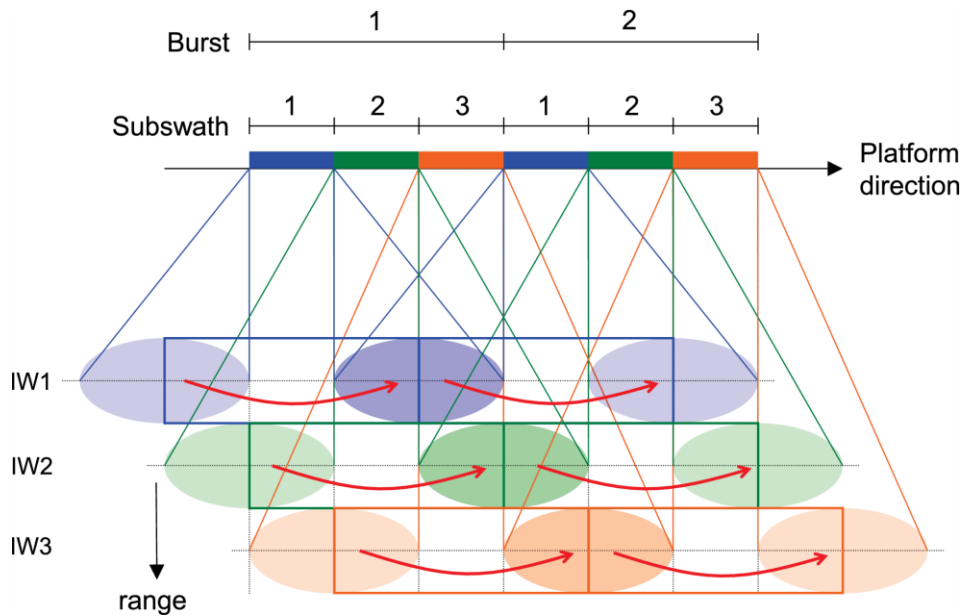
Figure 4.4: The TOPS Scan pattern for S-1 IW mode. The acquisition starts with the first burst of the first subswath (blue). Once this burst has been acquired, the antenna is switched in elevation, and the first burst of the second subswath (green) is acquired. Once the first of the third subswath (orange) is acquired, the beam is switched back to the first subswath, and the process is cyclically repeated. The figure has been adopted from (Yagüe-Martínez et al., 2016).

Radiometric resolution in radar is a measure of the uncertainty of the radar backscattering coefficient using the image intensity arising from speckle and noise for an otherwise perfect system (López-Dekker et al., 2013). It is expressed as the standard deviation of the measurement uncertainty normalized with respect to the mean, and is dependent on the signal to noise ratio (SNR), and the number of looks (N_L) during the multi-look process (Fritz & Werninghaus, 2007). This dependency is represented by **Equation 4.3**.

$$\gamma = 10.\log\left(1 + \frac{1 + SNR^{-1}}{\sqrt{N_L}}\right)$$

...**Equation 4.3**

Where:

Y = the radiometric resolution

SNR = the signal to noise ratio

N_L = the number of looks

Radiometric calibration was therefore carried out on the intensities of the images in order to minimize

the incompatibility in images taken under different observation conditions like the incidence angles or the ascending/descending mode, by the different radar sensors (van Zyl et al., 1993).

Speckle effect in general is a spatially random multiplicative noise due to coherent superposition of multiple backscatter sources within a SAR resolution element and which is caused by interference of backscattering objects below the geometric resolution within one resolution cell of the sensor, leading to grainy images even in homogenous objects (Lemp & Koch, 2009). The most appropriate filter for any study is therefore chosen by trial-and-error (Jones & Vaughan, 2010; Nezry, 2014). Optimal results could however be achieved by selecting the appropriate filter depending on the land morphology and scene texture. The scene texture is to be considered also in relationship with the data spatial resolution (Lemp & Koch, 2009). The removal of speckle noise should precede other pre-processing steps to avoid the noise being incorporated into and degrading the image (Inglehart, 1997). Images despeckling before classification improves accuracy of multi temporal classification as well (Sabour et al., 2008).

Multi-look intensity images are generated by averaging the neighbourhood pixels over range and/or azimuth resolution cells, with the aim of reducing speckle and compressing the data (Canty, 2014). The goal is to achieve approximately squared pixels considering the ground range resolution and the pixel spacing in azimuth. This improvement in radiometric resolution using multi-looks is however associated with degradation in spatial resolution. The number of looks is a function of pixel spacing in azimuth, pixel spacing in slant range, and incidence angle (López-Dekker et al., 2013). In order to avoid over- or undersampling effects, a multi-looked image corresponding to approximately the same spatial resolution of the input image is generated (Canty, 2014). For the data calibration, the calibration factor was obtained from an xml file that was delivered with the image metadata file. Absolute calibration allows taking into account all the contributions in the radiometric values that are not due to the target characteristics. This permits to minimize the differences in the image radiometry and to make any SAR images obtained from different incidence angles, ascending-descending geometries and/or opposite look directions easily comparable and even compatible to acquisitions made by other radar sensors (López-Dekker et al., 2013). This was done by the computation of Beta Naught β^0 (radar brightness) representing the radar reflectivity per unit area in slant range and Sigma Naught σ^0, which is the radar reflectivity per unit area in ground range (Breit et al., 2010).

β^0 was obtained by multiplying the calibration factor with the power of the digital numbers by applying **Equation 4.4**. This was then converted into decibel (dB) values using **Equation 4.5**.

$$\beta^0 = k_s * |DN|^2$$

...Equation 4.4

$$\beta_{dB}^0 = 10 * \log_{10}\left(\beta^0\right)$$

...Equation 4.5

Where:

β^0 = Beta Naught.

β_{db}^0 = Beta Naught in decibels

DN = Digital numbers or image pixel values

k_s = Calibration factor

For σ^0, the local incidence angle was necessary since the backscattering from a target is influenced by relative orientation of the cell and the sensor, as well as by the distance range between them (Breit et al., 2010).

The terrain correction is done to correct image geometry by correcting the geometric and relief distortions (Liu et al., 2004). These distortions are foreshortening, layover and shadowing (**Figure 4.5**). Foreshortening is a condition that occurs on slopes. Slopes, facing towards the sensor cause a displacement of the elevated parts of the terrain towards the sensor. Layover refers to the condition where the signal from the top of a mountain reaches the sensor before that at the base. It is an extreme form of foreshortening. It is indicated by the letter L (b-a) in (**Figure 4.5**). On the other hand, shadow occurs when areas aspecting away from the sensor or lying behind the top of a mountain are not illuminated. Thus, no backscatter is received from shadow regions. This is indicated by the letter S in (**Figure 4.5**). The 12 meter Tandem-X digital elevation model (**section 3.1.3**) is used to perform the terrain correction. Both the S-1 and TSX images were then resampled to 10 meters pixel size by applying the nearest neighbour interpolation method. (**Equation 4.5**) was then applied to convert the pixel values to decibels (dB).
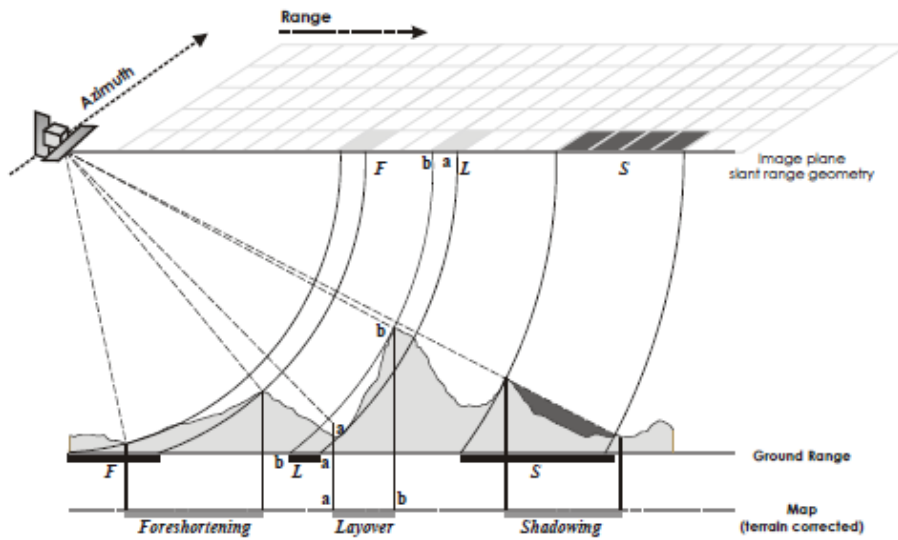
Figure 4.5: Geometric and Relief distortions (Kropatsch & Strobl, 1990).

4.5   Preprocessing Workflow of Optical Satellite Images

The preprocessing steps applied on the optical data are summarized in (**Figure 4.6**).
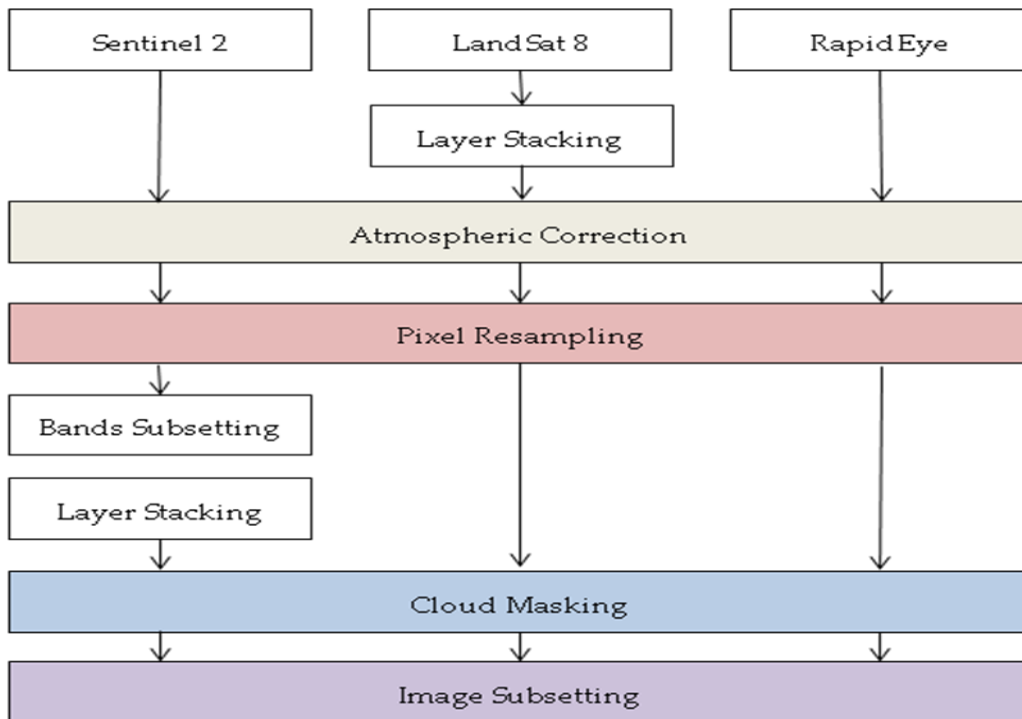
Figure 4.6: Optical data preprocessing workflow.

The Sentinel-2 (S-2) and Landsat-8 (L-8) images were freely accessed from the Copernicus open access hub (https://scihub.copernicus.eu/dhus/#/home), and from the United States Geological survey (USGS) website (https://earthexplorer.usgs.gov/) respectively. On the other hand, RapidEye (RE) being a commercial satellite, the images could only be accessed after being granted the prerequisite rights.

Apart from RE images that were acquired with the individual band layers already stacked, the S-2 and L-8 image bands were acquired as single image layers. The layer stacking procedure therefore had to be performed for the S-2 and L-8 images.

The next step was the atmospheric correction. Haze removal, de-shadowing and atmospheric-topographic corrections, which reduce atmospheric effects and variation in solar illumination before comparing the ground reflectance data retrieved from satellite images to ground-based measurements, were required (Alados et al., 2011). Atmospheric correction converts the image digital numbers (DN) to surface reflectance (Young et al., 2017). It was performed using the ATCOR processor for L-8 and RE images, and the Sen2Cor processor for the S-2 images. The atmospheric corrections were based on the application of catalogues of atmospheric correction functions, stored in look-up-tables, pre-calculated using the MODRAN and the libRadtran radiative transfer routines for ATCOR and Sen2Cor respectively (Richter, 1996; Vuolo et al., 2016). The catalogue consists of a broad range of atmospheric conditions (different altitude profiles of pressure, air temperature, and humidity; several aerosol types; ground elevations from 0-1 km above sea level; solar zenith angles ranging from 0° to 70°). The catalogue also covers visibilities (surface meteorological range) from 5-40 km, values which can be extrapolated down to 4 km and up to 80km (Richter, 1996). The algorithms consist of an interactive and an automatic part. In the interactive phase, the user interactively defines reference pixels, haze and cloud pixels, and selects one of the available atmospheres in the catalogue i.e. the altitude profile of pressure, temperature and humidity as well as the aerosol type (e.g. rural) are fixed (Richter, 1996; Richter & Schläpfer, 2005b). In the automatic phase, the algorithm automatically calculates the image visibility for the selected atmosphere by matching the measured signal to the model-derived signal in the spectral channel of known target reflectance. Next, it performs a haze removal by histogram matching the statistics of the haze regions to the statistics of the clear part of the scene for each sector and each channel. Finally, it calculates the ground reflectance image including the adjacency correction, and the computation of the ground brightness temperature image (Richter, 1996). Haze removal was performed before the atmospheric correction. However, the haze correction aborted for the images whose correlation coefficient for visible bands (RGB) was below the critical value of Pflug & Main-Knorn (2014). The Bidirectional Reflectance Distribution Function (BRDF) describes the interaction of the sun, the ground surface and the satellite sensor that affects the brightness or darkness of image

objects (Lillesand et al., 2014). The BRDF correction therefore takes into account the ruggedness of the terrain and is carried out after atmospheric correction (Richter & Schläpfer, 2005a). In low latitude areas of minimal rugged terrain, the BRDF effect on optical images are corrected by atmospheric correction (Motohka et al., 2009). The BRDF correction in small and flat areas can as well be ignored since the accuracy results are not affected by the bidirectional effects (Vaudour et al., 2008). Given that the study area was not extensive, and was located on a relatively flat terrain at a latitude of 1° N, the BRDF correction was omitted in the preprocessing.

After atmospheric correction, pixel resampling step was performed. The image pixel sizes were resampled to 10-meter size in order to have a uniform pixel size for all the images, both optical and radar, during the analysis. The nearest neighbour interpolation method was applied as proposed by Xiong et al. (2017).

The clouds appearing in the images were then masked by applying a cloud mask. Since the presence of clouds in the images did not affect the atmospheric correction process (Pflug & Main-Knorn, 2014), the cloud masking was performed after the atmospheric correction.

The images were then subset to the region of interest by clipping them to the study area boundary. This not only reduced the image sizes, but also the analysis process.

An example displaying a RE image scene, before atmospheric correction, after atmospheric correction, and after cloud masking is shown in (**Figure 4.7**).
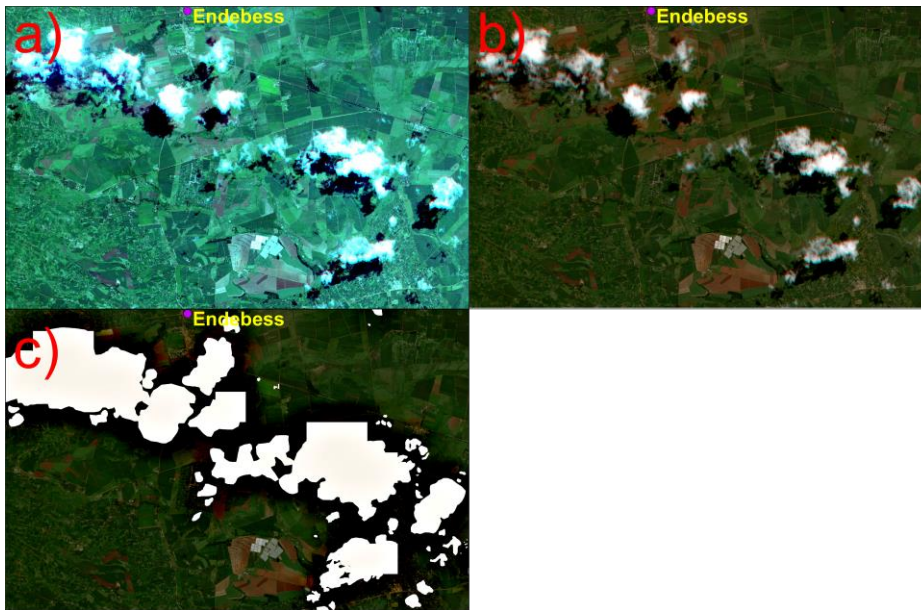
Figure 4.7: The preprocessing steps carried out on a RapidEye image scene acquired on 4/7/2015. a) the original image, b) atmospherically corrected image, c) atmospherically corrected image with the clouds extracted.

5. Analysis of Remote Sensing Data

The image analysis carried out involved two main approaches. a) Extraction of the backscatter (BS) values and calculation of the vegetation indices (VIs) per field, and correlating these BS values and VIs with the corresponding ground leaf area index (LAI) (**Figure 5.1**); b) performing an object based classification on the radar and optical images in order to accurately identify the maize fields (**Figure 5.2**).
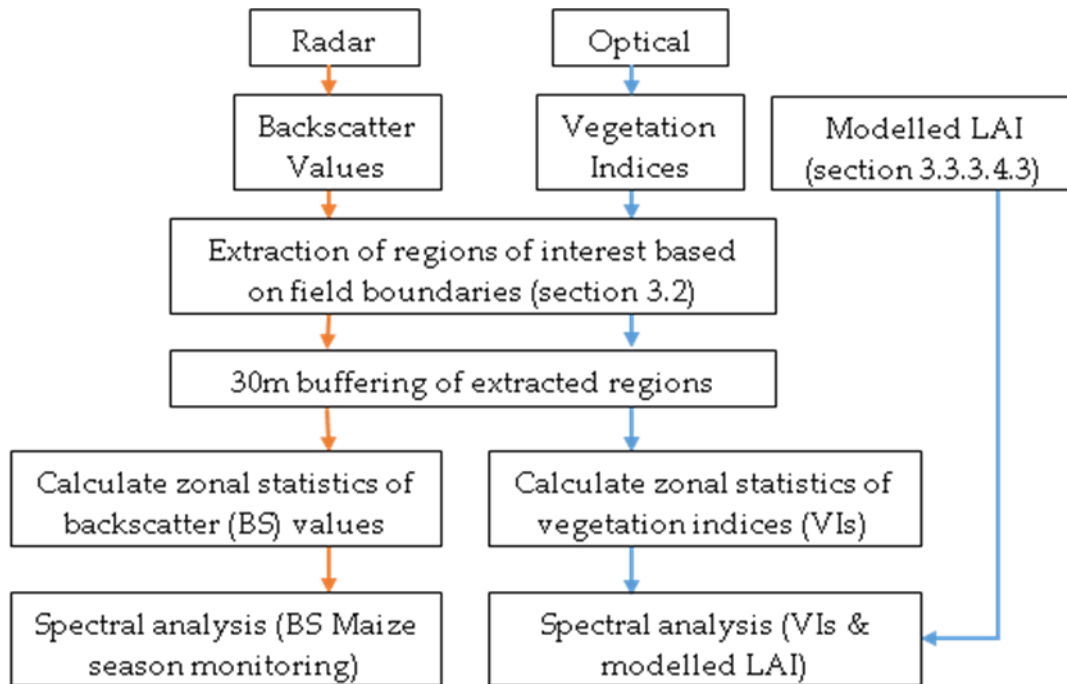
Figure 5.1: A scheme diagram showing the analysis of the satellite images to correlate the leaf area index to the vegetation indices and monitor the maize growth during the season using backscatter values.

From (**Figure 5.1**), the BS values were extracted from the radar images and the VIs calculated from the optical images. With the aid of the agriculture fields' boundaries, the BS values and VIs for each field was determined. An inside rectangular buffer corresponding to the largest image pixel size (L-8 30 meters) was applied around each agriculture field before determination of the final field BS and VIs values. The buffer was to remove any mixed pixels along the field borders (Bériaux et al., 2011; Mather & Koch, 2011). The zonal statistics tool (Kross et al., 2015) was then used to calculate the fields' descriptive statistics (mean and standard deviation values) for the BS values and the VIs. These were then correlated to the modeled LAI from (**Section 3.3.3.4.3**).
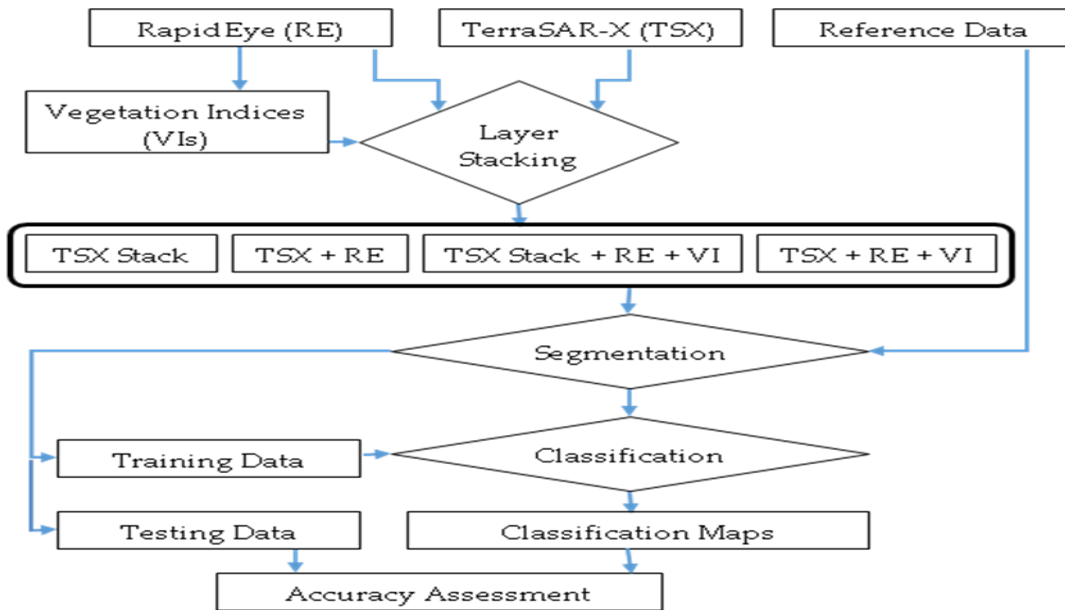
Figure 5.2: A scheme diagram showing the analysis of the satellite images to segment and classify the images. Four different combinations of the radar and optical images were classified.

For the object-based classification, 6-TSX images, 1-RE image, and 1-Normalized Difference Vegetation Index RedEdge (NDVIre) image were selected (**Table 5.1**). The NDVIre image was derived from the RE image. From (**Figure 5.2**), the TSX, RE, and NDVIre images were layer stacked in four combinations. A stack of the 6-TSX images (TSX Stack); a stack of the 26/08/2015 TSX image and the RE image (TSX+RE); a stack of the 6-TSX images, the RE image, and the NDVIre image (TSX Stack+RE+VI); a stack of the 26/08/2015 TSX image, the RE image, and the NDVIRE image (TSX+RE+VI). A segmentation algorithm automatically identified unique objects within the satellite images and from the resulting segments; training data (for classification) and testing data (for accuracy assessment) were selected from the images, corresponding to the ground reference data. A random forest classification was then performed.

Table 5.1: TerraSAR-X and RapidEye images used to perform the classification.

IMAGE	Acquisition Date		Acquisition Mode
TerraSAR-X	08/05/2015 21/06/2015 04/08/2015	30/05/2015 13/07/2015 26/08/2015	VV Descending mode Incidence angle 34.8°
RapidEye	24/08/2015		
RapidEye NDVIre	24/08/2015		

5.1   Mapping of the Maize Fields

The mapping of the maize fields exercise from the high resolution TSX and RE images involved the manual digitization of the field boundaries from the satellite images (**Chapter 3.3.2**, **Figure 3.14**). The boundaries could be clearly identified from the images. The area sizes of the digitized fields was then determined for the selected maize fields (**Chapter 3.3.2**, **Table 3.14**). These areas would later be compared to the reported area sizes recorded in the farm management records.

5.2   Classification of the Agriculture Fields

5.2.1   Image Segmentation

Image segmentation is identification of homogeneous regions in an image and later classifying them (Mather & Koch, 2011). This can be accomplished by utilizing the field boundaries to select the objects for training the classifier, or by automatically selecting and setting segmentation criteria. In comparison to the per pixel classification approach, object based/segmentation approach is preferred when classifying radar images due to the speckle effect that causes variation within a single field (Mather & Koch, 2011). It is also preferred when working with high resolution images whose pixel sizes are smaller than the classification objects (Blaschke, 2008). Darwish et al. (2003) grouped the segmentation approaches into three categories namely: point-based (e.g. grey-level thresholding), edge-based (e.g. edge detection techniques) and region-based (e.g. split and merge). Multi-Resolution Image Segmentation (MRIS), considered to be a region-based approach (Myint et al., 2011), was implemented in this study. The MRIS is a bottom-up approach that begins from a single pixel and merges a neighbour pixel with minimum heterogeneity increment until the heterogeneity of object exceeds the user-defined threshold, the so-called scale parameter. The basis of the merging decision is the local homogeneity criterion, describing the similarity between adjacent image objects. The process terminates when the smallest increase of homogeneity exceeds scale parameter. The homogeneity criterion is a combination of color (spectral values) and shape properties (smoothness and compactness) (Definiens, 2012). Segmentation is an iterative process requiring the user to apply different combinations of the scale, color, and shape criteria (Laurent et al., 2014; Muñoz et al., 2003). The scale factor is however considered as the most critical with most studies focusing on optimizing it (Liu et al., 2017). Varying combination values of the scale, color, and shape criteria of the MRIS algorithm were applied to the stacked TSX images, with the segmentation result of each combination being cross checked against the manually digitized fields by comparing their corresponding areas, and calculating the mean absolute error (MAE) and the mean error. The best segmentation results were achieved with the scale, color, and

compactness threshold factors set at 60, 0.1 and 0.4 respectively (**Figure 5.3**). After the segmentation, the various object classes were identified and labelled. Objects were then randomly selected for each class across the entire image, with 70% of these points being selected as training points, and 30% as validation points.
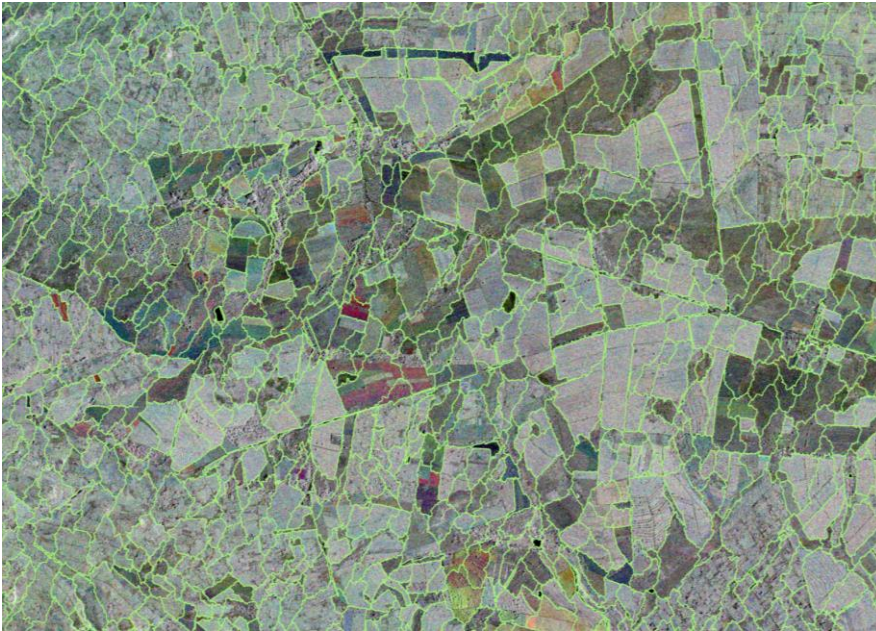
Figure 5.3: Results from iterative segmentation process for the object-based classification. Scale= 60 Color=0.1 Compactness=0.4. Image pixel size is 5 meters.

5.2.2   Object Based Classification

Classification of remote sensing images is a pattern recognition technique which uses machine learning algorithms to categorize the various image features (Canty, 2014). It can be generally categorized as either supervised classification, where the training classification data is selected prior to classification based on the knowledge of the area, or unsupervised classification, where spectral and pattern similarities define the classification process (Mather & Koch, 2011). The image land cover classes or themes are classified through either spectral pattern recognition techniques, spatial pattern recognition techniques or object based image analysis (OBIA) techniques (Lillesand et al., 2014). The spectral pattern recognition classifies each individual pixel based on its statistical or deterministic model reflectance or backscatter value. The spatial classifiers categorize pixels based on their spatial relationships with surrounding pixels by considering aspects like image texture, pixel proximity, feature size, shape, directionality, repetition and context. OBIA combines the use of both spectral and spatial pattern recognition (Lillesand et al., 2014; Mather & Koch, 2011). The image classification

approach taken is dependent upon the nature of data being analyzed, the computational resources available, and the intended application of the classified data (Lillesand et al., 2014). A supervised random forest (RF) classification algorithm was used for the classification in this study.

RF is a classification algorithm developed from the classification and regression trees (CART) (**Figure 5.4**). The algorithm iteratively constructs bootstrap samples from the original data, grows a tree at each node while randomly selecting variables at each node and permuting through to find the best split. It then validates each random tree using the withheld out-of-bag (OOB) data, outputs ensembles of RF trees, and performs a prediction of a new observation (Evans et al., 2011; Liaw & Wiener, 2002). It combines tree predictors in such a way that each tree depends on the values of a random vector sampled independently and with the same distribution for all trees in the forest with the generalization error of a forest tree classifiers depending on the strength of the individual trees in the forest and the correlation between them (Breiman, 2001).
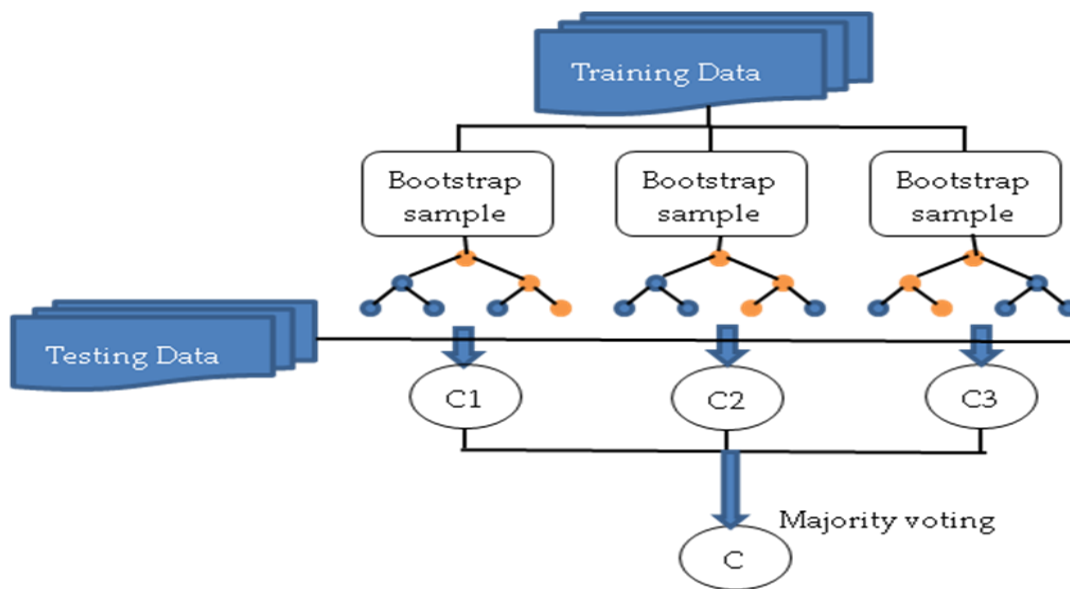
Figure 5.4: Random forest classification. Modified after Liu et al. (2017).

The RF algorithm has been used in combination with optical and radar data in parcel based agriculture image classification (Forkuor et al., 2014; Hütt et al., 2016; Ok et al., 2012), with the algorithm having an 8% better accuracy to other algorithms like the maximum likelihood (Ok et al., 2012). In addition, it is less sensitive to the number of training samples and perform well even with only a small number (Lebourgeois et al., 2017). It is computationally highly efficient and hence considered very well suited for land cover classifications of multifrequency and multitemporal stacks of SAR imagery (Waske & Braun, 2009).

5.3 Crop Growth Monitoring and Phenology Assessment

5.3.1 Monitoring of Maize with Optical Images

5.3.1.1 Sentinel-2 LAI

In order to exploit the Sentinel-2 (S-2) Multi Spectral Instrument (MSI) data, the European Space Agency (ESA), developed the S-2 toolbox level 2 biophysical variables algorithm (Li et al., 2015). The algorithm consists of a rich set of visualization, analysis, and processing tools, capable of generating a comprehensive database of vegetation characteristics and the associated S2 top of canopy (TOC) reflectance (Fernandes et al., 2014; Li et al., 2015). S2 level 2 products are derived from S2 TOC normalized reflectance data corresponding to a set of biophysical variables, including Leaf Area Index (LAI), the Fraction of Absorbed Photosynthetically Active Radiation (FAPAR), the fractional vegetation cover (FVC), the canopy chlorophyll content (CCC) and the canopy water content (CWC). The LAI range is 0 - 8.0, with a 0.01 resolution (Drusch et al., 2012; Frampton et al., 2013; Vuolo et al., 2016). Neural networks are then trained to estimate the canopy characteristics from the TOC reflectance, along with set corresponding angles defining the observational configuration. Neural networks are defined mainly by the type of neurons used (the transfer function), the way they are organized and connected (network architecture) and the learning rule. A neural networks algorithm was proposed for use in the estimation of biophysical variables for S-2 since the network coefficients can be easily changed, modified or upgraded in order to incorporate any new developments or advancement (Fernandes et al., 2014). For the TOC reflectance, individual daily reflectance observations are used, expressed in terms of reflectance factor, mainly varying between 0 - 0.7 for most land surfaces. Only eight bands are used: B3, B4, B5, B6, B7, B8a, B11 and B12. The geometry of acquisition inputs include: the cosine of the sun zenith angle, view zenith angle and relative azimuth angle at the time of the image acquisition (Fernandes et al., 2014).

The training of the database is done in 3 steps: generation of the database containing the input radiative transfer model variables; generation of the corresponding TOC reflectance for the 8 S-2 bands considered; addition of uncertainties to the simulated TOC reflectance values previously simulated. Generation of the diverse training database is normally achieved by pairing S-2 observations with accurate ground LAI measurements. However, due to the large uncertainties and variations attached to the ground measurements, coupled with the difficulty to collect such measurements within a large range of vegetation types, radiative transfer models are implored. The models simulate within a good accuracy the canopy reflectance as observed within S-2 bands and geometry over most vegetation types and conditions, observed over the earth. The leaf optical properties, the canopy structure, and the

background reflectance are normally considered (Vuolo et al., 2016). S-2 bands at 10 m spatial resolution are suitable for estimating LAI, avoiding the need for red-edge bands that are only available at 20 m and hence S-2 data is applicable in precision agriculture (Clevers et al., 2017).

5.3.1.2 Landsat-8 and RapidEye Vegetation Indices

The amount of light reflected from a surface is determined by the amount and composition of solar irradiance that strikes the surface, and the reflectance properties of the surface (Jackson & Huete, 1991). However, since the solar irradiance varies with time and atmospheric conditions, the measurement of light reflected from a surface cannot simply be sufficient to characterize the surface in a repeatable manner, hence the development of VIs to overcome this challenge. VIs are formed by combining data from two or more spectral bands with the intention to enhance the vegetation signal, while minimizing solar irradiance and soil background effects, while responding to subtle changes in plant health status amidst variable view, illumination and atmospheric conditions (Jackson & Huete, 1991). The basis of VIs is the measurement of the amount of sun light reflected by leaves (Davaasuren & Meesters, 2012). View and solar angles affect data from each spectral band differently, and thus may affect VI values (Jackson & Huete, 1991). Leaf reflectance properties, controlled by properties of pigments, water, and carbon, play a significant role in reflectance at the canopy level. Healthy vegetation strongly absorbs the sun light and reflects it back. The reflection of vegetation can be recorded in the red and infrared wavelengths. The strength of the vegetation reflectance depends on chlorophyll content and structural appearance (e.g. density of the vegetation). Very dense areas appear as very dark with transitions to more light and to very bright for sparsely vegetated areas. Soil background exerts a major influence on the vegetation reflectance and, in areas of dry land, reduce the reflectance of the sparse vegetation (Davaasuren & Meesters, 2012).

There are two general classes of VIs: ratios and linear combinations, both of which exploit the surface-dependent and/or wavelength-dependent features of the data (Jackson & Huete, 1991). Ratio VI may be the simple ratio of any two spectral bands, or the ratio of sums, differences or products of any number of bands whereas linear combinations are orthogonal sets of n linear equations calculated using data from n spectral bands (Jackson & Huete, 1991). The wavebands used to calculate VIs are chosen such that, one decreases and the other increases with increasing vegetation cover. Both ratio and linear combination indices decrease with increasing atmospheric turbidity (Jackson & Huete, 1991).

The development of VIs is an ongoing process with a great pool of available VIs for application in the various study and research fields (Bannari et al., 1995). There was a need therefore to narrow down to

the VIs that were relevant to the mapping of maize crops and the LAI biophysical parameter. This was achieved with the assistance of the Index Database (IDB) (Henrich et al., 2009). The IDB is a tool that provides a quick overview of which remote sensing VIs are usable for a specific sensor and a specific topic. The selected VIs for this study are listed in (**Table 5.2**).

Table 5.2: Vegetation indices that were calculated from the set of satellite images.

Index	Formula	Reference
Enhanced Vegetation Index two band (EVI2)	$2.4 \dfrac{NIR - REdge}{NIR + REdge + 1}$	(Elshorbagy, 2013; Jiang et al., 2008; Kang et al., 2016)
Green Normalized Difference Vegetation Index (gNDVI)	$\dfrac{NIR - Green}{NIR + Green}$	(Gitelson et al., 1996)
Normalized Difference Vegetation Index (NDVI)	$\dfrac{NIR - Red}{NIR + Red}$	(Nguy-Robertson et al., 2012; Rouse Jr et al., 1974)
Soil Adjusted Vegetation Index (SAVI)	$\dfrac{NIR - Red}{NIR + Red + L} (1 + L)$	(Fritsch et al., 2012)
Normalized Difference Vegetation Index Red Edge (NDVIre)	$\dfrac{NIR - REdge}{NIR + REdge}$	(Gitelson & Merzlyak, 1994)

Though the RE red-edge band has demonstrated success in the characterization of biophysical parameters, and in this case LAI (Ali et al., 2015; Beyer et al., 2015; Kross et al., 2015), only three images were available for the entire season (4/7/2015, 16/08/2015, 24/08/2015). The RE images were therefore complemented with the available L-8 images. This meant that the choice of VIs was limited to those with bands available for both L-8 and RE. However, the NDVIre VI was calculated to aid in the classification process described in (**Chapter 5.2**).

5.3.2   Monitoring of Maize with Radar Images

5.3.2.1   Analysis of the Backscatter Values from the Maize Fields

The backscatter values extracted from the TSX and S-1 images were analyzed for the 2015 cropping season. The aim of the analysis was to monitor the growth conditions of the maize in the selected fields by observing the behavior of the backscatter values. The images were categorized into four analysis groups, according to the sensor type and the acquisition. These were: S-1 ascending mode; S-1 descending mode; TSX ascending mode; TSX descending mode. A further analysis within each of the four analysis groups was undertaken based on the cultivated maize varieties (H6213, H628), the

cultivated field orientation (45°, 80°, 180°), and the different planting dates. This was undertaken in order to investigate the influence of the maize varieties, field orientations, and planting dates on the backscatter values characteristics.

5.3.2.2 Comparison of Sentinel-1 Backscatter Values for 2015 and 2016

The 2015 and 2016 S-1 backscatter values for each of the 18 ADC Olngatongo fields were analyzed. The objective was to observe if any similarities exist between the 2015 and 2016 backscatter values characteristics, and if the results were transferable from one year to the next. In the case that any similarities were observed, the backscatter values for the first year would form a baseline against which images acquired for the subsequent years would be compared. The analysis was carried for each of the three acquisition modes: ascending IW1; descending IW1; descending IW3.

5.3.2.3 Comparison of Sentinel-1 and TerraSAR-X Backscatter Values for 2015

In order to compare the performance of the S-1 and TSX images in the monitoring of the maize pheology, criteria were set in order to identify comparable image sets. The criteria were: a) The dates between any image set had to be three days or less in order to minimize the influence on the backscatter values by factors like rainfall; b) The image sets had to have similar acquisition modes (ascending or descending) and time (AM or PM); c) The difference in the incidence angles between any set of images had to be 10° or less. Four sets of S-1 and TSX images were identified in 2015 that met the set criteria (**Table 5.3**). The four sets were P1 (S-1-8/5/2015, TSX-8/5/2015), P2 (S-1-1/6/2015, TSX-30/5/2015), P3 (S-1-12/7/2015, TSX-13/7/2015), and P4 (S-1-29/8/2015, TSX-26/8/2015).

Table 5.3: TerraSAR-X (TSX) and Sentinel-1 (S-1) image pair set selected for the test sites. All images were acquired in descending mode. Information on the daily temperature and rainfall amounts, as well as the cumulative rainfall amount, is also provided.

Image	Acquisition Date & Time (UCT)	Incidence angle	Temp. (^{o}C)	Daily rainfall (mm)	Cumulative rainfall (mm)	Difference (Days)	Period
S-1	8/05/2015 (3:19 AM)	44.0°	17.9	0.4	267.2	0	P1
TSX	8/05/2015 (3:29 AM)	34.8°	17.9	0.4	267.2		
S-1	1/06/2015 (3:19 AM)	44.0°	18.8	2.8	363.8	2	P2
TSX	30/05/2015 (3:29 AM)	34.8°	17.5	70.2	438.2		
S-1	12/07/2015 (3:27 AM)	34.1°	18	0	569	1	P3
TSX	13/07/2015 (3:30 AM)	34.8°	18	0	569		
S-1	29/08/2015 (3:27 AM)	34.1°	18	0	753	3	P4
TSX	26/08/2015 (3:30 AM)	34.8°	17.9	0	753		

6. Results

6.1   Mapping of the Maize Fields

The reported planting area as recorded in the farm management records for 24 maize fields was compared with the estimated area from the RE and TSX satellite images. The unit of measurement was hectares (ha), rounded to the nearest whole number (**Table 6.1**).

Table 6.1: Comparison between the estimated area and the reported area in hectares (ha) for 24 maize fields within the study site for the 2015 season. The estimated area was derived from the TerraSAR-X and the RapidEye satellite images, while the reported area was taken from the farm management records. The mean bias was calculated as a difference between the reported and measured areas, while the Bias as % was calculated as a percentage of the estimated area.

Field	Estimated area (ha)	Reported area (ha)	Mean Bias (Reported-Estimated)	Bias as % of Estimated area
F1	12	16	4	33
F2	16	16	0	0
K5	23	18	-5	-22
S2	12	14	2	17
X2/1	8	16	8	100
X4/1	10	15	5	50
H1	14	14	0	0
H2	18	18	0	0
H3	16	16	0	0
H5	34	34	0	0
H6	18	16	-2	-11
H7	16	16	0	0
H8	21	19	-2	-10
H9	36	40	4	11
H10	28	24	-4	-14
H11	19	19	0	0
L2	13	13	0	0
L4	13	12	-1	-8
L5	10	11	1	10
L6	9	11	2	22
L7	8	11	3	38
L10	10	10	0	0
L17	19	18	-1	-5
T27	14	12	-2	-14

Four of the fields (F1; F2; K5; S2) were under ADC Sabwani management, two of them (X2/1; X4/1) under KSC management and the rest under ADC Olngatongo management. The mean bias (difference between the reported area and the estimated area) and the percentage bias (mean bias as a percentage of the estimated area) were computed in order to determine the difference between the estimated and reported areas (Carletto et al., 2015). In 9 of the fields (38%), there was no difference between the estimated and reported areas. There was overestimation of the area in 8 of the fields (33%) while the remaining 7 fields (29%) were underestimated. The percentage bias in the overestimated areas ranged from 17% to 100% while the percentage bias in the underestimated areas ranged between -5% and -22%. Two of the fields (X2/1; X4/1) reported biases of 100% and 50% respectively. Though the fields were under KSC management, they belonged to ADC Sabwani farm and KSC had hired them for the 2015 cropping season. It is therefore likely that the reported area in the records indicated the entire field sizes as opposed to the actual planted area. In some instances of large over reporting of the field sizes, an association to the government subsidies provided to the farmers in terms of farm inputs (Parry et al., 1988a; Sanchez et al., 2009) could be speculated from the information gathered during the field work exercise. Thus, the larger the reported field sizes, the higher the subsidy amounts. In other instances where there were large underestimations, a relation to the reported yields could be speculated. Since yields are reported normally per hectare of planted field size, underestimation of the field sizes ensures high reported yield production figures.

6.2   Classification of the Agriculture Fields

The images classification results for the different image combinations (a) TSX stack; b) TSX and RE; c) TSX stack, RE, and NDVIre; d) TSX, RE, and NDVIre) are displayed in the classification map (**Figure 6.1**). The classification results demonstrate that the study area is a predominant agricultural area, with cropping activities distributed over the area. The crops identified include beans, maize, sugarcane and wheat. However, maize was the most dominant crop covering the area.
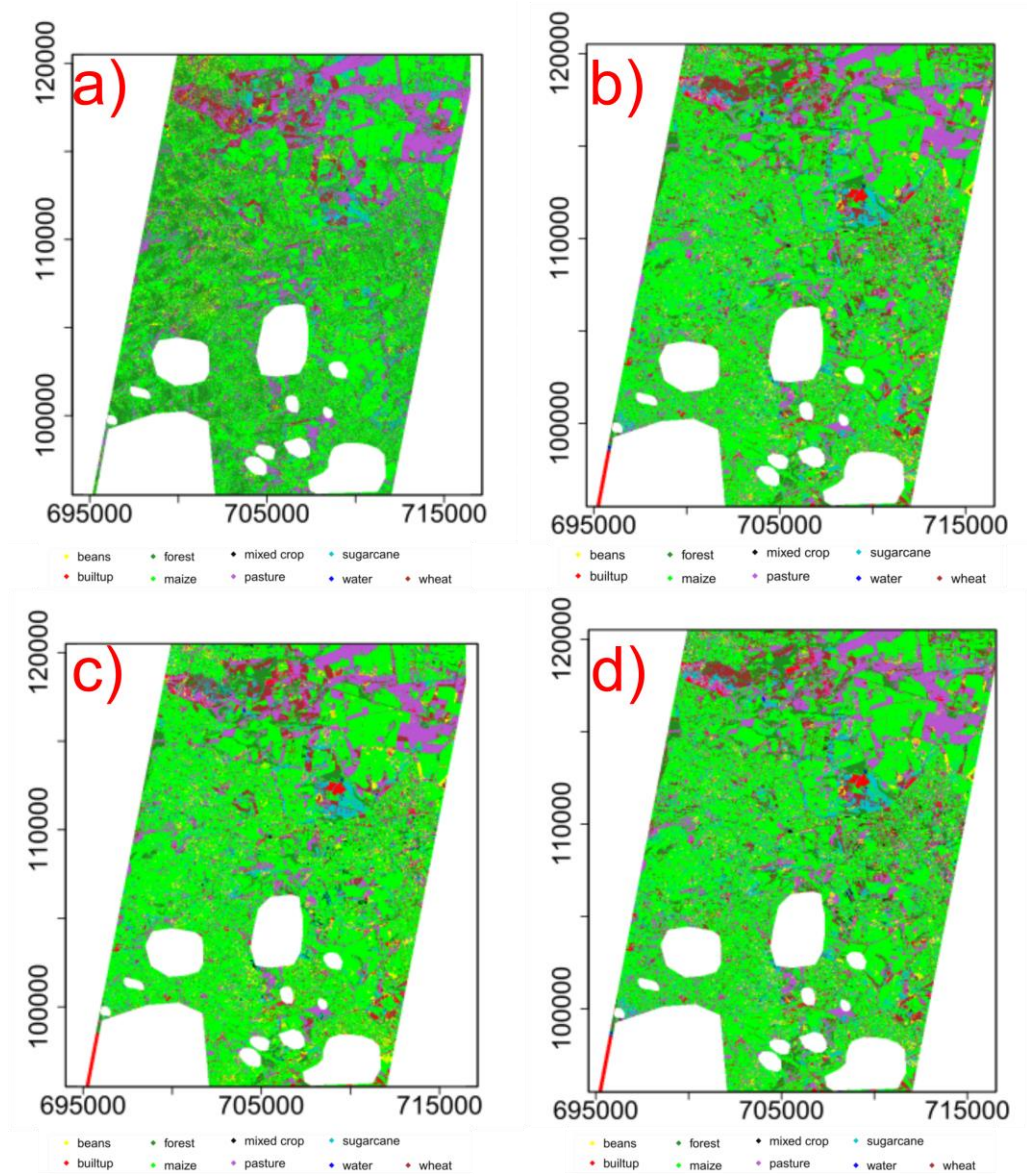
Figure 6.1: Classification maps. a) TSX Stack, b) TSX + RE, c) TSX Stacck + RE + NDVIRE, d) TSX + RE + NDVIRE.

The main results of the accuracy assessment (producer accuracy-PA, user accuracy-UA, overall accuracy-OA, and Kappa-Coefficient-KA), (Lillesand et al., 2014), are summarized in (**Table 6.2**), with the graphical representation of the PA and UA displayed in (**Figure 6.2**) and (**Figure 6.3**) respectively. The maize results are highlighted since this study focused on maize. The classification of the 6 stacked TSX images alone (TSX stack) achieves the lowest accuracies (PA-64%, UA-48%, OA-49%, and KA-0.39). Combining of a single TSX and a single RE image (TSX+RE) achieved accuracies of (PA-80%, UA-63%, OA-76%, and KA-0.72). Adding of the single RE and single NDVIre images to the stack of 6 TSX images (TSX STACK+RE+NDVIRE) achieved the highest accuracies of (PA-89%, UA-72%, OA-83%, and KA-

0.80). Finally, the combination of the single TSX, single RE, and single NDVIre images (TSX+RE+NDVIRE) achieved accuracies of (PA-79%, UA-65%, OA-77%, and KA-0.73).

In summary, adding of the RE and NDVIre images to the TSX STACK achieves the highest accuracies, whereas adding of the NDVIre image to the combination of the TSX+RE images does not significantly improve the results.

Table 6.2: Classification producer and user accuracy results.

	Images	Beans		Built-up		Forest		Maize		Mixed crop		Pasture		Sugar cane		Water		Wheat			
		PA	UA	PA	UA	PA	UA	PA	UA	PA	UA	PA	UA	PA	UA	PA	UA	PA	UA	OA	KA
a)	TSX STACK	30	39	1	50	49	49	64	48	0	0	68	57	37	39	96	86	53	51	49	39
b)	TSX+ RE	73	71	70	88	99	98	80	63	3	25	77	75	66	70	92	96	64	71	76	72
c)	TSX STACK+ RE + NDVIRE	81	79	70	79	98	99	89	72	3	20	89	87	67	79	96	96	81	80	83	80
d)	TSX+RE+ NDVIRE	76	74	67	81	99	97	79	65	9	38	78	75	65	71	88	96	68	72	77	73
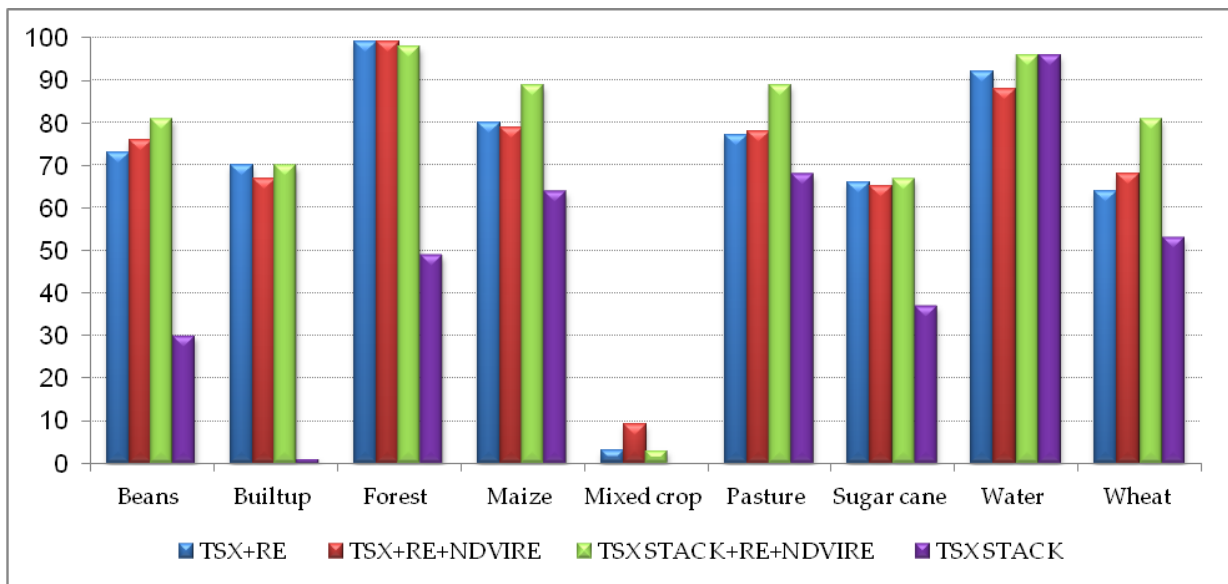
Figure 6.2: Graphical representation of the producer accuracies achieved from the classification.
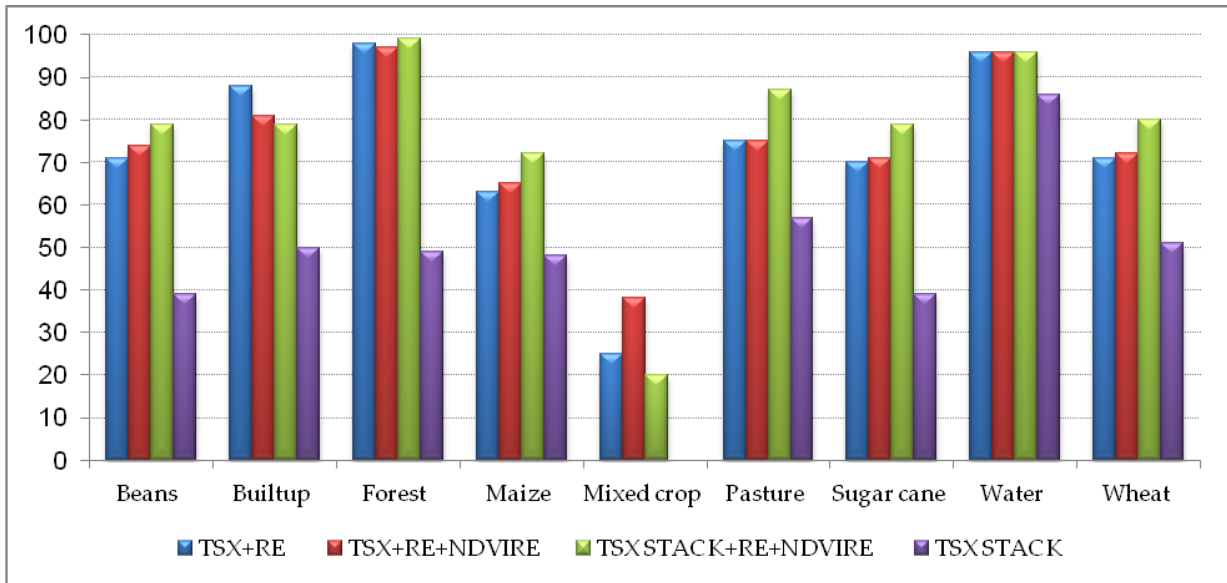
Figure 6.3: Graphical representation of the user accuracies achieved from the classification.

6.3 Maize Growth Monitoring and Phenology Assessment

6.3.1 Monitoring of Maize with Optical Images

6.3.1.1 Sentinel-2 LAI

The LAI for the 18 selected ADC Olngatongo maize fields was extracted from the S-2 images acquired on the 7/4/2016, 27/5/2016, 6/6/2016, 6/7/2016, 16/7/2016, 26/7/2016, 15/8/2016, 14/9/2016, and 4/10/2016, a map of which is displayed in (**Figure 6.4**). Though the number of acquired S-2 images was more, only images with minimum cloud cover influence were processed for LAI. The light green color indicates low LAI values while the dark green indicates high LAI values. (**Figure 6.4 a**) acquired at the beginning of the season (7/4/2016) displays the lowest LAI values, whereas (**Figure 6.4 d, e, f**) acquired in the vegetative stage (6/7/2016, 16/7/2016, 26/7/2016) displayed the highest LAI values. The infield variations in the LAI were noted as well, as seen from the variations in the LAI values within the single fields at any single image acquisition. The infield LAI reflects growth variability, a pattern typical of crops in rain-fed agriculture, and which are more sensitive to soil heterogeneity in comparison to irrigated crops (Richter et al., 2008).
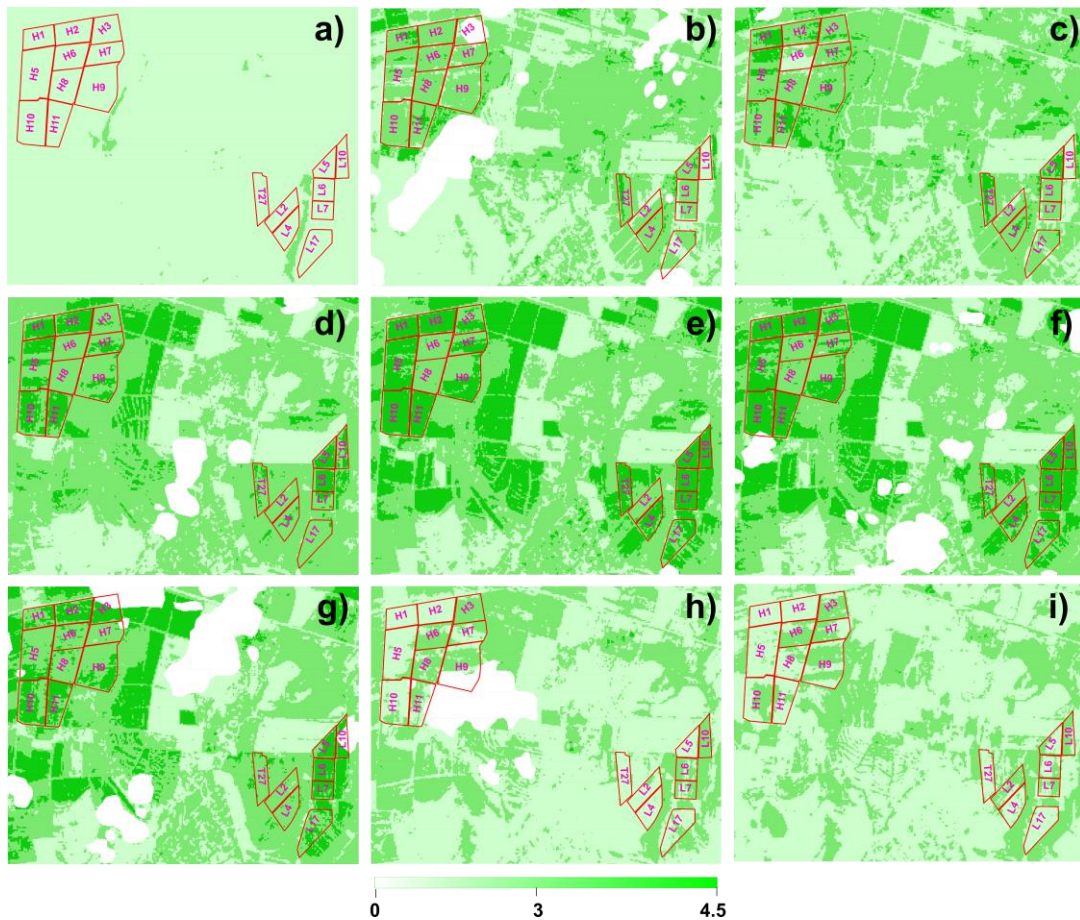
Figure 6.4: Sentinel-2 LAI maps for the 2016 planting season, extracted for the 18 ADC Olngatongo maize fields: a) 7/4/2016, b) 27/5/2016, c) 6/6/2016, d) 6/7/2016, e) 16/7/2016, f) 26/7/2016, g) 15/8/2016, h) 14/9/2016, and i) 4/10/2016. A cloud mask extracted the clouds on the images before the LAI processing.

In addition to the LAI map, the LAI values for each of the individual maize fields was plotted in order to analyze the LAI curve for the entire cropping season (**Figure 6.5**). There was a steady increase and decrease in the field LAI values, with the maximum LAI value occurring around the 200 day of the year. The LAI values ranged from a minimum of 0 m^2/m^2 to a maximum of 3.9 m^2/m^2, with the maximum LAI value coinciding with the end of the BBCH principal growth stage 6 (flowering, anthesis) and the start of the BBCH principal growth stage 7 (development of fruit).
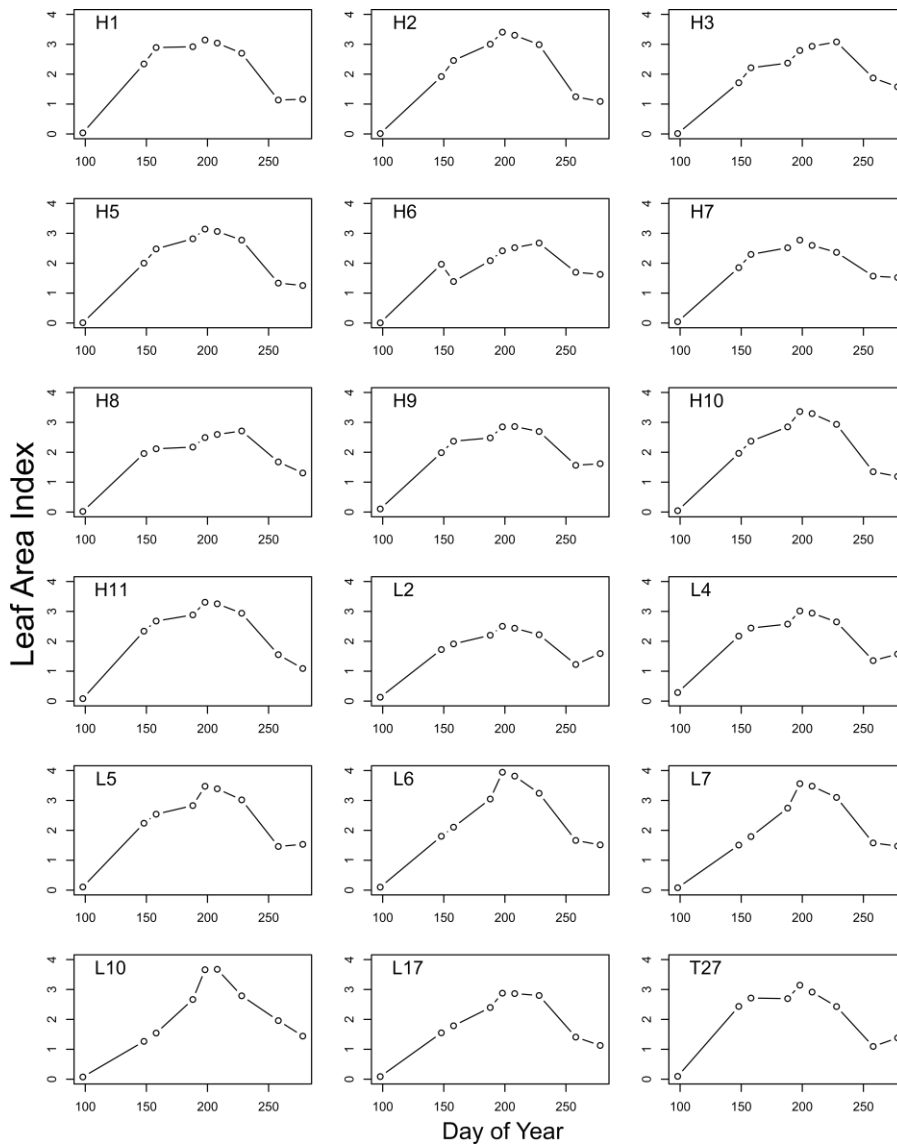
Figure 6.5: Sentinel-2 LAI product value for the 2016 planting season, extracted for the 18 ADC Olngatongo maize fields.

A closer analysis of the curves revealed variations mainly in: the smoothness of the curves and in the realized maximum LAI values. The various fields were therefore grouped according to some notable characteristics namely: the maize varieties cultivated (**Figure 6.6**); the orientation of the maize rows (**Figure 6.7**); the planting dates (**Figure 6.8**). The sets of vertical lines in the graphs indicate the planting dates, and the end of the maize growth period in the study site, as described by Jones (2013). The growing duration from planting to the end of the growth period is about 6 months.
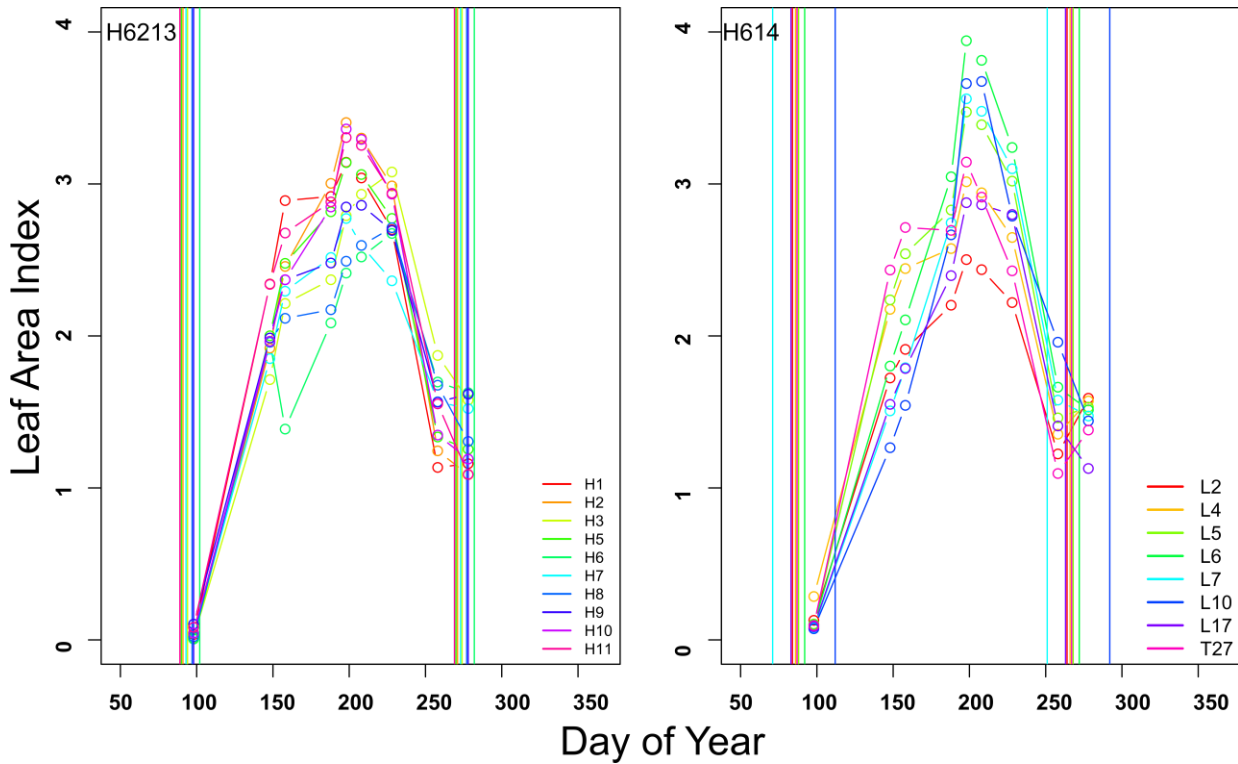
Figure 6.6: Sentinel-2 maize LAI values 2016 grouped according to maize varieties H6213 and H614. The vertical lines indicate the planting and end of growth period for the maize in the fields.

The LAI value of the H614 maize variety was higher in comparison to the H6213 (**Figure 6.6**). The infield variation in the LAI values was highest between the days of year 150 and 230 during tasseling (BBCH 5), flowering (BBCH 6) and the development of the maize fruit (BBCH 7). The direction and orientation of the maize plant rows appeared to have had no influence on the LAI values since the field variations were still evident during the cropping season (**Figure 6.7**). However, when the fields were grouped according to their planting dates, there was visible decrease in the field LAI variation (**Figure 6.8**). Fields whose planting dates were within a maximum of four days apart were grouped together. Group a) represents fields planted on the 11/3, b) fields planted between 28/3 and 31/3, c) fields planted between 1/4 and 3/4, d) fields planted on the 11/4, e) fields planted between 6/4 and 7/4, f) fields planted between 23/3 and 27/3, and g) fields planted on 21/4. The fields in b) had the least field LAI variation despite of them consisting both H6213 and H614 varieties. Some groups had only one field occurring and therefore no comparison could be made.

The analysis revealed that the LAI plots for the fields H6, L6, L7, and L10 exhibited unique characteristics. This could be attributed to farm management practices that may have altered the growth curve of the maize in these fields. However, the fieldwork exercise for the validation of these results could not be undertaken during the 2016 cropping season.
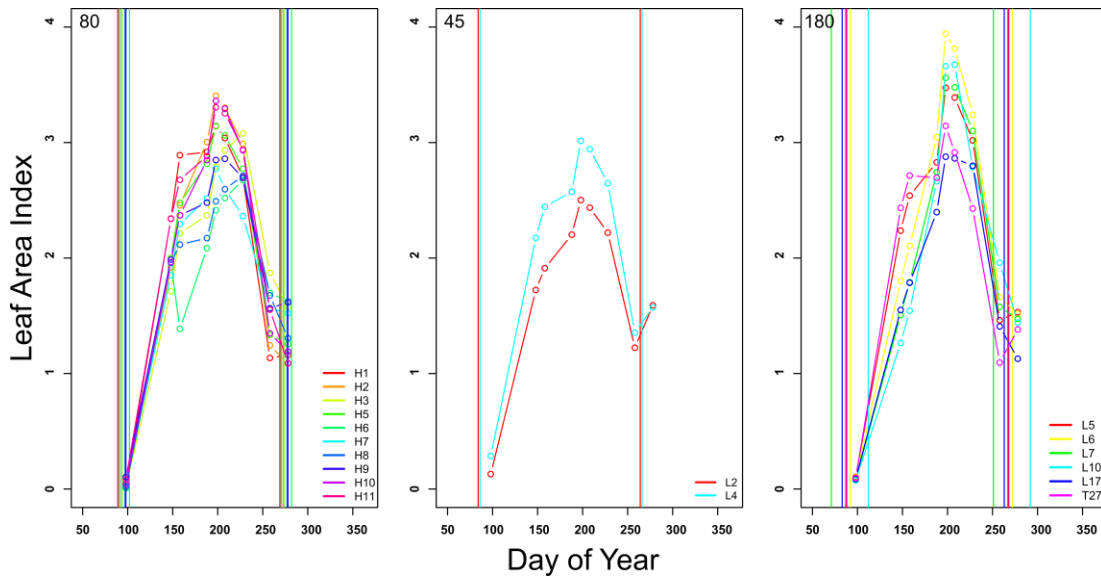
Figure 6.7: Sentinel-2 maize LAI values 2016 grouped according to field planting orientation (45°, 80°, and 180°). The vertical lines indicate the planting and end of growth period for the maize in the fields.
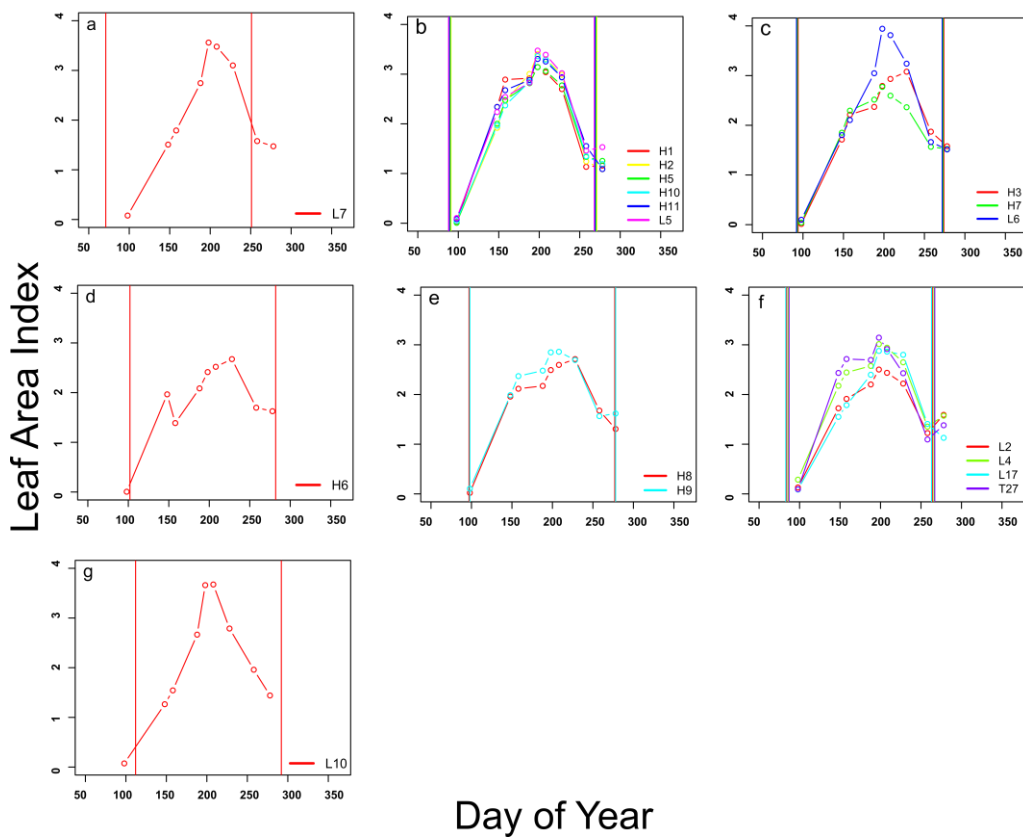
Figure 6.8: Sentinel-2 maize LAI values 2016 grouped according to planting dates. a) 11/3, b) 28/3-31/3, c) 1/4-3/4, d) 11/4, e) 6/4-7/4, f) 23/3-27/3, g) 21/4.

6.3.1.2   Modeled LAI

The LAI modeling results from (**Chapter 3.3.3.4.3**) for 18 ADC Olngatongo maize fields are displayed in (**Figure 6.9**). The multiplot displays symmetrical LAI curves with the peak LAI value (about 4.8 m^2/m^2) occurring around day of year 180 in majority of the fields and day of year 200 in the remaining fields. The maize plants were towards the end of principal growth stage 6 (flowering and anthesis) and the beginning of the principal growth stage 7 (development of fruit). A similar finding was reported by Liu et al., (2012). The high LAI value at this growth stage was attributed to the very high photosynthetic rates and assimilate production, associated with the fully developed leaves (Danalatos et al., 1994).
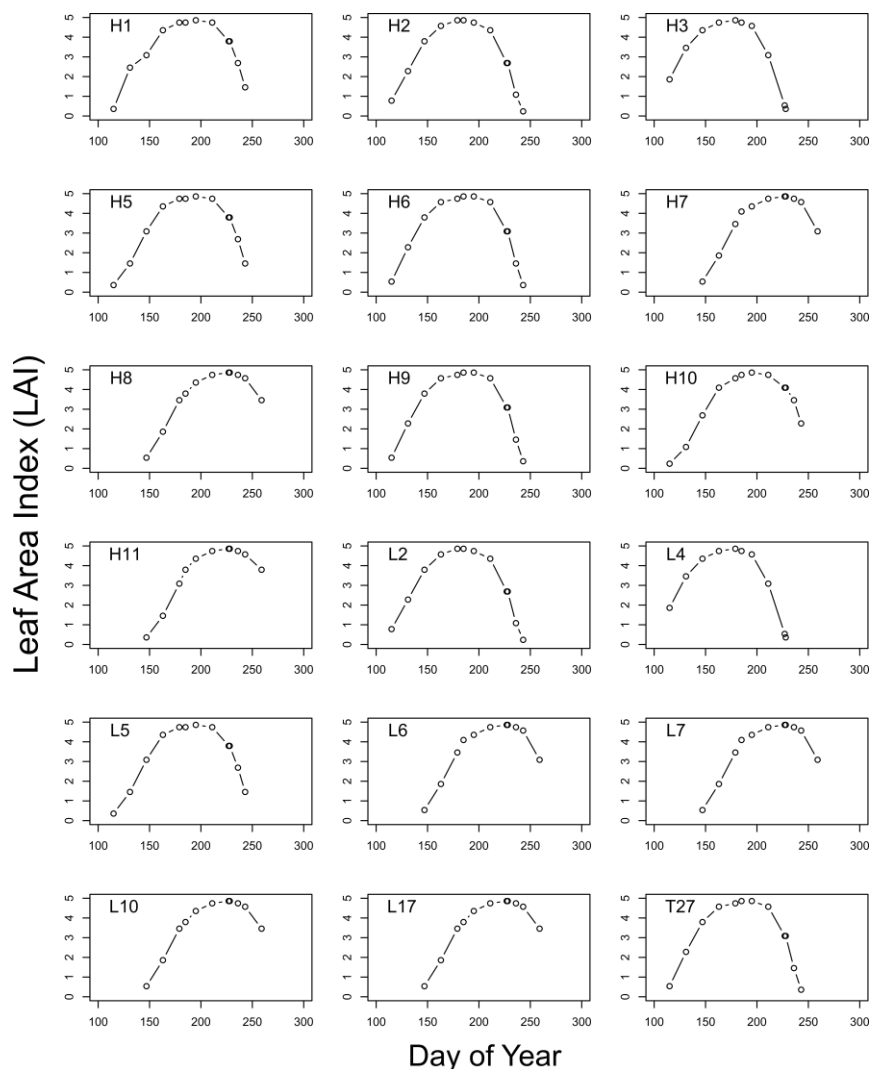
Figure 6.9: A multiplot showing the modeled leaf area index (LAI) values for 18 fields in the study site. The maximum LAI value was about 4.8 m^2/m^2 for all the fields. This was achieved around the day of year 200 when the maize was in the principal growth stage 7 (development of fruit).

6.3.1.3 Sentinel-2 LAI vs. modeled LAI

The LAI model developed for the 2015 cropping season (**Chapter 3.3.3.4.3**) was applied for the 2016 cropping season. The LAI results were validated with LAI values derived from the S-2 images for the 2016 cropping season in order to check the robustness of the model and its transferability from one year to the next. The S-2 LAI values were plotted against the modeled LAI values (**Figure 6.10**). The S-2 underestimated the LAI values, an observation that was also made by Richter et al., (2009). An R^2 value of 0.54 with an RMSE of 0.31 was achieved (**Table 6.3**). These results agreed with previous findings reported by Propastin & Erasmi (2010). In other previous studies (Chen et al., 2002; Tian et al., 2003; Zheng & Moskal, 2009) it was reported that the mismatch between S-2 LAI and the modeled LAI scales could have influenced the results, with the measured LAI being at a field-scale whereas the S-2 LAI was on a global scale.

The S2 LAI data availability at the beginning of the cropping season was limited by the presence of clouds, as compared to the tail end of the season when the maize was in the late growth development stages. Thus, only 60 data points were available for the sample data. Higher accuracies would have been achieved if the more values were available during the early development stages, when the maximum leaf growth takes place (Danalatos et al., 1994).
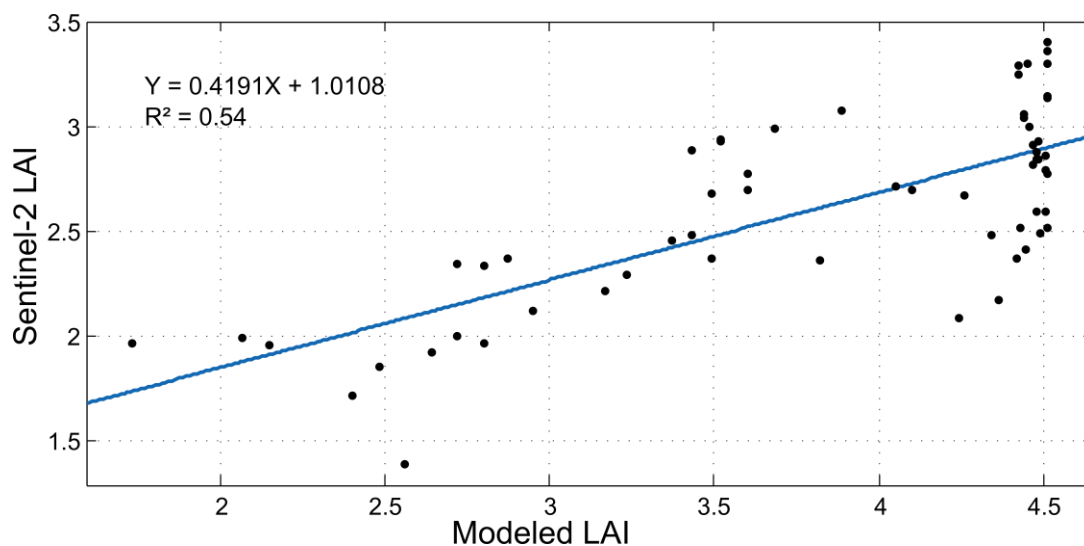
Figure 6.10: Sentinel-2 maize LAI values 2016 against modeled LAI values for validation of the results (n = 60).

Table 6.3: A summary of the accuracies achieved from the correlation between the Sentinel-2 LAI (2016) and the modeled LAI (2016).

R^2	N	RMSE	P-Value	SSE
0.54	60	0.31	< 0.001	5.63

6.3.1.4   LAI vs. Vegetation Indices

The vegetation indices (VIs), namely the EVI2, SAVI, NDVI and gNDVI were plotted against the measured LAI (**Figure 6.11**). There was an uneven distribution of data points across the plot, with the greatest concentration occurring at the high LAI and VIs values. This was due to the unavailability of cloud free images at the beginning of the season caused by the rainy weather conditions. The rains however subsided during the later half of the cropping season, and more cloud free images were available. The best correlation accuracies between the VIs and the LAI were achieved by a linear fit (**Table 6.4**). The R^2 values of 0.88 (RMSE 0.07), 0.81 (RMSE 0.09), 0.8 (RMSE 0.07), and 0.82 (RMSE 0.04) being achieved for EVI2, SAVI, NDVI and gNDVI respectively.
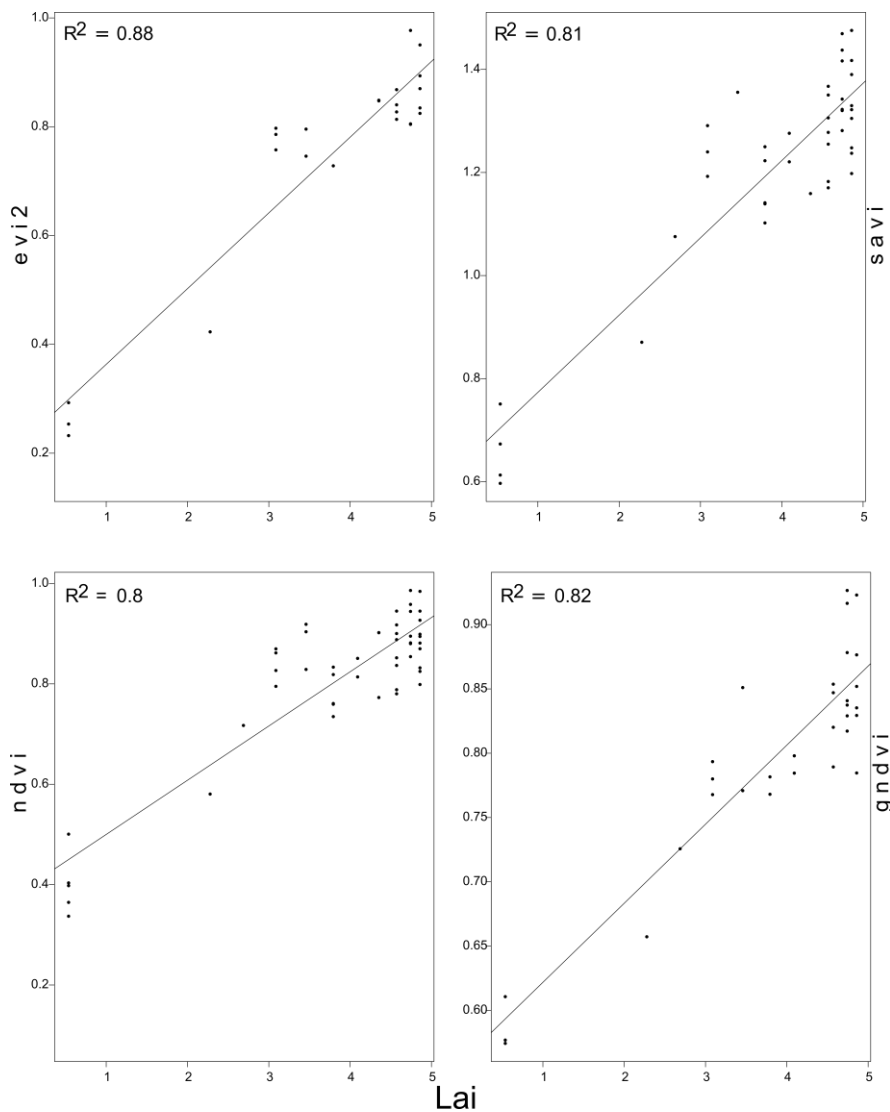
Figure 6.11: Plots of the lines of best fit for the correlation between the Vegetation Indices (VIs) and the Leaf Area Index (LAI). The VIs are EVI2, SAVI, NDVI, and gNDVI.

Table 6.4: Statistical results for the linear models correlation between the Vegetation Indices (VIs) and the Leaf Area Index (LAI). The coefficient of determination (R^2), the sample size (N), and the root mean square error (RMSE) are shown. The p-value for the four VIs was <0.05.

	R^2	N	RMSE (residual error)
Evi2	0.88	22	0.07
SAVI	0.81	39	0.09
NDVI	0.8	47	0.07
gNDVI	0.82	29	0.04

6.3.2 Monitoring of Maize with Radar Images

6.3.2.1   Analysis of the Backscatter Values from the Maize Fields

The backscatter values from the Sentinel-1 and TerraSAR-X images for the 2015 cropping season for the 18 ADC Olngatongo fields were plotted. The backscatter values were categorized into four according to their acquisition modes: ascending and descending modes (**Figure 6.12**).
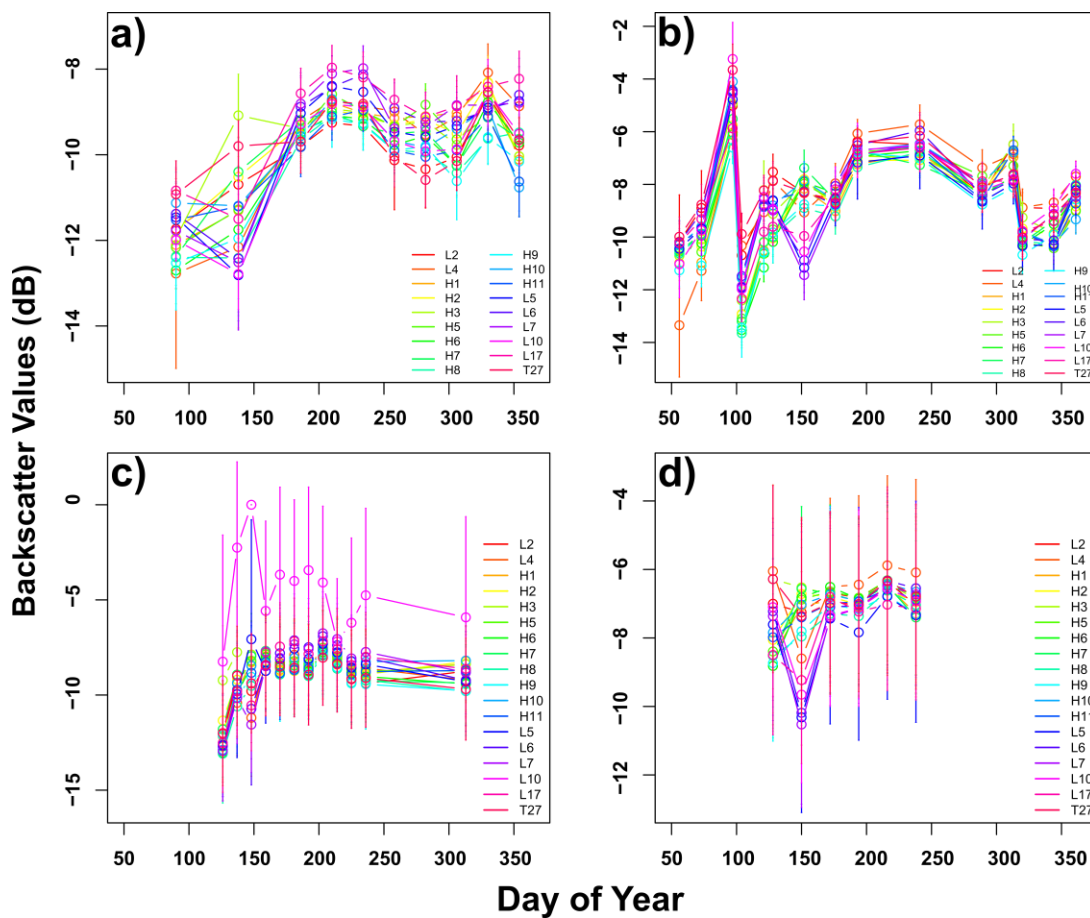
Figure 6.12: Sentinel-1 (S-1) and TerraSAR-X (TSX) backscatter value plots of the 18 ADC Olngatongo maize fields analyzed for the 2015 cropping season. a) S-1 ascending mode, b) S-1 descending mode, c) TSX ascending mode, d) TSX descending mode.

The S-1 ascending mode backscatter values ranged from -12.8 to -8.0 dB, with the standard deviation ranging from 0.4 to 2.2 dB, whereas the S-1 descending mode backscatter values ranged from -13.7 to -3.2 dB, with a standard deviation range of 0 to 6.7 dB. On the other side, the TSX ascending mode backscatter values ranged from -13.1 to 0 dB, with the standard deviation ranging from 0.4 to 2.2 dB, whereas the TSX descending mode backscatter values ranged from -10.5 to -5.9 dB, with a standard deviation range from 2.0 to 3.1 dB. The standard deviation from the mean of the TSX was greater than that of the S-1 since the shorter wavelength TSX-X band interacts less with the maize canopy compared to the longer wavelength S-1-C band, thus it is scattered more easily (Bargiel et al., 2010; Thiong'o et al., 2015). Whereas the TSX images were available during the cropping season, some S-1 images were available for the period before and after the cropping season. This was evidenced by the large fields backscatter variations in the first two and last two image acquisitions in (**Figure 6.12 a)** and **b)**). The change in the maize phenology could be detected by the backscatter values from the undulating shapes of the curves. The changes were more pronounced in the S-1 images as compared to the TSX images. The shapes of the curves, and hence the backscatter characteristics appeared consistent for all the maize fields, except for the field L10, whose backscatter values were inconsistent. The results from the field L10 provides a case study to underscore the importance of radar images in crop growth monitoring. An early detection in the backscatter discrepancy could assist the farmers to investigate its cause in the field, and undertake any mitigation measures where possible.

In order to carry out a field-by-field analysis of the different S-1 and TSX acquisitions mode, multiplots for the respective fields were plotted **(Figures 6.13-6.16)**. (**Figure 6.13**) shows the S-1 ascending mode backscatter characteristics. The backscatter values gradually increase from germination until the 210 day of year when the maximum backscatter value is realized. This coincides with the BBCH principal stage 8 (ripening), when the physiological maturity is achieved, after which it gradually declines as the maize enter the senescence stage (Meier, 2001). In field H3 however, the maximum value is first observed at day of year 138 during the emergence of the tassel stage. In (**Figure 6.14**) (S-1 descending mode), more maize phenological characteristics are visible. There is an increase in the backscatter values after germination, which generally coincides with the BBCH principal growth stage 1 (leaf development) and stage 3 (stem elongation). The backscatter values then decrease in the principal stage 5 (inflorescence emergence, heading) before gradually increasing and leveling at the beginning of the principal stage 6 (flowering, anthesis). The backscatter values again decrease towards the end of stage 6, before increasing again in the BBCH 5. A decrease in the backscatter values occurs again as the maize enters the senescence stage.
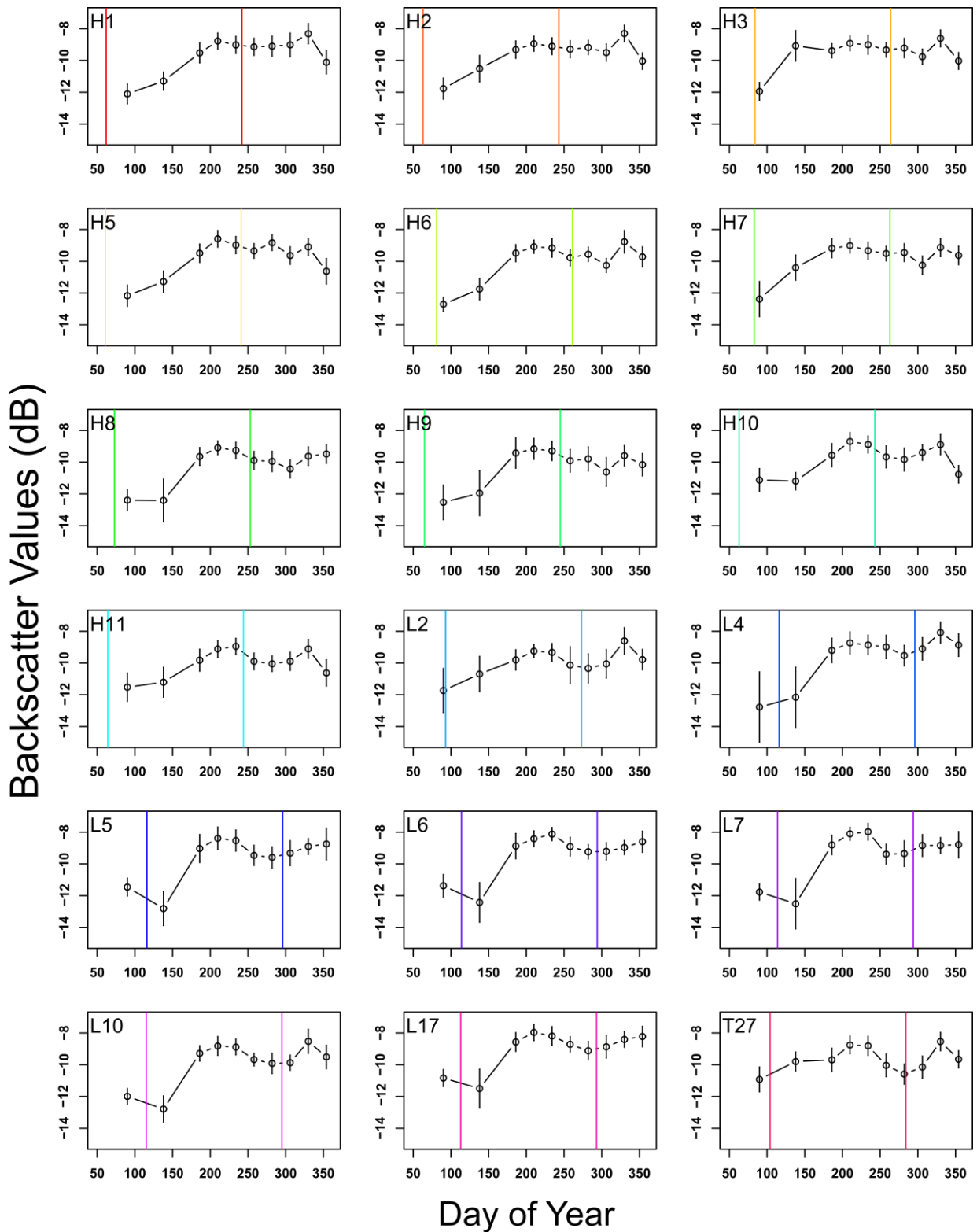
Figure 6.13: A multiplot of the Sentinel-1 (S-1) ascending mode backscatter values for the 18 ADC Olngatongo maize fields analyzed for the 2015 cropping season. The vertical lines indicate the planting and harvesting days repectively.
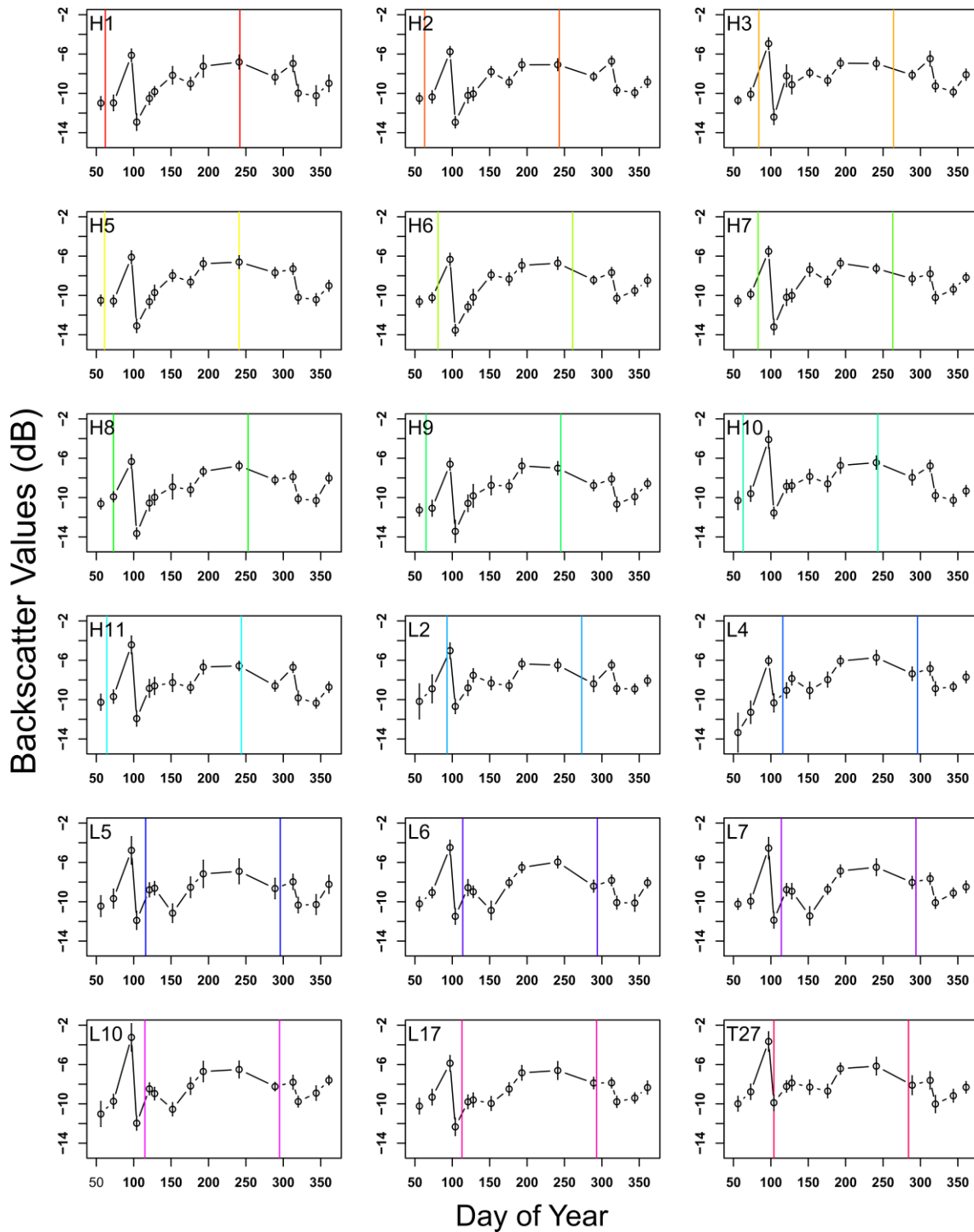
Figure 6.14: A multiplot of the Sentinel-1 (S-1) descending mode backscatter values for the 18 ADC Olngatongo maize fields analyzed for the 2015 cropping season. The vertical lines indicate the planting and harvesting days repectively.

The maize phenological characteristics in the TSX ascending mode backscatter values (**Figure 6.15**) were not as pronounced as the S-1 backscatter values, except for the field L10. The first TSX image was acquired when the maize was already in the principal growth stage 5 (inflorescence emergence,

115

heading). The backscatter values gradually increased until the end of the principal growth stage 6 (flowering, anthesis). There was a slight increase in the backscatter value as the maize entered the principal growth stage 8 (ripening) before again decreasing towards senescence.
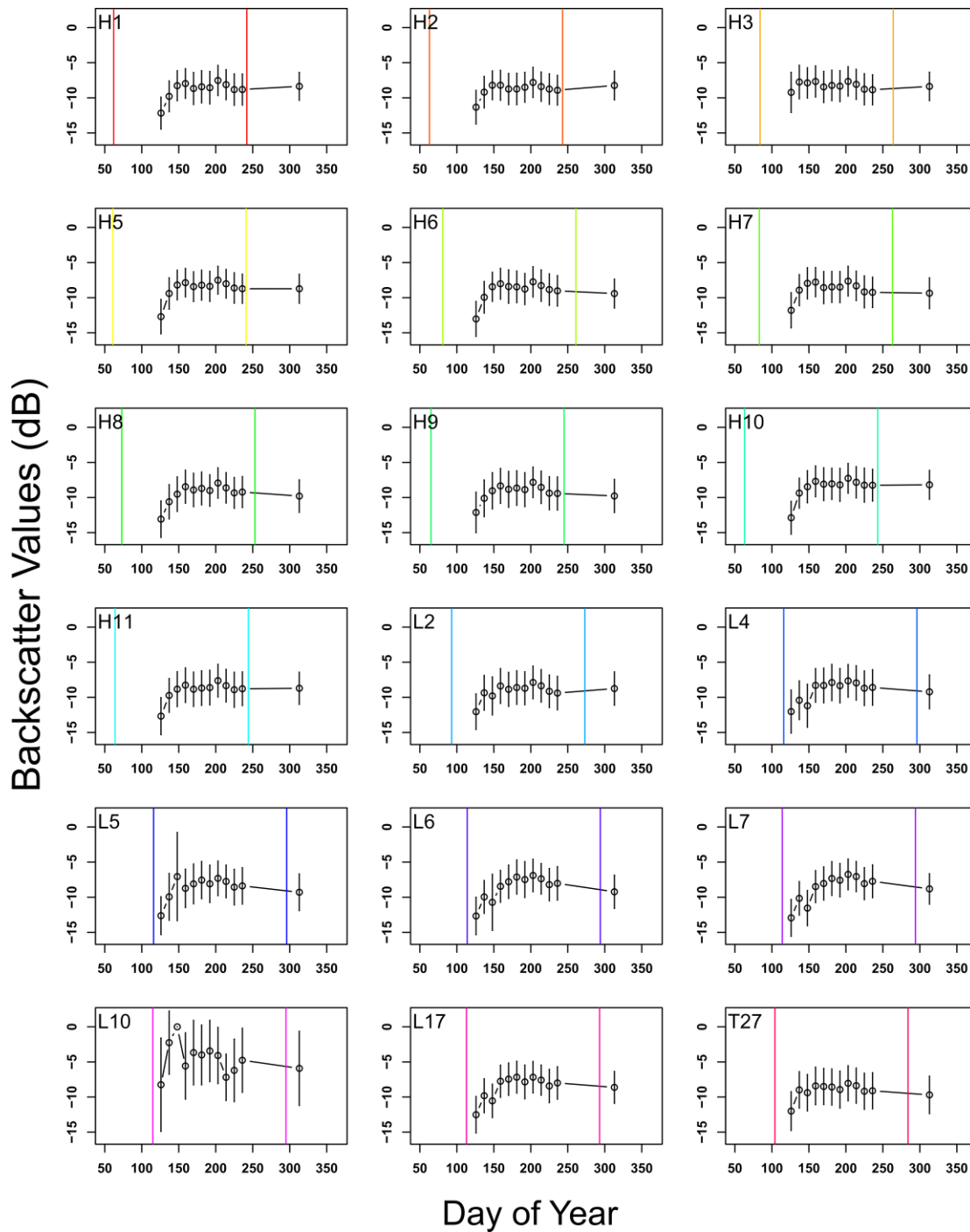
Figure 6.15: A multiplot of the TerraSAR-X (TSX) ascending mode backscatter values for the 18 ADC Olngatongo maize fields analyzed for the 2015 cropping season. The vertical lines indicate the planting and harvesting days repectively.

The TSX descending mode backscatter values in (**Figure 6.16**) displays two different sets of curves. For the fields that were planted around the day of year 70, the first TSX image is acquired in the principal growth stage 5 (inflorescence emergence, heading). The backscatter values increase gradually until the end of the principal growth stage 8 (ripening), after which the backscatter values decrease as the maize enter the senescence stage. The second set of curves are from fields that were planted around day of year 110. The first TSX image was acquired when the maize were in the principal growth stage 0 (germination). The values decrease in the second image acquisition acquired when the maize were in the principal growth stage 3 (stem elongation). The values then gradually increase until the beginning of the principal stage 7 (beginning of fruit development).
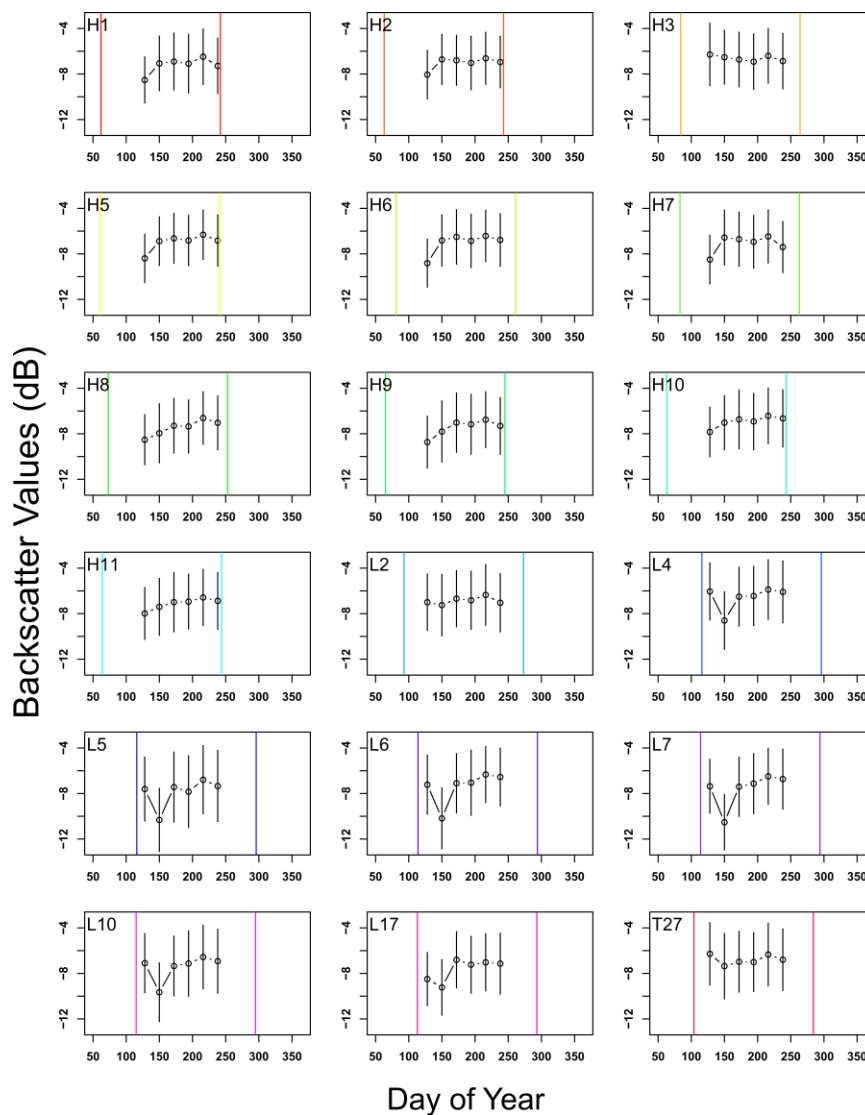
Figure 6.16: A multiplot of the TerraSAR-X (TSX) descending mode backscatter values for the 18 ADC Olngatongo maize fields analyzed for the 2015 cropping season. The vertical lines indicate the planting and harvesting days repectively.

In addition to the analysis of the individual maize fields, the influence of the maize varieties, field orientation and planting dates on the backscatter values was analyzed.

Analysis according to maize varieties
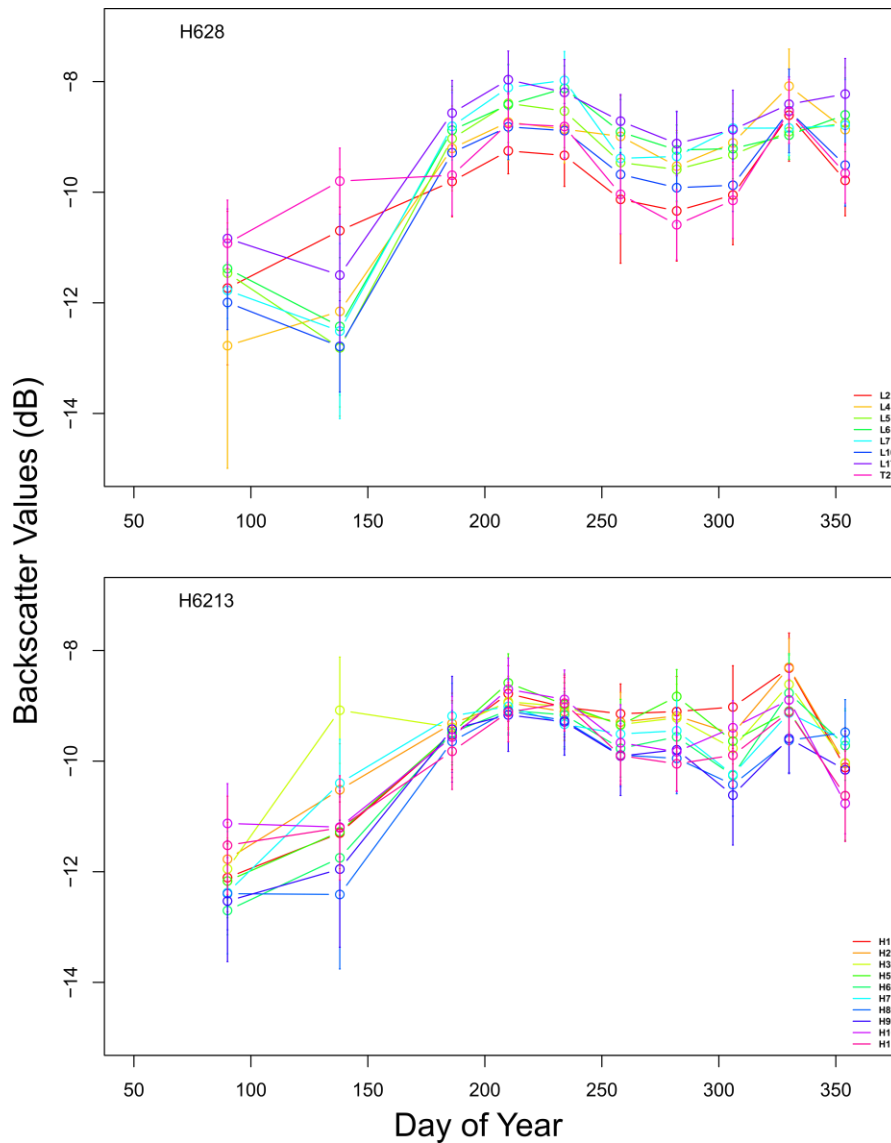
Figure 6.17: A plot of the Sentinel-1 (S-1) ascending mode backscatter values for the 18 ADC Olngatongo maize fields analyzed for the 2015 cropping season grouped according to the H628 and H6213 maize varieties planted.

In (**Figure 6.17**), the maize fields were categorized into the H628 and H6213 maize varieties for the S-1 ascending mode images. The line graphs for both graphs displayed similar phenological characteristics along the cropping season. From the similarities in the two graphs, coupled with the variations and

dispersion in the line graphs of the individual maize fields within any single plot, it could be concluded that the maize varieties as a factor on its own has no influence on the image backscatter values.

The S-1 descending mode backscatter values graphs also had similar characteristics for both H628 and H6213 maize varieties (**Figure 6.18**). This was however with the exception at day of year 150 whereby, whereas the backscatter values of the H628 decreased, the backscatter values for the H6213 increased. Notable was also the decreased variations and dispersion in the line graphs of the individual maize fields within any single plot, compared to the S-1 ascending graphs.
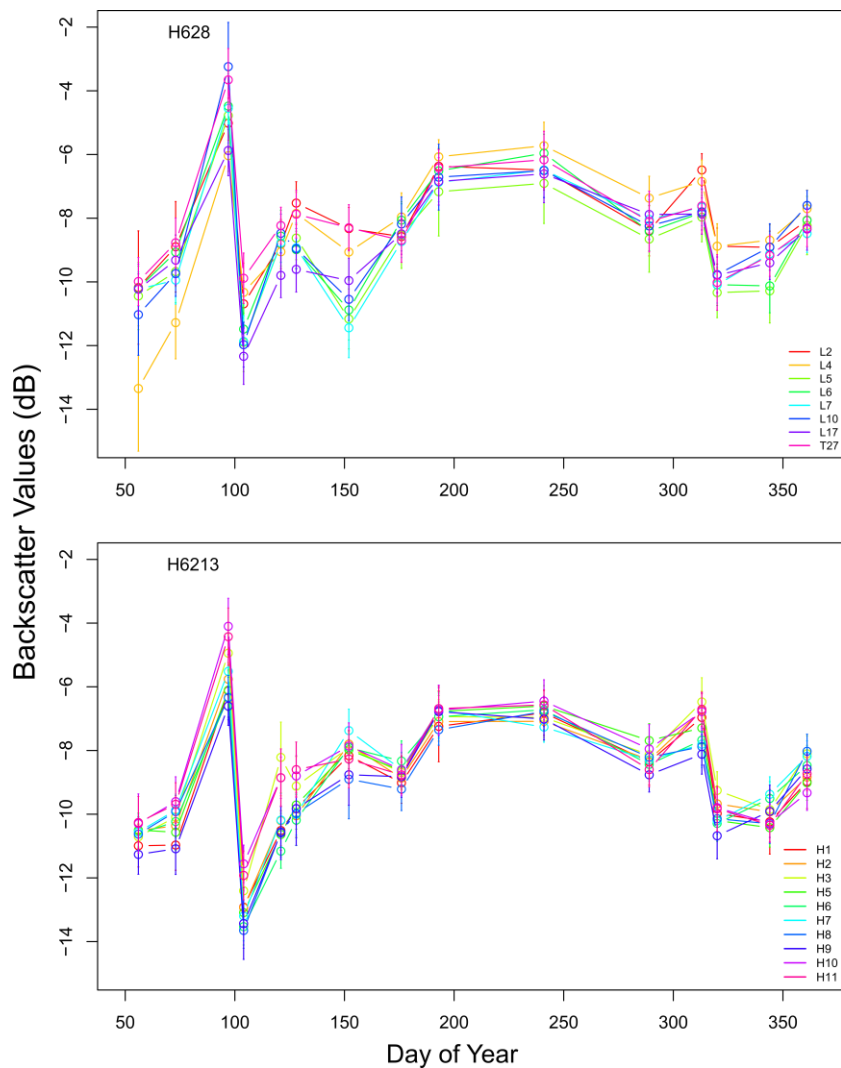
Figure 6.18: A plot of the Sentinel-1 (S-1) descending mode backscatter values for the 18 ADC Olngatongo maize fields analyzed for the 2015 cropping season grouped according to the H628 and H6213 maize varieties planted.
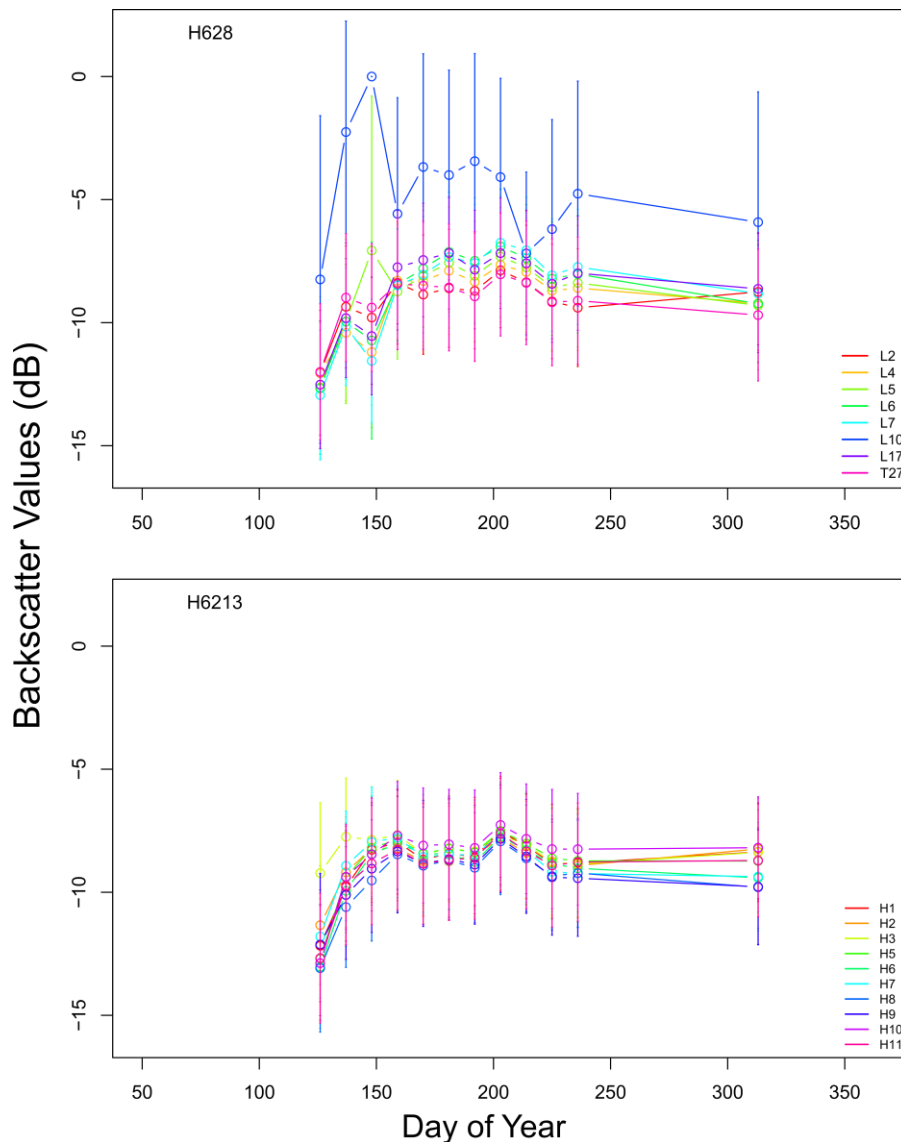
Figure 6.19: A plot of the TerraSAR-X (TSX) ascending mode backscatter values for the 18 ADC Olngatongo maize fields analyzed for the 2015 cropping season grouped according to the H628 and H6213 maize varieties planted.

From the TSX ascending mode backscatter values, similar trends in the phenological characteristics of both the H628 and the H6213 maize varieties were observed (**Figure 6.19**). This was again with the exception of the day of year 150 where, whereas there was a decrease in the backscatter values for H628, an increase in the backscatter values was observed for H6213. Another notable difference between the two varieties was the variation and dispersion in the line graphs of the individual maize fields within any single plot. The variation was minimal for the H6213 variety, in comparison to the H628 variety where greater variations were noted. The greatest variation occurred in field L10, which stood out from the rest of the fields.
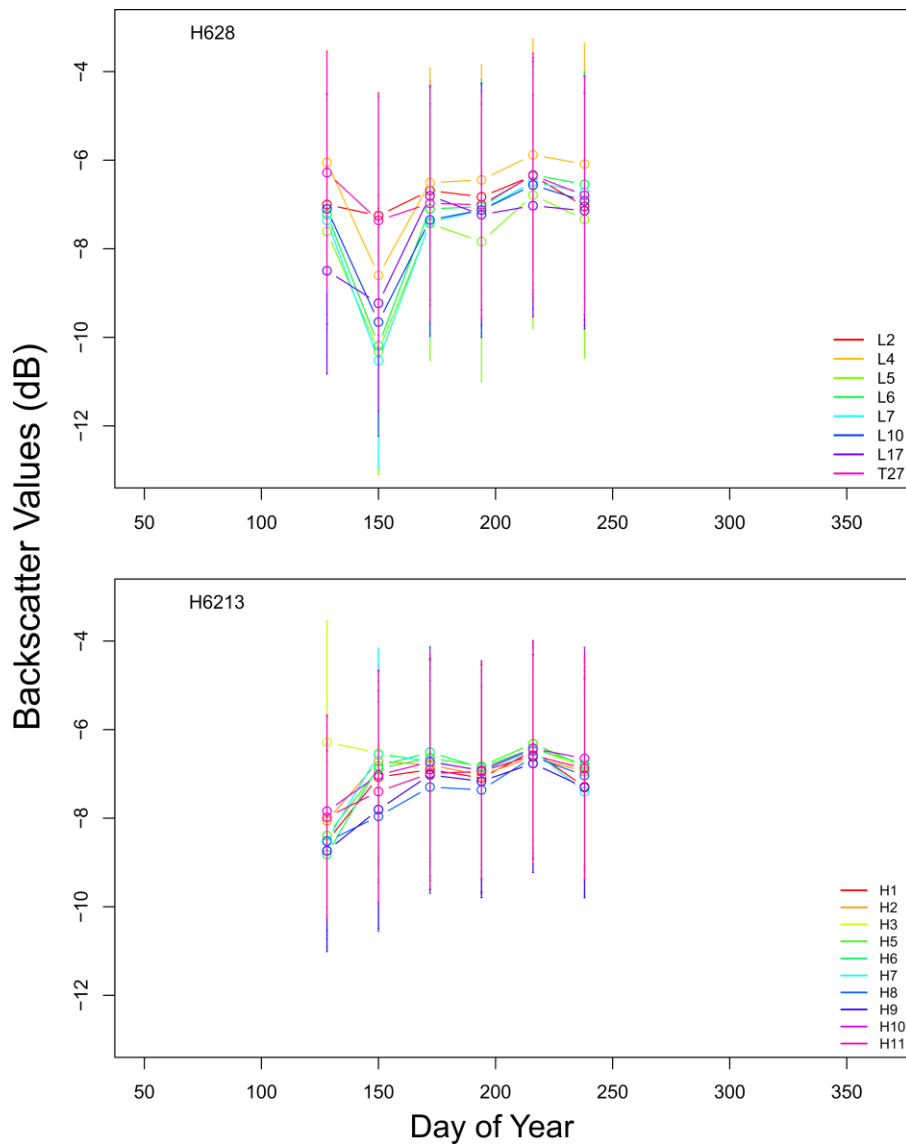
Figure 6.20: A plot of the TerraSAR-X (TSX) descending mode backscatter values for the 18 ADC Olngatongo maize fields analyzed for the 2015 cropping season grouped according to the H628 and H6213 maize varieties planted.

The TSX descending mode backscatter values displayed similar trends in the phenological characteristics of both the H628 and the H6213 maize varieties (**Figure 6.20**). The exception was again at the day of year 150 where, whereas there was a decrease in the backscatter values for H628, an increase in the backscatter values was observed for H6213. There was also a variation and dispersion in the line graphs of the individual maize fields within any single plot of the two varieties. Whereas the variation was minimal for the H6213 variety, the H628 variety had greater variations. The greatest variation occurred between days 130 and 170.

Analysis according to field orientations
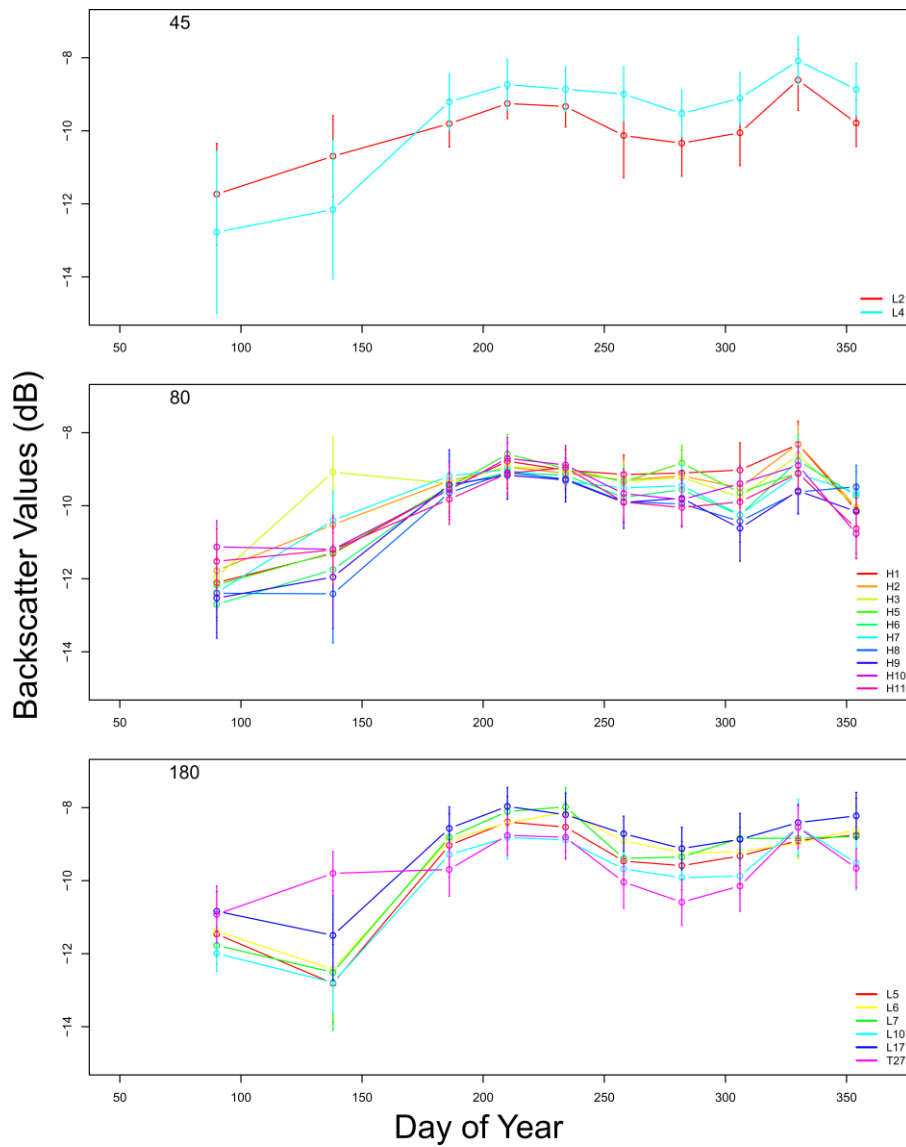
Figure 6.21: A plot of the Sentinel-1 (S-1) ascending mode backscatter values for the 18 ADC Olngatongo maize fields analyzed for the 2015 cropping season grouped according to the 45°, 80°, and 180° orientations.

The phenological characteristics of all three plots of the S-1 ascending mode backscatter values grouped according to the 45°, 80°, and 180° were identical, with the greatest variations and dispersion in the line graphs of the individual maize fields within any single plot occurring before day 180 (**Figure 6.21**).
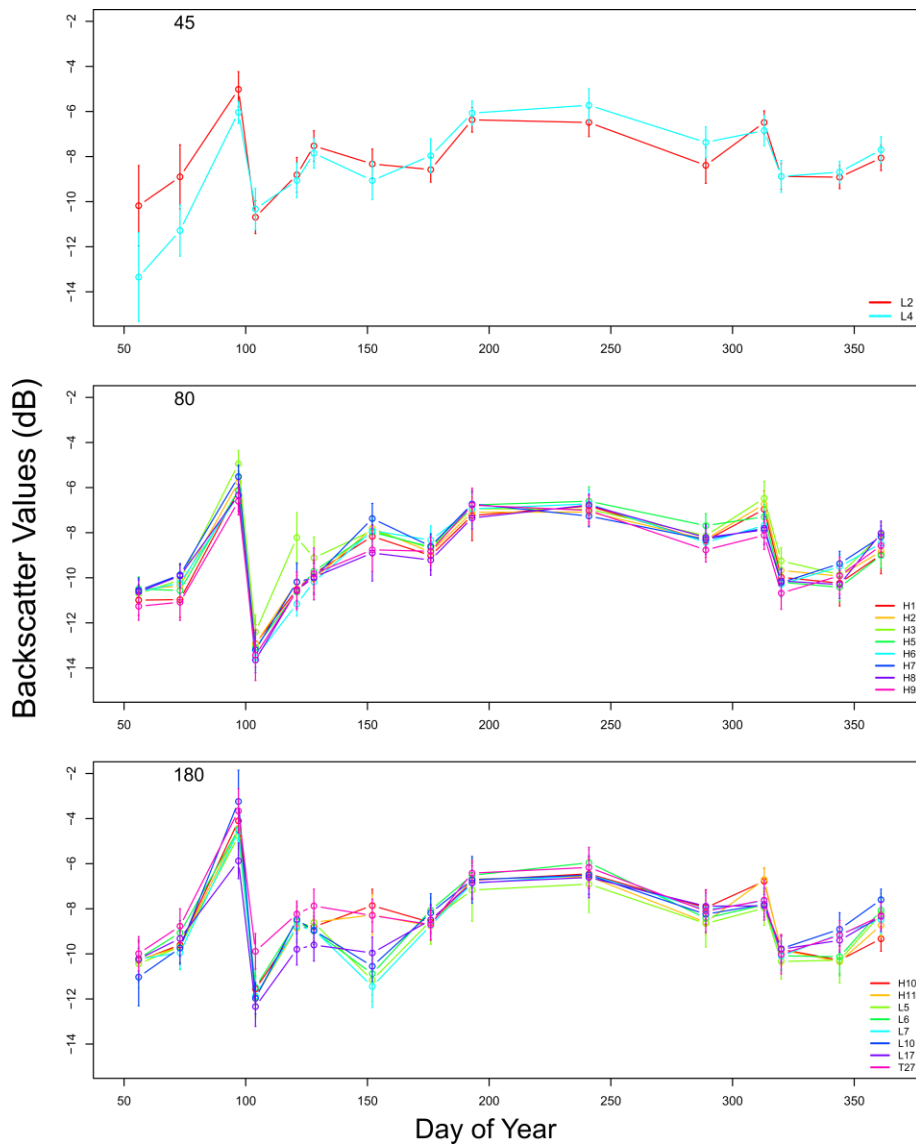
Figure 6.22: A plot of the Sentinel-1 (S-1) descending mode backscatter values for the 18 ADC Olngatongo maize fields analyzed for the 2015 cropping season grouped according to the 45°, 80°, and 180° orientations.

In (**Figure 6.22**) the phenological characteristics for the S-1 descending backscatter values were similar for all three orientation angles (45, 80, 180). An exception was during day 150 for the 180° plot where the variations in the field backscatter values were greatest.
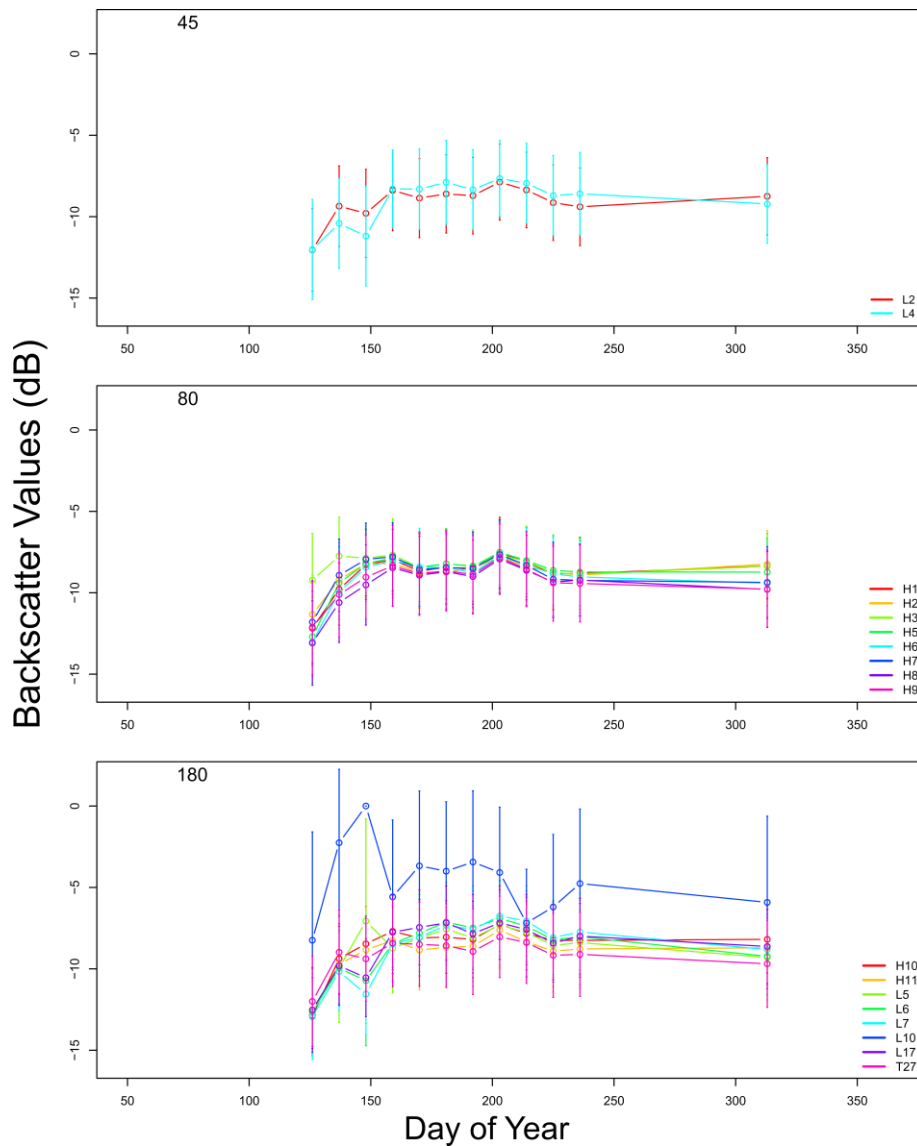
Figure 6.23: A plot of the TeraSAR-X (TSX) ascending mode backscatter values for the 18 ADC Olngatongo maize fields analyzed for the 2015 cropping season grouped according to the 45°, 80°, and 180° orientations.

The phenological characteristics of all three plots of the TSX ascending mode backscatter values grouped according to the 45°, 80°, and 180° were identical (**Figure 6.23**). During the day of year 150 however, whereas a decrease in the backscatter values was observed in the 45° and 180° plots, plot 80° recorded an increase in the backscatter values. The greatest variations and dispersion in the line graphs was noted in the 180° plot whereby the field L10 stood out from the rest of the fields of the individual maize fields within any single plot occurring before day 180.
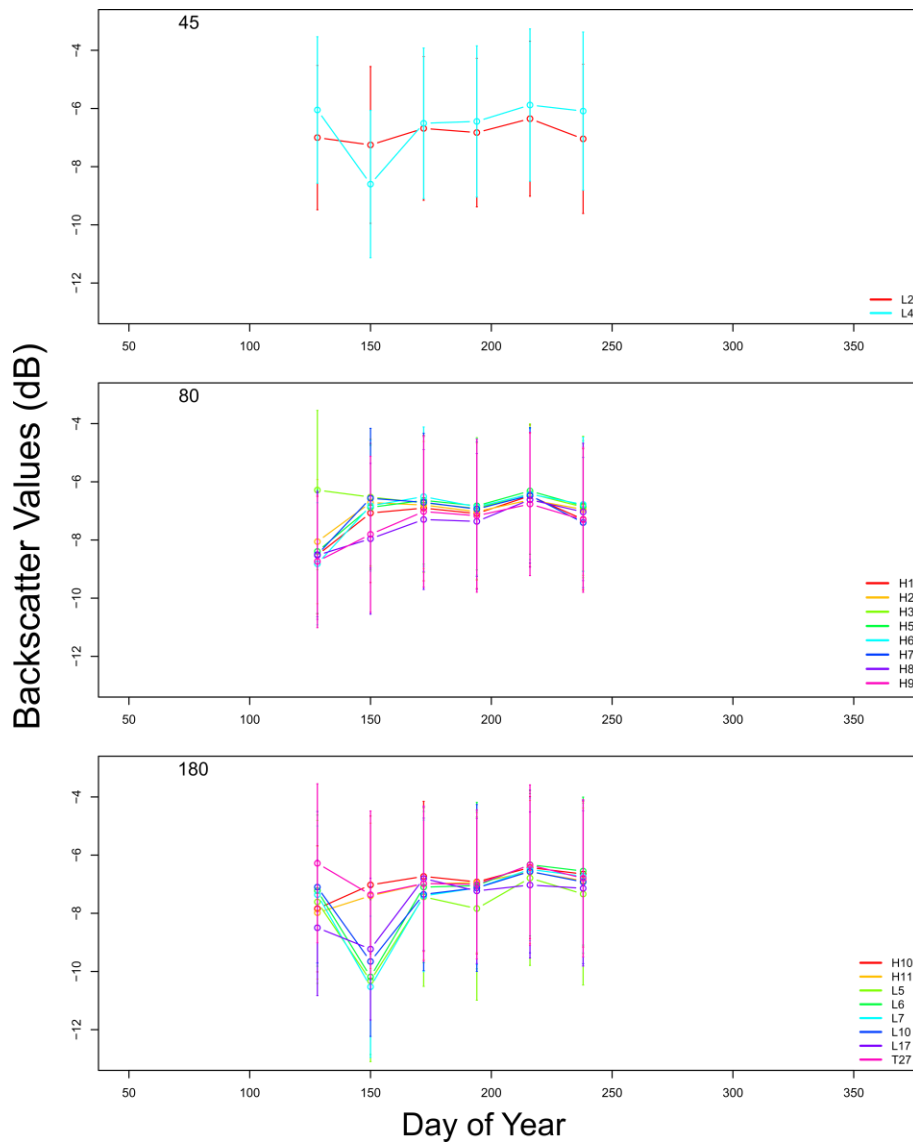
Figure 6.24: A plot of the TeraSAR-X (TSX) descending mode backscatter values for the 18 ADC Olngatongo maize fields analyzed for the 2015 cropping season grouped according to the 45°, 80°, and 180° orientations.

In (**Figure 6.24**) the phenological characteristics for the TSX descending backscatter values were similar for all three orientation angles (45, 80, 180). An exception was during day 150 for the 80° plot whereby an increase in the backscatter values was recorded. This is also the period when the greatest variations in the backscatter values within the individual fields were observed.

Analysis according to planting dates

Six groups of planting dates in 2015 were identified namely: planting dates A) 2/3-6/3 B) 14/3, C) 22/3-25/3, D) 3/4, E) 14/4, F) 23/4-26/4. The dates were grouped ensuring that the difference between the first and last planting dates was less than four days.
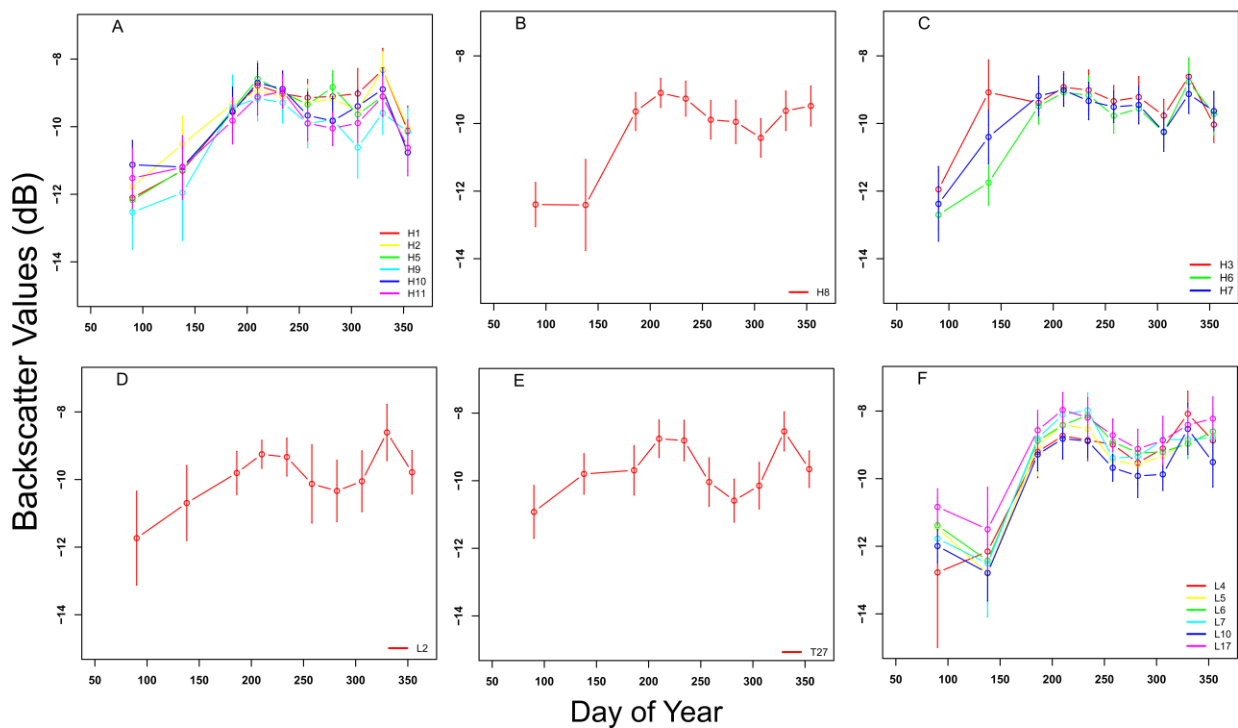
Figure 6.25: A plot of the Sentinel-1 (S-1) ascending mode backscatter values for the 18 ADC Olngatongo maize fields analyzed for the 2015 cropping season grouped according to the planting dates a) 2/3-6/3 b) 14/3, c) 22/3-25/3, d) 3/4, e) 14/4, f) 23/4-26/4. The vertical lines indicate the planting and end of growth period for the maize in the fields.

(**Figure 6.25**) groups the results of the S-1 ascending mode backscatter values according to their planting dates. The phenological characteristics for all the graphs were identical, with the greatest field variability in the backscatter values observed in the early growth stages, until day of year 180 which coincided with the end of the BBCH principal growth stage 6 (flowering, anthesis).
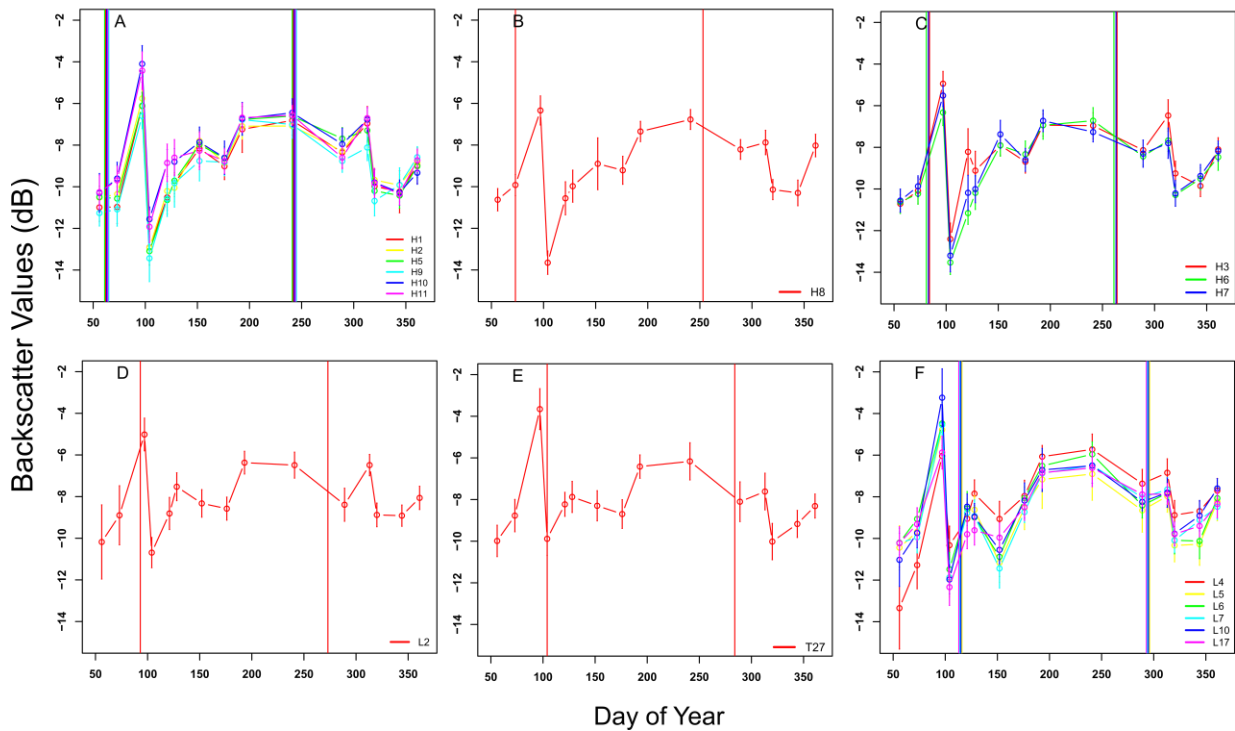
Figure 6.26: A plot of the Sentinel-1 (S-1) descending mode backscatter values for the 18 ADC Olngatongo maize fields analyzed for the 2015 cropping season grouped according to the planting dates a) 2/3-6/3 b) 14/3, c) 22/3-25/3, d) 3/4, e) 14/4, f) 23/4-26/4. The vertical lines indicate the planting and end of growth period for the maize in the fields.

The phenological characteristics from the S-1 descending mode backscatter values graphs grouped according to the planting dates were observed (**Figure 6.26**). The greatest infield variability in the individual fields backscatter values occurred in F) during day of year 150. This coincided with the later part of the BBCH principal growth stage 3 (stem elongation).

(**Figure 6.27**) groups the results of the TSX ascending mode backscatter values according to their planting dates. The phenological characteristics for all the graphs could be identified. The greatest field variability in the backscatter values was observed in F) where the field L10 backscatter values stood out from the rest.
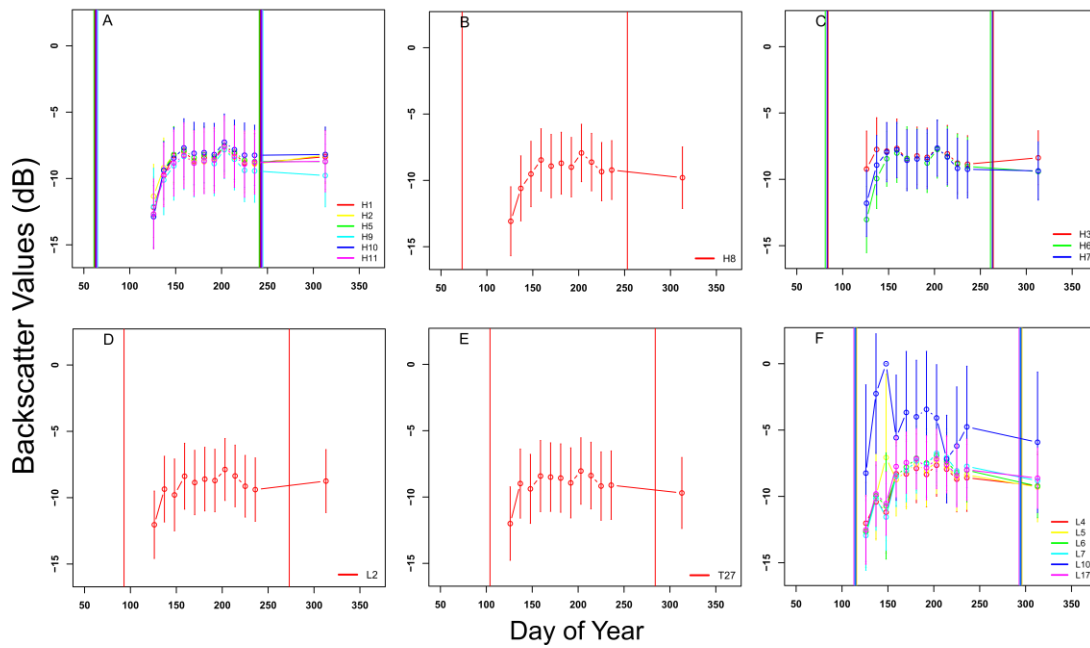
Figure 6.27: A plot of the TerrasSAR-X (TSX) ascending mode backscatter values for the 18 ADC Olngatongo maize fields analyzed for the 2015 cropping season grouped according to the planting dates a) 2/3-6/3 b) 14/3, c) 22/3-25/3, d) 3/4, e) 14/4, f) 23/4-26/4. The vertical lines indicate the planting and end of growth period for the maize in the fields.
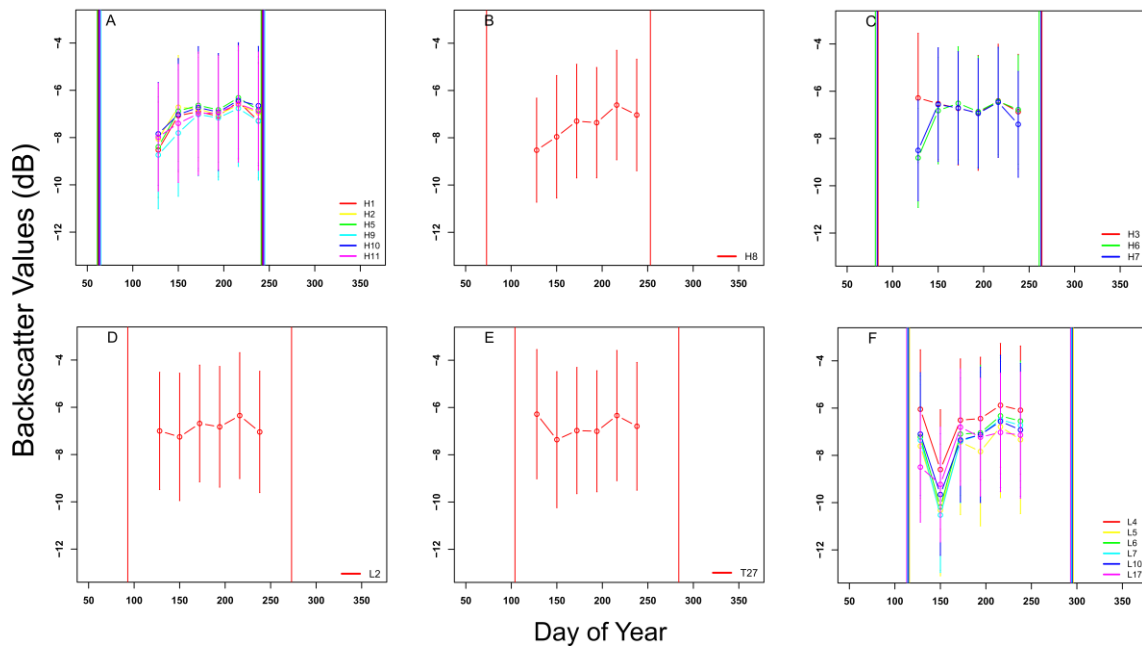
Figure 6.28: A plot of the TerrasSAR-X (TSX) descending mode backscatter values for the 18 ADC Olngatongo maize fields analyzed for the 2015 cropping season grouped according to the planting dates a) 2/3-6/3 b) 14/3, c) 22/3-25/3, d) 3/4, e) 14/4, f) 23/4-26/4. The vertical lines indicate the planting and end of growth period for the maize in the fields.

The phenological characteristics from the TSX descending mode backscatter values graphs grouped according to the planting dates were observed (**Figure 6.28**). The greatest infield variability in the individual fields backscatter values occurred again in F) during day of year 150, which coincided with the later part of the BBCH principal growth stage 3 (stem elongation).

6.3.2.2   Comparison of Sentinel-1 Backscatter Values for 2015 and 2016

The multiplots were divided into three according to the acquisition modes: ascending IW1; descending IW1; descending IW3. These are shown in (**Figures 6.29, 6.30, and 6.31**). The fields H1-H11 had the same maize variety for both years (H6213) whereas fields L2-T27 had the maize variety H628 for 2015, and H614 for 2016. Two sets of vertical lines, one for 2015 and the other for 2016 were utilized to capture the variation in the start and end of the cropping period between the two years.

From (**Figure 6.29**) showing the backscatter values for the ascending IW1, some phenological stages between the 2015 and 2016 backscatter values are comparable, despite the differences in the planting period or the maize variety cultivated. An example is H9 and L10. For fields whose planting dates were not far apart, their backscatter values are comparable (H7, L2, L10). There are also instances where, despite the planting dates being apart, the backscatter values for the two years are still comparable (H9, L17). The number of images available also determined the comparability between the two sets of images. More images were available in 2016 as compared to 2015 and thus time epochs within the growing season lacked images to compare (H7).

For the descending IW1 (**Figure 6.30**), comparison of the two years was limited mainly by the lack of enough images for 2015 for comparison with 2016. The same observation was noted for descending IW3 (**Figure 6.31**). Whereas 2015/2016 backscatter values were comparable for epochs where both sets of images were available, a comparison across the entire cropping season could not be conclusively undertaken.
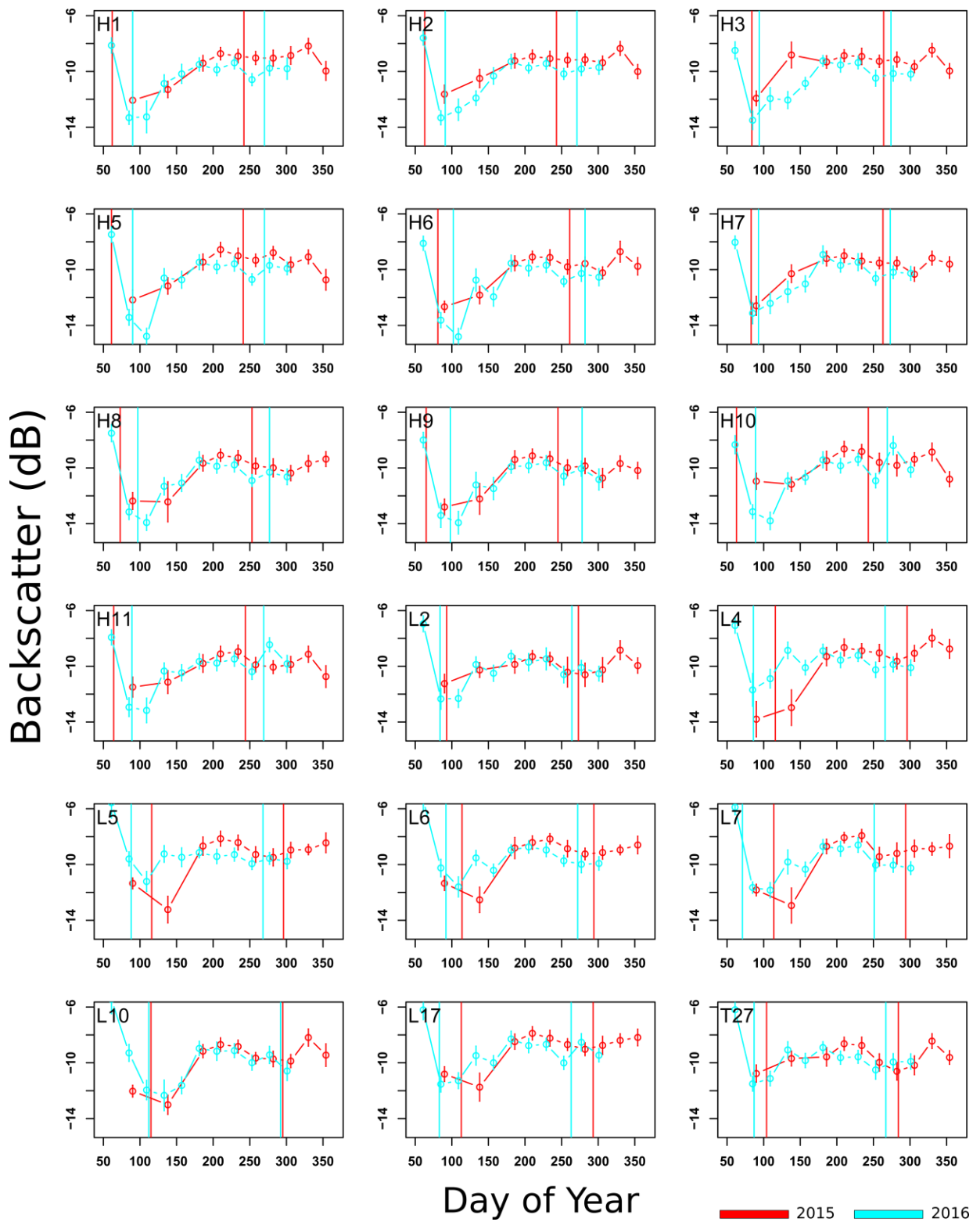
Figure 6.29: A multiplot of the Sentinel-1 (S-1) ascending IW1 mode backscatter values for the 18 ADC Olngatongo maize fields analyzed for the 2015 and 2016 cropping seasons. The vertical lines indicate the planting and end of growth period for the maize in the fields.
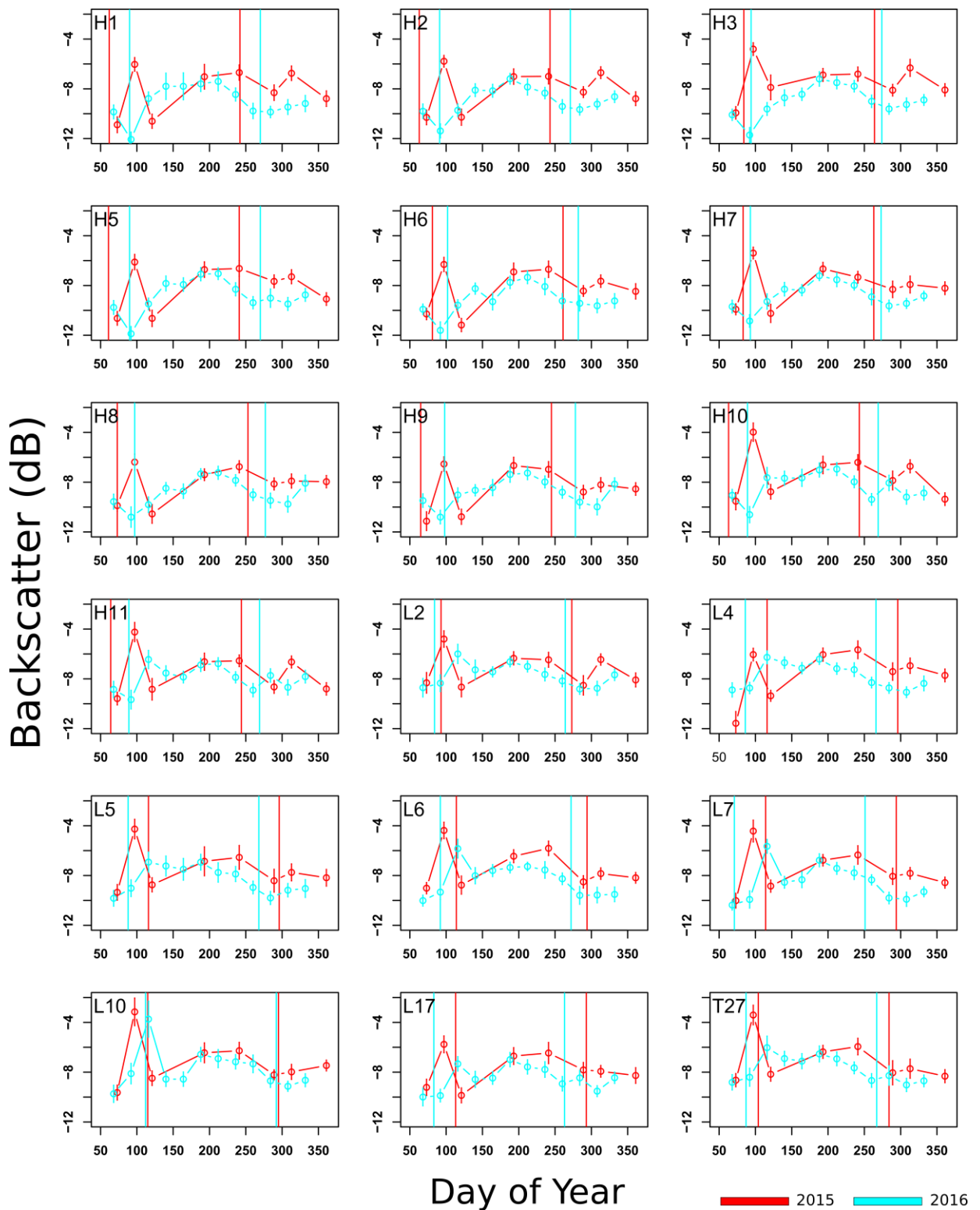
Figure 6.30: A multiplot of the Sentinel-1 (S-1) descending IW1 mode backscatter values for the 18 ADC Olngatongo maize fields analyzed for the 2015 and 2016 cropping seasons. The vertical lines indicate the planting and end of growth period for the maize in the fields.
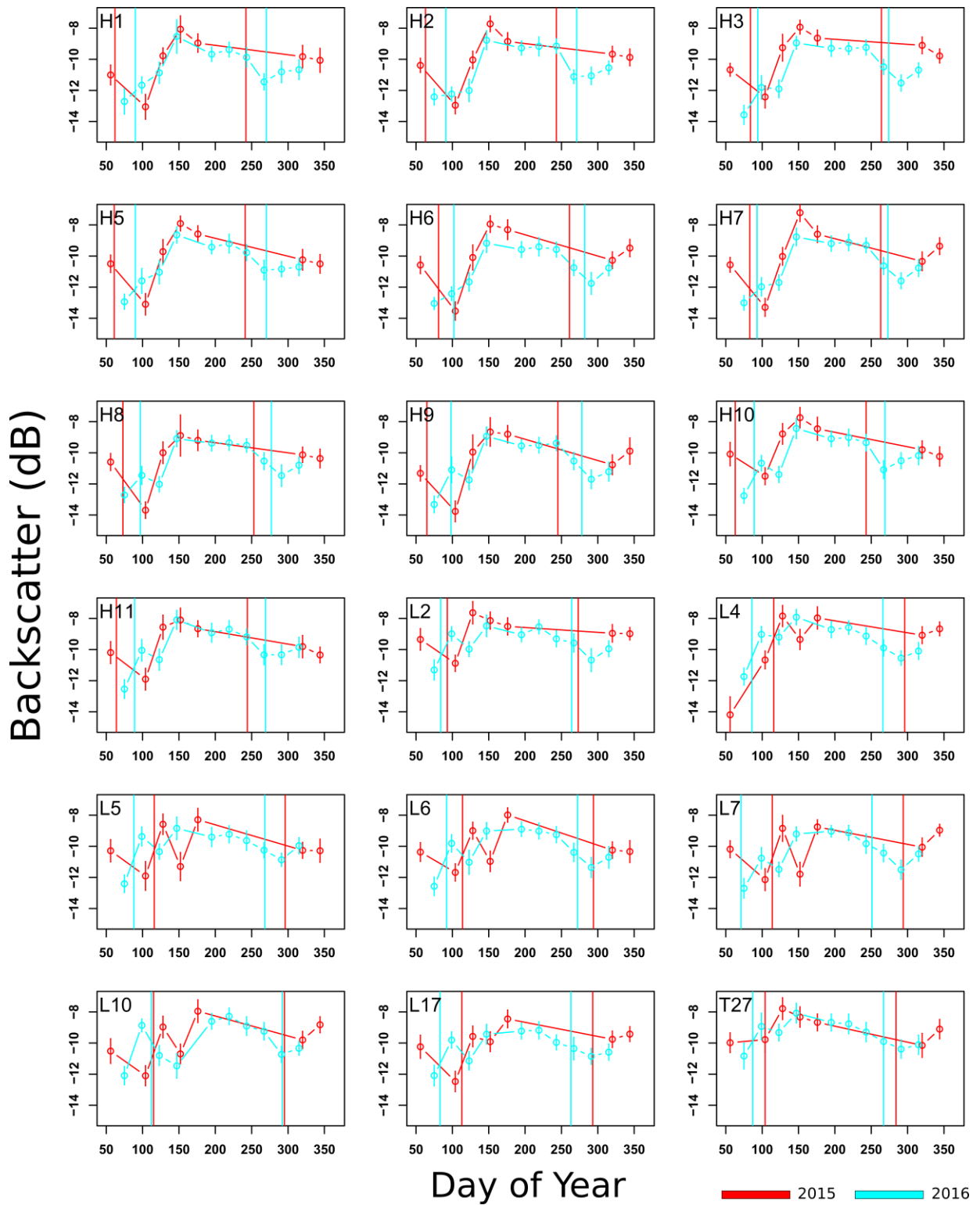
Figure 6.31: A multiplot of the Sentinel-1 (S-1) descending IW3 mode backscatter values for the 18 ADC Olngatongo maize fields analyzed for the 2015 and 2016 cropping seasons. The vertical lines indicate the planting and end of growth period for the maize in the fields.

6.3.2.3 Comparison of Sentinel-1 and TerraSAR-X Backscatter Values for 2015

The mean backscatter values observed ranged from -11.4 dB to -5.7 dB for S-1 with an average standard deviation of 0.7 dB and -10.5 dB to -6.1 dB for TSX with an average standard deviation of 2.5 dB (**Figure 6.32**). These values are similar to those from previous studies (Fieuzal et al., 2012; Thiong'o et al., 2015). The mean backscatter values from the TSX were higher than those from S-1 as the X-band is less penetrative than the C-band (Rowland et al., 2008). However, after the BBCH 6 stage, the S-1 backscatter values became higher than those of TSX in the majority of the fields which can be attributed to the maize canopy volumetric backscatter properties, since the maize canopy had already formed at this stage (Jones & Vaughan, 2010). The maize fields that exhibited the maximum backscatter values for S-1 were in the inflorescence emergence, heading stage (BBCH 5), flowering, anthesis stage (BBCH 6) and ripening stage (BBCH 8). These values were from the fields L2, H7, and L4. H7 had the H6213 planted at an orientation of 80° whereas L2 and L4 had the H628 maize variety planted at an orientation of 45°. TSX maximum backscatter values were from the fields L4 and H3. The H3 field had the H6213 maize variety planted at 80° orientation. The maize was at the leaf development stage (BBCH 1), flowering, anthesis stage (BBCH 6) and ripening stage (BBCH 8). The high backscatter values for both S-1 and TSX were mainly from the increased canopy green leaf area index that had already formed at this stage (Meier, 2001; Paris, 1986). An exception was the high backscatter value during the BBCH 1 stage which could be attributed to soil moisture and texture effects which are known to be significant during the early and end growth stages (Paris, 1986; Ulaby et al., 1984) since the maize leaves were not yet fully developed. The minimum S-1 backscatter values were in the fields H6, L7, H8, and H7 which were at the inflorescence emergence, heading stage (BBCH 5), the development of fruit stage (BBCH 7) and senescence (BBCH 9). The minimum TSX backscatter values were observed in the fields H6, L7, L5 and H7 which were in the inflorescence emergence, heading stage (BBCH 5), the flowering, anthesis stage (BBCH 6) and senescence (BBCH 9). The low mean backscatter values during the BBCH 5 and BBCH 7 stages resulted from the photosynthate that is responsible for plant reproduction process being transferred from the green leaves to the fruit (Paris, 1986), hence a reduction in the leaves backscatter values. The fields H6, H7, and H8 had the H6213 maize variety and were oriented in an 80° direction while the fields L5 and L7 had the H628 maize variety with a 180° orientation. Field L4 exhibited maximum backscatter values for both S-1 and TSX during the periods P3 and P4, while fields H6, L7, and H7 had minimum backscatter values for both S-1 and TSX for the periods P1, P2, and P4 respectively. The maximum and minimum backscatter values were observed from fields' orientations ranging from 45° to 80° respectively. These fields had their satellite look direction facing the rows

compared to the fields with a 180° orientation where the satellite look direction was along the rows (Jones & Vaughan, 2010). Since the surface soil moisture and texture effect on the backscatter values are significant during the early and end growth stages prior to harvesting compared to the leafing period (Paris, 1986; Ulaby et al., 1984) the highest mean backscatter values differences between the S-1 and TSX occurred in the 128 day of year in the majority of fields.
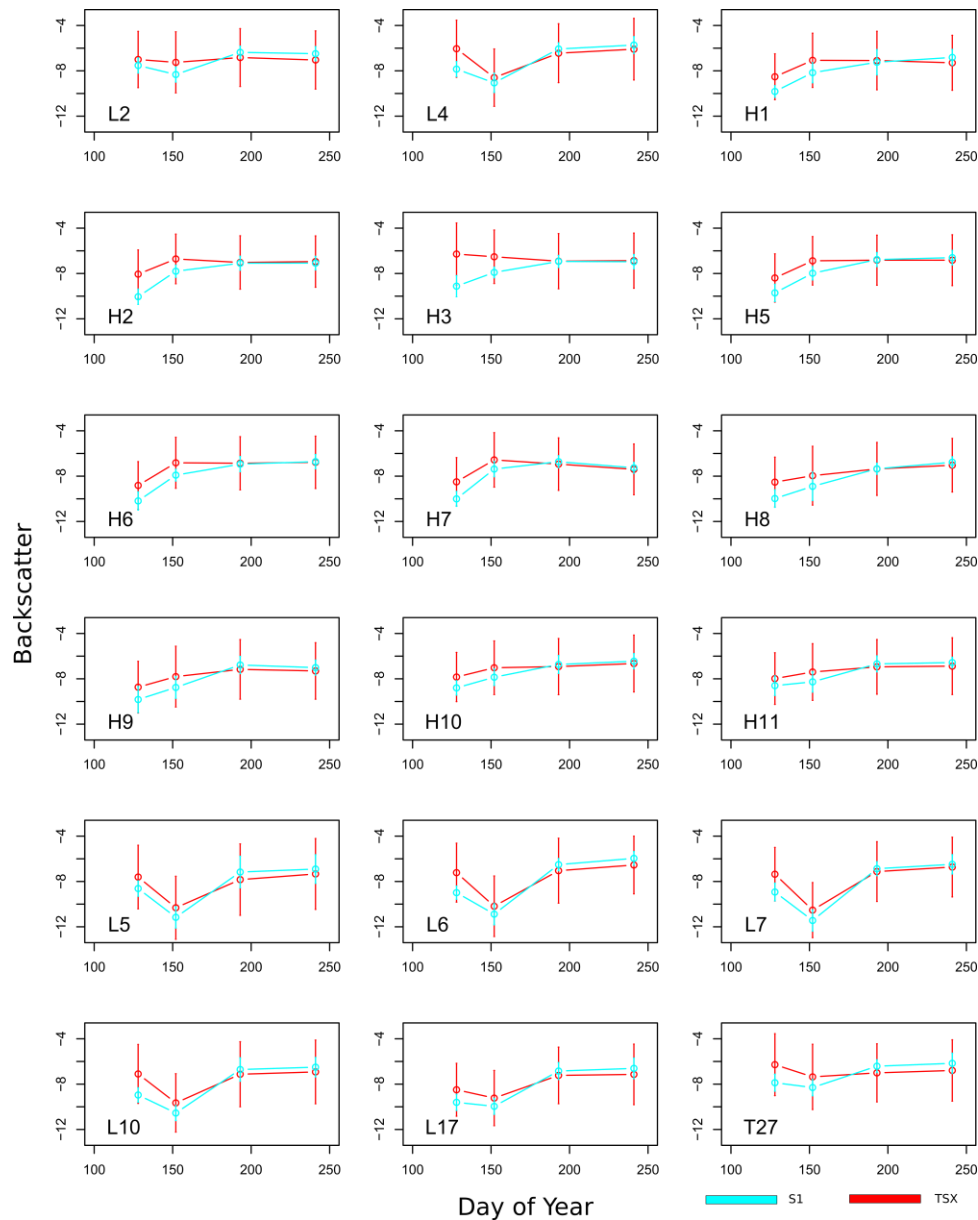
Figure 6.32: A multiplot of the Sentinel-1 (S-1) and TerraSAR-X backscatter values for the 18 ADC Olngatongo maize fields analyzed for the 2015 cropping season. The four sets were P1 (S-1-8/5/2015, TSX-8/5/2015), P2 (S-1-1/6/2015, TSX-30/5/2015), P3 (S-1-12/7/2015, TSX-13/7/2015), and P4 (S-1-29/8/2015, TSX-26/8/2015). The selection of the S-1-TSX image pairs was done such that the dates between any image set had to be three days or less, the image sets had to have similar acquisition modes (ascending or descending), and the difference in the incidence angles between any set of images had to be 10° or less.

7. Discussion

7.1 Mapping of the Maize Fields

Field-based representation is most appropriate for mapping agricultural land cover due to the distinct parcel structure with pure spectral responses away from the boundaries (Dean & Smith, 2003). The limitation of the field-based mapping however is that, it is heavily dependent on the field boundaries which need to be acquired prior to the start of such classification or mapping, and depending on the boundary acquisition time datasets collection, there may exist a mismatch between the datasets (Wu et al., 2007). The failure to adequately measure land not only limits the ability to analyse the actual agricultural impact on the economy but also leads to potentially biased estimates of the relationship between land and productivity (Burke & Lobell, 2017; Carletto et al., 2015). Satellite based data is relied upon to provide estimations of land areas necessary for statistics computations, at both global and regional scales (FAO, 2017). Mapping of agriculture fields with high resolution images has been reported to provide a fast, accurate and cost effective means of approximation of agriculture field sizes and areas (Lussem et al., 2016; McNairn et al., 2009). The digitization of the agriculture fields within the study area from the RE and TSX images produced an up to date map for the ADC farms. On average, farmers tend to overestimate land area (Burke & Lobell, 2017; Carletto et al., 2015), with large fields tending to be underestimated, and small fields being overestimated (De Groote & Traoré, 2005). From the selected study fields, 38% showed similar areas between the satellites estimated areas, and the reported areas recorded by the farmers. However, 33% of the fields' areas were overestimated while the remaining 29% were underestimated. This was attributed to the fact that, despite the change in the field boundaries and sizes through the subdivision or merging of some of the fields over the years, the areas in the records had not been updated in order to indicate the change in the field sizes. Another contributing factor to the large difference between the estimated and reported field sizes was that, some of the fields were only partially planted with maize; with the other part left either uncultivated or planted with another crop. However, the area again recorded was that of the whole field and not the planted area. Moreover, provison of subsidies by the government to the farmers in form of maize seeds and farm inputs (fertilizer, herbicides), may also influence the farmers in overestimating their land sizes, whereas the need to report high yield production per field may on the other hand influence the farmers in underestimating their land sizes (Parry et al., 1988b).

7.2   Classification of the Agriculture Fields

In addition to the manual digitization of the field boundaries, the segmentation of the satellite images successfully extracted the field boundaries within the study area. In some cases, the field boundaries results from the segmentation matched with the observed ground field boundaries while in other cases it did not. In instances where there was a difference in the images reflectance and backscatter values between adjacent fields and fields next to each other, the segmentation field boundaries coincided with the observed ground field boundaries. In other instances, where neighboring fields had similar cultivated crop types, and were therefore at the same phenological growth stage, the segmentation algorithm merged the fields into one. This could be attributed to the fact that since the algorithm's identification of the homogeneous segments within the images relies on the reflectance and backscatter values (Mather & Koch, 2011), the segmentation algorithm could not identify the artificial field boundaries, which are in most cases demarcated by a fence or pathways.

The approaches of combining radar images from two or more acquisition dates (Dusseux et al., 2014; Mahmoud et al., 2011; Sonobe et al., 2014), or the combination of optical and radar images (Burini et al., 2008; Löhnertz et al., 2006; Lussem et al., 2016; Sabour et al., 2008), have shown improvements in the classification results. Although the maize classification accuracy results achieved in this study after combining the TSX and RE images (user accuracy 63%, producer accuracy 80%), and combining the TSX, RE and RE-NDVIre images (user accuracy 72%, producer accuracy 89%) were comparable to the results from the previous studies (Dusseux et al., 2014; Hütt et al., 2016), the overall accuracy achieved was lower. The overall accuracy for the TSX and RE images was 76% and that of the TSX, RE and RE-NDVIre images was 83%. The difference in the achieved overall accuracies from previous studies and this study is, whereas the previous studies were carried out mainly in homogeneous agricultural landscapes, the study site in this research was located in a heterogeneous landscape and thus a misclassification of some of the land cover classes. In addition, the classification of heterogeneous agricultural areas often gets more challenging due to highly similar spectral signatures of different crop types. Thus combining of the crop phenology information has been proposed as a technique for selection of specific satellite images where the differences in the crop phenological cycles would be detectable (Bargiel, 2017; Gerstmann et al., 2015). Some of the previous studies have also proposed the application of a crop mask before the classification of the images in identifying the agricultural land while leaving out the non-agricultural land (Forkuor et al., 2014; Lebourgeois et al., 2017; Richard et al., 2017). Incidences of misclassification would be reduced and hence improve the overall accuracy.

7.3 Maize Growth Monitoring and Phenology Assessment

7.3.1 Monitoring of Maize with Optical Images

7.3.1.1 Sentinel-2 LAI and Modeled LAI

The LAI remains one of the major biophysical parameters in indicating crop growth status and condition (Reichenau et al., 2016). Its accurate estimation provides reliable estimates of the yields at the end of any crop growing season (Ruiz et al., 2004). Crop models for example APSIM (McCown et al., 1996) and DSSAT (Jones et al., 2003) provide a means for best estimating the LAI and the expected yield. The reliability of the model output is however dependent on the accuracy in the calibration of the model. Some of the basic input model parameters required for the calibration and parameterization include the meteorological data, soil data, and management data (Jones et al., 2003). Due to the technical and financial challenges in collecting all this data from the study area, coupled with the fact that there is no single model that has proven satisfactory in all simulation conditions Ruiz et al., (2004), LAI measurements are either alternatively directly measured from the field or indirectly inferred to from remote sensing data (Baret et al., 2014). In this study, maize LAI was measured directly from the fields at given times during the 2015 cropping season. The measurements were then used to model the LAI over the entire cropping season based on an intensive LAI modeling study that had been undertaken in the area of study by Cooper (1979), an approach described in (**Chapter 3.3.3.4.2**). The model LAI results (**Chapter 3.3.3.4.3**) were checked and validated with LAI results derived from S-2 images in 2016 (**Figure 6.10**). An R^2 of 0.54 (RMSE 0.31) was achieved, an improvement to a previous study carried out by Richter et al., (2009) where S-2 LAI was compared to results from a radiative transfer model (R^2 0.35, RMSE 0.43). Vuolo et al. (2016) however achieved better results (R2=0.83) and a RMSE of 0.32 when the LAI values for sugarbeet, maize, onion, potatoes, and winter cereals, measured with a Licor LAI-2200 Plant Canopy Analyzer, were compared with those derived from the S-2 images. It was however noted that, whereas the S-2 LAI data points in their research were distributed across the entire cropping season, the majority of the validation points for this study from the S-2 LAI were available towards the end of the cropping season. The maize had attained LAI values above 2 m^2/m^2, and were thus considered already developed (Nguy-Robertson et al., 2012). This lack of evenly distributed data points was due to lack of cloud free images during the early stages of the maize growth, characterized by regular rainfall and thus high cloud occurrence.

7.3.1.2 LAI vs. Vegetation Indices (VIs)

The VIs are qualitative and quantitative measurements that indicate the vegetation vigor (Bannari et al., 1995) and thus can be correlated to the LAI in monitoring the maize growth condition (Nguy-Robertson et al., 2012). Four VIs, namely the EVI2, SAVI, NDVI and gNDVI were selected. Schmidt et al (2015) proposed combining various optical sensor images in order to increase the number of images available for the entire cropping season. Thus, in this study RE images (3 acquisition epochs) and LS-8 images (9 acquisition epochs) for the 2015 cropping season were combined to facilitate a meaningful assessment of the maize phenological conditions. Despite the combination of the RE and LS-8 images, cloud free images were only available in the later stages of the maize cropping season. This is as evidenced in the plot of LAI against the VIs (**Figure 6.11**) whereby the majority of the sample points are towards the higher LAI values. The line of best fit produced linear response models with R^2 values of 0.88 (0.07 RMSE), 0.81 (0.09 RMSE), 0.8 (0.07 RMSE), and 0.82 (0.04 RMSE) being achieved for EVI2, SAVI, NDVI and gNDVI respectively. Though the linear models achieved high accuracy levels, the correlation between the LAI and the VIs deviated from the conventional exponential model fits (Kross et al., 2015; Nguy-Robertson et al., 2012) due to the lack of cloud free images during the early maize growth stages. Thus, no sampling points were available from the images during this period.

7.3.2 Monitoring of Maize with Radar Images

The backscatter (BS) values analysis was carried out in threefold: the analysis of the TSX and S-1 BS values separately; comparison of the 2015 and 2016 S-1 BS values; comparison of TSX and S-1 BS values.

7.3.2.1 Analysis of the Backscatter Values from the Maize Fields

Crop monitoring during the early growth stages has always been a challenge due to the unavailability of cloud free optical images (McNairn et al., 2014). Radar images are however, independent of prevailing weather conditions and can therefore complement the optical images. The S-1 and TSX radar images were therefore included in the study, to complement the optical images in monitoring the maize growth for the entire cropping season. 18 ADC Olngatongo maize fields were analyzed for this study in order to establish their relationship with the image BS values. The fields were grouped according to the cultivated maize varieties, the orientation angles and the planting dates. Of the three factors, the orientation angle appeared to influence the backscatter the most. The maximum and minimum backscatter values were both observed from fields' orientations ranging from 45° to 80°. These fields had their satellite look direction facing the rows compared to the fields with a 180° orientation where

the satellite look direction was along the rows (Jones & Vaughan, 2010). Grouping of the images according to the planting dates assisted in visualizing the numbers of visible growth stages, as they were dependent on the planting dates of the maize fields. The effect of the various maize varieties appeared to be negligible since there were no visible differences.

7.3.2.2   Comparison of Sentinel-1 Backscatter Values for 2015 and 2016

The capability of comparing the maize phenological characteristics from one year to the next with S-1 data was investigated. The images were available in ascending IW1, descending IW1, and descending IW3. From the results (**Figures 6.29, 6.30, and 6.31**), the VV ascending IW1 mode produced the best results. Notably, this also had the highest number of images for both 2015 and 2016. Thus, the limitation occasioned by the unavailability of adequate S-1 images in 2015 to match the 2016 acquisitions rendered the outcome inconclusive. Comparing the maize varieties cultivated for the two seasons (H6213 for both years; and H628 for 2015 and H614 for 2016), the backscatter values were found to be independent of the maize varieties planted. The backscatter values were rather influenced by the planting dates for the two years. For fields whose planting dates were not far apart, their backscatter values were comparable, compared to fields whose planting dates were far apart. Examples are the fields H7, L2, and L10. The maize phenological stages could also be detected from the backscatter values for the two years. This was the case for even fields with a difference in the 2015 and 2016 planting dates. As long as the maize crops were at similar phenological development stages for the two years, then their backscatter values were comparable. An example is the fields H9 and L10.

7.3.2.3   Comparison of Sentinel-1 and TerraSAR-X Backscatter Values for 2015

The backscatter values increased during the rapid growth stages, before saturating at around BBCH 7, and remained minimally unchanged until the end of the growing season (**Figure 6.32**). This observation is a characteristic of broad leafed crops like maize (Moran et al., 2012; Soria-Ruiz et al., 2009). The phenological stages were identifiable from the image backscatter values, with either a sudden increase or decrease in the backscatter values at the main growth stages, as described by the BBCH scale. The sudden increases and decreases were greater in the S-1 images in comparison to the TSX images. This was due to higher penetrative capability of the S-1-C band compared to the TSX-X band. Thus the S-1 could better detect the changes in the plant structure from one phenological stage to the next (Rowland et al., 2008). However, after around the BBCH 6 stage, the S-1 backscatter values were generally higher than those of TSX in the majority of the fields which was attributed to the maize canopy volumetric

backscatter properties as the maize canopy had already fully formed at this stage (Jones & Vaughan, 2010; Meier, 2001; Paris, 1986). The low mean backscatter values during the BBCH 6 stage resulted from the photosynthate that is responsible for plant reproduction process being transferred from the green leaves to the fruit (Paris, 1986). The variation and dispersion in the fields backscatter values was greatest at the beginning and end of the seasons. This was attributed to the surface soil moisture and texture effect on the backscatter values that are significant during the early and end growth stages prior to harvesting compared to the leafing period (Paris, 1986; Ulaby et al., 1984).

7.4   Integration of Research Findings into Policy Advise

Policy formulation is a continuous process, which requires constant review in order to support foreseen challenges (Alila & Atieno, 2006). An immediate area of concern is the accurate estimation of land acreage under cultivation in any one cropping season. This would assist in forecasting the expected maize yield at the end of a cropping season and in turn inform the government on the necessary and timely steps to take towards ensuring a food secure nation (Parry et al., 1988b; Stewart & Faught, 1984). Approximately 62% of the selected fields in this study had their sizes either overestimated or underestimated. Estimation of the field sizes from satellite images provided a fast and cost effective method of acreage estimation in comparison to the conventional land survey methods (Burke & Lobell, 2017). Some of the decisions for which accurate acreage estimations is necessary include: provision of subsidy to farmers in terms of seeds and fertilizer (Parry et al., 1988b); determination of the maize buying price from the farmers (Kirimi, 2012); availing of funds for maize importation in case of a shortfall, or purchase of the extra produced maize in case of overproduction (Timmer et al., 1983).

Lack of data and information to support policy formulation in the agriculture sector in order to advise the policy decision makers in a timely and accurate manner has been noted as one of the challenges (Timmer et al., 1983; Waswa & Juma, 2012). Remote sensing data has unfortunately most of the time being associated with high costs in terms of acquisition, processing or storage. However, with the increase in the number of freely available high-resolution optical and radar satellite images, and with a high repeat cycle, agriculture fields can be mapped, and crops monitored for the entire cropping season. In this study, the performance of the freely available S-2 and L-8 optical images and the Sl-1 radar image were compared with the commercial RE optical images and TSX radar images. From the results, the performance of the freely available satellites is comparable to that of the commercial satellites. They can therefore provide information on crop monitoring. An additional advantage with the radar images is that they accurately captured the crop information even during the rainy season, when most of the

agriculture fields are rendered inaccessible. The phenological analysis of the backscatter values provides a tool that can be implemented in the monitoring and evaluation of the maize fields, an area in which an existing policy gap has been identified.

Food insecurity continues to be prevalent in the country mainly due to the unpredictable weather patterns that disturb the largely rain fed agriculture by altering the beginning of the cropping season (Dixit et al., 2011). Thus, investing in water harvesting technology, and formulation of policies geared towards water management reforms and technology, would ease the pressure currently on rain-fed agriculture (Rosegrant et al., 2002). This shift from overreliance on rainfed agriculture would however rely greatly on the availability of relevant and up to date agriculture data such as that provided by the results of this study.

8. Conclusions

8.1   Synopsis

Remote sensing techniques provided a faster and economic method of mapping out the boundaries of the agriculture fields within the study area. The segmentation algorithm developed identified some of the maize fields, especially those that were bordering other crop types. An up to date digital map showing the well-defined field boundaries for both the ADC Sabwani and ADC Olngatongo farms was produced as well.

Combination of the TerraSAR-X, RapidEye, and the NDVIre images produced the highest classification results. Despite the low overall accuracy levels occasioned by the heterogeneity landscape of the study area, the maize fields were identified with a user and producer accuracies of 72% and 89% respectively.

An empirical model was developed to estimate the field maize LAI by considering the physical leaf area measurements from the fields. The results of the model were validated with Sentinel-2 generated LAI product achieving an R^2 value of 0.54 with an RMSE of 0.31. The achieved accuracy results however were influenced by the unavailability of cloud free Sentinel-2 images during the beginning of the season. Thus, most of the validation points were concentrated towards the tail end of the cropping season.

High correlation results were realised between VIs and LAI. However, the unavailability of cloud free images at the beginning of the cropping season presented a challenge in finding the line of best fit for the correlation model. In addition, the consideration of the VIs from the LS-8 implied foregoing the VIs incorporating the RedEdge band.

 From the general universal BBCH scale, a regional detailed BBCH stage identification schema was defined, specific to the maize phenological development cycle within the study area. It considered the duration of the maize cropping season in the study area.

Maize phenological characteristics were successfully mapped with radar images, capturing the entire phenology, from planting to harvesting. Monitoring of the maize crops during growth is possible, facilitating the making of timely interventions.

By comparing the Sentinel-1 information for the 2015 and 2016 cropping seasons, similarities in the maize phenology characteristics were identified. From this data, baseline data for monitoring and evaluation of the maize phenology could be established.

By choosing government affiliated maize fields, it is envisaged that the results and outcomes of this study will demonstrate the importance of remote sensing data, and especially the radar images, in the mapping and monitoring of the agriculture fields. This would then mark a great milestone towards

implementing radar images for consideration in the formulation of policy regarding crop monitoring, and thus food security.

8.2 Outlook

The classification of the study site was done without the masking out of the agricultural land. From the results however, the heterogeneous landscape of the area appeared to influence the accuracies achieved. A classification exercise with the agricultural land masked out would provide better accuracy results.

Previous studies have demonstrated improved yield prediction results when crop growth models and high-resolution remote sensing data are coupled. The results from this study could therefore form a base for maize yield prediction by coupling them with a crop growth model. The next step would therefore be modelling based on the study results. However, the challenge of lack of enough data for the calibration of crop growth model exists.

The maize phenological stages could be identified from the study. The planting and harvesting dates were however taken from the farm management records. Identification and verification of these dates from the backscatter values would be an added advantage.

The study provides evidence and results in support of the implementation of radar data in the formulation of policy towards crop monitoring and food security. However, there is the foreseen challenge of translating the research findings into action points that are easily understood and acceptable by the policy makers.

9. References

Adam, E., Mutanga, O., Odindi, J., & Abdel-Rahman, E. M. (2014). Land-use/cover classification in a heterogeneous coastal landscape using RapidEye imagery: evaluating the performance of random forest and support vector machines classifiers. *International Journal of Remote Sensing*, *35*(10), 3440–3458. https://doi.org/10.1080/01431161.2014.903435

African Union. (2014). *Science, technology and innovation strategy for Africa 2024 (STISA-2024)*. Addis Ababa: African Union Commission.

African Union. (2016, January 12). African Space Policy. Retrieved February 19, 2018, from https://spacekenya.org/2016/01/12/african-space-policy/

Alados, C., Puigdefábregas, J., & Martínez-Fernández, J. (2011). Ecological and socio-economical thresholds of land and plant-community degradation in semi-arid Mediterranean areas of southeastern Spain. *Journal of Arid Environments*, *75*(12), 1368–1376. https://doi.org/10.1016/j.jaridenv.2010.12.004

Ali, M., Montzka, C., Stadler, A., Menz, G., Thonfeld, F., & Vereecken, H. (2015). Estimation and Validation of RapidEye-Based Time-Series of Leaf Area Index for Winter Wheat in the Rur Catchment (Germany). *Remote Sensing*, *7*(3), 2808–2831. https://doi.org/10.3390/rs70302808

Alila, P. O., & Atieno, R. (2006). Agricultural policy in Kenya: Issues and processes. In *A paper for the future agricultures consortium workshop, institute of development studies* (pp. 20–22). Retrieved from http://sh.st/st/787f28ed3e745c14417e4aec27303038/http://www.fao.org/fileadmin/user_upload/fsn/docs/Ag_policy_Kenya.pdf

Allan, A. Y., & Allan, A. Y. (1971). *The influence of agronomic factors on maize yields in Western Kenya with special reference to time of planting*.

Amanullah, M. J. H., Nawab, K., & Ali, A. (2007). Response of specific leaf area (SLA), leaf area index (LAI) and leaf area ratio (LAR) of maize (Zea mays L.) to plant density, rate and timing of nitrogen application. *World Applied Sciences Journal*, *2*(3), 235–243.

Apfelbeck, J., Huigen, M., & Krimly, T. (2007). The importance of spatial, temporal and social scales in integrated modeling; simulating the effects of climatic change on district-and farm-level decision making in the Danube catchment area. In *81st Annual Conference, April* (Vol. 24, p. 2007).

Araya, A., Hoogenboom, G., Luedeling, E., Hadgu, K., Kisekka, I., & Martorano, L. (2015). Assessment of maize growth and yield using crop models under present and future climate in southwestern Ethiopia. *Agricultural and Forest Meteorology*, *214–215*, 252–265. https://doi.org/10.1016/j.agrformet.2015.08.259

Asrar, G. (1989). *Theory and Applications of Optical Remote Sensing*. John Wiley & Sons. Retrieved from http://infoscience.epfl.ch/record/51350

Attema, E., Davidson, M., Snoeij, P., Rommen, B., & Floury, N. (2009a). Sentinel-1 mission overview (p. I-36-I-39). IEEE. https://doi.org/10.1109/IGARSS.2009.5416921

Attema, E., & Ulaby, F. (1978). Vegetation modeled as a water cloud. *Radio Science*, *13*(2), 357–364.

Aubert, M., Baghdadi, N., Zribi, M., Douaoui, A., Loumagne, C., Baup, F., Garrigues, S. (2011). Analysis of TerraSAR-X data sensitivity to bare soil moisture, roughness, composition and soil crust. *Remote Sensing of Environment*, *115*(8), 1801–1810. https://doi.org/10.1016/j.rse.2011.02.021

Baghdadi, N., Boyer, N., Todoroff, P., El Hajj, M., & Bégué, A. (2009). Potential of SAR sensors TerraSAR-X, ASAR/ENVISAT and PALSAR/ALOS for monitoring sugarcane crops on Reunion Island. *Remote Sensing of Environment*, *113*(8), 1724–1738. https://doi.org/10.1016/j.rse.2009.04.005

Bannari, A., Morin, D., Bonn, F., & Huete, A. R. (1995). A review of vegetation indices. *Remote Sensing Reviews*, *13*(1–2), 95–120. https://doi.org/10.1080/02757259509532298

Baret, F., Camacho, F., Fang, H., Garrigues, S., Gobron, N., Lang, M., Martinez, B. (2014). *Global Leaf Area Index Product Validation Good Practices*. Version. Retrieved from http://www.academia.edu/download/43534921/CEOS_Global_LAI_Product_Validation_Good_20160309-7926-k1lbr6.pdf

Bargiel, D. (2017). A new method for crop classification combining time series of radar images and crop phenology information. *Remote Sensing of Environment*, *198*, 369–383. https://doi.org/10.1016/j.rse.2017.06.022

Bargiel, D., Herrmann, S., Lohmann, P., & Sörgel, U. (2010). Land use classification with high-resolution satellite radar for estimating the impacts of land use change on the quality of ecosystem services. *International Archives of the Photogrammetry, Remote Sensing and Spatial Information Sciences:[100 Years ISPRS Advancing Remote Sensing Science, Pt 1] 38 (2010), Nr. 7B*, *38*(7B), 68–73.

Bassu, S., Brisson, N., Durand, J.-L., Boote, K., Lizaso, J., Jones, J., Waha, K. (2014). How do various maize crop models vary in their responses to climate change factors? *Global Change Biology*, *20*(7), 2301–2320. https://doi.org/10.1111/gcb.12520

Battude, M., Al Bitar, A., Morin, D., Cros, J., Huc, M., Marais Sicre, C., Demarez, V. (2016). Estimating maize biomass and yield over large areas using high spatial and temporal resolution Sentinel-2 like remote sensing data. *Remote Sensing of Environment*, *184*, 668–681. https://doi.org/10.1016/j.rse.2016.07.030

Bériaux, E., Lambot, S., & Defourny, P. (2011). Estimating surface-soil moisture for retrieving maize leaf-area index from SAR data. *Canadian Journal of Remote Sensing*, *37*(1), 136–150.

Bernstein, R. (1976). Digital image processing of earth observation sensor data. *IBM Journal of Research and Development*, *20*(1), 40–57.

Beyer, F., Jarmer, T., & Siegmann, B. (2015). Identification of Agricultural Crop Types in Northern Israel using Multitemporal RapidEye Data. *Photogrammetrie - Fernerkundung - Geoinformation*, *2015*(1), 21–32. https://doi.org/10.1127/pfg/2015/0249

Birch, C. J., Hammer, G. L., & Rickert, K. G. (1998). Improved methods for predicting individual leaf area and leaf senescence in maize (Zea mays). *Australian Journal of Agricultural Research*, *49*(2), 249–262. https://doi.org/10.1071/a97010

Bisanda, S., Mwangi, W. M., Verkuijl, H., Moshi, A. J., & Anandajayasekeram, P. (1998). *Adoption of maize production technologies in the southern highlands of Tanzania*. CIMMYT. Retrieved from https://books.google.com/books?hl=en&lr=&id=7SdTpxeLS68C&oi=fnd&pg=PR4&dq=%22of+fe rtilizer+used.+Future+maize+research+should+address+the+problem+of+stalk+borers,+cutworm s,+and%22+%22Finally,+policy+makers+should+continue+to+encourage+and+support+the+priv ate+sector+to+invest+in%22+&ots=O3kxNwsWOW&sig=ASk6xYTYnas4mBcFFEylm58ul_4

Blaes, X., Defourny, P., Wegmuller, U., Della Vecchia, A., Guerriero, L., & Ferrazzoli, P. (2006). C-band polarimetric indexes for maize monitoring based on a validated radiative transfer model. *IEEE Transactions on Geoscience and Remote Sensing*, *44*(4), 791–800. https://doi.org/10.1109/TGRS.2005.860969

Blaschke, T. (Ed.). (2008). *Object-based image analysis: spatial concepts for knowledge-driven remote sensing applications*. Berlin: Springer.

Borowiecki, J., & Filipiak, K. (1992). Wybor lisci wskaznikowych do okreslania powierzchni lisciowej kukurydzy, *100*, 77–85.

Breidenbach, J., Ortiz, S. M., & Reich, M. (2010). Forest monitoring with TerraSAR-X: first results. *European Journal of Forest Research*, *129*(5), 813–823. https://doi.org/10.1007/s10342-009-0318-y

Breiman, L. (2001). Random forests. *Machine Learning*, *45*(1), 5–32.

Breit, H., Fritz, T., Balss, U., Lachaise, M., Niedermeier, A., & Vonavka, M. (2010). TerraSAR-X SAR Processing and Products. *Institute of Electrical & Electronics Engineers (IEEE)*, *48*(2), 727--740. https://doi.org/10.1109/tgrs.2009.2035497

Burini, A., Putignano, C., Del Frate, F., Licciardi, G., Pratola, C., Schiavon, G., & Solimini, D. (2008). TerraSAR-X/SPOT-5 fused images for supervised land cover classification. In *Geoscience and*

Remote Sensing Symposium, 2008. IGARSS 2008. IEEE International (Vol. 5, p. V–373). IEEE. Retrieved from http://ieeexplore.ieee.org/xpls/abs_all.jsp?arnumber=4780106

Burke, M., & Lobell, D. B. (2017). Satellite-based assessment of yield variation and its determinants in smallholder African systems. *Proceedings of the National Academy of Sciences*, *114*(9), 2189–2194.

Cairns, J. E., Sonder, K., Zaidi, P. H., Verhulst, N., Mahuku, G., Babu, R., Prasanna, B. M. (2012). Maize Production in a Changing Climate. In *Advances in Agronomy* (Vol. 114, pp. 1–58). Elsevier. Retrieved from http://linkinghub.elsevier.com/retrieve/pii/B9780123942753000067

Canty, M. J. (2014). Image analysis, classification, and change detection in remote sensing: with algorithms for ENVI/IDL and Python.

Carletto, C., Gourlay, S., & Winters, P. (2015). From Guesstimates to GPStimates: Land Area Measurement and Implications for Agricultural Analysis. *Journal of African Economies*, *24*(5), 593–628. https://doi.org/10.1093/jae/ejv011

Castillejo-González, I. L., López-Granados, F., García-Ferrer, A., Peña-Barragán, J. M., Jurado-Expósito, M., de la Orden, M. S., & González-Audicana, M. (2009). Object- and pixel-based analysis for mapping crops and their agro-environmental associated measures using QuickBird imagery. *Computers and Electronics in Agriculture*, *68*(2), 207–215. https://doi.org/10.1016/j.compag.2009.06.004

Chander, G., Haque, M. O., Sampath, A., Brunn, A., Trosset, G., Hoffmann, D., Anderson, C. (2013). Radiometric and geometric assessment of data from the RapidEye constellation of satellites. *International Journal of Remote Sensing*, *34*(16), 5905–5925. https://doi.org/10.1080/01431161.2013.798877

Chen, J. M., & Black, T. A. (1992). Defining leaf area index for non-flat leaves. *Plant, Cell & Environment*, *15*(4), 421–429.

Chen, J. M., Pavlic, G., Brown, L., Cihlar, J., Leblanc, S. G., White, H. P., Trofymow, J. A. (2002). Derivation and validation of Canada-wide coarse-resolution leaf area index maps using high-

resolution satellite imagery and ground measurements. *Remote Sensing of Environment*, *80*(1), 165–184.

Clevers, J., Kooistra, L., & van den Brande, M. (2017). Using Sentinel-2 Data for Retrieving LAI and Leaf and Canopy Chlorophyll Content of a Potato Crop. *Remote Sensing*, *9*(5), 405. https://doi.org/10.3390/rs9050405

Conrad, C., Dech, S., Dubovyk, O., Fritsch, S., Klein, D., Löw, F., Zeidler, J. (2014). Derivation of temporal windows for accurate crop discrimination in heterogeneous croplands of Uzbekistan using multitemporal RapidEye images. *Computers and Electronics in Agriculture*, *103*, 63–74. https://doi.org/10.1016/j.compag.2014.02.003

Cookmartin, G., Cordey, R., Saich, P., Burgess-Allen, P., Sowter, A., & Quegan, S. (1998). Using Backscattering Models to Define the Limits of Crop Information Recovery from SAR Data. *EUROPEAN SPACE AGENCY-PUBLICATIONS-ESA SP*, *441*, 107–114.

Cooper, P. (1979). The association between altitude, environmental variables, maize growth and yields in Kenya. *The Journal of Agricultural Science*, *93*(03), 635–649.

Cooper, P., D., R., Noguer, M., & M., J. (2013). Climate Change Adaptation Strategies in Sub-Saharan Africa: Foundations for the Future. In B. R. Singh (Ed.), *Climate Change - Realities, Impacts Over Ice Cap, Sea Level and Risks*. InTech. Retrieved from http://www.intechopen.com/books/climate-change-realities-impacts-over-ice-cap-sea-level-and-risks/climate-change-adaptation-strategies-in-sub-saharan-africa-foundations-for-the-future

Cooper, P., Dimes, J., Rao, K. P. C., Shapiro, B., Shiferaw, B., & Twomlow, S. (2008). Coping better with current climatic variability in the rain-fed farming systems of sub-Saharan Africa: An essential first step in adapting to future climate change? *Agriculture, Ecosystems & Environment*, *126*(1–2), 24–35. https://doi.org/10.1016/j.agee.2008.01.007

Cooper, P., & Law, R. (1977). Soil temperature and its association with maize yield variations in the highlands of Kenya. *The Journal of Agricultural Science*, *89*(02), 355–363.

Cooper, P., & Law, R. (1978). Enhanced soil temperature during very early growth and its association with maize development and yield in the Highlands of Kenya. *The Journal of Agricultural Science*, *91*(03), 569–577.

Corbane, C., Baghdadi, N., Descombes, X., Wilson, G., Villeneuve, N., & Petit, M. (2009). Comparative study on the performance of multiparameter SAR data for operational urban areas extraction using textural features. *Geoscience and Remote Sensing Letters, IEEE*, *6*(4), 728–732.

Craig Dobson, M., Ulaby, F. T., & Pierce, L. E. (1995). Land-cover classification and estimation of terrain attributes using synthetic aperture radar. *Remote Sensing of Environment*, *51*(1), 199–214. https://doi.org/10.1016/0034-4257(94)00075-X

Daily Nation. (2017). Destructive army worms invade farms. Retrieved June 9, 2017, from http://www.nation.co.ke/newsplex/army-worm-maize/2718262-3880606-sfbeorz/index.html

Danalatos, N. G., Kosmas, C. S., Driessen, P. M., & Yassoglou, N. (1994). The change in the specific leaf area of maize grown under Mediterranean conditions. *Agronomie*, *14*(7), 433–443.

Darwish, A., Leukert, K., & Reinhardt, W. (2003). Image segmentation for the purpose of object-based classification. In *Geoscience and Remote Sensing Symposium, 2003. IGARSS'03. Proceedings. 2003 IEEE International* (Vol. 3, pp. 2039–2041). Ieee.

Davaasuren, N., & Meesters, H. W. G. (2012). Extent and health of mangroves in Lac Bay Bonaire using satellite data.

De Groote, H., & Traoré, O. (2005). The cost of accuracy in crop area estimation. *Agricultural Systems*, *84*(1), 21–38. https://doi.org/10.1016/j.agsy.2004.06.008

de Zoysa, U. (2015). Planning for Sustainable Futures.

Dean, A. M., & Smith, G. M. (2003). An evaluation of per-parcel land cover mapping using maximum likelihood class probabilities. *International Journal of Remote Sensing*, *24*(14), 2905–2920. https://doi.org/10.1080/01431160210155910

Definiens. (2012). Definiens Imaging, eCognition user guide [Online]. Retrieved from http://www.imperial.ac.uk/media/imperial-college/medicine/facilities/film/Definiens-Developer-User-Guide-XD-2.0.4.pdf

Demarez, V., Duthoit, S., Baret, F., Weiss, M., & Dedieu, G. (2008). Estimation of leaf area and clumping indexes of crops with hemispherical photographs. *Agricultural and Forest Meteorology*, *148*(4), 644–655. https://doi.org/10.1016/j.agrformet.2007.11.015

Devadas, R., Denham, R., & Pringle, M. (2012). Support Vector Machine Classification of Object-based Data for Crop Mapping, Using Multi-temporal Landsat Imagery. *ISPRS Archives*, *39*, B7.

Dewitte, O., Jones, A., Spaargaren, O., Breuning-Madsen, H., Brossard, M., Dampha, A., … Zougmore, R. (2013). Harmonisation of the soil map of Africa at the continental scale. *Geoderma*, *211–212*, 138–153. https://doi.org/10.1016/j.geoderma.2013.07.007

Di Stefano, C., Ferro, V., & Mirabile, S. (2010). Comparison between grain-size analyses using laser diffraction and sedimentation methods. *Biosystems Engineering*, *106*(2), 205–215.

Dimov, D., Kuhn, J., & Conrad, C. (2016). Assessment of Cropping System Diversity in the Fergana Valley through Image Fusion of Landsat 8 and Sentinel-1. *ISPRS Annals of Photogrammetry, Remote Sensing and Spatial Information Sciences*, *III-7*, 173–180. https://doi.org/10.5194/isprsannals-III-7-173-2016

Dixit, P. N., Cooper, P., Dimes, J., & Rao, K. P. (2011). Adding Value to Field-Based Agronomic Research through Climate Risk Assessment: A Case Study of Maize Production in Kitale, Kenya. *Experimental Agriculture*, *47*(02), 317–338. https://doi.org/10.1017/S0014479710000773

Doraiswamy, P. (2004). Crop condition and yield simulations using Landsat and MODIS. *Remote Sensing of Environment*, *92*(4), 548–559. https://doi.org/10.1016/j.rse.2004.05.017

Dowman, I., & Kufoniyi, O. (2010). Policies for applying earth observation in Africa: an ISPRS perspective. *International Archives of the Photogrammetry, Remote Sensing and Spatial Information Science*, *38*(Part 8), 1088–1093.

Drusch, M., Del Bello, U., Carlier, S., Colin, O., Fernandez, V., Gascon, F., Bargellini, P. (2012). Sentinel-2: ESA's Optical High-Resolution Mission for GMES Operational Services. *Remote Sensing of Environment*, *120*, 25–36. https://doi.org/10.1016/j.rse.2011.11.026

Dusseux, P., Corpetti, T., Hubert-Moy, L., & Corgne, S. (2014). Combined Use of Multi-Temporal Optical and Radar Satellite Images for Grassland Monitoring. *Remote Sensing*, *6*(7), 6163–6182. https://doi.org/10.3390/rs6076163

Earth Observation Research Branch Team, & Agriculture and Agri-Food Canada. (2011). Crop Identification and BBCH Staging Manual: SMAP-12 Field Campaign. Retrieved from https://smapvex12.espaceweb.usherbrooke.ca/BBCH_STAGING_MANUAL_CEREALS_CORN. pdf

Edwards, D. C. (1940). A Vegetation Map of Kenya with Particular Reference to Grassland Types. *The Journal of Ecology*, *28*(2), 377. https://doi.org/10.2307/2256235

Eineder, M., Fritz, T., Mittermayer, J., Roth, A., Boerner, E., & Breit, H. (2008). *TerraSAR-X Ground Segment, Basic Product Specification Document*. DTIC Document. Retrieved from http://oai.dtic.mil/oai/oai?verb=getRecord&metadataPrefix=html&identifier=ADA515513

Elshorbagy, A. M. A. (2013). A low-cost rice mapping remote sensing based algorithm. Retrieved from http://dar.aucegypt.edu/handle/10526/3576

Esch, T., Metz, A., Marconcini, M., & Keil, M. (2014). Combined use of multi-seasonal high and medium resolution satellite imagery for parcel-related mapping of cropland and grassland. *International Journal of Applied Earth Observation and Geoinformation*, *28*, 230–237. https://doi.org/10.1016/j.jag.2013.12.007

Evans, J. S., Murphy, M. A., Holden, Z. A., & Cushman, S. A. (2011). Modeling Species Distribution and Change Using Random Forest. In C. A. Drew, Y. F. Wiersma, & F. Huettmann (Eds.), *Predictive Species and Habitat Modeling in Landscape Ecology* (pp. 139–159). New York, NY: Springer New York. https://doi.org/10.1007/978-1-4419-7390-0_8

FAO. (2010). Crop calendar. Retrieved April 12, 2017, from http://www.fao.org/agriculture/seed/cropcalendar/cropcalendar.do

FAO. (2017). *State of Food and Agriculture 2017: leveraging food systems for inclusive rural transformation.* S.l.: FOOD & AGRICULTURE ORGANISATION.

Fernandes, R., Weiss, M., Camacho, F., Berthelot, B., Baret, F., & Duca, R. (2014). Development and assessment of leaf area index algorithms for the Sentinel-2 multispectral imager (pp. 3922–3925). IEEE. https://doi.org/10.1109/IGARSS.2014.6947342

Fieuzal, R., & Baup, F. (2017). Forecast of wheat yield throughout the agricultural season using optical and radar satellite images. *International Journal of Applied Earth Observation and Geoinformation*, *59*, 147–156. https://doi.org/10.1016/j.jag.2017.03.011

Fieuzal, R., Baup, F., & Marais-Sicre, C. (2012). Sensitivity of TerraSAR-X, RADARSAT-2 and ALOS satellite radar data to crop variables.

In *2012 IEEE International Geoscience and Remote Sensing Symposium* (pp. 3740–3743). IEEE. Retrieved from http://ieeexplore.ieee.org/xpls/abs_all.jsp?arnumber=6350504

Fieuzal, R., Marais Sicre, C., & Baup, F. (2017). Estimation of corn yield using multi-temporal optical and radar satellite data and artificial neural networks. *International Journal of Applied Earth Observation and Geoinformation*, *57*, 14–23. https://doi.org/10.1016/j.jag.2016.12.011

Finke, C., Möller, K., Schlink, S., Gerowitt, B., & Isselstein, J. (1999). The environmental impact of maize cultivation in the European Union: Practical options for the improvement of the environmental impact.-Case study Germany.

Fletcher, K., & European Space Agency (Eds.). (2012). *Sentinel-2: ESA's optical high-resolution mission for GMES operational services*. Noordwijk: ESA Communications.

Forkuor, G., Conrad, C., Thiel, M., Ullmann, T., & Zoungrana, E. (2014). Integration of Optical and Synthetic Aperture Radar Imagery for Improving Crop Mapping in Northwestern Benin, West Africa. *Remote Sensing, 6*(7), 6472–6499. https://doi.org/10.3390/rs6076472

Frampton, W. J., Dash, J., Watmough, G., & Milton, E. J. (2013). Evaluating the capabilities of Sentinel-2 for quantitative estimation of biophysical variables in vegetation. *ISPRS Journal of Photogrammetry and Remote Sensing*, *82*, 83–92. https://doi.org/10.1016/j.isprsjprs.2013.04.007

Fritsch, S., Machwitz, M., Ehammer, A., Conrad, C., & Dech, S. (2012). Validation of the collection 5 MODIS FPAR product in a heterogeneous agricultural landscape in arid Uzbekistan using multitemporal RapidEye imagery. *International Journal of Remote Sensing*, *33*(21), 6818–6837. https://doi.org/10.1080/01431161.2012.692834

Fritz, T., & Werninghaus, R. (2007). *TerraSAR-X ground segment level 1b product format specification. Clustert Applied Remote Sensing (CAF), German Aerospace Center (DLR)* (Technical No. TX-GS-DD-3307). German Aerospace Center (DLR). Retrieved from http://www-igm.univ-mlv.fr/~riazano/enseignement/SR-FUSION-COURS/TX-GS-DD-3302_SAR_Basic_Products.pdf

FURP. (1987). *The Fertilizer Use Recommendation Project. Final Report. Annex I: Fertilizer trial documentation (FERDOC).* Min. of Agriculture, Nairobi.

Gachene, C., & Kimaru, G. (2004). *Soil fertility and land productivity. A guide for extension workers in the eastern Africa region. RELMA Technical Handbook Series 30. Nairobi, Kenya RELMA/Sida*. ISBN 9966-896-66-X, 146+ xiv pp.

Gallego, F. J., Kussul, N., Skakun, S., Kravchenko, O., Shelestov, A., & Kussul, O. (2014). Efficiency assessment of using satellite data for crop area estimation in Ukraine. *International Journal of Applied Earth Observation and Geoinformation*, *29*, 22–30. https://doi.org/10.1016/j.jag.2013.12.013

Gao, S., Niu, Z., Huang, N., & Hou, X. (2013). Estimating the Leaf Area Index, height and biomass of maize using HJ-1 and RADARSAT-2. *International Journal of Applied Earth Observation and Geoinformation*, *24*, 1–8. https://doi.org/10.1016/j.jag.2013.02.002

Garrigues, S., Allard, D., Baret, F., & Weiss, M. (2006). Influence of landscape spatial heterogeneity on the non-linear estimation of leaf area index from moderate spatial resolution remote sensing data. *Remote Sensing of Environment*, *105*(4), 286–298. https://doi.org/10.1016/j.rse.2006.07.013

Gerstmann, H., Möller, M., Thürkow, D., & Glaesser, C. (2015). PHENOS–PHENOLOGICAL STRUCTURING TO DETERMINE OPTIMAL ACQUISITION DATES FOR SENTINEL-2 DATA FOR FIELD CROP CLASSIFICATION. Retrieved from http://paradigmaps.geo.uni-halle.de/phenos/sites/default/files/FullPaper_Sentinel4Science_GerstmannMoellerGlaesser_mm_reviewed.pdf

Geudtner, D., Torres, R., Snoeij, P., Davidson, M., & Rommen, B. (2014). Sentinel-1 System capabilities and applications (pp. 1457–1460). IEEE. https://doi.org/10.1109/IGARSS.2014.6946711

Gitelson, A. A., Kaufman, Y. J., & Merzlyak, M. N. (1996). Use of a green channel in remote sensing of global vegetation from EOS-MODIS. *Remote Sensing of Environment*, *58*(3), 289–298. https://doi.org/10.1016/S0034-4257(96)00072-7

Gitelson, A., & Merzlyak, M. N. (1994). Spectral Reflectance Changes Associated with Autumn Senescence of Aesculus hippocastanum L. and Acer platanoides L. Leaves. Spectral Features and Relation to Chlorophyll Estimation. *Journal of Plant Physiology*, *143*(3), 286–292. https://doi.org/10.1016/S0176-1617(11)81633-0

Government of Kenya. (1965). Agriculture Development Corporation Act CAP. 444. Retrieved from http://www.kenyalaw.org/lex//actview.xql?actid=CAP.%20444

Government of Kenya. (2007). *Kenya: Vision 2030*. Government of the Republic of Kenya, Ministry of Planning and National Development and the National Economic and Social Council (NESC), Office of the President. Retrieved from https://books.google.de/books?id=wZYnAQAAIAAJ

Government of Kenya. (2012). Environmental and Social Management Framework for Kenya Agricultural Productivity and Agribusiness Project (KAPAP); and Kenya Adaptation to Climate Change in Arid and Semi-Arid Lands Project (KACCAL).

Guissard, V., Lucau-Danila, C., & Defourny, P. (2005). Crop specific LAI retrieval using optical and radar satellite data for regional crop growth monitoring and modelling. In M. Owe & G. D'Urso (Eds.) (p. 59760S). https://doi.org/10.1117/12.627495

Harrell, D. M., Wilhelm, W. W., & McMaster, G. S. (1998). Scales 2: Computer program to convert among developmental stage scales for corn and small grains. *Agronomy Journal*, *90*(2), 235–238.

Hassan, R. M. (1998). *Maize technology development and transfer: a GIS application for research planning in Kenya*. (International Maize and Wheat Improvement Center & Kenya Agricultural Research Institute, Eds.). Oxon ; New York: Cab International in association with the International Maize and Wheat Improvement Centre and the Kenya Agricultural Research Institute.

Hawkins, R., & Cooper, P. (1981). Growth, development and grain yield of maize. *Experimental Agriculture*, *17*(02), 203–207.

Henrich, V., Götze, E., Jung, A., Sandow, C., Thürkow, D., & Glässer, C. (2009). Development of an Online indices-database: motivation, concept and implementation. *EARSeL Proceedings, EARSeL, Tel Aviv*.

Homolová, L., Malenovskỳ, Z., Hanuš, J., Tomášková, I., Dvořáková, M., & Pokornỳ, R. (2007). Comparaison of different ground techniques to map leaf area index of Norway spruce forest canopy. *YOUNG*, *28*(14), 12–5.

Hosseini, M., McNairn, H., Merzouki, A., & Pacheco, A. (2015). Estimation of Leaf Area Index (LAI) in corn and soybeans using multi-polarization C- and L-band radar data. *Remote Sensing of Environment*, *170*, 77–89. https://doi.org/10.1016/j.rse.2015.09.002

Hütt, C., Koppe, W., Miao, Y., & Bareth, G. (2016). Best Accuracy Land Use/Land Cover (LULC) Classification to Derive Crop Types Using Multitemporal, Multisensor, and Multi-Polarization SAR Satellite Images. *Remote Sensing*, *8*(8), 684. https://doi.org/10.3390/rs8080684

Improved Maize (Zea mays) Variety List From Kenya, Uganda and Tanzania. (n.d.). Retrieved from http://afsta.org/wp-content/uploads/2013/07/AFSTA-MAIZE-TRADED-VARIETIES-IN-KE-UG-TZ.pdf

Inglehart, R. (1997). *Modernization and postmodernization: Cultural, economic, and political change in 43 societies* (Vol. 19). Cambridge Univ Press. Retrieved from

http://journals.cambridge.org/production/action/cjoGetFulltext?fulltextid=6296904

Inoue, Y., Kurosu, T., Maeno, H., Uratsuka, S., Kozu, T., Dabrowska-Zielinska, K., & Qi, J. (2002). Season-long daily measurements of multifrequency (Ka, Ku, X, C, and L) and full-polarization backscatter signatures over paddy rice field and their relationship with biological variables. *Remote Sensing of Environment*, *81*(2–3), 194–204. https://doi.org/10.1016/S0034-4257(01)00343-1

Irons, J. R., Dwyer, J. L., & Barsi, J. A. (2012). The next Landsat satellite: The Landsat Data Continuity Mission. *Landsat Legacy Special Issue*, *122*, 11–21. https://doi.org/10.1016/j.rse.2011.08.026

Jackson, R. D., & Huete, A. R. (1991). Interpreting vegetation indices. *Preventive Veterinary Medicine*, *11*(3), 185–200.

Jaetzold, R., & Schmidt, H. (1982). *Farm management handbook of Kenya* (Vol. 2).

Jayne, T. S., Chamberlin, J., & Headey, D. D. (2014). Land pressures, the evolution of farming systems, and development strategies in Africa: A synthesis. *Food Policy*, *48*, 1–17. https://doi.org/10.1016/j.foodpol.2014.05.014

Jayne, T. S., Chamberlin, J., Traub, L., Sitko, N., Muyanga, M., Yeboah, F. K., … Kachule, R. (2016). Africa's changing farm size distribution patterns: the rise of medium-scale farms. *Agricultural Economics*, *47*(S1), 197–214. https://doi.org/10.1111/agec.12308

Jiang, Z., Huete, A., Didan, K., & Miura, T. (2008). Development of a two-band enhanced vegetation index without a blue band. *Remote Sensing of Environment*, *112*(10), 3833–3845. https://doi.org/10.1016/j.rse.2008.06.006

Jonckheere, I., Fleck, S., Nackaerts, K., Muys, B., Coppin, P., Weiss, M., & Baret, F. (2004). Review of methods for in situ leaf area index determination: Part I. Theories, sensors and hemispherical photography. *Agricultural and Forest Meteorology*, *121*(1–2), 19–35.

Jones, H. G., & Vaughan, R. A. (2010). *Remote sensing of vegetation: principles, techniques, and applications*. Oxford university press.

Jones, J. (2013, July 19). Details on crop information to calibrate crop models for kenya. Retrieved from http://www.yieldgap.org/gygamaps/pdf/Details%20on%20crop%20information%20to%20calibrate%20crop%20models%20for%20Kenya.pdf

Jones, J., Hoogenboom, G., Porter, C. H., Boote, K. J., Batchelor, W. D., Hunt, L. A., Ritchie, J. T. (2003). The DSSAT cropping system model. *European Journal of Agronomy*, *18*(3), 235–265.

Juma, C. (2015). *The new harvest: agricultural innovation in Africa* (Second edition). New York, NY: Oxford University Press.

Kang, Y., Özdoğan, M., Zipper, S. C., Román, M. O., Walker, J., Hong, S. Y., Loheide, S. P. (2016). How Universal Is the Relationship between Remotely Sensed Vegetation Indices and Crop Leaf Area Index? A Global Assessment. *Remote Sensing*, *8*(7), 597. https://doi.org/10.3390/rs8070597

Keating, B., & Wafula, B. (1992). Modelling the fully expanded area of maize leaves. *Field Crops Research*, *29*(2), 163–176.

Kenia. (2013). *The Constitution of Kenya: 2010*. Chief Registrar of the Judiciary.

Kenya, L. O. (1963). *The Constitution of Kenya*. Government Print.

Kenya National Bureau of Statistics. (2015). *Economic Survey 2015*. Retrieved from http://apps.unep.org/redirect.php?file=/.../-Economic_Survey-2015Kenya_EconomicSurvey_2015.pdf.pdf

Kenya National Bureau of Statistics. (2016). *Strategic Plan for Agricultural and Rural Statistics SPARS-KENYA 2015-2022*. KNBS. Retrieved from https://www.knbs.or.ke/download/spars-kenya-2015-2022/

Kenya National Bureau of Statistics. (2017). *Economic Survey 2017* (p. 333). Retrieved from https://www.knbs.or.ke/2017/03/

Khorram, S., Koch, F. H., van der Wiele, C. F., & Nelson, S. A. C. (2012). International Agreements and Policies. In S. Khorram, S. A. C. Nelson, F. H. Koch, & C. F. van der Wiele, *Remote Sensing* (pp. 113–124). Boston, MA: Springer US. https://doi.org/10.1007/978-1-4614-3103-9_7

Khorram, S., van der Wiele, C. F., Koch, F. H., Nelson, S. A. C., & Potts, M. D. (2016). *Principles of Applied Remote Sensing*. Cham: Springer International Publishing. https://doi.org/10.1007/978-3-319-22560-9

Kihara, J., Fatondji, D., Jones, J., Hoogenboom, G., Tabo, R., & Bationo, A. (2012). *Improving Soil Fertility Recommendations in Africa Using the Decision Support System for Agrotechnology Transfer (DSSAT)*. Springer Science & Business Media.

Kimanga, R. (1986). *Rural Land Resources Cover Inventorying and Monitoring: An Evaluation of a Low Leve1 Àerial Photographic Sampling Method*. Retrieved from https://www.google.de/search?q=Epp%2C+H.%2C+Killmayer+A.+and+Peden+D.%2C+KREMU +1983&ie=utf-8&oe=utf-8&client=firefox-b-ab&gfe_rd=cr&dcr=0&ei=vT50WqWnCsvR8gfP-JzwCA

Kipkorir, E. C., Raes, D., Bargerei, R. J., & Mugalavai, E. M. (2007). Evaluation of two risk assessment methods for sowing maize in Kenya. *Agricultural and Forest Meteorology*, *144*(3–4), 193–199. https://doi.org/10.1016/j.agrformet.2007.02.008

Kirimi, L. (2012). History of Kenyan maize production, marketing and policies. *Tegemeo Institute of Agricultural Policy and Development. Nairobi, Kenya*.

Kisaka, M. O., Mucheru-Muna, M., Ngetich, F. K., Mugwe, J. N., Mugendi, D. N., Mairura, F., & Muriuki, J. (2016). Using APSIM-Model as a Decision-Support-Tool for Long-Term Integrated-Nitrogen-Management and Maize Productivity under Semi-Arid Conditions in Kenya. *Experimental Agriculture*, *52*(02), 279–299. https://doi.org/10.1017/S0014479715000095

Koetz, B., Baret, F., Poilvé, H., & Hill, J. (2005). Use of coupled canopy structure dynamic and radiative transfer models to estimate biophysical canopy characteristics. *Remote Sensing of Environment*, *95*(1), 115–124. https://doi.org/10.1016/j.rse.2004.11.017

Korhonen, L., Hadi, Packalen, P., & Rautiainen, M. (2017). Comparison of Sentinel-2 and Landsat 8 in the estimation of boreal forest canopy cover and leaf area index. *Remote Sensing of Environment*, *195*, 259–274. https://doi.org/10.1016/j.rse.2017.03.021

Kottek, M., Grieser, J., Beck, C., Rudolf, B., & Rubel, F. (2006). World Map of the Köppen-Geiger climate classification updated. *Meteorologische Zeitschrift*, *15*(3), 259–263. https://doi.org/10.1127/0941-2948/2006/0130

Krieger, G., Moreira, A., Fiedler, H., Hajnsek, I., Werner, M., Younis, M., & Zink, M. (2007). TanDEM-X: A Satellite Formation for High-Resolution SAR Interferometry. *IEEE Transactions on Geoscience and Remote Sensing*, *45*(11), 3317–3341. https://doi.org/10.1109/TGRS.2007.900693

Kropatsch, W. G., & Strobl, D. (1990). The generation of SAR layover and shadow maps from digital elevation models. *IEEE Transactions on Geoscience and Remote Sensing*, *28*(1), 98–107. https://doi.org/10.1109/36.45752

Kross, A., McNairn, H., Lapen, D., Sunohara, M., & Champagne, C. (2015). Assessment of RapidEye vegetation indices for estimation of leaf area index and biomass in corn and soybean crops. *International Journal of Applied Earth Observation and Geoinformation*, *34*, 235–248. https://doi.org/10.1016/j.jag.2014.08.002

Kumar, K., Suryanarayana Rao, H. P., & Arora, M. K. (2015). Study of water cloud model vegetation descriptors in estimating soil moisture in Solani catchment: Water Cloud Model Vegetation Descriptors. *Hydrological Processes*, *29*(9), 2137–2148. https://doi.org/10.1002/hyp.10344

Lancashire, P. D., Bleiholder, H., Boom, T., Langelüddeke, P., Stauss, R., WEBER, E., & Witzenberger, A. (1991). A uniform decimal code for growth stages of crops and weeds. *Annals of Applied Biology*, *119*(3), 561–601.

Lang, A. (1986). Estimation of leaf area index from transmission of direct sunlight in discontinuous canopies. *Agricultural and Forest Meteorology*, *37*(3), 229–243. https://doi.org/10.1016/0168-1923(86)90033-X

Latorre, C. (2014). Vegetation Field Data and Production of Ground-Based Maps:"25 DE MAYO SITE, LA PAMPA, ARGENTINA" 7TH-9TH FEBRUARY 2014. Retrieved from http://fp7-imagines.eu/media/Documents/ImagineS_RP7.5_FieldCampaign_25Mayo2014_I1.00.pdf

Laurent, V. C. E., Schaepman, M. E., Verhoef, W., Weyermann, J., & Chávez, R. O. (2014). Bayesian object-based estimation of LAI and chlorophyll from a simulated Sentinel-2 top-of-atmosphere radiance image.

Remote Sensing of Environment, *140*, 318–329. https://doi.org/10.1016/j.rse.2013.09.005

Law, R., & Cooper, P. (1976). The effect and importance of soil temperature in determining the early growth rate and final grain yields of maize in Western Kenya. *East African Agricultural and Forestry Journal*, *41*(3), 189–200.

Lebourgeois, V., Dupuy, S., Vintrou, É., Ameline, M., Butler, S., & Bégué, A. (2017). A Combined Random Forest and OBIA Classification Scheme for Mapping Smallholder Agriculture at Different Nomenclature Levels Using Multisource Data (Simulated Sentinel-2 Time Series, VHRS and DEM). *Remote Sensing*, *9*(3), 259. https://doi.org/10.3390/rs9030259

Lemp, D., & Koch, B. (2009). Forest monitoring using TerraSAR-X data—evaluation of processing methods and first results. In *Proceedings of TerraSAR-X science meeting*. Retrieved from http://terrasar-x.dlr.de/papers_sci_meet_3/poster/MTH0384_lemp.pdf

Lewis, J. E., Rowland, J., & Nadeau, A. (1998). Estimating maize production in Kenya using NDVI: Some statistical considerations. *International Journal of Remote Sensing*, *19*(13), 2609–2617. https://doi.org/10.1080/014311698214677

Li, W., Weiss, M., Waldner, F., Defourny, P., Demarez, V., Morin, D., … Baret, F. (2015). A Generic Algorithm to Estimate LAI, FAPAR and FCOVER Variables from SPOT4_HRVIR and Landsat

Sensors: Evaluation of the Consistency and Comparison with Ground Measurements. *Remote Sensing*, *7*(12), 15494–15516. https://doi.org/10.3390/rs71115494

Liaw, A., & Wiener, M. (2002). Classification and regression by randomForest. *R News*, *2*(3), 18–22.

Lillesand, T., Kiefer, R. W., & Chipman, J. (2014). *Remote sensing and image interpretation*. John Wiley & Sons.

Liu, C., Shang, J., Vachon, P. W., & McNair, H. (2012). *Multi-year crop monitoring using polarimetric RADARSAT-2 data* (Scientific Literature No. DRDC Ottawa TR 2012-010) (p. 20). Canada - Ottawa: Defence Research and Development. Retrieved from http://cradpdf.drdc-rddc.gc.ca/PDFS/unc236/p804260_A1b.pdf

Liu, H., Zhao, Z., & Jezek, K. C. (2004). Correction of positional errors and geometric distortions in topographic maps and DEMs using a rigorous SAR simulation technique. *Photogrammetric Engineering & Remote Sensing*, *70*(9), 1031–1042.

Liu, K., Ding, H., Tang, G., Zhu, A.-X., Yang, X., Jiang, S., & Cao, J. (2017). An object-based approach for two-level gully feature mapping using high-resolution DEM and imagery: a case study on hilly loess plateau region, China. *Chinese Geographical Science*, *27*(3), 415–430. https://doi.org/10.1007/s11769-017-0874-x

Lohmann, P., Soergel, U., Tavakkoli, M., Farghaly, D., & others. (2009). Multi-temporal Classification for Crop Discrimination using TerraSAR–X Spotlight images. *Proceedings IntArchPhRS*, *38*. Retrieved from http://www.isprs.org/proceedings/xxxviii/1_4_7-W5/paper/Lohmann-129.pdf

Löhnertz, M., Schlerf, M., & Seeling, S. (2006). Land Cover and Land Use: Description of Vegetation Cover During the Growth Period and Crop Classification with Multitemporal High Resolution SPOT Images. *Proceedings EARSeL SIG*, *2*, 80–88.

López-Dekker, P., Krieger, G., & Moreira, A. (2013). Multistatic Radar Systems. In M. D'Errico (Ed.), *Distributed Space Missions for Earth System Monitoring* (pp. 61–122). New York, NY: Springer New York. https://doi.org/10.1007/978-1-4614-4541-8_2

Louwaars, N. P. (2005). *Impacts of strengthened intellectual property rights on the plant breeding industry in developing countries: a synthesis of five case studies*. Wageningen: Wageningen UR.

Lussem, U., Hütt, C., & Waldhoff, G. (2016). Combined Analysis of Sentinel-1 and RapidEye Data for Improved Crop Type Classification: An Early Season Appraoch for Rapseed and Cereals. *ISPRS - International Archives of the Photogrammetry, Remote Sensing and Spatial Information Sciences*, *XLI-B8*, 959–963. https://doi.org/10.5194/isprsarchives-XLI-B8-959-2016

MacRobert, J., Setimela, P., Gethi, J., & Regasa, M. W. (2014). Maize hybrid seed production manual. Retrieved from http://www.seedsectorplatformkenya.com/files/download/7eee47a4df1fa0e

Mahmoud, A., Elbialy, S., Pradhan, B., & Buchroithner, M. (2011). Field-based landcover classification using TerraSAR-X texture analysis. *Advances in Space Research*, *48*(5), 799–805. https://doi.org/10.1016/j.asr.2011.04.005

Malenovský, Z., Rott, H., Cihlar, J., Schaepman, M. E., García-Santos, G., Fernandes, R., & Berger, M. (2012). Sentinels for science: Potential of Sentinel-1, -2, and -3 missions for scientific observations of ocean, cryosphere, and land. *Remote Sensing of Environment*, *120*, 91–101. https://doi.org/10.1016/j.rse.2011.09.026

Martimort, P., Arino, O., Berger, M., Biasutti, R., Carnicero, B., Del Bello, U., Sy, O. (2007). Sentinel-2 optical high resolution mission for GMES operational services (pp. 2677–2680). IEEE. https://doi.org/10.1109/IGARSS.2007.4423394

Martinez, B., Baret, F., Camacho-de Coca, F., Garcia-Haro, F. J., Verger, A., & Melia, J. (2004). Validation of MSG vegetation products: part I. Field retrieval of LAI and FVC from hemispherical photographs. In M. Owe, G. D'Urso, B. T. Gouweleeuw, & A. M. Jochum (Eds.) (p. 57). https://doi.org/10.1117/12.565491

Mather, P. M., & Koch, M. (2011). *Computer processing of remotely-sensed images: an introduction* (4th ed). Chichester, West Sussex, UK ; Hoboken, NJ: Wiley-Blackwell.

McCown, R. L., Hammer, G. L., Hargreaves, J. N. G., Holzworth, D. P., & Freebairn, D. M. (1996). APSIM: a novel software system for model development, model testing and simulation in agricultural systems research. *Agricultural Systems*, *50*(3), 255–271.

McNairn, H., Kross, A., Lapen, D., Caves, R., & Shang, J. (2014). Early season monitoring of corn and soybeans with TerraSAR-X and RADARSAT-2. *International Journal of Applied Earth Observation and Geoinformation*, *28*, 252–259. https://doi.org/10.1016/j.jag.2013.12.015

McNairn, H., Shang, J., Champagne, C., & Jiao, X. (2009). TerraSAR-X and RADARSAT-2 for crop classification and acreage estimation. In *Geoscience and Remote Sensing Symposium, 2009 IEEE International, IGARSS 2009* (Vol. 2, p. II–898). IEEE.

Retrieved from http://ieeexplore.ieee.org/abstract/document/5418243/

Meier, U. (2001). Growth stages of mono-and dicotyledonous plants. BBCH Monograph. *German Federal Biological Research Centre for Agriculture and Forestry, Berlin*.

Retrieved from http://www.bba.de/veroeff/bbch/bbcheng.pdf

Meier, U., Bleiholder, H., Buhr, L., Feller, C., Hack, H., Hess, M. (2010). Das BBCH-System zur Codierung der phänologischen Entwicklungsstadien von Pflanzen–Geschichte und Veröffentlichungen. *Journal Für Kulturpflanzen*, *61*(2), 41–52.

Mittermayer, J., Prats, P., Piantanida, R., Sauer, S., Guarnieri, A. M., Attema, E. (2010). TOPS Sentinel-1 and TerraSAR-X processor comparison based on simulated data. In *Synthetic Aperture Radar (EUSAR), 2010 8th European Conference on* (pp. 1–4). VDE. Retrieved from http://ieeexplore.ieee.org/xpls/abs_all.jsp?arnumber=5758741

Moeller, M., Glaesser, C., & Birger, J. (2011). Automatic interpolation of phenological phases in Germany. In *Analysis of Multi-temporal Remote Sensing Images (Multi-Temp), 2011 6th International Workshop on the* (pp. 37–40). IEEE. Retrieved from

http://ieeexplore.ieee.org/xpls/abs_all.jsp?arnumber=6005041

Mohd Noor, M. (2013). Assessing complex interactions between human and agro-ecosystem using satellite information. A case study in Katuk Odeyo, Western Kenya.

Mokhtarpour, H., Teh, C. B., Saleh, G., Selamat, A. B., Asadi, M. E., & Kamkar, B. (2010). Non-destructive estimation of maize leaf area, fresh weight, and dry weight using leaf length and leaf width. *Communications in Biometry and Crop Science*, *5*(1), 19–26.

Moore, N., Serafin, L., & Jenkins, L. (2014). Summer crop production guide 2 0 14. NSW Department of Primary Industries.

Retrieved from http://www.dpi.nsw.gov.au/__data/assets/pdf_file/0005/303485/Summer-crop-production-guide-2014.pdf

Moran, M. S., Alonso, L., Moreno, J. F., Cendrero Mateo, M. P., de la Cruz, D. F., & Montoro, A. (2012). A RADARSAT-2 Quad-Polarized Time Series for Monitoring Crop and Soil Conditions in Barrax, Spain. *IEEE Transactions on Geoscience and Remote Sensing*, *50*(4), 1057–1070. https://doi.org/10.1109/TGRS.2011.2166080

Moreira, A., Krieger, G., Hajnsek, I., Hounam, D., Werner, M., Riegger, S., & Settelmeyer, E. (2004). TanDEM-X: a terraSAR-X add-on satellite for single-pass SAR interferometry (Vol. 2, pp. 1000–1003). IEEE. https://doi.org/10.1109/IGARSS.2004.1368578

Motohka, T., Nasahara, K. N., Miyata, A., Mano, M., & Tsuchida, S. (2009). Evaluation of optical satellite remote sensing for rice paddy phenology in monsoon Asia using a continuous in situ dataset. *International Journal of Remote Sensing*, *30*(17), 4343–4357.

https://doi.org/10.1080/01431160802549369

Mróz, M., & Mleczko, M. (2008). Potential of Terrasar-X stripmap data in early and rapid agricultural crops mapping. In *TerraSAR-X Science Team Meeting, DLR–Oberpfaffenhofen, Germany*. Retrieved from http://phoenix.caf.dlr.de/papers_sci_meet_3/paper/LAN0167_mroz.pdf

Muchena, F. N., & Gachene, C. K. K. (1988). Soils of the Highland and Mountainous Areas of Kenya with Special Emphasis on Agricultural Soils. *Mountain Research and Development*, *8*(2/3), 183. https://doi.org/10.2307/3673446

Muñoz, X., Freixenet, J., Cufí, X., & Martí, J. (2003). Strategies for image segmentation combining region and boundary information. *Pattern Recognition Letters*, *24*(1–3), 375–392. https://doi.org/10.1016/S0167-8655(02)00262-3

Murthy, V. R. K. (2004). Crop growth modeling and its applications in agricultural meteorology. *Satellite Remote Sensing and GIS Applications in Agricultural Meteorology. Ed. Sivakumar, MV K*, 235–261.

Mwidau, H. A. (1990). Managing Remote Sensing Technology Transfer And Applications In Kenya (pp. 2337–2340). IEEE. https://doi.org/10.1109/IGARSS.1990.689006

Myint, S. W., Gober, P., Brazel, A., Grossman-Clarke, S., & Weng, Q. (2011). Per-pixel vs. object-based classification of urban land cover extraction using high spatial resolution imagery. *Remote Sensing of Environment*, *115*(5), 1145–1161. https://doi.org/10.1016/j.rse.2010.12.017

Naughton, D., Brunn, A., Czapla-Myers, J., Douglass, S., Thiele, M., Weichelt, H., & Oxfort, M. (2011). Absolute radiometric calibration of the RapidEye multispectral imager using the reflectance-based vicarious calibration method. *Journal of Applied Remote Sensing*, *5*(1), 053544–053544.

Nezry, E. (2014). Adaptive Speckle Filtering in Radar Imagery. In D. Closson, F. Holecz, P. Pasquali, & N. Milisavljević (Eds.), *Land Applications of Radar Remote Sensing*. InTech. https://doi.org/10.5772/58593

Ngome, A. F., Mtei, K. M., Mussgnug, F., & Becker, M. (2012). Management options and soil types differentially affect weeds in maize fields of Kakamega, Western Kenya. *Journal of Agricultural Science and Technology. A*, *2*(1A), 104.

Nguy-Robertson, A., Gitelson, A., Peng, Y., Viña, A., Arkebauer, T., & Rundquist, D. (2012). Green Leaf Area Index Estimation in Maize and Soybean: Combining Vegetation Indices to Achieve Maximal Sensitivity. *Agronomy Journal*, *104*(5), 1336. https://doi.org/10.2134/agronj2012.0065

Nix, H. A. (1983). Minimum data sets for agrotechnology transfer. In *Proceedings of the International Symposium on Minimum Data Sets for Agrotechnology Transfer* (pp. 181–188).

Norman, J. M., & Campbell, G. S. (1989). Canopy structure. In R. W. Pearcy, J. R. Ehleringer, H. A. Mooney, & P. W. Rundel (Eds.), *Plant Physiological Ecology: Field methods and instrumentation* (pp. 301–325). Dordrecht: Springer Netherlands. https://doi.org/10.1007/978-94-009-2221-1_14

NSW Department of Primary Industries. (2017, August 16). Retrieved January 27, 2018, from https://www.dpi.nsw.gov.au/

Nyoro, J. K., Kirimi, L., & Jayne, T. S. (2004). Competitiveness of Kenyan and Ugandan maize production: Challenges for the future. *Nairobi: International Development Collaborative Working Papers KE-TEGEMEO-WP-10, Department of Agricultural Economics, Michigan State University*. Retrieved from http://fsg.afre.msu.edu/kenya/wp9.pdf

O'Callaghan, J., Maende, C., & Wyseure, G. (1994). Modelling the intercropping of maize and beans in Kenya. *Computers and Electronics in Agriculture*, *11*(4), 351–365.

Odendo, M., De Groote, H., & Odongo, O. M. (2001). Assessment Of Farmers' Preferences And Constraints To Maize Production In Moist Midaltitude Zone Of Western Kenya. In *5th International Conference of the African Crop Science Society, Lagos, Nigeria October* (Vol. 2126, p. 2001). Retrieved from

http://www.syngentafoundation.org/__temp/kenya_irma_maize_production.pdf

Odhiambo, J. A., Norton, U., Ashilenje, D., Omondi, E. C., & Norton, J. B. (2015). Weed Dynamics during Transition to Conservation Agriculture in Western Kenya Maize Production. *PLOS ONE*, *10*(8), e0133976. https://doi.org/10.1371/journal.pone.0133976

Ok, A. O., Akar, O., & Gungor, O. (2012). Evaluation of random forest method for agricultural crop classification. *European Journal of Remote Sensing*, *45*(1), 421–432. https://doi.org/10.5721/EuJRS20124535

O'Keeffe, K., New South Wales, & Department of Primary Industries. (2009). *Maize growth & development*. Orange, N.S.W.: NSW Dept. of Primary Industries.

Onyango, O. C. (2009). Decreased row spacing as an option for increasing maize (Zea mays L.) yield in Trans Nzoia district, Kenya. *Journal of Plant Breeding and Crop Science*, *1*(8), 281–283.

Onyatta, J. O., & Huang, P. M. (1999). Chemical speciation and bio availability index of cadmium for selected tropical soils in Kenya. *Geoderma*, *91*(1), 87–101.

Paris, J. F. (1986). The effect of leaf size on the microwave backscattering by corn. *Remote Sensing of Environment*, *19*(1), 81–95.

Parry, M. L., Carter, T. R., & Konijn, N. T. (1988a). Implications for Policy. In *The Impact of Climatic Variations on Agriculture* (pp. 249–270). Springer, Dordrecht. https://doi.org/10.1007/978-94-009-2965-4_10

Parry, M. L., Carter, T. R., & Konijn, N. T. (1988b). *The Impact of Climatic Variations on Agriculture: Volume 2: Assessments in Semi-Arid Regions*.

Retrieved from http://public.eblib.com/choice/publicfullrecord.aspx?p=3102984

Pearce, R. B., Mock, J. J., & Bailey, T. B. (1975). Rapid Method for Estimating Leaf Area Per Plant in Maize 1. *Crop Science*, *15*(5), 691–694.

https://doi.org/10.2135/cropsci1975.0011183X001500050023x

Peel, M. C., Finlayson, B. L., & McMahon, T. A. (2007). Updated world map of the Köppen-Geiger climate classification. *Hydrology and Earth System Sciences Discussions*, *4*(2), 439–473.

Peter, L., Uwe, S., & Dalia, F. (2010). Classification of Agricultural Sites Using Time-Series of High-Resolution Dual-Polarisation TerraSAR – X Spotlight Images. *Stand Alone*, 249–260. https://doi.org/10.3233/978-1-60750-494-8-249

Pfeifer, M., & Gonsamo, A. (2015). Manual to measure and model leaf area index and its spatial variability on local and landscape scale. Retrieved from

http://www.academia.edu/download/38929449/Pfeifer_2015_Protocol_LAI_Measurements_V3.0.pdf

Pflug, B., & Main-Knorn, M. (2014). Validation of atmospheric correction algorithm ATCOR. In A. Comerón, E. I. Kassianov, K. Schäfer, R. H. Picard, K. Stein, & J. D. Gonglewski (Eds.) (p. 92420W). https://doi.org/10.1117/12.2067435

Propastin, P., & Erasmi, S. (2010). A physically based approach to model LAI from MODIS 250m data in a tropical region. *International Journal of Applied Earth Observation and Geoinformation*, *12*(1), 47–59. https://doi.org/10.1016/j.jag.2009.09.013

Ramoelo, A., Skidmore, A. K., Cho, M. A., Schlerf, M., Mathieu, R., & Heitkönig, I. M. A. (2012). Regional estimation of savanna grass nitrogen using the red-edge band of the spaceborne RapidEye sensor. *International Journal of Applied Earth Observation and Geoinformation*, *19*, 151–162. https://doi.org/10.1016/j.jag.2012.05.009

Ransom, J., Palmer, A., Zambezi, B., Mduruma, Z., Waddington, S., Pixley, K., & Jewell, D. (1997). *Maize productivity gains through research and technology dissemination*. CIMMYT.

Ranson, K. J., C. S. T.|Biehl,.L|Bauer,M E. (1985). Sun-view angle effects on reflectance factors of corn canopies. *Remote Sensing of Environment*, *18*(2), 147–161.

RapidEye, A. (2011). Satellite imagery product specifications.

Reichenau, T. G., Korres, W., Montzka, C., Fiener, P., Wilken, F., Stadler, A., Schneider, K. (2016). Spatial Heterogeneity of Leaf Area Index (LAI) and Its Temporal Course on Arable Land: Combining Field Measurements, Remote Sensing and Simulation in a Comprehensive Data Analysis Approach (CDAA). *PLoS ONE*, *11*(7). https://doi.org/10.1371/journal.pone.0158451

Reinartz, P., Müller, R., Schwind, P., Suri, S., & Bamler, R. (2011). Orthorectification of VHR optical satellite data exploiting the geometric accuracy of TerraSAR-X data. *ISPRS Journal of Photogrammetry and Remote Sensing*, *66*(1), 124–132. https://doi.org/10.1016/j.isprsjprs.2010.10.003

Renard, G., & Storr, S. (2014). Maize CRP Annual Report 2013. Retrieved from http://repository.cimmyt.org/xmlui/handle/10883/4083

Richard, K., Abdel-Rahman, E. M., Subramanian, S., Nyasani, J. O., Thiel, M., Jozani, H., Landmann, T. (2017). Maize Cropping Systems Mapping Using RapidEye Observations in Agro-Ecological Landscapes in Kenya. *Sensors*, *17*(11), 2537. https://doi.org/10.3390/s17112537

Richards, J. A. (2013). *Remote Sensing Digital Image Analysis*. Berlin, Heidelberg: Springer Berlin Heidelberg. https://doi.org/10.1007/978-3-642-30062-2

Richter, K., Atzberger, C., Vuolo, F., Weihs, P., & D'Urso, G. (2009). Experimental assessment of the Sentinel-2 band setting for RTM-based LAI retrieval of sugar beet and maize. *Canadian Journal of Remote Sensing*, *35*(3), 230–247. https://doi.org/10.5589/m09-010

Richter, K., Rischbeck, P., Eitzinger, J., Schneider, W., Suppan, F., & Weihs, P. (2008). Plant growth monitoring and potential drought risk assessment by means of Earth observation data. *International Journal of Remote Sensing*, *29*(17–18), 4943–4960. https://doi.org/10.1080/01431160802036268

Richter, R. (1996). A spatially adaptive fast atmospheric correction algorithm. *International Journal of Remote Sensing*, *17*(6), 1201–1214. https://doi.org/10.1080/01431169608949077

Richter, R., & Schläpfer, D. (2005a). Atmospheric/topographic correction for satellite imagery. *DLR Report DLR-IB*, 565-01.

Richter, R., & Schläpfer, D. (2005b). Atmospheric/topographic correction for satellite imagery. *DLR Report DLR-IB*, 565–01.

Rodriguez-Cassola, M., Prats, P., Schulze, D., Tous-Ramon, N., Steinbrecher, U., Marotti, L., Moreira, A. (2012). First Bistatic Spaceborne SAR Experiments With TanDEM-X. *IEEE Geoscience and Remote Sensing Letters*, *9*(1), 33–37. https://doi.org/10.1109/LGRS.2011.2158984

Rohrbach, D. D., Minde, I. J., & Howard, J. (2003). Looking beyond national boundaries: regional harmonization of seed policies, laws and regulations. *Food Policy*, *28*(4), 317–333.

Rosegrant, M. W., Cai, X., & Cline, S. A. (2002). Global water outlook to 2025. *Averting an Impending Crisis. IWMI, Colombo, Sri Lanka*.

Rossi, C., Rodriguez Gonzalez, F., Fritz, T., Yague-Martinez, N., & Eineder, M. (2012). TanDEM-X calibrated Raw DEM generation. *ISPRS Journal of Photogrammetry and Remote Sensing*, *73*, 12–20. https://doi.org/10.1016/j.isprsjprs.2012.05.014

Rouse Jr, J., Haas, R. H., Schell, J. A., & Deering, D. W. (1974). Monitoring vegetation systems in the Great Plains with ERTS.

Rowland, C. S., Balzter, H., Dawson, T. P., Luckman, A., Patenaude, G., & Skinner, L. (2008). Airborne SAR monitoring of tree growth in a coniferous plantation. *International Journal of Remote Sensing*, *29*(13), 3873–3889. https://doi.org/10.1080/01431160801891796

Royo, C., & Villegas, D. (2011). *Field measurements of canopy spectra for biomass assessment of small-grain cereals*. INTECH Open Access Publisher. Retrieved from http://www.intechopen.com/source/pdfs/19066/InTech-Field_measurements_of_canopy_spectra_for_biomass_assessment_of_small_grain_cereals.pdf

Ruiz, J. S., Ordóñez, Y. F., & Ramírez, R. G. (2004). Methodology for prediction of corn yield using remote sensing satellite data in Central Mexico. *Investigaciones Geográficas, Boletín Del Instituto de Geografía, UNAM*, (55), 61–78.

Sabour, S. T., Lohmann, P., & Soergel, U. (2008). Monitoring Agricultural Activities Using Multi-Temporal ASAR ENVISAT Data. *The International Archives of the Photogrammetry, Remote Sensing and Spatial Information Sciences*, *37*, 735–742.

Sanchez, P. A., Denning, G. L., & Nziguheba, G. (2009). The African Green Revolution moves forward. *Food Security*, *1*(1), 37–44. https://doi.org/10.1007/s12571-009-0011-5

Sangoi, L. (2001). Understanding plant density effects on maize growth and development: an important issue to maximize grain yield. *Ciência Rural*, *31*(1), 159–168.

Santos, J. R., Mura, J. C., Kux, H. J. H., Garcia, C. E., Kuntz, S., Brown, I. F., & Pantoja, N. V. (2010). Classification of TerraSAR-X imagery for the characterization of Amazon tropical forests. In *30th EARSeL Symposium: Remote Sensing for Science, Education and Culture, 31 May–03 June 2010* (pp. 329–334). Retrieved from

https://www.researchgate.net/profile/Hermann_Kux/publication/267853891_Classification_of_TerraSAR-

X_Imagery_for_the_Characterization_of_Amazon_Tropical_Forests/links/54916dd20cf214269f2

85b05.pdf

Sapsford, R., & Jupp, V. (2006). *Data collection and analysis*. Sage.

Saseendran, S. A., Ma, L., Nielsen, D. C., Vigil, M. F., & Ahuja, L. R. (2005). Simulating planting date effects on corn production using RZWQM and CERES-Maize models. *Agronomy Journal*, *97*(1), 58–71.

Schmidt, T., Forster, M., Gartner, P., & Kleinschmit, B. (2015). Prediction of NDVI for grassland habitats by fusing RapidEye and Landsat imagery (pp. 1–4). Presented at the Analysis of Multitemporal Remote Sensing Images (Multi-Temp), 2015 8th International Workshop on the, IEEE.

Schuster, C., Förster, M., & Kleinschmit, B. (2012). Testing the red edge channel for improving land-use classifications based on high-resolution multi-spectral satellite data. *International Journal of Remote Sensing*, *33*(17), 5583–5599. https://doi.org/10.1080/01431161.2012.666812

Schwarz, T. (2015). Climate-data. org. *AmbiWeb GmbH: Gernsbach, Germany) Available at Http://Es. Climate-Data. Org/[Verified 15 December 2015]*.

Shang, J., Liu, J., Huffman, T., Qian, B., Pattey, E., Wang, J. (2014). Estimating plant area index for monitoring crop growth dynamics using Landsat-8 and RapidEye images. *Journal of Applied Remote Sensing*, *8*(1), 085196–085196.

Sharifi, R. S., & Namvar, A. (2016). Plant density and intra-row spacing effects on phenology, dry matter accumulation and leaf area index of maize in second cropping. *Biologija*, *62*(1).

Shikin, E. V., & Plis, A. I. (1995). *Handbook on Splines for the User*. CRC Press.

Sonobe, R., Tani, H., Wang, X., Kobayashi, N., Kimura, A., & Shimamura, H. (2014). Application of Multi-temporal TerraSAR-X Data to Map Winter Wheat Planted Areas in Hokkaido, Japan. *Japan Agricultural Research Quarterly: JARQ*, *48*(4), 465–470.

Sonobe, R., Tani, H., Wang, X., Kobayashi, N., & Shimamura, H. (2014). Discrimination of crop types with TerraSAR-X-derived information. *Physics and Chemistry of the Earth, Parts A/B/C*. https://doi.org/10.1016/j.pce.2014.11.001

Soria-Ruiz, J., Fernandez-Ordonez, Y., & McNair, H. (2009). Corn Monitoring and Crop Yield Using Optical and Microwave Remote Sensing. In P.-G. Peter (Ed.), *Geoscience and Remote Sensing*. InTech. https://doi.org/10.5772/8311

Stewart, J. I., & Faught, W. A. (1984). Response farming of maize and beans at Katumani, Machakos District, Kenya: Recommendations, yield expectations, and economic benefits. *East African Agricultural and Forestry Journal*, *44*, 29–51.

Szulc, P., Piechota, T., Jagla, M., & Kowalski, M. (2015). A comparative analysis of growth in maize (Zea mays L.) hybrids of different genetic profiles depending on type of nitrogen fertilizer and magnesium dose. *Communications in Biometry and Crop Science10*, 73–81.

Tadross, M., Suarez, P., Lotsch, A., Hachigonta, S., Mdoka, M., Unganai, L., Muchinda, M. (2009). Growing-season rainfall and scenarios of future change in southeast Africa: implications for cultivating maize. *Climate Research*, *40*, 147–161. https://doi.org/10.3354/cr00821

Tanase, M. A., Perez-Cabello, F., de la Riva, J., & Santoro, M. (2010). TerraSAR-X Data for Burn Severity Evaluation in Mediterranean Forests on Sloped Terrain. *IEEE Transactions on Geoscience and Remote Sensing*, *48*(2), 917–929. https://doi.org/10.1109/TGRS.2009.2025943

Tapsall, B., Milenov, P., & Tasdemir, K. (2010). *Analysis of RapidEye imagery for annual landcover mapping as an aid to European Union (EU) common agricultural policy*. na. Retrieved from http://www.isprs.org/proceedings/xxxviii/part7/b/pdf/568_XXXVIII-part7B.pdf

Taubenböck, H., Esch, T., Felbier, A., Wiesner, M., Roth, A., & Dech, S. (2012). Monitoring urbanization in mega cities from space. *Remote Sensing of Environment*, *117*, 162–176. https://doi.org/10.1016/j.rse.2011.09.015

Thiong'o, K., Pasternak, R., Kleusberg, A., Thonfeld, F., & Menz, G. (2015). Separability of Dominant Crop Cultures in Southern Germany Using TerraSAR-X Data. *Advances in Remote Sensing*, *04*(02), 97–107. https://doi.org/10.4236/ars.2015.42009

Thornton, P., Bowen, W., Ravelo, A., Wilkens, P., Farmer, G., Brock, J., & Brink, J. (1997). Estimating millet production for famine early warning: an application of crop simulation modelling using satellite and ground-based data in Burkina Faso. *Agricultural and Forest Meteorology*, *83*(1), 95–112.

Tian, Y., Wang, Y., Zhang, Y., Knyazikhin, Y., Bogaert, J., & Myneni, R. B. (2003). Radiative transfer based scaling of LAI retrievals from reflectance data of different resolutions. *Remote Sensing of Environment*, *84*(1), 143–159.

Timmer, C. P., Falcon, W. P., Pearson, S. R., Agriculture, W. B., Economics, R. D. D., & Division, P. (1983). *Food policy analysis* (Vol. 1983). Johns Hopkins University Press Baltimore.

Torres, R., Snoeij, P., Geudtner, D., Bibby, D., Davidson, M., Attema, E., Rostan, F. (2012). GMES Sentinel-1 mission. *Remote Sensing of Environment*, *120*, 9–24. https://doi.org/10.1016/j.rse.2011.05.028

Uddin, K., Shrestha, H. L., Murthy, M. S. R., Bajracharya, B., Shrestha, B., Gilani, H., Dangol, B. (2015). Development of 2010 national land cover database for the Nepal. *Journal of Environmental Management*, *148*, 82–90. https://doi.org/10.1016/j.jenvman.2014.07.047

Ulaby, F., Allen, C., Eger, G., & Kanemasu, E. (1984). Relating the microwave backscattering coefficient to leaf area index. *Remote Sensing of Environment*, *14*(1–3), 113–133.

United Nations. (2017). Hunger and food security. Retrieved December 11, 2017, from http://www.un.org/sustainabledevelopment/hunger/

van Zyl, J. J., Chapman, B. D., Dubois, P., & Shi, J. (1993). The effect of topography on SAR calibration. *IEEE Transactions on Geoscience and Remote Sensing*, *31*(5), 1036–1043. https://doi.org/10.1109/36.263774

Vaudour, E., Moeys, J., Gilliot, J. M., & Coquet, Y. (2008). Spatial retrieval of soil reflectance from SPOT multispectral data using the empirical line method. *International Journal of Remote Sensing*, *29*(19), 5571–5584. https://doi.org/10.1080/01431160802060920

Veloso, A., Mermoz, S., Bouvet, A., Le Toan, T., Planells, M., Dejoux, J.-F., & Ceschia, E. (2017). Understanding the temporal behavior of crops using Sentinel-1 and Sentinel-2-like data for agricultural applications. *Remote Sensing of Environment*, *199*, 415–426. https://doi.org/10.1016/j.rse.2017.07.015

Vinciková, H., Hais, M., Brom, J., Procházka, J., & Pecharová, E. (2010). Use of remote sensing methods in studying agricultural landscapes–. *Journal of Landscape Studies*, *3*, 53–63.

Vuolo, F., Żółtak, M., Pipitone, C., Zappa, L., Wenng, H., Immitzer, M., Atzberger, C. (2016). Data Service Platform for Sentinel-2 Surface Reflectance and Value-Added Products: System Use and Examples. *Remote Sensing*, *8*(11), 938. https://doi.org/10.3390/rs8110938

Wang, Y.-P., Chang, K.-W., Chen, R.-K., Lo, J.-C., & Shen, Y. (2010). Large-area rice yield forecasting using satellite imageries. *International Journal of Applied Earth Observation and Geoinformation*, *12*(1), 27–35. https://doi.org/10.1016/j.jag.2009.09.009

Waske, B., & Braun, M. (2009). Classifier ensembles for land cover mapping using multitemporal SAR imagery. *ISPRS Journal of Photogrammetry and Remote Sensing*, *64*(5), 450–457. https://doi.org/10.1016/j.isprsjprs.2009.01.003

Waswa, P. M., & Juma, C. (2012). Establishing a space sector for sustainable development in Kenya. *International Journal of Technology and Globalisation*, *6*(1–2), 152–169.

Weichelt, H., Rosso, P., Marx, A., Reigber, S., Douglass, K., & Heynen, M. (2011). White Paper–The RapidEye Red Edge Band. *RapidEye White Papers*, 1–6.

Weiss, M., & Baret, F. (2016). S2ToolBox Level 2 products: LAI, FAPAR, FCOVER, *1*(1), 53.

Weiss, M., & Baret, F. (2017). CAN_EYE V6. 4.91 USER MANUAL.

Weiss, M., Baret, F., Smith, G. J., Jonckheere, I., & Coppin, P. (2004). Review of methods for in situ leaf area index (LAI) determination. *Agricultural and Forest Meteorology*, *121*(1–2), 37–53. https://doi.org/10.1016/j.agrformet.2003.08.001

Wilhelm, W. W., Ruwe, K., & Schlemmer, M. R. (2000). Comparison of three leaf area index meters in a corn canopy. *Crop Science*, *40*(4), 1179–1183.

Woodhouse, H. I. (2006). *Introduction to Microwave Remote Sensing*. CRC Press.

Wu, S., Silvánhyphen;Cárdenas, J., & Wang, L. (2007). Per-field urban land use classification based on tax parcel boundaries. *International Journal of Remote Sensing*, *28*(12), 2777–2801. https://doi.org/10.1080/01431160600981541

Wulder, M. A., White, J. C., Goward, S. N., Masek, J. G., Irons, J. R., Herold, M., Woodcock, C. E. (2008). Landsat continuity: Issues and opportunities for land cover monitoring. *Remote Sensing of Environment*, *112*(3), 955–969. https://doi.org/10.1016/j.rse.2007.07.004

Xiong, J., Thenkabail, P. S., Tilton, J. C., Gumma, M. K., Teluguntla, P., Oliphant, A., Gorelick, N. (2017). Nominal 30-m Cropland Extent Map of Continental Africa by Integrating Pixel-Based and Object-Based Algorithms Using Sentinel-2 and Landsat-8 Data on Google Earth Engine. *Remote Sensing*, *9*(10), 1065. https://doi.org/10.3390/rs9101065

Yagüe-Martínez, N., Prats-Iraola, P., González, F. R., Brcic, R., Shau, R., Geudtner, D., Bamler, R. (2016). Interferometric Processing of Sentinel-1 TOPS Data. *IEEE Transactions on Geoscience and Remote Sensing*, *54*(4), 2220–2234. https://doi.org/10.1109/TGRS.2015.2497902

Yin, X., Lantinga, E. A., Schapendonk, A. H., & Zhong, X. (2003). Some quantitative relationships between leaf area index and canopy nitrogen content and distribution. *Annals of Botany*, *91*(7), 893–903.

Young, N. E., Anderson, R. S., Chignell, S. M., Vorster, A. G., Lawrence, R., & Evangelista, P. H. (2017). A survival guide to Landsat preprocessing. *Ecology*, *98*(4), 920–932. https://doi.org/10.1002/ecy.1730

Yousif, N. Z. M., & Abdalla, A. A. I. (2011). The Effect of the Number of Control Points on the Adjusted Satellite Images. *International Journal*.

Zech, W. (2016). Geology and Soils. In L. Pancel & M. Köhl (Eds.), *Tropical Forestry Handbook* (pp. 93–283). Berlin, Heidelberg: Springer Berlin Heidelberg. https://doi.org/10.1007/978-3-642-54601-3_96

Zhang, Y., Chen, J. M., & Miller, J. R. (2005). Determining digital hemispherical photograph exposure for leaf area index estimation. *Agricultural and Forest Meteorology*, *133*(1–4), 166–181. https://doi.org/10.1016/j.agrformet.2005.09.009

Zheng, G., & Moskal, L. M. (2009). Retrieving Leaf Area Index (LAI) Using Remote Sensing: Theories, Methods and Sensors. *Sensors*, *9*(4), 2719–2745. https://doi.org/10.3390/s90402719

Zillmann, E., Schönert, M., Lilienthal, H., Siegmann, B., Jarmer, T., Rosso, P., & Weichelt, T. (2015). Crop Ground Cover Fraction and Canopy Chlorophyll Content Mapping using RapidEye imagery. *ISPRS - International Archives of the Photogrammetry, Remote Sensing and Spatial Information Sciences*, *XL-7/W3*, 149–155. https://doi.org/10.5194/isprsarchives-XL-7-W3-149-2015

Zink, M., Fiedler, H., Hajnsek, I., Krieger, G., Moreira, A., & Werner, M. (2006). The TanDEM-X Mission Concept (pp. 1938–1941). IEEE. https://doi.org/10.1109/IGARSS.2006.501

Appendix (in CD)

A.1 Copy of questionnaire administered to the farmers

A.2 Farm management data
A.2.1 Field Data collected and LAI Simulation Approach
A.2.2 ADC Sabwani fields data
A.2.3 ADC Olngatongo fields data

A.3 Soil data
A.3.1 Collected field soil samples for texture and moisture analysis
A.3.2 Soil carbon/nitrogen analysis results
A.3.3 Soil texture analysis results

A.4 Weather data recorded in the study area for 2015 and 2016

A.1 Copy of questionnaire administered to the farmers

GROUND REFERENCING QUESTIONNAIRE   Date _____

Name of Farmer:	Telephone:
Parcel ID:	BBCH Code::
Observed Land-Cover:	Previous Land-Cover:
Expected yield (in 90 kg bags):	Actual yield (in 90 kg bags):

For Maize record the following:

1) Reason for growing maize

☐ Subsistence   ☐ Sale   ☐ Fodder   ☐ Seed crop

2) What maize variety do you grow?

Variety	Acreage	Row spacing (cm)	Line spacing (cm)

3) Do you practice mono cropping or mixed cropping (farming system)?

☐ Mixed cropping   ☐ Mono-cropping

4) What fertilizers do you use in your farm?

Type	Amount (kg)	Acreage

5) What top dressing do you apply in the farm after planting?

Type of Top Dressing	Acreage

6) What type of pesticide do you apply in your farm?

Type	Amount	Acreage

7) Do you practice irrigation?

☐ Yes   ☐ No

8) Do you carry out any weeding, and how often?

Method	Frequency per planting season
Herbicides	
Manual	

9) How do you harvest your crop?

☐ Manual   ☐ Machine

10) If actual yield is differs from expected yield, what could be the cause?

A.2 Farm management data

A.2.1 Field Data collected and LAI Simulation Approach

field name	culti	Acreage_	Acreage_me	planting	emergence	flowering	bulking onset	physiological ma	harvest	fertilizer	fertilizer am	top dressing	top dressing a	pesticide	pesticide amnt L/ha
ADC Sabwani F1	H62	39.5	32	28/03/2015	04/04/2015	22.06.2015	28.07.2015	15.09.2015		NPK 23:23:0	75 kg	CAN 26% n	100 kg	thunder	0.3
ADC Sabwani F1	H62	39.5	32	28/03/2015	04/04/2015	22.06.2015	28.07.2015	15.09.2015		NPK 23:23:0	75 kg	CAN 26% n	100 kg	thunder	0.3
ADC Sabwani F1	H62	39.5	32	28/03/2015	04/04/2015	22.06.2015	28.07.2015	15.09.2015		NPK 23:23:0	75 kg	CAN 26% n	100 kg	thunder	0.3
ADC Sabwani F2	H62	39.5	36	20/03/2015	31/03/2015	22.06.2015	29.07.2015	15.09.2015		NPK 23:23:0	75 kg	CAN 26% n	100 kg	thunder	0.3
ADC Sabwani F2	H62	39.5	36	20/03/2015	31/03/2015	22.06.2015	29.07.2015	15.09.2015		NPK 23:23:0	75 kg	CAN 26% n	100 kg	thunder	0.3
ADC Sabwani F2	H62	39.5	36	20/03/2015	31/03/2015	22.06.2015	29.07.2015	15.09.2015		NPK 23:23:0	75 kg	CAN 26% n	100 kg	thunder	0.3
ADC Sabwani K5	H62	44.5	55.2	07/03/2015	31/03/2015	22.06.2015	6.07.2015	15.09.2015		NPK 23:23:0	75 kg	CAN 26% n	100 kg	thunder	0.3
ADC Sabwani K5	H62	44.5	55.2	07/03/2015	31/03/2015	22.06.2015	6.07.2015	15.09.2016		NPK 23:23:0	75 kg	CAN 26% n	100 kg	thunder	0.3
ADC Sabwani K5	H62	44.5	55.2	07/03/2015	31/03/2015	22.06.2015	6.07.2015	15.09.2017		NPK 23:23:0	75 kg	CAN 26% n	100 kg	thunder	0.3
ADC Sabwani S2	H62	34.6	29	28/03/2015	04/04/2015	22.06.2015	6.07.2015	15.09.2015		NPK 23:23:0	75 kg	CAN 26% n	100 kg	thunder	0.3
ADC Sabwani S2	H62	34.6	29	28/03/2015	04/04/2015	22.06.2015	6.07.2015	15.09.2015		NPK 23:23:0	75 kg	CAN 26% n	100 kg	thunder	0.3
ADC Sabwani S2	H62	34.6	29	28/03/2015	04/04/2015	22.06.2015	6.07.2015	15.09.2015		NPK 23:23:0	75 kg	CAN 26% n	100 kg	thunder	0.3
ADC Olngatongo H6	H62	38.8	75	22/03/2015	01/04/2015	4.07.2015	15.08.2015	15.09.2015		NPK 23:23:0	75 kg	CAN 26% n	100 kg	thunder	0.3
ADC Olngatongo H6	H62	38.8	43	22/03/2015	01/04/2015	4.07.2015	15.08.2015	15.09.2015		NPK 23:23:0	75 kg	CAN 26% n	100 kg	thunder	0.3
ADC Olngatongo H6	H62	38.8	43	22/03/2015	01/04/2015	4.07.2015	15.08.2015	15.09.2015		NPK 23:23:0	75 kg	CAN 26% n	100 kg	thunder	0.3
ADC Olngatongo L6	H62	25.7	24.7	24/04/2015	04/05/2015	25.07.2015	15.09.2015			NPK 23:23:0	75 kg	CAN 26% n	100 kg	thunder	0.3
ADC Olngatongo L6	H62	25.7	24.7	24/04/2015	04/05/2015	25.07.2015	15.09.2015			NPK 23:23:0	75 kg	CAN 26% n	100 kg	thunder	0.3
ADC Olngatongo L6	H62	25.7	24.7	24/04/2015	04/05/2015	25.07.2015	15.09.2015			NPK 23:23:0	75 kg	CAN 26% n	100 kg	thunder	0.3
ADC Olngatongo L10	H62	25	22	25/04/2015	05/05/2015	25.07.2015	15.09.2015			NPK 23:23:0	75 kg	CAN 26% n	100 kg	thunder	0.3
ADC Olngatongo L10	H62	25	22	25/04/2015	05/05/2015	25.07.2015	15.09.2015			NPK 23:23:0	75 kg	CAN 26% n	100 kg	thunder	0.3
ADC Olngatongo L10	H62	25	22	25/04/2015	05/05/2015	25.07.2015	15.09.2015			NPK 23:23:0	75 kg	CAN 26% n	100 kg	thunder	0.3
Kenya Seed Company X4/1	H61	36		28/04/2015	31/05/2015	june, 2015	july,2015	15.09.2015	15/10/2015	NPK 23:23:0	75 kg	CAN 26% n	100 kg	thunder	0.2 per acre
Kenya Seed Company X4/1	H61	36		28/04/2015	31/05/2015	june, 2015	july,2015	15.09.2015	15/10/2015	NPK 23:23:0	75 kg	CAN 26% n	100 kg	thunder	0.2 per acre
Kenya Seed Company X2/1	H61	39	20	02/04/2015	16/04/2015	17.06.2015	15.07.2015	10.09.2015	05/10/2015	NPK 23:23:0	75 kg	CAN 26% n	100 kg	thunder	0.2 per acre
Kenya Seed Company X2/1	H61	39	20	02/04/2015	16/04/2015	17.06.2015	15.07.2015	10.09.2015	05/10/2015	NPK 23:23:0	75 kg	CAN 26% n	100 kg	thunder	0.2 per acre

field name	herbicides	Herbicide application	weeding	weeding	weeding time	Field_visit_Da	No_of_days_e	plant num	plant num	plant num	plant num	plant no.	planting de	row spa	line spa
ADC Sabwani F1	Twiga Methane& Primagram	pre-emergence	manual	twice		11/06/2015	68	27	29	34	34	31	10.16	75	25
ADC Sabwani F1	Twiga Methane& Primagram	pre-emergence	manual	twice		23/06/2015	80	21	33			27	10.16	75	25
ADC Sabwani F1	Twiga Methane& Primagram	pre-emergence	manual	twice		16/07/2015	103	23	24			24	10.16	75	25
ADC Sabwani F2	Twiga Methane& Primagram	pre-emergence	manual	twice		11/06/2015	72	7	5	12		8	10.16	75	25
ADC Sabwani F2	Twiga Methane& Primagram	pre-emergence	manual	twice		23/06/2015	84	17	10	23		17	10.16	75	25
ADC Sabwani F2	Twiga Methane& Primagram	pre-emergence	manual	twice		16/07/2015	107	22	25	23		23	10.16	75	25
ADC Sabwani K5	Twiga Methane& Primagram	pre-emergence	manual	twice		11/06/2015	72	26	22	29		26	10.16	75	25
ADC Sabwani K5	Twiga Methane& Primagram	pre-emergence	manual	twice		23/06/2015	84	29	15	13		19	10.16	75	25
ADC Sabwani K5	Twiga Methane& Primagram	pre-emergence	manual	twice		16/07/2015	107	24	17			21	10.16	75	25
ADC Sabwani S2	Twiga Methane& Primagram	pre-emergence	manual	twice		11/06/2015	68	28	23			26	10.16	75	25
ADC Sabwani S2	Twiga Methane& Primagram	pre-emergence	manual	twice		23/06/2015	80	14	15			15	10.16	75	25
ADC Sabwani S2	Twiga Methane& Primagram	pre-emergence	manual	twice		16/07/2015	103	21	24			23	10.16	75	25
ADC Olngatongo H6	Twiga Methane& Primagram	pre-emergence	manual	once	knee height	11/06/2015	71	21	25			23	10.16	75	15
ADC Olngatongo H6	Twiga Methane& Primagram	pre-emergence	manual	once	knee height	23/06/2015	83	22	17			20	10.16	75	15
ADC Olngatongo H6	Twiga Methane& Primagram	pre-emergence	manual	once	knee height	16/07/2015	106	17	17			17	10.16	75	15
ADC Olngatongo L6	Twiga Methane& Primagram	pre-emergence	manual	once	knee height	11/06/2015	38	16	22	23		20	10.16	75	15
ADC Olngatongo L6	Twiga Methane& Primagram	pre-emergence	manual	once	knee height	24/06/2015	51	14	16	17		16	10.16	75	15
ADC Olngatongo L6	Twiga Methane& Primagram	pre-emergence	manual	once	knee height	16/07/2015	73	14				14	10.16	75	15
ADC Olngatongo L10	Twiga Methane& Primagram	pre-emergence	manual	once	knee height	11/06/2015	37	14	21			18	10.16	75	15
ADC Olngatongo L10	Twiga Methane& Primagram	pre-emergence	manual	once	knee height	24/06/2015	50	17	17	17		17	10.16	75	15
ADC Olngatongo L10	Twiga Methane& Primagram	pre-emergence	manual	once	knee height	16/07/2015	72	25				25	10.16	75	15
Kenya Seed Company X4/1	Lumax+2-4 D Ammine/Auxo	pre-emergence	manual	once	knee height	24/06/2015	24	17	19			18	10.16	75	25
Kenya Seed Company X4/1	Lumax+2-4 D Ammine/Auxo	pre-emergence	manual	once	knee height	16/07/2015	46	18	12			15	10.16	75	25
Kenya Seed Company X2/1	Lumax+2-4 D Ammine/Auxo	pre-emergence	manual	once	knee height	24/06/2015	69	35	36			36	10.16	75	25
Kenya Seed Company X2/1	Lumax+2-4 D Ammine/Auxo	pre-emergence	manual	once	knee height	16/07/2015	91	27	21			24	10.16	75	25

field name	plant population	orienta	BBCH	No. Of le	LAI	leaf length sa	leaf length sa	leaf length sa	avg leaf l	leaf middle s	leaf middle s	leaf middle s	avg leaf m	leaf base sa	leaf base sa	leaf base sa	avg leaf	leaf Ar	Total_leaf
ADC Sabwani F1	4.4	E-W	37	17	4	110	98	76	76	9.2	11	12	9	8	9.4	9.1	9	481	8182.31
ADC Sabwani F1	4.4	E-W	61	18	4	100			77	9.9			9	9			9	497	8939.7
ADC Sabwani F1	4.4	E-W	71	23	5				78				9					538	12378.6
ADC Sabwani F2	4.4	E-W	38	19	4	88	82.6	95.6	76				9	11.1	10.4	10.2	11	502	9530.4
ADC Sabwani F2	4.4	E-W	59	20	5				77				9					520	10395
ADC Sabwani F2	4.4	E-W	71	21	5	80			78	9			9	9.8			10	527	11056.5
ADC Sabwani K5	4.4	E-W	39	18	4	113	102	100	76	11.2	11	10.2	9	9	10	8	9	496	8926.2
ADC Sabwani K5	4.4	E-W	65	19	4	117	94	80	77	9.2	11.9	8.9	9	9.8	10.4	8.9	10	508	9655.8
ADC Sabwani K5	4.4	E-W	79	21	5	110			79	10			9	8.3			8	533	11198.3
ADC Sabwani S2	4.4	E-W	37	17	4	112	108	103	76	12	12	8	9	10	10	6	9	482	8193.15
ADC Sabwani S2	4.4	E-W	61	18	4	83	79	75	76	9	9.4	9.8	9	7.9	9.9	9.4	9	495	8902.71
ADC Sabwani S2	4.4	E-W	71	22	5	83			79	9.2			9	8.8			9	532	11701.8
ADC Olngatongo H6	4.4	E-W	38	17	4	152	186	128	76	10.8	10	10.8	9	10.6	9.4	9.8	10	483	8203.99
ADC Olngatongo H6	4.4	E-W	59	19	4	106	110	115	77	10	10.8	10	9	9	11	9	10	514	9765.53
ADC Olngatongo H6	4.4	E-W	73	23	5	94			78	11.2			9	10			10	529	12165.6
ADC Olngatongo L6	4.4	N-S	33	12	2	96	85.4	70.4	68	10	8.6	6.8	6	9	8.2	6.4	8	316	3794.4
ADC Olngatongo L6	4.4	N-S	38	16	3	97	106	88	75	12	11	12	8	14	10	14	13	449	7180.8
ADC Olngatongo L6	4.4	N-S	59	18	4	114			76	11			9	10			10	495	8902.71
ADC Olngatongo L10	4.4	N-S	33	12	2	84.4	78	60	72	8.8	8.6	9	7	6.2	7.8	8	7	357	4282.74
ADC Olngatongo L10	4.4	N-S	38	15	3	76	104	100	73	10	11	9	8	11	10	9	10	427	6405.75
ADC Olngatongo L10	4.4	N-S	59	18	4	93		78	79	11			9	10			10	514	9243.32
Kenya Seed Company X4	4.4	E-W	33	10	1	94	69	92	68	9	11	11	6	8	11	11	10	302	3017.85
Kenya Seed Company X4	4.4	E-W	69	13	2	103			69	11.1			7	12			12	368	4783.45
Kenya Seed Company X2	4.4	N-S	32	12	2	90	90	80	69	8	7	5	6	6	4	2	4	317	3799.08
Kenya Seed Company X2	4.4	N-S	39	15	3	87			71	9.2			8	8			8	422	6336.79

individual leaf number	kitale	sum_kitale	LAI_kitale_5,3
1	8.2	8.2	0
2	17.2	25.4	0.01
3	32	57.4	0.02
4	57.1	114.5	0.05
5	98.2	212.7	0.08
6	162	374.7	0.15
7	217	591.7	0.24
8	311	902.7	0.36
9	449	1351.7	0.54
10	609	1960.7	0.78
11	764	2724.7	1.08
12	936	3660.7	1.46
13	1015	4675.7	1.86
14	1055	5730.7	2.28
15	1031	6761.7	2.69
16	1004	7765.7	3.09
17	933	8698.7	3.46
18	843	9541.7	3.79
19	753	10294.7	4.09
20	656	10950.7	4.35
21	550	11500.7	4.57
22	430	11930.7	4.74
23	293	12223.7	4.86
24	163	12386.7	4.92
25	70	12456.7	4.95
26	16	12472.7	4.96

Leaf Area Index vs Leaf Number

Leaf Area Index (y-axis) vs Leaf Number (x-axis)

LAI_kitale_5,3

Kitale

days after emergence   leaf number
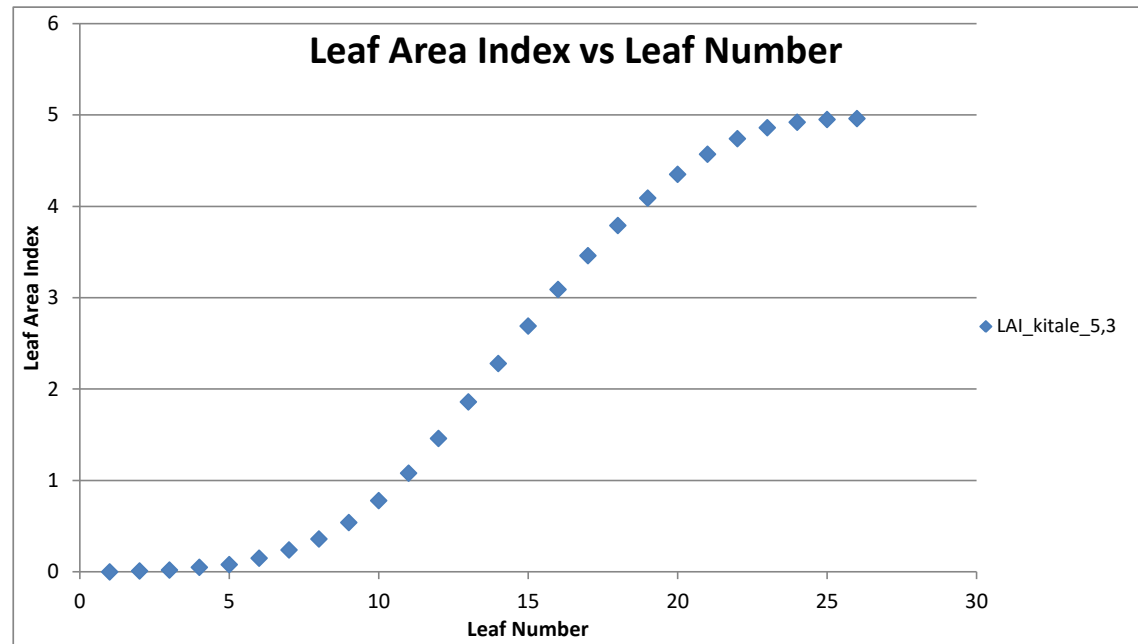
days after emergence	leaf number		
6	4.5	6	4.5
10	5.5	10	5.5
19	7.8	19	7.8
29	10.5	29	10.5
37	12.6	37	12.6
47	15.3	47	15.2
57	17.3	56	17.3
69	20	69	20
82	22	82	22
95	23.1	95	23.1
102	23.2	102	23.2

$R^2 = 0.9975$
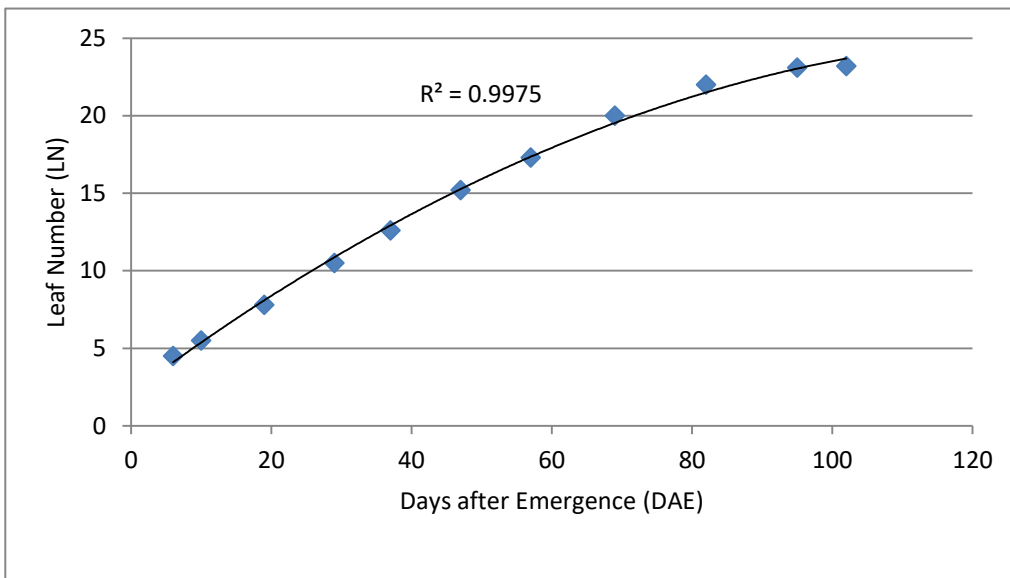
field name	cultivar	DOY	LAI	planting	emergence	Date visit	Date RE 1	Date RE 2	Date RE 3	Date RE 4	Date RE 5	Date LS	plant-emerg	emerg-visit	emerg-RE1	emerg-RE2	emerg-RE3	emerg-RE4	emerg-RE5	emerg-LS	visit LN
ADC Sabwani F1	H628	161	1.37	28/03/2015	04/04/2015	11/06/2015	07/06/2015	04/07/2015	16/08/2015	24/08/2015	07/10/2015	27/05/2015	7	68	64	91	134	142	186	53	19
ADC Sabwani F1	H628	173	2.23	28/03/2015	04/04/2015	23/06/2015	07/06/2015	04/07/2015	16/08/2015	24/08/2015	07/10/2015	27/05/2015	7	80	64	91	134	142	186	53	21
ADC Sabwani F1	H628	196	3.56	28/03/2015	04/04/2015	16/07/2015	07/06/2015	04/07/2015	16/08/2015	24/08/2015	07/10/2015	27/05/2015	7	103	64	91	134	142	186	53	23
ADC Sabwani F2	H628	161	1.32	20/03/2015	27/03/2015	11/06/2015	07/06/2015	04/07/2015	16/08/2015	24/08/2015	07/10/2015	27/05/2015	7	76	72	99	142	150	194	61	21
ADC Sabwani F2	H628	173	1.53	20/03/2015	27/03/2015	23/06/2015	07/06/2015	04/07/2015	16/08/2015	24/08/2015	07/10/2015	27/05/2015	7	88	72	99	142	150	194	61	22
ADC Sabwani F2	H628	196	1.62	20/03/2015	27/03/2015	16/07/2015	07/06/2015	04/07/2015	16/08/2015	24/08/2015	07/10/2015	27/05/2015	7	111	72	99	142	150	194	61	22
ADC Sabwani K5	H6213	161	2.04	07/03/2015	14/03/2015	11/06/2015	07/06/2015	04/07/2015	16/08/2015	24/08/2015	07/10/2015	27/05/2015	7	89	85	112	155	163	207	74	22
ADC Sabwani K5	H6213	173	2.18	07/03/2015	14/03/2015	23/06/2015	07/06/2015	04/07/2015	16/08/2015	24/08/2015	07/10/2015	27/05/2015	7	101	85	112	155	163	207	74	23
ADC Sabwani K5	H6213	196	3.47	07/03/2015	14/03/2015	16/07/2015	07/06/2015	04/07/2015	16/08/2015	24/08/2015	07/10/2015	27/05/2015	7	124	85	112	155	163	207	74	20
ADC Sabwani S2	H6213	161	2.07	28/03/2015	04/04/2015	11/06/2015	07/06/2015	04/07/2015	16/08/2015	24/08/2015	07/10/2015	27/05/2015	7	68	64	91	134	142	186	53	19
ADC Sabwani S2	H6213	173	2.67	28/03/2015	04/04/2015	23/06/2015	07/06/2015	04/07/2015	16/08/2015	24/08/2015	07/10/2015	27/05/2015	7	80	64	91	134	142	186	53	21
ADC Sabwani S2	H6213	196	2.41	28/03/2015	04/04/2015	16/07/2015	07/06/2015	04/07/2015	16/08/2015	24/08/2015	07/10/2015	27/05/2015	7	103	64	91	134	142	186	53	23
ADC Olngatongo H6	H6213	161	3.68	22/03/2015	29/03/2015	11/06/2015	07/06/2015	04/07/2015	16/08/2015	24/08/2015	07/10/2015	27/05/2015	7	74	70	97	140	148	192	59	20
ADC Olngatongo H6	H6213	173	3.4	22/03/2015	29/03/2015	23/06/2015	07/06/2015	04/07/2015	16/08/2015	24/08/2015	07/10/2015	27/05/2015	7	86	70	97	140	148	192	59	22
ADC Olngatongo H6	H6213	196	4.74	22/03/2015	29/03/2015	16/07/2015	07/06/2015	04/07/2015	16/08/2015	24/08/2015	07/10/2015	27/05/2015	7	109	70	97	140	148	192	59	22
ADC Olngatongo L6	H628	161	1.07	24/04/2015	01/05/2015	11/06/2015	07/06/2015	04/07/2015	16/08/2015	24/08/2015	07/10/2015	27/05/2015	7	41	37	64	107	115	159	26	13
ADC Olngatongo L6	H628	174	2.55	24/04/2015	01/05/2015	24/06/2015	07/06/2015	04/07/2015	16/08/2015	24/08/2015	07/10/2015	27/05/2015	7	54	37	64	107	115	159	26	16
ADC Olngatongo L6	H628	196	3.76	24/04/2015	01/05/2015	16/07/2015	07/06/2015	04/07/2015	16/08/2015	24/08/2015	07/10/2015	27/05/2015	7	76	37	64	107	115	159	26	21
ADC Olngatongo L10	H628	161	1.96	25/04/2015	02/05/2015	11/06/2015	07/06/2015	04/07/2015	16/08/2015	24/08/2015	07/10/2015	27/05/2015	7	40	36	63	106	114	158	25	13
ADC Olngatongo L10	H628	174	2.1	25/04/2015	02/05/2015	24/06/2015	07/06/2015	04/07/2015	16/08/2015	24/08/2015	07/10/2015	27/05/2015	7	53	36	63	106	114	158	25	16
ADC Olngatongo L10	H628	196	3.07	25/04/2015	02/05/2015	16/07/2015	07/06/2015	04/07/2015	16/08/2015	24/08/2015	07/10/2015	27/05/2015	7	75	36	63	106	114	158	25	21
KSC X4/1	H614	174	1.58	28/04/2015	05/05/2015	24/06/2015	07/06/2015	04/07/2015	16/08/2015	24/08/2015	07/10/2015	27/05/2015	7	50	33	60	103	111	155	22	15
KSC X4/1	H614	196	2.57	28/04/2015	05/05/2015	16/07/2015	07/06/2015	04/07/2015	16/08/2015	24/08/2015	07/10/2015	27/05/2015	7	72	33	60	103	111	155	22	20
KSC X2/1	H614	174	1.04	02/04/2015	09/04/2015	24/06/2015	07/06/2015	04/07/2015	16/08/2015	24/08/2015	07/10/2015	27/05/2015	7	76	59	86	129	137	181	48	21
KSC X2/1	H614	196	1.8	02/04/2015	09/04/2015	16/07/2015	07/06/2015	04/07/2015	16/08/2015	24/08/2015	07/10/2015	27/05/2015	7	98	59	86	129	137	181	48	23

field name	RE1 LN	RE2 LN	RE3 LN	RE4 LN	RE5 LN	LS LN	visit LN sum	RE1 LN sum	RE2 LN sum	RE3 LN sum	RE4 LN sum	RE5 LN sum	LS LN sum	visit LAI	RE1 LAI	RE2 LAI	RE3 LAI	RE4 LAI	RE5 LAI	LS LAI	sum Kitale	LAI Kitale
ADC Sabwani F1	19	22	18	15	-15	16	10294.7	10294.7	11930.7	9541.7	6761.7	0	07765.7	4.09214325	4.09214325	4.74245325	3.79282575	2.68777575	0	3.08686575	10950.7	4.35
ADC Sabwani F1	19	22	18	15	-15	16	11500.7	10294.7	11930.7	9541.7	6761.7	0	07765.7	4.57152825	4.09214325	4.74245325	3.79282575	2.68777575	0	3.08686575	11500.7	4.57
ADC Sabwani F1	19	22	18	15	-15	16	12223.7	10294.7	11930.7	9541.7	6761.7	0	07765.7	4.85892075	4.09214325	4.74245325	3.79282575	2.68777575	0	3.08686575	12223.7	4.86
ADC Sabwani F2	20	23	15	11	-24	18	11500.7	10950.7	12223.7	6761.7	2724.7	0	09541.7	4.57152825	4.35290325	4.85892075	2.68777575	1.08306825	0	3.79282575	10950.7	4.35
ADC Sabwani F2	20	23	15	11	-24	18	11930.7	10950.7	12223.7	6761.7	2724.7	0	09541.7	4.74245325	4.35290325	4.85892075	2.68777575	1.08306825	0	3.79282575	11930.7	4.74
ADC Sabwani F2	20	23	15	11	-24	18	11930.7	10950.7	12223.7	6761.7	2724.7	0	09541.7	4.74245325	4.35290325	4.85892075	2.68777575	1.08306825	0	3.79282575	12223.7	4.86
ADC Sabwani K5	22	22	8	3	-41	20	11930.7	11930.7	11930.7	902.7	57.4	0	010950.7	4.74245325	4.74245325	4.74245325	0.35882325	0.0228165	0	4.35290325	10950.7	4.35
ADC Sabwani K5	22	22	8	3	-41	20	12223.7	11930.7	11930.7	902.7	57.4	0	010950.7	4.85892075	4.74245325	4.74245325	0.35882325	0.0228165	0	4.35290325	11930.7	4.74
ADC Sabwani K5	22	22	8	3	-41	20	10950.7	11930.7	11930.7	902.7	57.4	0	010950.7	4.35290325	4.74245325	4.74245325	0.35882325	0.0228165	0	4.35290325	12223.7	4.86
ADC Sabwani S2	19	22	18	15	-15	16	10294.7	10294.7	11930.7	9541.7	6761.7	0	07765.7	4.09214325	4.09214325	4.74245325	3.79282575	2.68777575	0	3.08686575	10950.7	4.35
ADC Sabwani S2	19	22	18	15	-15	16	11500.7	10294.7	11930.7	9541.7	6761.7	0	07765.7	4.57152825	4.09214325	4.74245325	3.79282575	2.68777575	0	3.08686575	11500.7	4.57
ADC Sabwani S2	19	22	18	15	-15	16	12223.7	10294.7	11930.7	9541.7	6761.7	0	07765.7	4.85892075	4.09214325	4.74245325	3.79282575	2.68777575	0	3.08686575	12223.7	4.86
ADC Olngatongo H6	20	23	16	12	-22	18	10950.7	10950.7	12223.7	7765.7	3660.7	0	09541.7	4.35290325	4.35290325	4.85892075	3.08686575	1.45512825	0	3.79282575	10950.7	8.71
ADC Olngatongo H6	20	23	16	12	-22	18	11930.7	10950.7	12223.7	7765.7	3660.7	0	09541.7	4.74245325	4.35290325	4.85892075	3.08686575	1.45512825	0	3.79282575	11930.7	9.48
ADC Olngatongo H6	20	23	16	12	-22	18	11930.7	10950.7	12223.7	7765.7	3660.7	0	09541.7	4.74245325	4.35290325	4.85892075	3.08686575	1.45512825	0	3.79282575	12223.7	9.72
ADC Olngatongo L6	12	19	23	22	6	9	4675.7	3660.7	10294.7	12223.7	11930.7	374.7	01351.7	1.85859075	1.45512825	4.09214325	4.85892075	4.74245325	0.14894325	0.53730075	4675.7	3.72
ADC Olngatongo L6	12	19	23	22	6	9	7765.7	3660.7	10294.7	12223.7	11930.7	374.7	01351.7	3.08686575	1.45512825	4.09214325	4.85892075	4.74245325	0.14894325	0.53730075	7765.7	6.17
ADC Olngatongo L6	12	19	23	22	6	9	11500.7	3660.7	10294.7	12223.7	11930.7	374.7	01351.7	4.57152825	1.45512825	4.09214325	4.85892075	4.74245325	0.14894325	0.53730075	10950.7	8.71
ADC Olngatongo L10	12	18	23	22	7	9	4675.7	3660.7	9541.7	12223.7	11930.7	591.7	01351.7	1.85859075	1.45512825	3.79282575	4.85892075	4.74245325	0.23520075	0.53730075	4675.7	3.72
ADC Olngatongo L10	12	18	23	22	7	9	7765.7	3660.7	9541.7	12223.7	11930.7	591.7	01351.7	3.08686575	1.45512825	3.79282575	4.85892075	4.74245325	0.23520075	0.53730075	7765.7	6.17
ADC Olngatongo L10	12	18	23	22	7	9	11500.7	3660.7	9541.7	12223.7	11930.7	591.7	01351.7	4.57152825	1.45512825	3.79282575	4.85892075	4.74245325	0.23520075	0.53730075	10950.7	8.71
KSC X4/1	11	18	23	22	8	8	6761.7	2724.7	9541.7	12223.7	11930.7	902.7	0902.7	2.68777575	1.08306825	3.79282575	4.85892075	4.74245325	0.35882325	0.35882325	1960.7	0.78
KSC X4/1	11	18	23	22	8	8	10950.7	2724.7	9541.7	12223.7	11930.7	902.7	0902.7	4.35290325	1.08306825	3.79282575	4.85892075	4.74245325	0.35882325	0.35882325	6761.7	2.69
KSC X2/1	18	22	19	17	-10	15	11500.7	9541.7	11930.7	10294.7	8698.7	0	06761.7	4.57152825	3.79282575	4.74245325	4.09214325	3.45773325	0	2.68777575	10950.7	4.35
KSC X2/1	18	22	19	17	-10	15	12223.7	9541.7	11930.7	10294.7	8698.7	0	06761.7	4.85892075	3.79282575	4.74245325	4.09214325	3.45773325	0	2.68777575	11930.7	4.74

A.2 Farm management data
A.2.2 ADC Sabwani fields data

field_data

F_NAME	2014 crop	variety	planting date	planting area	harvesting	(note)	2015 crop	variety	planting date	planting area (ha)	harvesting	(note)	2016 crop	variety	planting date	planting area (ha)	harvesting	(note)
A1	maize	kenya seed				kenya seed						kenya seed						kenya seed
A2	maize	kenya seed				kenya seed						kenya seed						kenya seed
A3	maize	kenya seed				kenya seed						kenya seed						kenya seed
A4	maize	kenya seed				kenya seed						kenya seed						kenya seed
A5	maize	kenya seed				kenya seed						kenya seed						kenya seed
A5(3)													cane		03/11/2016	15.9	missing	
A5(6)													cane		08/12/2016	8.8	missing	
AB1	maize	kenya seed											cane		19/11/2016	12.1	missing	
AB2	maize	kenya seed											cane		17/12/2016	12.9	missing	
AB3	maize	kenya seed											cane					
AB4	maize	kenya seed											cane		08/12/2016	8	missing	
AB5	maize	kenya seed											cane		12/11/2016	24	missing	
AB6	maize	kenya seed																
AB7	maize	kenya seed										kenya seed	maize	labour plot	april	12	november	
AC1	maize	people				kenya seed							cane		26/10/2016	14.2	missing	
AC2	maize	people											cane					
AC2A													cane		26/10/2016	10.1	missing	
AC21						kenya seed												
AC25													cane			not planted		
AC3	maize	people											cane					
AC3A													cane		19/11/2016	2.4	missing	
AC3(5)													cane			not planted		
AC4	maize	people											cane		11/11/2016	21	missing	
AC5	maize	people																
AD													cane	missing	missing		missing	
AD1	maize	COMM																
AD2	maize	people																
AD3	maize	people																
AE	beans	labour plots					maize	labour plots					maize	labour plots	april		november	
AE1	maize	people																
AE2	maize	people																
B1	maize	H6210	06/03/2014	11.6	*	COMM	maize	COMM	02/03/2015	20	01/10/2015		maize	missing	02/03/2016	missing	missing	COMM
B2	maize	missing	18/03/2014	30	missing		maize	COMM KH600-23A		30			maize	missing	22/03/2016	missing	28/10/2016	COMM
C1	maize	H6210	21/03/2014	7.5	*	SIL	maize	COMM KH600-23A	27/02/2015	11	06/10/2015		maize	missing	01/03/2016	missing	07/09/2016	COMM
C2						kenya seed	kenya seed						fallow					
D1	maize	H629	04/04/2014	16	29/10/2014		maize	H628	24/04/2015	16	03/12/2015		maize	H614/H628	29/03/2016	16		
D2	maize	H629	31/03/2014	16	07/10/2014		maize	H628	20/04/2015	16	02/12/2015		maize	H614/H628	30/03/2016	16	07/10/2016	
E1	maize	H629	19/04/2014	30	06/12/2014								maize	H614/H628	13/04/2016	30	18/11/2016	
E1A							maize	H628	01/04/2015	14	19/11/2015							
E1B							maize	H628	10/04/2015	16								
E2	maize	H629	09/04/2014	12	18/11/2014		maize	H628	20/04/2015	12	05/12/2015		maize	H614/H628	29/03/2016	12	28/09/2016	
E3/E4	maize	H629	18/04/2014	21	03/12/2014		maize	H628	23/04/2015	24	30/11/2015							
E3/E4							Hay			6								
E3/E4A													maize	H614	14/04/2016	12	10/12/2016	24 ha. Combined with E3/E4B
E3/E4B													maize	H614	14/04/2016	12	10/12/2016	
F1	maize	H629	18/03/2014	16	06/10/2014		maize	H628	28/03/2015	16	11/11/2015		maize	H614/H628	31/03/2016	16	19/10/2016	
F2	maize	H629	23/04/2014	16	10/12/2014		maize	H628	20/03/2015	16	13/11/2015		maize	H614/H628	03/04/2016	16	21/10/2016	
F3	maize	H629	14/04/2014	10	10/12/2014		maize	H628	23/03/2015	17	17/11/2015		maize	H614/H628	05/04/2016	18	03/11/2016	
F4	maize	H629	14/04/2014	16	09/12/2014		maize	H628	27/03/2015	18	02/11/2015		maize	H614/H628	13/04/2016	18	04/11/2016	
F5	maize	H629	24/03/2014	16	09/10/2014		maize	H628	31/03/2015	16	26/10/2015		maize	H614/H628	05/04/2016	16	01/12/2016	
F6	maize	H629	21/03/2014	4	08/10/2014		maize	H628	30/03/2015	4	26/10/2015		maize	H614/H628	06/04/2016	4	02/12/2016	
F7	rough grazing						rough grazing						rough grazing					
G1	maize	H6213	06/04/2014	20									maize seed	H6213	02/04/2016	20	05/10/2016	recorded under G1A
G1A	maize	H6213	06/04/2014	10.2	28/11/2014		maize	H6213	18/03/2015	9	17/10/2015							
G1B	maize	H6213	16/04/2014	9.8	28/11/2014		maize	H6213	23/04/2015	11	18/11/2015							
G2	maize	H6213	09/04/2014	20									maize seed	H6213	02/04/2016	20	22/10/2016	recorded under G2B
G2A	maize	H6213	09/04/2014	13.5	12/11/2014		maize	H6213	21/03/2015	4	16/10/2015							
G2B	maize	H6213	19/04/2014	6.5	12/11/2014		maize	H6213	24/04/2015	16	16/11/2015							
H1	maize	H6213	17/04/2014	33	10/11/2014		maize	H6213	12/03/2015	30	12/10/2015							
H1A													maize seed	H6213	06/04/2016	15	18/10/2016	combined with H1B under H1
H1B													maize seed	H6213	06/04/2016	15	18/10/2016	
H2	wheat	kwale	09/07/2014	18	07/12/2014	COMM	maize	H6213	03/03/2015	18	25/09/2015		maize seed	H6213	01/04/2016	18	23/09/2016	seed
I1	maize	H629	26/03/2014	14	21/10/2014		maize	H628	11/04/2015	14	27/11/2015		maize	H614	13/04/2016	14	11/11/2016	
I2	maize	H629	27/03/2014	13	15/10/2014		maize	H628	29/03/2015	13	26/11/2015		maize	H614	04/04/2016	13	17/11/2016	
J1	maize	H629	27/03/2014	14	18/10/2014		maize	H628	30/03/2015	14	24/11/2015		maize	H614	13/04/2016	14	08/11/2016	
J2	maize	H629	27/03/2014	6	16/10/2014		maize	H628	25/04/2015	7	30/11/2015		maize	H614	12/04/2016	9	14/11/2016	
K1	maize	H6213	12/03/2014	21	13/09/2014		maize	H6213	04/03/2015	21	29/10/2015		maize seed	H6213	31/03/2016	21	30/09/2016	seed
K2	maize	H6213	06/04/2014	16	27/11/2014		maize	H6213	07/03/2015	16	20/10/2015		maize seed	H6213	31/03/2016	16	11/10/2016	
K3	maize	H6213	13/03/2014	12.8	17/09/2014		maize	H6213	05/03/2015	16	22/10/2015		maize seed	H6213	01/04/2016	13	17/10/2016	
K4							reys	missing	missing	16	missing		reys	missing	missing	missing	missing	
K5	maize	H6213	05/04/2014	21	26/11/2014		maize	H6213	06/03/2015	18	24/10/2015		maize seed	H6213	27/03/2016	21	14/10/2016	
KF2	maize	KH600-23A	21/04/2014	16	12/01/2015		wheat	COMM		10			maize	KH600-23A	25/04/2016	8	05/12/2016	

Plot	crop	variety	planted	qty	harvested		crop	variety	planted	qty	harvested		crop	variety	planted	qty	harvested	notes
KF3																		
KF4	maize	H624	13/04/2014	20	03/10/2014		maize	KH600-23A	29/04/2015	19	17/12/2015		maize	KH600-23A	25/04/2016	20	06/11/2016	
KF4							wheat	COMM		1.2								
KF5	reys	bomarods	20/07/2013	missing	missing		maize	KH600-23A	02/04/2015	5	14/12/2015		maize	KH600-23A	08/04/2016	5	10/12/2016	
KF8	maize	missing	missing	missing	missing		maize	SEED	22/04/2015	3	19/11/2015		maize	research purpose		3	11/12/2016	
KF9																		
KF10	maize	H624	08/04/2014	20	05/11/2014		maize	SEED	18/04/2015	20	12/12/2015		maize	KH600-23A	22/04/2016	20	15/11/2016	
KF11							maize	SEED	18/04/2015	10.5	07/12/2015		maize	KH600-23A	18/04/2016	12	12/11/2016	
KF11							wheat	COMM		13.5								
KF11(A)	maize	H624	25/03/2014	2	23/09/2014													
KF11(B)	maize	H624	13/04/2014	18	20/11/2014								cane	missing	24/06/2016	12	missing	
KF11C	maize	H624	16/04/2014	4	20/11/2014													
KF12	maize	H624	04/04/2014	28	21/11/2014		maize	KH600-23A	16/04/2015	27.5	20/10/2015		maize	KH600-23A	23/04/2016	16	12/11/2016	
KF12													cane		18/07/2016	10	missing	not sure
KF13	maize	H624	09/04/2014	16	25/11/2014		maize	KH600-23A	20/04/2015	16	28/11/2015		maize	KH600-23A	16/04/2016	17	13/11/2016	
KF14	wheat	kwale	18/06/2014	10	04/11/2014	COMM	wheat	COMM		10			cane		10/06/2016	10	missing	
KF15	wheat	kwale	23/06/2014	8	05/11/2014	COMM	wheat	COMM		8			cane		22/07/2016	8	missing	
KF16													cane		17/06/2016	10	missing	
L1													maize seed	H6213	29/03/2016	20	26/10/2016	seed. Recorded under L1/L1A
L1/L1A	maize	H6213	03/04/2014	20	04/11/2014		maize	H6213	22/03/2015	8	20/11/2015							
L1B							maize	H6213	22/04/2015	12	23/11/2015							
L2	maize	H6213	29/03/2014	20	24/10/2014		maize	H6213	24/03/2015	20	24/11/2015		maize seed	H6213	31/03/2016	20	26/10/2016	
M1	maize	KH600-23A	11/04/2014	24	07/01/2015		maize	H6213	09/03/2015	24	07/11/2015		maize seed	H6213	06/04/2016	24	08/11/2016	
M2	maize	KH600-23A	09/04/2014	24	13/09/2014		maize	H6213	10/03/2015	24	11/11/2015		maize seed	H6213	06/04/2016	24	14/11/2016	
N1	maize	KH600-23A	11/04/2014	11	09/01/2015								maize seed	H6213	16/04/2016	13.5	11/11/2016	
N1A							maize	H6213	14/04/2015	11	05/12/2015							
N1B	wheat	kwale	18/07/2014	3	07/12/2014	COMM	maize	H6213	26/04/2015	3	05/12/2015							
N2																		
O1	maize	KH600-23A	10/04/2014	20	17/09/2014		maize	H6213	07/04/2015	20	07/12/2015		maize seed	H6213	09/04/2016	20	15/11/2016	
O2	maize	KH600-23A	11/04/2014	20	23/01/2015		maize	H6213	09/04/2015	20	08/12/2015		maize seed	H6213	10/04/2016	20	16/11/2016	
O3	maize	KH600-23A	17/03/2014	20	20/01/2015		maize	H6213	16/04/2015	20	10/12/2015		maize seed	H6213	11/04/2016	20	25/11/2016	seed
P1	maize	KH600-23A	21/04/2014	9	20/01/2015													
P1A							maize	H6213	15/04/2015	7	11/12/2015		maize seed	H6213	15/04/2016	7	24/11/2016	seed. Recorded with P1B under P1
P1B	wheat	kwale	30/06/2014	6	17/11/2014	COMM	maize	H6213	28/04/2015	6			maize seed	H6213	25/04/2016	7	24/11/2016	
P2																		
Q1	maize	KH600-23A	18/04/2014	8	16/01/2015								maize	KH600-23A	07/04/2016	16	09/11/2016	
Q1A	maize	KH600-23A	18/04/2014	missing	missing		maize	KH600-23A	15/03/2015	7.5	04/01/2016							
Q1B	reys	bomarods	20/07/2013	8	missing		maize	KH600-23A	14/04/2015	8.5								
Q2							maize	KH600-23A	25/03/2015	12	30/12/2015		maize	KH600-23A	10/04/2016	12	05/11/2016	
Q3							maize	KH600-23A	02/04/2015	24	10/10/2015		maize	KH600-23A	08/04/2016	24	09/11/2016	
Q2A	maize	KH600-23A	16/03/2014	6.6	19/11/2014													
Q2B	maize	KH600-23A	02/04/2014	5.4	19/11/2014													
Q3	maize	KH600-23A	11/04/2014	24	09/01/2015		maize	H6213	02/04/2015	24								
S1	maize	H6213	16/04/2014	12	19/12/2014		maize	H6213	02/04/2015	12	01/12/2015		maize seed	H6213	08/04/2016	12	02/11/2016	seed
S2	maize	H6213	01/04/2014	14	15/10/2014		maize	H6213	28/03/2015	14	30/11/2015		maize seed	H6213	08/04/2016	14/17	19/11/2016	seed
S3/S4	maize	H6213	28/03/2014	28	03/10/2014		maize	H6213	31/03/2015	28	27/11/2015		maize seed	H6213	10/04/2016	28	22/11/2016	seed
S4B							maize	H6213	12/04/2015	2	08/12/2015		maize seed	H6213	11/04/2016	2	23/11/2016	
T1	maize	H6213	20/04/2014	10	19/12/2014								isolation					
T1A							maize	H6213	14/04/2015	10	02/12/2015							
T1B	wheat	kwale	08/06/2014	4	14/10/2014		maize	H6213	25/04/2015	4	02/12/2015							
T2	maize	H6213	12/04/2014	14	19/12/2014		maize	H6213	01/04/2015	14	03/12/2015							
T3	maize	H6213	18/04/2014	14	17/12/2014		maize	H6213	06/04/2015	14	03/12/2015							
U1	maize	H6213	07/04/2014	30	15/12/2014								Bull station					
U2	maize	H6213	20/03/2014	20	25/09/2014		maize	H6213	12/04/2015	20	26/11/2015		maize	H6213				isolation or maize?
V1/V2													maize seed	H6213	30/03/2016	19.5		appears to be a combination of V1 and V2
V1	maize	H6213	09/03/2014	14	18/09/2014		maize	H6213	26/03/2015	14	28/10/2015		maize seed	H6213	30/03/2016	14	24/10/2016	
V2	maize	H6213	10/03/2014	12	20/09/2014								maize seed	H6213	30/03/2016	5.5	24/10/2016	
V2A	maize	H6213	10/03/2014	12	20/09/2014		maize	H6213	11/04/2015	12	28/10/2015		maize seed	H6213	missing	missing	missing	
V2B	maize	H6213	19/04/2014	2	20/09/2014		maize	H6213	10/04/2015	2	28/10/2015							
W	maize	H6213	13/04/2014	18	29/11/2014		maize	H6213	25/03/2015	18	25/11/2015		maize seed	H6213	30/03/2016	18	01/11/2016	
X1	rough grazing						rough grazing						rough grazing					grazing/COMM
X2						kenya seed	maize	SIL		24		kenya seed						
X2A													maize	missing	28/03/2016	24	14/12/2016	COMM
X2B													reys	missing	missing		24	missing
X3						kenya seed	maize	COMM KH 600 23A		23		kenya seed	maize	missing	27/03/2016	24	27/12/2016	COMM
X4						kenya seed	maize	COMM KH 600 23A		10		kenya seed						
X4A													maize	missing	26/03/2016	19.6	03/01/2017	COMM
X4B													reys	missing	missing			missing
X5						kenya seed						kenya seed						kenya seed
Y1																		
Y2																		
Y3																		
Y4																		
Y3/4						kenya seed	maize	COMM KH 600 23A		11		kenya seed	maize	missing	26/03/2016	11	missing	labour maize/COMM
Z1							maize	COMM	02/03/2015	40	09/10/2015							
Z2																		

A.2 Farm management data

A.2.3 ADC Olngatongo fields data

field_data

F_NAM	crop	variety	planting date	planting area	harvesting		crop	variety	planting date	planting area	harvesting		production	clean kgs	production	crop	variety	planting date	planting area	harvesting		production	clean kgs	production
			2014						**2015**									**2016**						
H1	Hay	Bomarhodes		14.1			maize	H6213	03/03/2015	14.1	22/10/2015		1537	66973	137	maize	H6213	30/03/2016	14.1			1347	60099	187
H2	Hay	Bomarhodes		16.1			maize	H6213	04/03/2015	18.2	26/10/2015		1808	74239	125	maize	H6213	31/03/2016	18.2			1797	75726.4	180
H3	maize	H6213	15/04/2014	16.1	20/11/2014		maize	H6213	25/03/2015	16.1	03/11/2015		1339	55580	74	maize	H6213	03/04/2016	16.1			1500	48009.16	118
H4	maize	H6213	18/04/2014	24.3	06/12/2014		maize	H6213	29/03/2015	24	05/11/2015		1814	75430	170	maize	H6213	13/04/2016	24			1871	61456.6	290
H5	maize	H6213	02/04/2014	30.6	06/11/2014		maize	H6213	02/03/2015	33.9	25/09/2015		3862	168595.34	185	maize	H6213	30/03/2016	33.9			3016	130507.2	342
H6	maize	H6213	05/04/2014	17.1	10/11/2014		maize	H6213	22/03/2015	15.7	11/12/2015		1536	64711	61	maize	H6213	11/04/2016	16.1			1005	46136.1	100
H7	maize	H6213	12/04/2014	16.1	19/11/2014		maize	H6213	24/03/2015	16.1	03/12/2015		1269	50022	53	maize	H6213	02/04/2016	16.1			936	40280.3	72
H8	maize	H6213	03/04/2014	17.3	13/11/2014		maize	H6213	14/03/2015			replanted on 26.4.15 7.8 ha, 1(	704	28584	99	maize	H6213	06/04/2016	18			1430	46230	190
H8A							maize	H6213	22/03/2015	10.4	11/12/2015													
H8B							maize	H6213	26/04/2015	7.8	15/12/2015		594	25011	44									
H9	maize	H6213	21/04/2014	44.2	11/12/2014		maize	H6213	06/03/2015	40		replanted on 24.4.15 5.7 ha, 34	1848	75430	62	maize	H6213	07/04/2016	18	40kg real		2682	82212	341
H9A							maize	H6213	14/03/2015	34.3	04/12/2015													
H9B							maize	H6213	24/03/2015	5.7	10/12/2015		220	9528	83									
H10	fallow	-	-	-	-		maize	H6213	04/03/2015	24	09/10/2015		3425	141332	95	maize	H6213	29/03/2016	24.2	24.2 real		3120	133326.8	314
H11	maize	H6213	07/04/2014	10.5	18/11/2014		maize	H6213	05/03/2015	19.2	20/10/2015		1845	75430	78	maize	H6213	29/03/2016	19.2			1902	83616.7	255
H12	swampy	-	-	-	-		swampy	-								swampy	-							
H13	fallow	-	-	-	-		maize	H6213	06/03/2015	10.1	19/10/2015		1047	44662.5	38	maize	H6213	26/03/2016	9.2			1111	54579.4	129
H14	maize	H626					maize	ADC SE	10/03/2015	5.7	06/10/2015		304		28	maize	ADC SE	24/04/2016	5.7			257		72
H15	maize	H626					fallow	-								Hay	Bomarhodes			established				
H16	maize	H626					maize	ADC SE	24/04/2015	3.2	15/01/2016		96		28	maize	ADC SE	24/04/2016	4.8	4.8 real		297		66
H17	maize	H626					maize	ADC SE	09/03/2015	16.1	20/10/2015		1560		48	maize	ADC SE	24/04/2016	19.9			942		279
H18	maize	H626					maize	ADC SE	24/04/2015	8	11/01/2016		256		61	maize	ADC SE	24/04/2016	8			450		114
H19	maize	H626					maize	ADC SE	23/04/2015	6	08/01/2016		160		25	maize	ADC SE	23/04/2016	5.6			179		52
H20	maize	H626					maize	ADC SE	16/04/2015	14.8	28/12/2015		619		89	maize	ADC SE	26/04/2016	14.2			516		136
H20	maize	H626																						
H20						isolation						isolation									isolation				
H21	maize	H626					maize	ADC SE	17/04/2015	13.4	26/11/2015		546		48	maize	ADC SE	29/04/2016	12.2			414		105
H22	maize	H626					maize	ADC SE	12/03/2015	31						maize	ADC SE	22/04/2016	8.9			495		121
H22A	maize	H626					maize	ADC SE	12/03/2015	7.6	04/11/2015		661		16	fallow	-	-	-	-				
H22B	maize	H626					maize	ADC SE	13/04/2015	23.4	09/11/2015		1565		134	fallow	-	-	-	-				
H23	maize	H626					maize	ADC SE	15/03/2015	27.3						maize	ADC SE	23/04/2016	7.6			639		102
H23A	maize	H626					maize	ADC SE	15/03/2015	7.3	05/11/2015		657		22	fallow	-	-	-	-				
H23B	maize	H626					maize	ADC SE	19/04/2015	20	16/11/2015		863		23	fallow	-	-	-	-				
H24	maize	H626					maize	ADC SE	21/04/2015	16.4	21/11/2015		937		151	maize	ADC SE	01/05/2016	19.6			1022		207
H25	maize	H626					maize	ADC SE	11/03/2015	17.1	07/10/2015	whole planted	1439		123	fallow	-	-	-	-				
H25	maize	H626														fallow	-	-	-	-				
H26	fallow	-	-	-	-		fallow	-								fallow	-	-	-	-				
H27	fallow	-	-	-	-		fallow	-								fallow	-	-	-	-				
H27	fallow	-	-	-	-											fallow	-	-	-	-				
L1	maize	H6210	17/03/2014	9.1	24/09/2014		maize	H628	14/04/2015	9	09/11/2015		632	25888	107	maize	H614	26/03/2016	9			503	16130.03	115
L1	-	-	-	-	-	isolation	-					isolation					-				-	isolation			
L2	maize	H6210	18/03/2014	12.1	22/09/2014		maize	H628	03/04/2015	13.4	26/10/2015		872	33275	136	maize	H614	24/03/2016	13.3			552	18220	148
L3	maize	H6210	28/03/2014	17.3	25/09/2014		maize	H628	26/04/2015	14.8	25/11/2015		1390	43830.11	136	maize	H614	24/03/2016	15	14.9 real		1367	65095	249
L3	-	-	-	-	-	isolation	-					isolation					-				-	isolation			
L4	maize	H6210	20/03/2014	13.9	29/09/2014		maize	H628	26/04/2015	12.5	26/11/2015		1	7703.11	121	maize	H614	26/03/2016	12.3	harvested as con		1027		
L5	maize	H6210	17/03/2014	11.1	17/09/2014		maize	H628	26/04/2015	11.1	02/11/2015	first planted 20.3.15	702	22167.1	67	maize	H614	28/03/2016	10.1			516	15280.02	196
L6	maize	H6210	26/03/2014	11.1	17/10/2014		maize	H628	24/04/2015	10.4	09/12/2015	first planted 20.3.15	879	25636	72	maize	H614	01/04/2016	10.1			677	16120	188
L7	maize	H6210	26/03/2014	11.1	27/10/2014		maize	H628	24/04/2015	10.4	08/12/2015	first planted 20.3.15	726	24607	49	maize	H614	11/03/2016	10.1			521	15490.01	134
L9	maize	H6210	20/03/2014	4	02/10/2014		maize	H628	08/04/2015	4	30/10/2015		317	13885.9	11	maize	H614	11/03/2016	4			224	9820	39
L9	-	-	-	-	-	isolation	-					isolation					-				-	isolation			
L10	maize	H6210	13/03/2014	12.1	18/09/2014		maize	H628	25/04/2015	10.1	26/11/2015	first planted 22.3.15	769	21870	83	maize	H614	21/04/2016	10.1			476	14465	74
L11	fallow						maize	H628	26/04/2015	20		planted by outsider				fallow								
L12	maize	H6210	26/03/2014	12	18/10/2014		maize	H628	25/04/2015	12.5	18/12/2015	first planted 21.3.15	810	28653	52	maize	H614	21/04/2016	12.5			560	17380	171
L13	fallow	-	-	-	-		maize	H628	26/04/2015	20		planted by outsider				fallow	-	-	-	-				
L14							fallow	-								maize	SIL		5.7	labour plots-people planted				
L15	maize	H6210	23/03/2014	6.2	14/10/2014		maize	H628	22/04/2015	6	09/10/2015	first planted 16.3.15	593	21866.2	12	maize	H614	22/03/2016	6			218	9820.04	99
L15	-	-	-	-	-	isolation	-					isolation					-				-	isolation			
L15	-	-	-	-	-	isolation	-					isolation					-				-	isolation			
L16	maize	H6210	23/03/2014	8	13/10/2014		maize	H628	22/04/2015	8	07/12/2015	first planted 16.3.15	608	20094.1	38	maize	H614	22/03/2016	8			427	11500.01	89

ID	crop	variety	plant	val	harvest	note	crop	variety	plant	val	harvest	note	n	n	n	crop	variety	plant	val	note	n	n	n
L17	maize	H6210	21/03/2014	19.1	03/10/2014		maize	H628	23/04/2015	18.1	03/12/2015	first planted 19.3.15	1496	39962	79	maize	H614	23/03/2016	18.2		1462	64220	170
L18	maize	H6210	22/03/2014	10.1	08/10/2014		maize	H628	23/04/2015	10.1	02/12/2015	first planted 17.3.15	711	25638	50	maize	H614	22/03/2016	10.1		476	11508.02	90
L18	fallow	-	-	-	-	isolation	fallow	-	-	-	-	isolation	-	-	-	-	-	-		isolation			
L19	maize	H6210	22/03/2014	8	07/10/2014		maize	H628	23/04/2015	8.1	02/12/2015	first planted 18.3.15	657	25834.5	52	maize	H614	23/03/2016	8		416	21782	91
L19	fallow	-	-	-	-	isolation	fallow	-	-	-	-	isolation								isolation			
L21	maize	KH600-23A		40		commercial	maize	COMM	28/02/2015	29.4			3298			maize	SIL	29/04/2016	10.2	combined for all	2839		
L21							maize	SIL	26/04/2015	9.6						maize	COMM	25/04/2016	29.8				
L21A	maize	SIL KH600-	11/03/2014	6																			
L21B	maize	SIL KH600-	27/04/2014	37.4																			
L26	maize	H6210	29/03/2014	16.1		not existing						not existing								not existing			
T1	maize	H6213	14/04/2014	22.1	14/11/2014		maize	H6213	26/03/2015	20.7	07/11/2015		1559	65822.6	100	maize	H6213	12/04/2016	20		1987	64448	452
T1A	maize	H6213	14/04/2014	19.3																			
T1B	maize	H6213	23/04/2014	2.8																			
T2	maize	H6213	23/04/2014	26	02/12/2014		maize	H6213	27/03/2015	24.1	19/10/2015		2341	94486	203	maize	H6213	16/04/2016	23		2478	80962.8	513
T3	Hay	Bomarhodes				existing	fallow									fallow				rough grazing			
T4	maize	H614		6		commercial	maize	COMM	27/02/2015	6			548			maize	COMM	17/03/2016	6		755		
T5	fallow	-	-	-	-	uncultivated	maize	H6213	15/04/2015	9.2	18/11/2015		591	26202	61	maize	H6213	21/04/2016	8		734	24170.7	38
T6	maize	H6213	21/04/2014	17.7	09/12/2014		maize	H6213	30/03/2015	16.7	16/11/2015		1492	52920	96	maize	H6213	18/04/2016	16		1478	48441	175
T7	fallow	-	-	-	-	uncultivated	Hay	Bomarhodes				established				Hay	Bomarhodes			existing			
T9							fallow	-	-	-	-	rough grazing				fallow	-	-	-	-	rough grazing		
T9A	maize	COMM KH6	09/03/2014	16	09/10/2014		fallow	-				rough grazing				fallow					rough grazing		
T9B	maize	COMM KH6	05/03/2014	11.5	14/11/2014		fallow	-				rough grazing				fallow					rough grazing		
T10-a	maize	COMM KH6	07/03/2014	11.3	26/09/2014		maize	COMM	26/02/2015	14.1		combined cob bags for all T10	2569			maize	COMM	11/04/2016	14	combined for all	1855		
T10-b	maize	COMM KH6	07/03/2014	10.1	20/09/2014		maize	COMM	27/02/2015	10.5						maize	COMM	11/04/2016	9				
T10-c	fallow	-	-	-			fallow	-	-	-		rough grazing					COMM	21/04/2016	1.2				
T11	maize	KH600-16A	11/03/2014	15.9	10/11/2014		maize	H6213	31/03/2015	20.5	19/11/2015		1507	42320.2	93	maize	H6213	18/04/2016	20.1		1685	52364	185
T11A	maize	KH600-16A	11/03/2014	10.7																			
T11B	maize	KH600-16A	21/04/2014	5.2																			
T12	maize	KH600-16A	11/03/2014	14.1	27/10/2014		maize	H6213	01/04/2015	12.5	24/11/2015		1090	39700	94	maize	H6213	19/04/2016	12.5		1124	32240	108
T13	fallow	-	-	-			Hay	Bomarhodes				established				Hay	Bomarhodes			existing			
T13							Hay	Bomarhodes				established				Hay	Bomarhodes			existing			
T14	maize	SIL KH600-	10/03/2014	1.2			fallow	-				rough grazing				fallow					rough grazing		
T15	maize	SIL KH600-	10/03/2014	5			maize	SIL	02/03/2015	5		cob bags harvested only for 1.	122			maize	SIL	02/04/2016	65.5				
T16	grazing	-					fallow	-	-	-	-	rough grazing				fallow					rough grazing		
T17	grazing	-					fallow	-	-	-	-	rough grazing				fallow					rough grazing		
T18	Hay	Bomarhode	-	-	-		Hay	Bomarhodes				established				fallow					rough grazing		
T19A	grazing	-					fallow	-	-	-	-	rough grazing				fallow					rough grazing		
T19B	Hay	Bomarhode	-	-	-		Hay	Bomarhodes				established				fallow					rough grazing		
T20	maize	H6213		26			maize	ADC Basic		6		research				maize	RESEA	16/04/2016	6				
T20	maize	ADC Basic		6		research	fallow	-				rough grazing				fallow					rough grazing		
T20	fallow						Hay	Bomarh	Oct-15			established				Hay	Bomarhodes			existing			
T23	maize	KH600-16A	09/04/2014	12.1	21/11/2014		fallow	-	-	-	-	individuals beans planting				maize	H6213	21/04/2016	10.1		1039	32224	184
T24	fallow	-	-	-	-		fallow	-	-	-	-	rough grazing				fallow					-		
T25	grazing	-					maize	SIL	28/02/2015	4						maize	SIL	03/04/2016	4				
T26	maize	H6210	27/03/2014	16.1	31/10/2014		maize	H628	02/04/2015	16.1	11/11/2015		1434	56916	176	maize	H614	26/03/2016	16.1		823	11070.01	134
T27	maize	H6210	12/03/2014	12.1	11/09/2014		maize	H628	14/04/2015	12.1	08/11/2015		880	32432	108	maize	H614	27/03/2016	12.1		763	19480.01	197
T28	maize	H6210	13/03/2014	11.1	15/09/2014		maize	H628	13/04/2015	10.1	21/11/2015		789	33260	120	maize	H614	28/03/2016	10.1		692	17805	152
T29	maize	H6210	18/03/2014	4	19/09/2014		maize	H628	14/04/2015	4	23/10/2015		425	16399.5	46	maize	H614	28/03/2016	4		280	10870	35
T30	maize	KH600-16A	10/04/2014	7.9	20/11/2014											maize	H6213	08/04/2016	20.4	20.1 real	1972	75576	220
T30	fallow	-		-		rest of T30	maize	H6213				planted earlier than other T30											
T30A	fallow	-		-			maize	H6213	09/04/2015	2.2													
T30B/T	fallow						maize	H6213	26/04/2015	9.5	01/12/2015		464	19850	48								
T31	fallow	-	-	-	-	one field separat	maize	H6213	20/04/2015	33.8	26/11/2015		2041	84958	214	maize	H6213	09/04/2016	30		3023	120437.2	573
T31	fallow	-																					
T33	fallow	-		-			maize	SIL	28/02/2015	4						maize	SIL		4	rest is fallow			
T34	maize	SIL KH600-	13/04/2014	8			maize	SIL	16/04/2015	21.4			745			maize	SIL	03/04/2016	20.3				
T35	wheat	ndovu					maize	H628	04/04/2015	9.5	11/11/2015		1111	36987	112	maize	H614	26/03/2016	10	9 real	743	25681	82
T35						isolation						isolation								isolation			
T36	maize	H626					maize	ADC SE	10/03/2015	7.5	06/10/2015		555		59	maize	ADC SE	25/04/2016	7.5		419		78
CAMP																							
T32-CAMP																							

A.3 Soil data

A.3.1 Collected field soil samples for texture and moisture analysis

SOIL MOISTURE CONTENT

FIELD NAME   F1

Date	Sample ID	Soil Depth	Wet Weight	Dry Weight (:	Moisture content	Notes
06/11/2015	1	0-20	66	58	8	
		20-40	60	52	8	
	2	0-20	60	54	6	
		20-40	60	58	2	
	3	0-20	54	50	4	
		20-40	68	58	10	
	4	0-20	66	56	10	
		20-40	52	46	6	
23/6/2015		0-10	62	52	10	16.12903
		10-20	68	60	8	
		20-30	70	60	10	
		30-40	58	50	8	
		40-60	60	52	8	

SOIL MOISTURE CONTENT
FIELD NAME   F2

Date	Sample ID	Soil Depth	Wet Weight	Dry Weight	Moisture content	Notes
06/10/2015	1	0-20	64	56	8	
		20-40	56	48	8	
	2	0-20	58	50	8	
		20-40	54	52	2	
	3	0-20	56	50	6	
		20-40	60	46	14	

SOIL MOISTURE CONTENT

FIELD NAME   K5

Date	Sample ID	Soil Depth	Wet Weight	Dry Weight	Moisture content	Notes
06/11/2015	1	0-20	54	44	10	
		20-40	64	52	12	
	2	0-20	56	46	10	
		20-40	50	42	8	
	3	0-20	62	52	10	
		20-40	66	54	12	

SOIL MOISTURE CONTENT

FIELD NAME   K5

Date	Sample ID	Soil Depth	Wet Weight	Dry Weight	Moisture content	Notes
06/11/2015	1	0-20	54	44	10	
		20-40	64	52	12	
	2	0-20	56	46	10	
		20-40	50	42	8	
	3	0-20	62	52	10	
		20-40	66	54	12	

SOIL MOISTURE CONTENT
FIELD NAME   S2

Date	Sample ID	Soil Depth	Wet Weight	Dry Weight	Moisture content	Notes
06/11/2015	1	0-20	50	42	8	
		20-40	56	48	8	
	2	0-20	58	48	10	
		20-40	56	46	10	
23/6/2015		0-10	54	48	6	11
		10-20	64	54	10	16
		20-30	64	56	8	13
		30-40	60	52	8	13
		40-60	62	52	10	16

SOIL MOISTURE CONTENT

FIELD NAME   H6

Date	Sample ID	Soil Depth	Wet Weight	Dry Weight	Moisture content	Notes
13/6/2015	1	0-20	52	44	8	
		20-40	48	40	8	
	2	0-20	54	44	10	
		20-40	50	42	8	
23/6/2015		0-10	58	46	12	
		10-20	60	46	14	
		20-30	68	56	12	
		30-40	56	50	6	
		40-60	54	46	8	

SOIL MOISTURE CONTENT
FIELD NAME   L6

Date	Sample ID	Soil Depth	Wet Weight	Dry Weight	Moisture content	Notes
13/6/2015	1	0-20	52	42	10	
		20-40	54	44	10	
	2	0-20	54	46	8	
		20-40	56	46	10	
	3	0-20	56	46	10	
		20-40	60	50	10	

SOIL MOISTURE CONTENT

FIELD NAME   L10

Date	Sample ID	Soil Depth	Wet Weight	Dry Weight	Moisture content	Notes
13/6/2015	1	0-20	44	36	8	
		20-40	48	40	8	
	2	0-20	46	38	8	
		20-40	60	50	10	
24/6/2015		0-10	52	44	8	
		10-20	56	46	10	
		20-30	56	46	10	
		30-40	54	44	10	
		40-60	62	50	12	

SOIL MOISTURE CONTENT

FIELD NAME   X4/1

Date	Sample ID	Soil Depth	Wet Weight	Dry Weight	Moisture content	Notes
24/6/2015		0-10	68	60	8	
		10-20	56	48	8	
		20-30	64	58	6	
		30-40	64	52	12	
		40-60	62	54	8	

A.3 Soil data

A.3.2 Soil carbon/nitrogen analysis results

<u>C/N   Herr Kuria</u>   kuria@geographie.uni-bonn.de

Probe	N%	C%	C/N Verhältnis	MW N%	MW C%	MW C/N Verhältnis
2016 1-1	0.215	2.58	11.9589	**0.217**	**2.56**	**11.8372**
2016 1-1	0.218	2.55	11.7155			
2016 1-2	0.147	1.72	11.7334	**0.149**	**1.72**	**11.5846**
2016 1-2	0.151	1.73	11.4357			
2016 1-3	0.203	2.47	12.1592	**0.201**	**2.46**	**12.2409**
2016 1-3	0.198	2.44	12.3225			
2016 1-4	0.176	2.17	12.3051	**0.175**	**2.16**	**12.3616**
2016 1-4	0.174	2.16	12.4181			
2016 1-5	0.199	2.48	12.4643	**0.197**	**2.48**	**12.5867**
2016 1-5	0.194	2.47	12.709			
2016 1-6	0.136	1.59	11.6858	**0.138**	**1.58**	**11.4361**
2016 1-6	0.140	1.57	11.1864			
2016 1-7	0.201	2.40	11.9744	**0.200**	**2.40**	**11.9885**
2016 1-7	0.199	2.39	12.0025			
2016 1-8	0.142	1.63	11.4584	**0.145**	**1.64**	**11.3565**
2016 1-8	0.147	1.65	11.2546			
2016 1-9	0.209	2.62	12.5363	**0.210**	**2.63**	**12.5133**
2016 1-9	0.212	2.65	12.4902			
2016 1-10	0.170	2.05	12.0609	**0.170**	**2.05**	**12.0292**
2016 1-10	0.171	2.05	11.9975			
2016 1-11	0.222	2.75	12.3981	**0.224**	**2.75**	**12.2962**
2016 1-11	0.226	2.75	12.1943			
2016 1-12	0.170	2.10	12.3661	**0.171**	**2.08**	**12.1133**
2016 1-12	0.173	2.05	11.8605			
2016 1-13	0.226	2.95	13.0294	**0.223**	**2.89**	**12.9681**
2016 1-13	0.219	2.83	12.9067			
2016 1-14	0.165	2.05	12.4575	**0.164**	**2.03**	**12.3915**
2016 1-14	0.164	2.01	12.3254			
2016 1-15	0.206	2.53	12.3032	**0.206**	**2.54**	**12.3027**
2016 1-15	0.207	2.54	12.3022			

A.3 Soil data

A.3.3 Soil texture analysis results

2016-1
Kuria, samples from Kenya

diameter μm	MW1	MW2	MW3	MW4	MW5	MW6
0.011	0.000	0.000	0.000	0.000	0.000	0.000
0.013	0.000	0.000	0.000	0.000	0.000	0.000
0.015	0.000	0.000	0.000	0.000	0.000	0.000
0.017	0.000	0.000	0.000	0.000	0.000	0.000
0.020	0.000	0.000	0.000	0.000	0.000	0.000
0.023	0.000	0.000	0.000	0.000	0.000	0.000
0.026	0.000	0.000	0.000	0.000	0.000	0.000
0.030	0.000	0.000	0.000	0.000	0.000	0.000
0.034	0.000	0.000	0.000	0.000	0.000	0.000
0.039	0.000	0.000	0.000	0.000	0.000	0.000
0.044	0.000	0.000	0.000	0.000	0.000	0.105
0.051	0.487	0.510	0.449	0.453	0.475	0.548
0.058	0.980	1,030	0.884	0.892	0.944	1,110
0.067	1,968	2,086	1,742	1,773	1,895	2,266
0.076	3,524	3,765	3,100	3,193	3,456	4,149
0.087	5,237	5,626	4,666	4,856	5,315	6,306
0.100	6,315	6,742	5,802	6,013	6,609	7,656
0.115	7,283	7,792	6,861	7,138	7,870	8,930
0.131	7,890	8,440	7,664	7,981	8,787	9,740
0.150	7,613	8,131	7,688	7,998	8,746	9,417
0.172	6,489	6,908	6,855	7,114	7,678	7,990
0.197	4,863	5,148	5,396	5,579	5,900	5,914
0.226	3,287	3,451	3,838	3,948	4,061	3,913
0.259	1,960	2,033	2,408	2,463	2,441	2,259
0.296	1,071	1,093	1,383	1,405	1,328	1,181
0.339	0.539	0.538	0.730	0.737	0.655	0.562
0.389	0.269	0.259	0.377	0.377	0.312	0.259
0.445	0.173	0.163	0.241	0.243	0.189	0.155
0.510	0.139	0.127	0.189	0.192	0.141	0.116
0.584	0.141	0.126	0.185	0.188	0.132	0.078
0.669	0.175	0.154	0.218	0.221	0.152	0.129
0.766	0.248	0.218	0.292	0.295	0.200	0.174
0.877	0.382	0.339	0.426	0.428	0.291	0.260
1,005	0.586	0.530	0.625	0.627	0.430	0.393
1,151	0.807	0.744	0.840	0.839	0.587	0.543
1,318	0.989	0.925	1,017	1,012	0.723	0.671
1,510	1,126	1,061	1,150	1,139	0.829	0.770
1,729	1,274	1,213	1,289	1,275	0.947	0.878
2,000	1,502	1,443	1,511	1,492	1,129	1,044
2,269	1,364	1,318	1,369	1,350	1,039	0.955
2,599	1,492	1,448	1,499	1,477	1,157	1,054
2,976	1,482	1,442	1,493	1,470	1,172	1,054
3,409	1,454	1,415	1,469	1,447	1,173	1,041
3,905	1,421	1,381	1,440	1,419	1,168	1,022
4,472	1,390	1,347	1,412	1,393	1,165	1,002
5,122	1,363	1,315	1,387	1,371	1,164	0.985
5,867	1,339	1,284	1,365	1,351	1,164	0.969
6,300	0.689	0.655	0.703	0.697	0.610	0.500
6,720	0.624	0.594	0.637	0.632	0.553	0.452
7,697	1,281	1,205	1,308	1,299	1,154	0.930
8,816	1,235	1,148	1,263	1,256	1,133	0.900
10,097	1,132	1,044	1,162	1,161	1,062	0.834
11,565	0.924	0.837	0.954	0.948	0.878	0.682
13,246	0.748	0.666	0.774	0.768	0.722	0.556
15,172	0.649	0.570	0.674	0.668	0.638	0.490
17,377	0.637	0.555	0.666	0.658	0.640	0.492
20,000	0.706	0.612	0.746	0.734	0.723	0.561
22,797	0.705	0.610	0.758	0.738	0.733	0.575
26,111	0.761	0.660	0.838	0.801	0.801	0.637

29,907	0.762	0.664	0.865	0.805	0.809	0.654
34,255	0.738	0.650	0.867	0.779	0.789	0.650
39,234	0.706	0.628	0.856	0.736	0.757	0.634
44,938	0.690	0.616	0.852	0.696	0.736	0.623
50,000	0.547	0.484	0.675	0.524	0.573	0.486
51,471	0.149	0.132	0.183	0.142	0.156	0.132
58,985	0.730	0.632	0.878	0.653	0.738	0.621
67,523	0.780	0.651	0.891	0.643	0.746	0.616
77,340	0.849	0.678	0.909	0.638	0.760	0.613
88,583	0.936	0.710	0.911	0.636	0.770	0.599
100,000	0.844	0.613	0.719	0.521	0.624	0.457
116,210	0.756	0.515	0.566	0.418	0.477	0.325
125,000	0.332	0.229	0.189	0.166	0.172	0.101
133,103	0.286	0.198	0.163	0.143	0.148	0.087
152,453	0.696	0.515	0.316	0.332	0.300	0.152
174,616	0.648	0.509	0.239	0.308	0.232	0.047
200,000	0.479	0.442	0.148	0.237	0.146	0.000
229,075	0.276	0.291	0.035	0.118	0.000	0.000
250,000	0.055	0.091	0.000	0.000	0.000	0.000
262,376	0.030	0.050	0.000	0.000	0.000	0.000
300,518	0.000	0.000	0.000	0.000	0.000	0.000
344,206	0.000	0.000	0.000	0.000	0.000	0.000
451,556	0.000	0.000	0.000	0.000	0.000	0.000
500,000	0.000	0.000	0.000	0.000	0.000	0.000
592,387	0.000	0.000	0.000	0.000	0.000	0.000
678,504	0.000	0.000	0.000	0.000	0.000	0.000
777,141	0.000	0.000	0.000	0.000	0.000	0.000
890,116	0.000	0.000	0.000	0.000	0.000	0.000
1,000,000	0.000	0.000	0.000	0.000	0.000	0.000
1,167,720	0.000	0.000	0.000	0.000	0.000	0.000
1,337,480	0.000	0.000	0.000	0.000	0.000	0.000
1,531,910	0.000	0.000	0.000	0.000	0.000	0.000
1,754,610	0.000	0.000	0.000	0.000	0.000	0.000
2,000,000	0.000	0.000	0.000	0.000	0.000	0.000
3,000,000	0.000	0.000	0.000	0.000	0.000	0.000

	q(%)							
MW7	MW8	MW9	MW10	MW11	MW12	MW13	MW14	MW15
0.000	0.000	0.000	0.000	0.000	0.000	0.000	0.000	0.000
0.000	0.000	0.000	0.000	0.000	0.000	0.000	0.000	0.000
0.000	0.000	0.000	0.000	0.000	0.000	0.000	0.000	0.000
0.000	0.000	0.000	0.000	0.000	0.000	0.000	0.000	0.000
0.000	0.000	0.000	0.000	0.000	0.000	0.000	0.000	0.000
0.000	0.000	0.000	0.000	0.000	0.000	0.000	0.000	0.000
0.000	0.000	0.000	0.000	0.000	0.000	0.000	0.000	0.000
0.000	0.000	0.000	0.000	0.000	0.000	0.000	0.000	0.000
0.000	0.000	0.000	0.000	0.000	0.000	0.000	0.000	0.000
0.000	0.000	0.000	0.000	0.000	0.000	0.000	0.000	0.000
0.000	0.315	0.000	0.204	0.000	0.000	0.000	0.308	0.000
0.502	0.580	0.515	0.553	0.480	0.521	0.509	0.573	0.482
1,002	1,188	1,030	1,121	0.939	1,027	1,044	1,186	0.951
2,018	2,451	2,082	2,288	1,863	2,054	2,139	2,452	1,895
3,675	4,513	3,806	4,193	3,394	3,756	3,868	4,462	3,442
5,625	6,844	5,839	6,390	5,286	5,841	5,724	6,600	5,302
6,959	8,228	7,227	7,800	6,732	7,391	6,759	7,703	6,646
8,255	9,508	8,575	9,143	8,185	8,935	7,664	8,695	7,975
9,182	10,257	9,534	10,030	9,351	10,137	8,151	9,169	8,988
9,102	9,768	9,440	9,768	9,574	10,281	7,680	8,538	9,068
7,955	8,133	8,235	8,361	8,682	9,213	6,363	6,970	8,102
6,084	5,886	6,284	6,249	6,914	7,233	4,619	4,971	6,366
4,167	3,797	4,292	4,178	4,939	5,084	3,019	3,185	4,498
2,491	2,132	2,559	2,439	3,084	3,118	1,739	1,793	2,789
1,346	1,083	1,380	1,289	1,740	1,725	0.920	0.924	1,570
0.659	0.500	0.675	0.620	0.889	0.864	0.449	0.439	0.806
0.310	0.224	0.317	0.288	0.435	0.414	0.218	0.207	0.400
0.183	0.131	0.187	0.168	0.263	0.246	0.137	0.129	0.249
0.133	0.035	0.133	0.120	0.193	0.177	0.078	0.070	0.188
0.120	0.000	0.118	0.107	0.173	0.158	0.078	0.069	0.174
0.134	0.073	0.126	0.115	0.187	0.169	0.132	0.124	0.193
0.173	0.137	0.155	0.142	0.230	0.208	0.184	0.176	0.242
0.246	0.203	0.210	0.193	0.310	0.280	0.279	0.271	0.331
0.361	0.306	0.295	0.272	0.429	0.387	0.428	0.421	0.461
0.497	0.426	0.398	0.367	0.561	0.505	0.599	0.591	0.602
0.621	0.533	0.497	0.457	0.675	0.606	0.751	0.740	0.724
0.725	0.619	0.585	0.536	0.764	0.682	0.876	0.857	0.818
0.840	0.714	0.680	0.622	0.858	0.762	1,014	0.989	0.919
1,017	0.859	0.832	0.757	1,010	0.891	1,227	1,188	1,081
0.950	0.794	0.786	0.713	0.923	0.808	1,141	1,095	0.988
1,074	0.886	0.902	0.814	1,024	0.887	1,282	1,215	1,096
1,102	0.896	0.940	0.843	1,034	0.886	1,309	1,223	1,107
1,115	0.893	0.964	0.859	1,031	0.872	1,319	1,212	1,105
1,120	0.885	0.980	0.866	1,022	0.852	1,323	1,193	1,097
1,121	0.875	0.989	0.867	1,010	0.829	1,328	1,174	1,088
1,120	0.867	0.992	0.863	0.998	0.806	1,336	1,156	1,080
1,117	0.860	0.990	0.854	0.985	0.783	1,347	1,140	1,072
0.581	0.447	0.514	0.440	0.508	0.398	0.711	0.589	0.557
0.526	0.405	0.466	0.398	0.460	0.360	0.644	0.533	0.505
1,085	0.841	0.957	0.813	0.946	0.730	1,354	1,098	1,044
1,049	0.823	0.919	0.777	0.913	0.697	1,336	1,064	1,016
0.965	0.771	0.842	0.709	0.842	0.639	1,255	0.986	0.945
0.783	0.639	0.678	0.570	0.686	0.517	1,046	0.807	0.777
0.629	0.529	0.542	0.455	0.557	0.420	0.861	0.658	0.635
0.542	0.473	0.464	0.392	0.488	0.371	0.757	0.580	0.561
0.529	0.482	0.452	0.384	0.489	0.377	0.749	0.582	0.563
0.581	0.555	0.498	0.426	0.557	0.440	0.829	0.665	0.642
0.574	0.570	0.496	0.427	0.572	0.467	0.821	0.685	0.658
0.611	0.624	0.539	0.465	0.638	0.541	0.871	0.767	0.731

0.603	0.623	0.551	0.473	0.662	0.583	0.848	0.797	0.753
0.577	0.591	0.558	0.473	0.665	0.606	0.794	0.802	0.750
0.547	0.542	0.572	0.472	0.655	0.608	0.730	0.787	0.734
0.533	0.498	0.608	0.485	0.643	0.588	0.684	0.763	0.718
0.421	0.373	0.520	0.403	0.496	0.433	0.519	0.578	0.554
0.114	0.101	0.141	0.109	0.135	0.118	0.141	0.157	0.151
0.561	0.477	0.736	0.563	0.617	0.497	0.665	0.705	0.697
0.600	0.468	0.812	0.632	0.585	0.422	0.688	0.660	0.676
0.653	0.513	0.904	0.724	0.555	0.352	0.725	0.621	0.657
0.723	0.562	0.996	0.852	0.506	0.274	0.782	0.573	0.623
0.661	0.489	0.864	0.822	0.351	0.159	0.709	0.422	0.461
0.571	0.390	0.677	0.721	0.227	0.019	0.654	0.303	0.322
0.252	0.145	0.237	0.296	0.045	0.000	0.312	0.093	0.100
0.217	0.125	0.204	0.255	0.039	0.000	0.269	0.080	0.086
0.515	0.249	0.371	0.509	0.000	0.000	0.749	0.170	0.152
0.455	0.181	0.241	0.344	0.000	0.000	0.835	0.122	0.041
0.309	0.084	0.095	0.166	0.000	0.000	0.767	0.092	0.000
0.140	0.038	0.000	0.000	0.000	0.000	0.557	0.056	0.000
0.000	0.000	0.000	0.000	0.000	0.000	0.198	0.000	0.000
0.000	0.000	0.000	0.000	0.000	0.000	0.110	0.000	0.000
0.000	0.000	0.000	0.000	0.000	0.000	0.000	0.000	0.000
0.000	0.000	0.000	0.000	0.000	0.000	0.000	0.000	0.000
0.000	0.000	0.000	0.000	0.000	0.000	0.000	0.000	0.000
0.000	0.000	0.000	0.000	0.000	0.000	0.000	0.000	0.000
0.000	0.000	0.000	0.000	0.000	0.000	0.000	0.000	0.000
0.000	0.000	0.000	0.000	0.000	0.000	0.000	0.000	0.000
0.000	0.000	0.000	0.000	0.000	0.000	0.000	0.000	0.000
0.000	0.000	0.000	0.000	0.000	0.000	0.000	0.000	0.000
0.000	0.000	0.000	0.000	0.000	0.000	0.000	0.000	0.000
0.000	0.000	0.000	0.000	0.000	0.000	0.000	0.000	0.000
0.000	0.000	0.000	0.000	0.000	0.000	0.000	0.000	0.000
0.000	0.000	0.000	0.000	0.000	0.000	0.000	0.000	0.000
0.000	0.000	0.000	0.000	0.000	0.000	0.000	0.000	0.000
0.000	0.000	0.000	0.000	0.000	0.000	0.000	0.000	0.000

Labor-Nr.	:	2016-1
Datenbezeichnung	:	MW1
Arbeitsgruppe	:	Prof Menz
Brechungsindex (R)	:	1.60-0.10i(1.33)[1.60-0.10(1.600 - 0.100i),1.33(1.333)]
Brechungsindex (B)	:	1.60-0.10i(1.33)[1.60-0.10(1.600 - 0.100i),1.33(1.333)]
Techniker/in	:	Kuria

2016.02.04 10:19:40

Median	:	0.18303(µm)	Q(x)-Wert :	(1)2000 (µm)-	100.000(%)
Modalwert	:	0.1229(µm)	:	(2)630.0 (µm)-	100.000(%)
D10	:	0.08248(µm)	:	(3)200.0 (µm)-	99.639(%)
D90	:	32.95662(µm)	:	(4)63.00 (µm)-	93.410(%)
R-Parameter	:	6.4754E-2	:	(5)20.00 (µm)-	87.245(%)
			:	(6)6.300 (µm)-	79.310(%)
			:	(7)2.000 (µm)-	67.315(%)

x(Q)-Wert :
(1)5.000 (%)-	0.0707(µm)
(2)10.00 (%)-	0.0825(µm)
(3)20.00 (%)-	0.1028(µm)
(4)30.00 (%)-	0.1231(µm)
(5)50.00 (%)-	0.1830(µm)
(6)60.00 (%)-	0.4694(µm)
(7)70.00 (%)-	2.5584(µm)
(8)80.00 (%)-	6.7668(µm)
(9)90.00 (%)-	32.9566(µm)
(10)95.00 (%)-	81.2465(µm)

Datenbezeichnung	Darstellung	Datum
MW1		Donnerstag, 4. Februar 2016 10:19:40

Labor-Nr.	: 2016-1	
Datenbezeichnung	: MW2	
Arbeitsgruppe	: Prof Menz	2016.02.04 10:56:07
Brechungsindex (R)	: 1.60-0.10i(1.33)[1.60-0.10(1.600 - 0.100i),1.33(1.333)]	
Brechungsindex (B)	: 1.60-0.10i(1.33)[1.60-0.10(1.600 - 0.100i),1.33(1.333)]	
Techniker/in	: Kuria	

Median	: 0.16865(µm)	Q(x)-Wert :	(1)2000 (µm)- 100.000(%)	x(Q)-Wert :	(1)5.000 (%)- 0.0699(µm)
Modalwert	: 0.1229(µm)	:	(2)630.0 (µm)- 100.000(%)	:	(2)10.00 (%)- 0.0812(µm)
D10	: 0.08118(µm)	:	(3)200.0 (µm)- 99.567(%)	:	(3)20.00 (%)- 0.1004(µm)
D90	: 22.59241(µm)	:	(4)63.00 (µm)- 94.825(%)	:	(4)30.00 (%)- 0.1191(µm)
R-Parameter	: 7.2979E-2	:	(5)20.00 (µm)- 89.432(%)	:	(5)50.00 (%)- 0.1687(µm)
		:	(6)6.300 (µm)- 82.201(%)	:	(6)60.00 (%)- 0.2314(µm)
		:	(7)2.000 (µm)- 70.596(%)	:	(7)70.00 (%)- 1.8835(µm)
				:	(8)80.00 (%)- 4.9858(µm)
				:	(9)90.00 (%)- 22.5924(µm)
				:	(10)95.00 (%)- 65.3280(µm)

Datenbezeichnung	Darstellung	Datum
MW2		*Donnerstag, 4. Februar 2016 10:56:07*

Labor-Nr.	: 2016-1	
Datenbezeichnung	: MW3	2016.02.04 11:19:51
Arbeitsgruppe	: Prof Menz	
Brechungsindex (R)	: 1.60-0.10i(1.33)[1.60-0.10(1.600 - 0.100i),1.33(1.333)]	
Brechungsindex (B)	: 1.60-0.10i(1.33)[1.60-0.10(1.600 - 0.100i),1.33(1.333)]	
Techniker/in	: Kuria	

Median	: 0.19162(μm)	Q(x)-Wert : (1)2000 (μm)- 100.000(%)	x(Q)-Wert : (1)5.000 (%)- 0.0724(μm)
Modalwert	: 0.1394(μm)	: (2)630.0 (μm)- 100.000(%)	: (2)10.00 (%)- 0.0852(μm)
D10	: 0.08520(μm)	: (3)200.0 (μm)- 99.965(%)	: (3)20.00 (%)- 0.1069(μm)
D90	: 27.21108(μm)	: (4)63.00 (μm)- 95.347(%)	: (4)30.00 (%)- 0.1285(μm)
R-Parameter	: 5.7840E-2	: (5)20.00 (μm)- 88.141(%)	: (5)50.00 (%)- 0.1916(μm)
		: (6)6.300 (μm)- 79.958(%)	: (6)60.00 (%)- 0.4251(μm)
		: (7)2.000 (μm)- 67.823(%)	: (7)70.00 (%)- 2.4411(μm)
			: (8)80.00 (%)- 6.3271(μm)
			: (9)90.00 (%)- 27.2111(μm)
			: (10)95.00 (%)- 59.7658(μm)

Datenbezeichnung	Darstellung	Datum
MW3		*Donnerstag, 4. Februar 2016 11:19:51*

Labor-Nr.   : 2016-1
Datenbezeichnung   : MW4
Arbeitsgruppe   : Prof Menz
Brechungsindex (R)   : 1.60-0.10i(1.33)[1.60-0.10(1.600 - 0.100i),1.33(1.333)]
Brechungsindex (B)   : 1.60-0.10i(1.33)[1.60-0.10(1.600 - 0.100i),1.33(1.333)]
Techniker/in   : Kuria

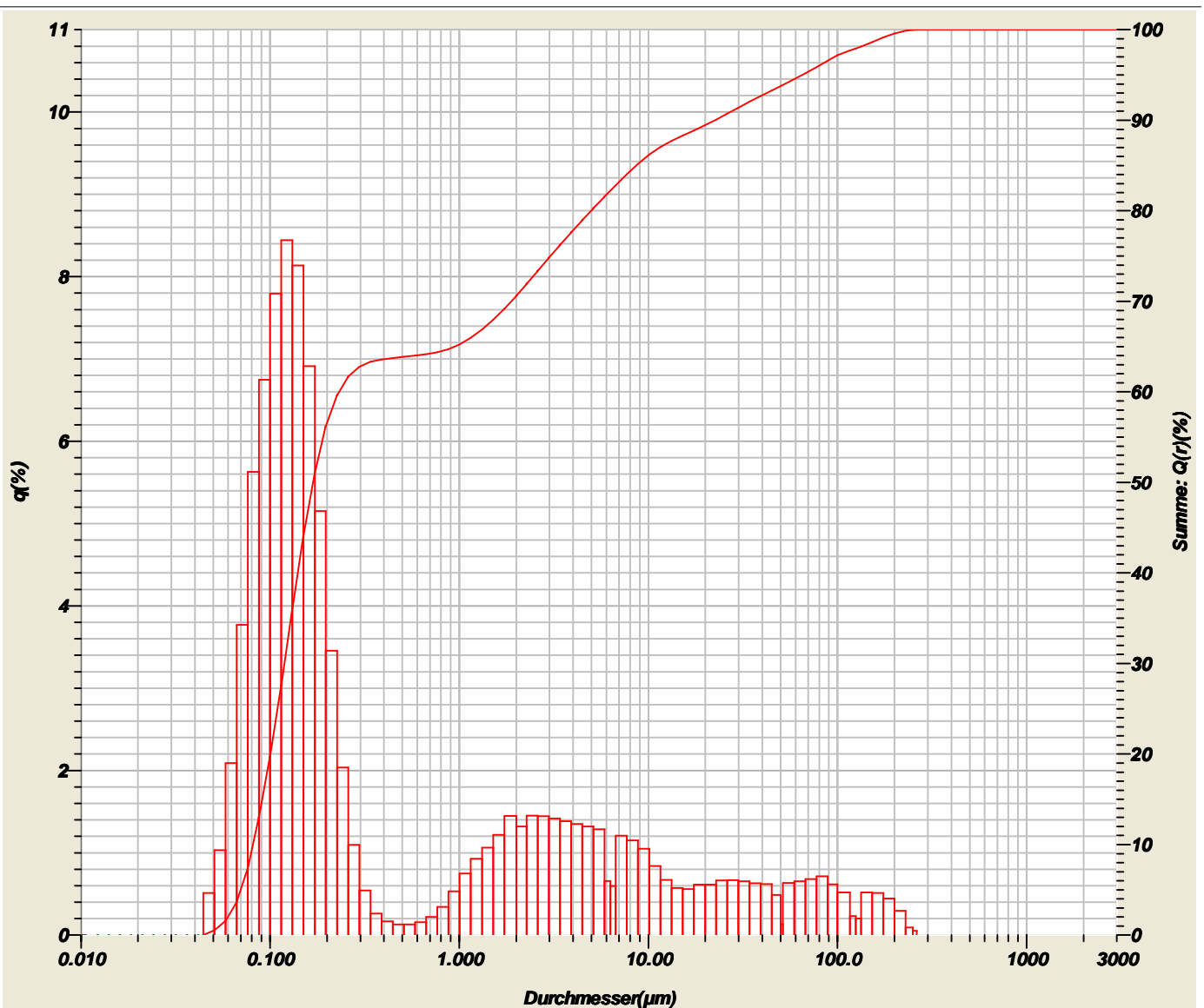2016.02.05 10:45:32

Median : 0.18323(µm)	Q(x)-Wert : (1)2000 (µm)- 100.000(%)	x(Q)-Wert : (1)5.000 (%)- 0.0721(µm)
Modalwert : 0.1394(µm)	: (2)630.0 (µm)- 100.000(%)	: (2)10.00 (%)- 0.0845(µm)
D10 : 0.08451(µm)	: (3)200.0 (µm)- 99.882(%)	: (3)20.00 (%)- 0.1055(µm)
D90 : 20.11374(µm)	: (4)63.00 (µm)- 96.154(%)	: (4)30.00 (%)- 0.1262(µm)
R-Parameter : 6.1597E-2	: (5)20.00 (µm)- 89.968(%)	: (5)50.00 (%)- 0.1832(µm)
	: (6)6.300 (µm)- 81.846(%)	: (6)60.00 (%)- 0.2740(µm)
	: (7)2.000 (µm)- 69.871(%)	: (7)70.00 (%)- 2.0241(µm)
		: (8)80.00 (%)- 5.2271(µm)
		: (9)90.00 (%)- 20.1137(µm)
		: (10)95.00 (%)- 49.5362(µm)

Datenbezeichnung Darstellung Datum
MW4   Freitag, 5. Februar 2016 10:45:32

Labor-Nr.   : 2016-1
Datenbezeichnung   : MW5
Arbeitsgruppe   : Prof Menz
Brechungsindex (R) : 1.60-0.10i(1.33)[1.60-0.10(1.600 - 0.100i),1.33(1.333)]
Brechungsindex (B) : 1.60-0.10i(1.33)[1.60-0.10(1.600 - 0.100i),1.33(1.333)]
Techniker/in   : Kuria

2016.02.05 11:25:28

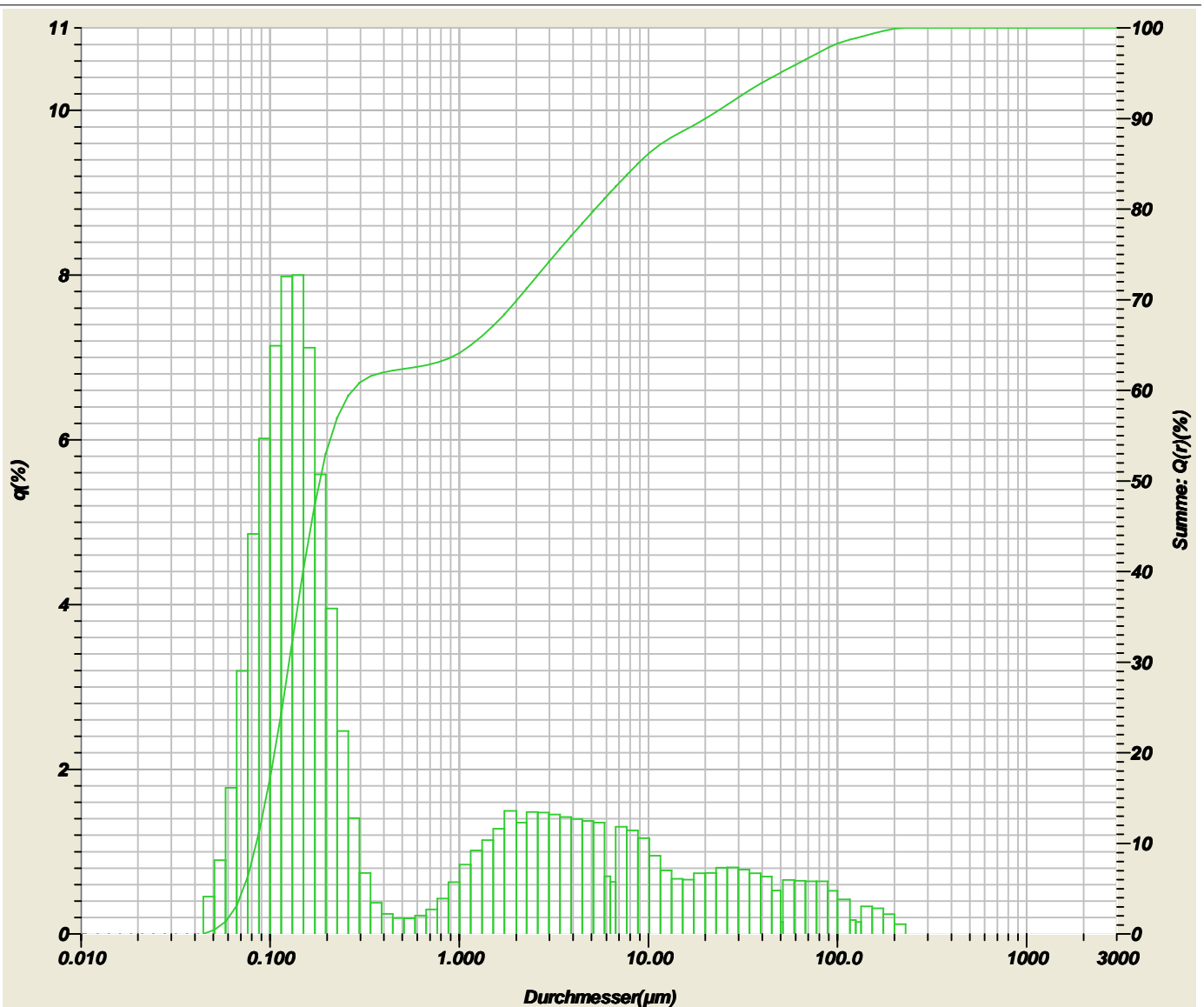|		Q(x)-Wert		x(Q)-Wert	
Median	: 0.16678(µm)	: (1)2000 (µm)- 100.000(%)		: (1)5.000 (%)- 0.0711(µm)	
Modalwert	: 0.1234(µm)	: (2)630.0 (µm)- 100.000(%)		: (2)10.00 (%)- 0.0828(µm)	
D10	: 0.08278(µm)	: (3)200.0 (µm)- 100.000(%)		: (3)20.00 (%)- 0.1023(µm)	
D90	: 21.73776(µm)	: (4)63.00 (µm)- 95.988(%)		: (4)30.00 (%)- 0.1208(µm)	
R-Parameter	: 6.1385E-2	: (5)20.00 (µm)- 89.533(%)		: (5)50.00 (%)- 0.1668(µm)	
		: (6)6.300 (µm)- 82.032(%)		: (6)60.00 (%)- 0.2130(µm)	
		: (7)2.000 (µm)- 72.220(%)		: (7)70.00 (%)- 1.4747(µm)	
				: (8)80.00 (%)- 4.9710(µm)	
				: (9)90.00 (%)- 21.7378(µm)	
				: (10)95.00 (%)- 52.5593(µm)	

Labor-Nr.   : 2016-1
Datenbezeichnung   : MW6
Arbeitsgruppe   : Prof Menz
Brechungsindex (R)   : 1.60-0.10i(1.33)[1.60-0.10(1.600 - 0.100i),1.33(1.333)]
Brechungsindex (B)   : 1.60-0.10i(1.33)[1.60-0.10(1.600 - 0.100i),1.33(1.333)]
Techniker/in   : Kuria

2016.02.05 11:05:13

Median	: 0.14977(µm)	Q(x)-Wert : (1)2000 (µm)- 100.000(%)	x(Q)-Wert : (1)5.000 (%)- 0.0687(µm)
Modalwert	: 0.1230(µm)	: (2)630.0 (µm)- 100.000(%)	: (2)10.00 (%)- 0.0793(µm)
D10	: 0.07928(µm)	: (3)200.0 (µm)- 100.000(%)	: (3)20.00 (%)- 0.0963(µm)
D90	: 11.87565(µm)	: (4)63.00 (µm)- 97.302(%)	: (4)30.00 (%)- 0.1127(µm)
R-Parameter	: 6.3676E-2	: (5)20.00 (µm)- 91.990(%)	: (5)50.00 (%)- 0.1498(µm)
		: (6)6.300 (µm)- 86.093(%)	: (6)60.00 (%)- 0.1793(µm)
		: (7)2.000 (µm)- 77.513(%)	: (7)70.00 (%)- 0.2540(µm)
			: (8)80.00 (%)- 2.7638(µm)
			: (9)90.00 (%)- 11.8757(µm)
			: (10)95.00 (%)- 38.0731(µm)

Datenbezeichnung Darstellung Datum
MW6   Freitag, 5. Februar 2016 11:05:13

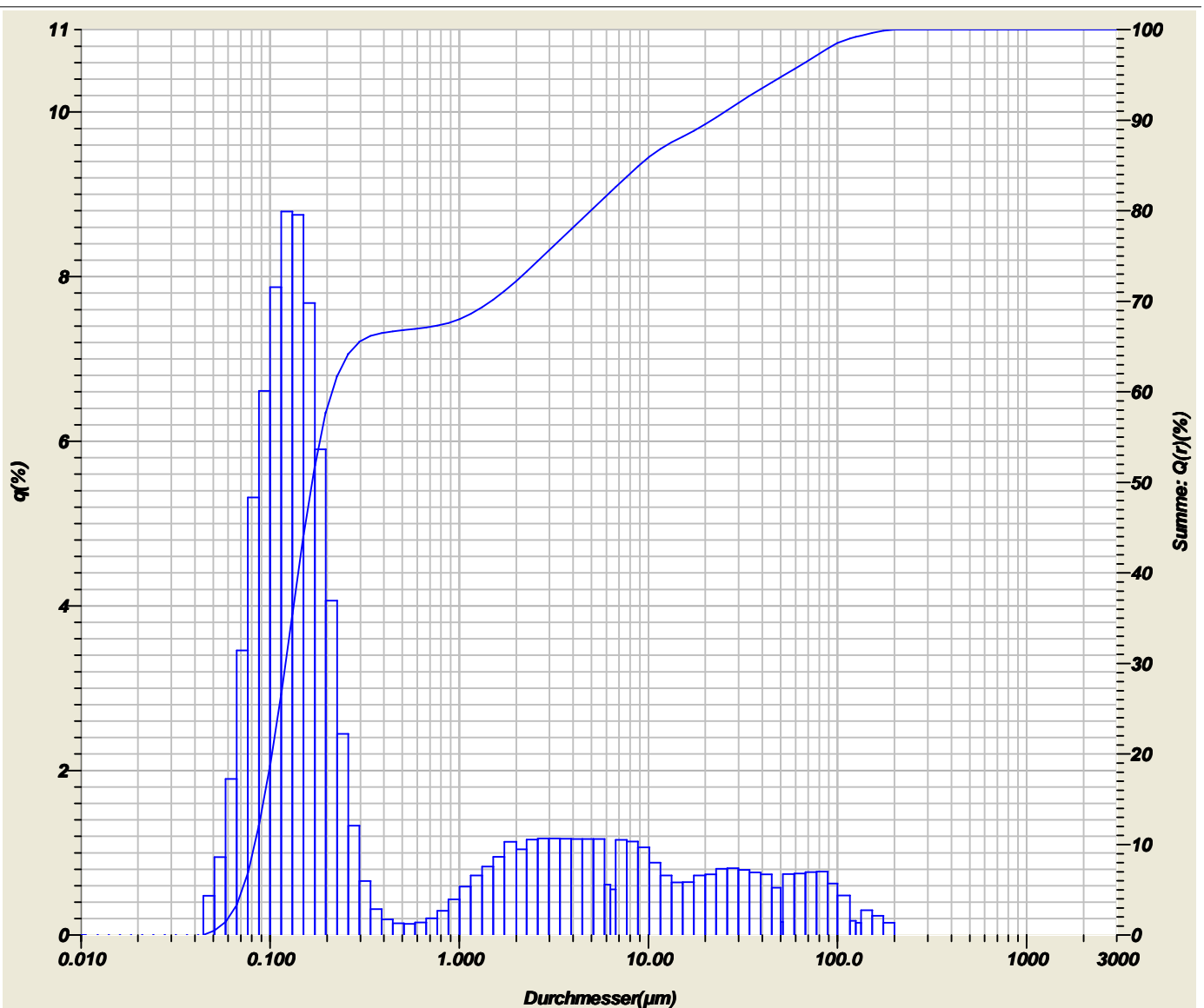|		
Labor-Nr.	:	2016-1
Datenbezeichnung	:	MW7
Arbeitsgruppe	:	Prof Menz
Brechungsindex (R)	:	1.60-0.10i(1.33)[1.60-0.10(1.600 - 0.100i),1.33(1.333)]
Brechungsindex (B)	:	1.60-0.10i(1.33)[1.60-0.10(1.600 - 0.100i),1.33(1.333)]
Techniker/in	:	Kuria

2016.02.04 11:41:10

			Q(x)-Wert		x(Q)-Wert	
Median	:	0.16000(µm)	: (1)2000 (µm)- 100.000(%)		: (1)5.000 (%)- 0.0703(µm)
Modalwert	:	0.1234(µm)	: (2)630.0 (µm)- 100.000(%)		: (2)10.00 (%)- 0.0816(µm)
D10	:	0.08156(µm)	: (3)200.0 (µm)- 99.861(%)		: (3)20.00 (%)- 0.1004(µm)
D90	:	18.30566(µm)	: (4)63.00 (µm)- 95.198(%)		: (4)30.00 (%)- 0.1179(µm)
R-Parameter	:	6.4699E-2	: (5)20.00 (µm)- 90.366(%)		: (5)50.00 (%)- 0.1600(µm)
			: (6)6.300 (µm)- 83.679(%)		: (6)60.00 (%)- 0.1954(µm)
			: (7)2.000 (µm)- 74.380(%)		: (7)70.00 (%)- 0.7229(µm)
					: (8)80.00 (%)- 4.0295(µm)
					: (9)90.00 (%)- 18.3057(µm)
					: (10)95.00 (%)- 60.2496(µm)

Datenbezeichnung	Darstellung	Datum
MW7		*Donnerstag, 4. Februar 2016 11:41:10*

Labor-Nr.	:	2016-1
Datenbezeichnung	:	MW8
Arbeitsgruppe	:	Prof Menz
Brechungsindex (R)	:	1.60-0.10i(1.33)[1.60-0.10(1.600 - 0.100i),1.33(1.333)]
Brechungsindex (B)	:	1.60-0.10i(1.33)[1.60-0.10(1.600 - 0.100i),1.33(1.333)]
Techniker/in	:	Kuria

2016.02.05 11:43:16

Median	:	0.14283(µm)	Q(x)-Wert :	(1)2000 (µm)- 100.000(%)	x(Q)-Wert :	(1)5.000 (%)-	0.0675(µm)
Modalwert	:	0.1228(µm)	:	(2)630.0 (µm)- 100.000(%)	:	(2)10.00 (%)-	0.0777(µm)
D10	:	0.07768(µm)	:	(3)200.0 (µm)- 99.962(%)	:	(3)20.00 (%)-	0.0934(µm)
D90	:	10.80694(µm)	:	(4)63.00 (µm)- 96.985(%)	:	(4)30.00 (%)-	0.1088(µm)
R-Parameter	:	6.2760E-2	:	(5)20.00 (µm)- 92.358(%)	:	(5)50.00 (%)-	0.1428(µm)
			:	(6)6.300 (µm)- 86.840(%)	:	(6)60.00 (%)-	0.1671(µm)
			:	(7)2.000 (µm)- 79.438(%)	:	(7)70.00 (%)-	0.2142(µm)
					:	(8)80.00 (%)-	2.1866(µm)
					:	(9)90.00 (%)-	10.8069(µm)
					:	(10)95.00 (%)-	36.3224(µm)

Datenbezeichnung	Darstellung	Datum
MW8		Freitag, 5. Februar 2016 11:43:16

Labor-Nr.   : 2016-1
Datenbezeichnung   : MW9
Arbeitsgruppe   : Prof Menz
Brechungsindex (R)   : 1.60-0.10i(1.33)[1.60-0.10(1.600 - 0.100i),1.33(1.333)]
Brechungsindex (B)   : 1.60-0.10i(1.33)[1.60-0.10(1.600 - 0.100i),1.33(1.333)]
Techniker/in   : Kuria

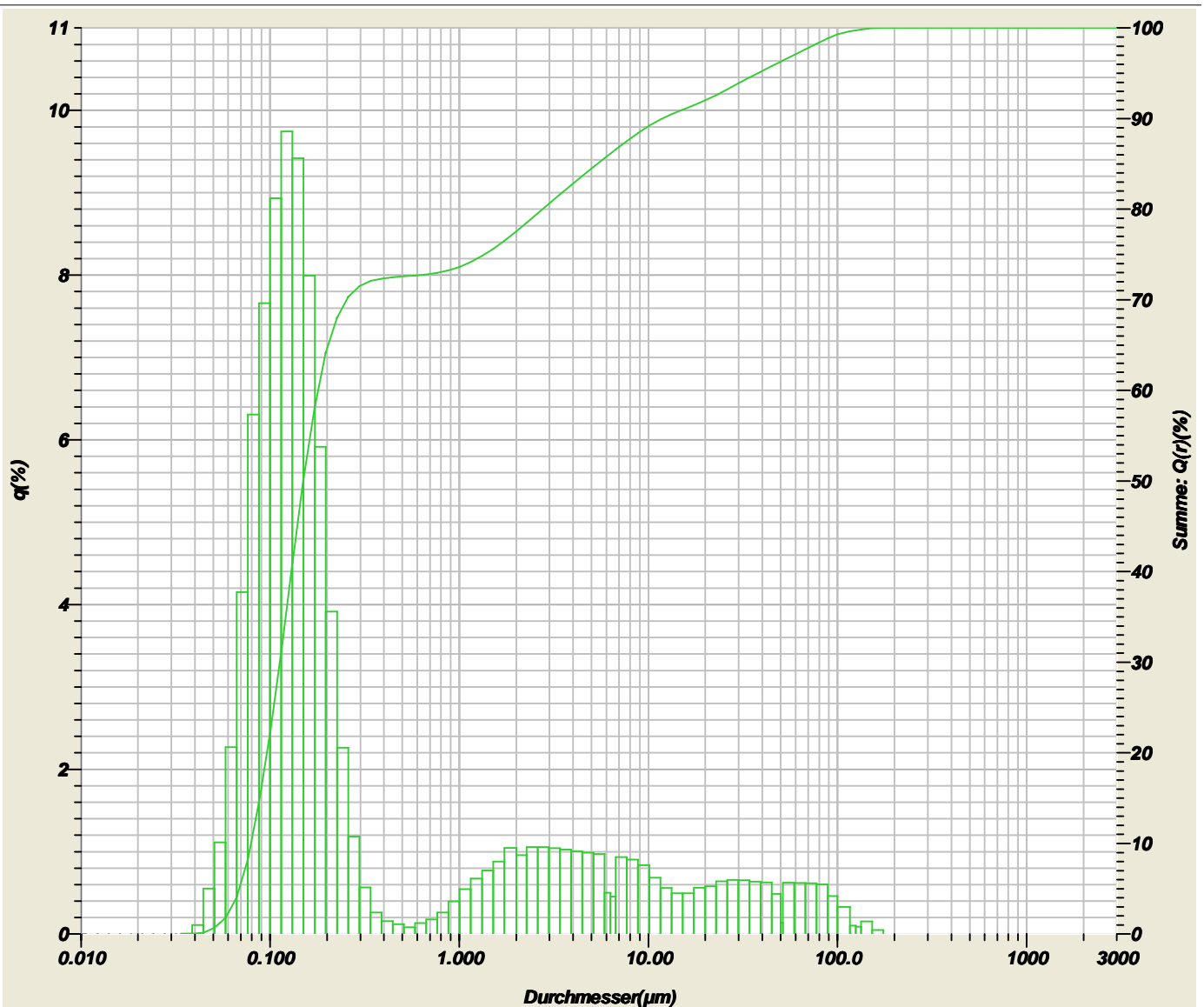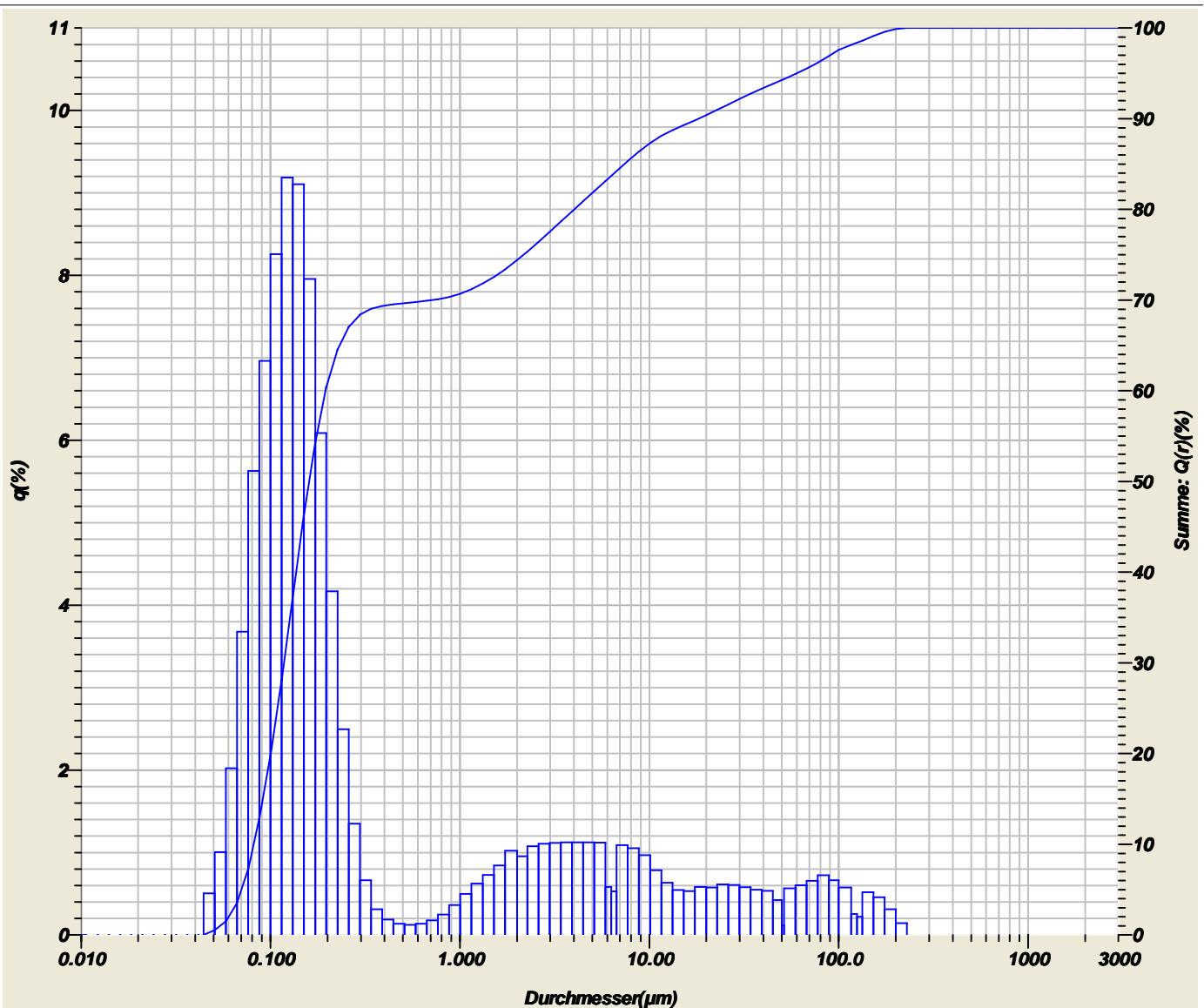2016.02.05 09:20:29

Median : 0.15517(µm)	Q(x)-Wert : (1)2000 (µm)- 100.000(%)	x(Q)-Wert : (1)5.000 (%)- 0.0699(µm)
Modalwert : 0.1233(µm)	: (2)630.0 (µm)- 100.000(%)	: (2)10.00 (%)- 0.0809(µm)
D10 : 0.08092(µm)	: (3)200.0 (µm)- 100.000(%)	: (3)20.00 (%)- 0.0991(µm)
D90 : 20.65955(µm)	: (4)63.00 (µm)- 94.993(%)	: (4)30.00 (%)- 0.1161(µm)
R-Parameter : 6.8718E-2	: (5)20.00 (µm)- 89.877(%)	: (5)50.00 (%)- 0.1552(µm)
	: (6)6.300 (µm)- 84.060(%)	: (6)60.00 (%)- 0.1864(µm)
	: (7)2.000 (µm)- 76.003(%)	: (7)70.00 (%)- 0.2739(µm)
		: (8)80.00 (%)- 3.6058(µm)
		: (9)90.00 (%)- 20.6595(µm)
		: (10)95.00 (%)- 63.0732(µm)

Datenbezeichnung Darstellung Datum
MW9   Freitag, 5. Februar 2016 09:20:29

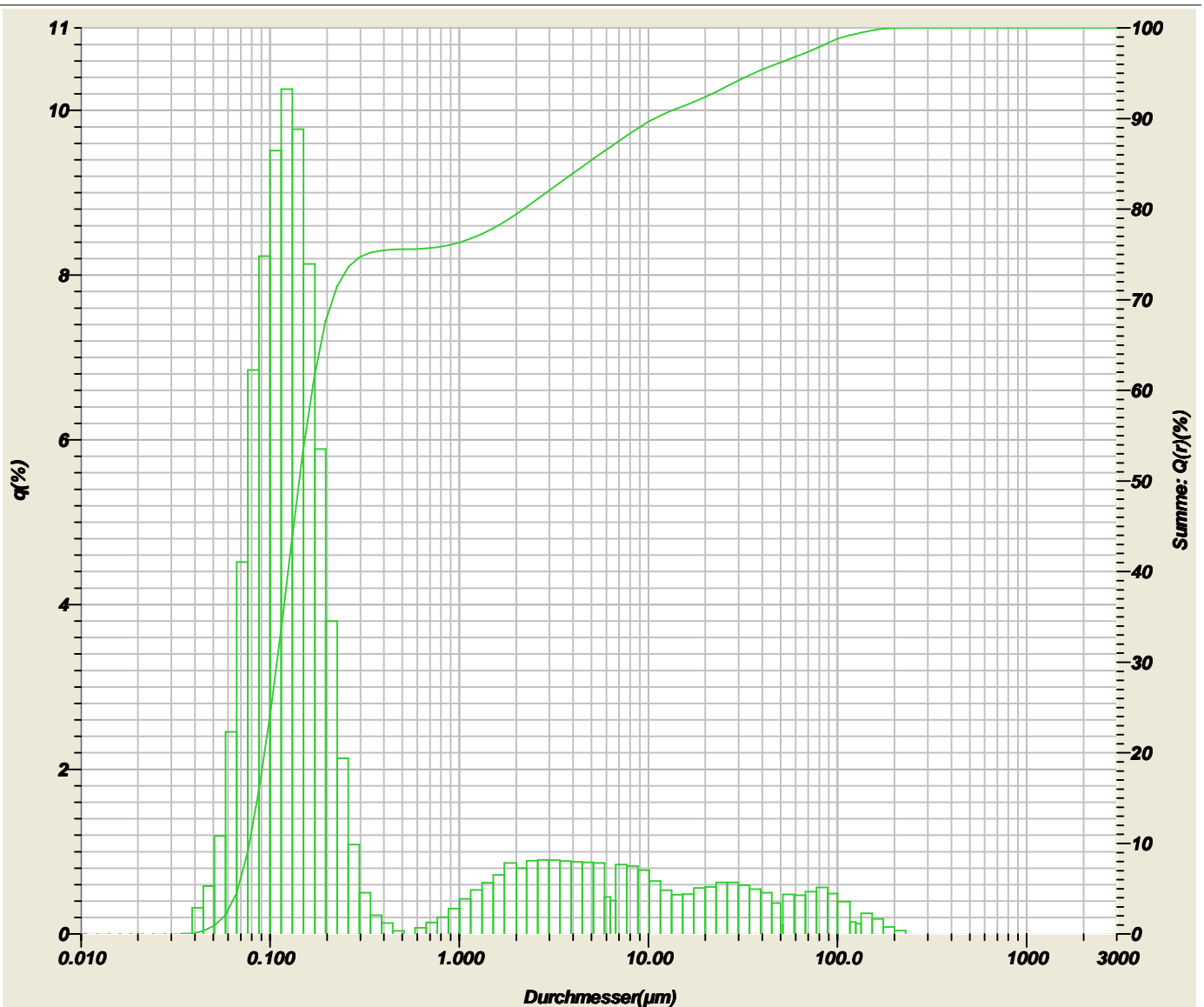| Labor-Nr. | : 2016-1 |
Datenbezeichnung	: MW10
Arbeitsgruppe	: Prof Menz
Brechungsindex (R)	: 1.60-0.10i(1.33)[1.60-0.10(1.600 - 0.100i),1.33(1.333)]
Brechungsindex (B)	: 1.60-0.10i(1.33)[1.60-0.10(1.600 - 0.100i),1.33(1.333)]
Techniker/in	: Kuria

2016.02.05 09:41:35

Median	: 0.14718(µm)
Modalwert	: 0.1231(µm)
D10	: 0.07893(µm)
D90	: 15.17286(µm)
R-Parameter	: 6.4951E-2

Q(x)-Wert :
(1)2000 (µm)- 100.000(%)
(2)630.0 (µm)- 100.000(%)
(3)200.0 (µm)- 100.000(%)
(4)63.00 (µm)- 94.987(%)
(5)20.00 (µm)- 90.809(%)
(6)6.300 (µm)- 85.886(%)
(7)2.000 (µm)- 78.768(%)

x(Q)-Wert :
(1)5.000 (%)- 0.0684(µm)
(2)10.00 (%)- 0.0789(µm)
(3)20.00 (%)- 0.0957(µm)
(4)30.00 (%)- 0.1117(µm)
(5)50.00 (%)- 0.1472(µm)
(6)60.00 (%)- 0.1727(µm)
(7)70.00 (%)- 0.2237(µm)
(8)80.00 (%)- 2.4739(µm)
(9)90.00 (%)- 15.1729(µm)
(10)95.00 (%)- 63.1793(µm)

| Datenbezeichnung | Darstellung | Datum |
| MW10 | | Freitag, 5. Februar 2016 09:41:35 |

Labor-Nr.   : 2016-1
Datenbezeichnung   : MW11
Arbeitsgruppe   : Prof Menz   2016.02.05 12:00:31
Brechungsindex (R) : 1.60-0.10i(1.33)[1.60-0.10(1.600 - 0.100i),1.33(1.333)]
Brechungsindex (B) : 1.60-0.10i(1.33)[1.60-0.10(1.600 - 0.100i),1.33(1.333)]
Techniker/in   : Kuria

Median : 0.16044(µm)	Q(x)-Wert : (1)2000 (µm)- 100.000(%)	x(Q)-Wert : (1)5.000 (%)- 0.0713(µm)
Modalwert : 0.1397(µm)	: (2)630.0 (µm)- 100.000(%)	: (2)10.00 (%)- 0.0830(µm)
D10 : 0.08302(µm)	: (3)200.0 (µm)- 100.000(%)	: (3)20.00 (%)- 0.1022(µm)
D90 : 10.43318(µm)	: (4)63.00 (µm)- 97.979(%)	: (4)30.00 (%)- 0.1198(µm)
R-Parameter : 5.7946E-2	: (5)20.00 (µm)- 92.611(%)	: (5)50.00 (%)- 0.1604(µm)
	: (6)6.300 (µm)- 86.674(%)	: (6)60.00 (%)- 0.1917(µm)
	: (7)2.000 (µm)- 78.138(%)	: (7)70.00 (%)- 0.2705(µm)
		: (8)80.00 (%)- 2.5693(µm)
		: (9)90.00 (%)- 10.4332(µm)
		: (10)95.00 (%)- 33.2323(µm)

Datenbezeichnung Darstellung Datum
MW11   Freitag, 5. Februar 2016 12:00:31

Labor-Nr.   : 2016-1
Datenbezeichnung   : MW12
Arbeitsgruppe   : Prof Menz
Brechungsindex (R)   : 1.60-0.10i(1.33)[1.60-0.10(1.600 - 0.100i),1.33(1.333)]
Brechungsindex (B)   : 1.60-0.10i(1.33)[1.60-0.10(1.600 - 0.100i),1.33(1.333)]
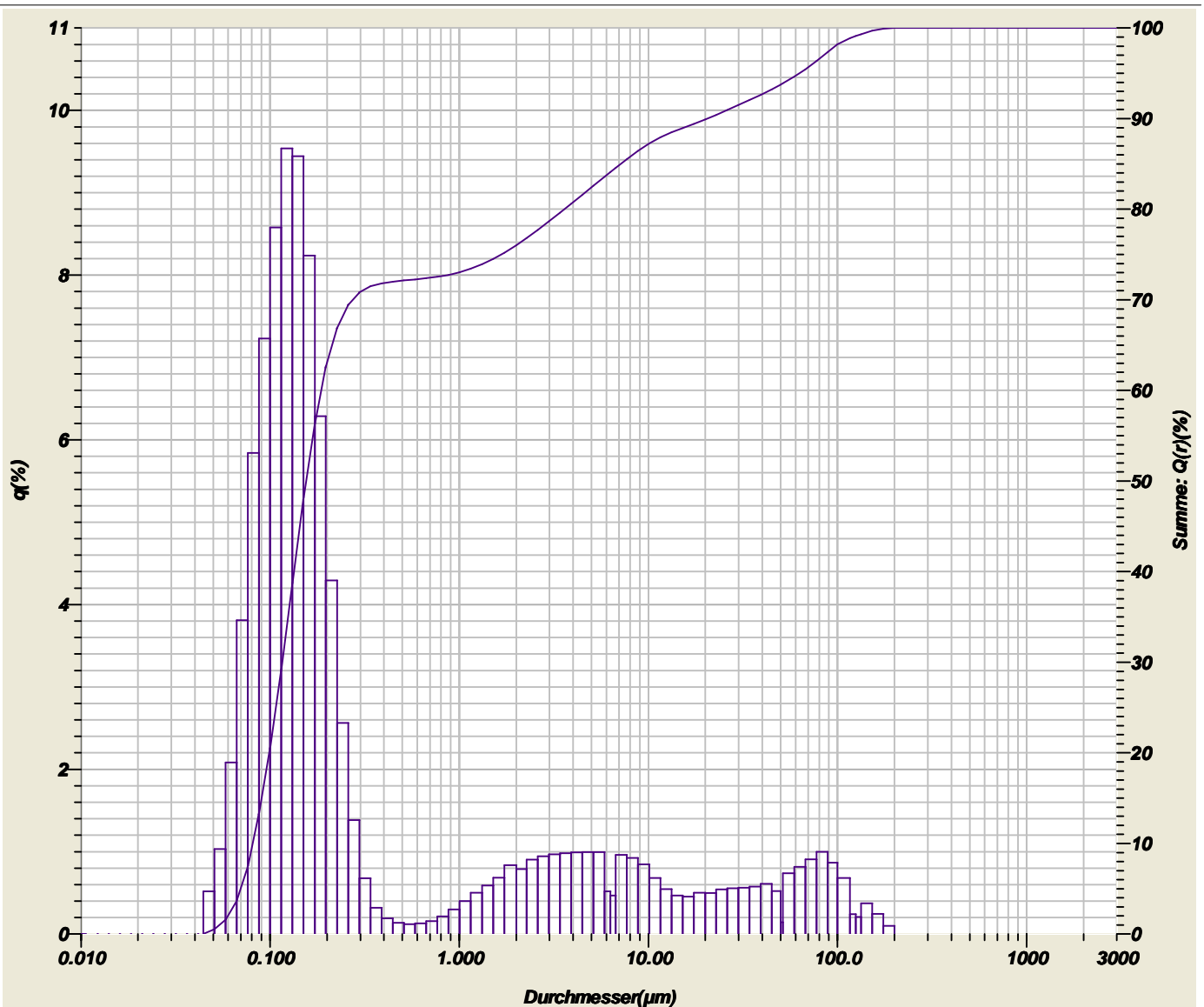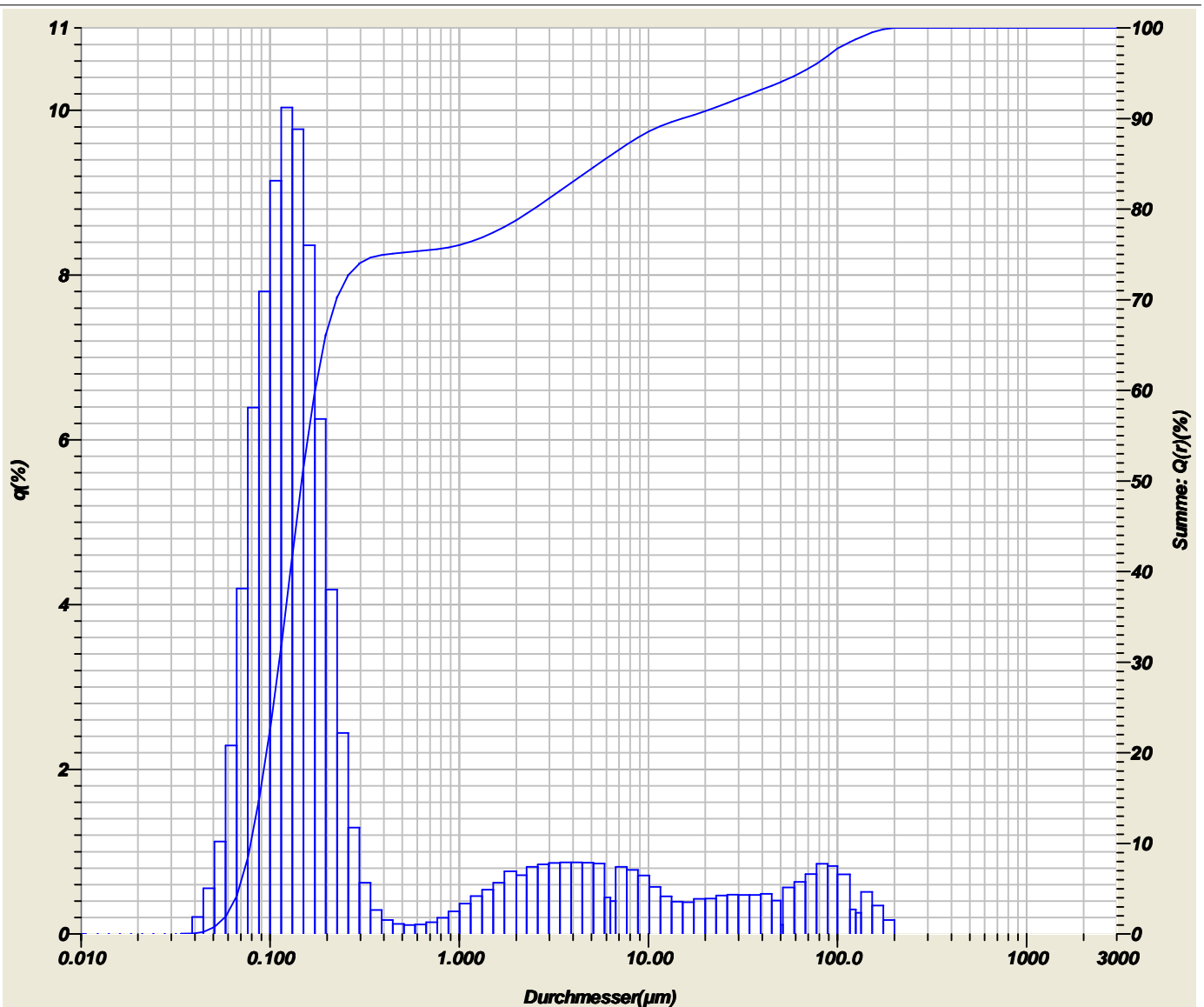Techniker/in   : Kuria

2016.02.05 12:34:24

Median	: 0.15039(µm)	Q(x)-Wert :	(1)2000 (µm)- 100.000(%)	x(Q)-Wert :	(1)5.000 (%)- 0.0700(µm)
Modalwert	: 0.1395(µm)	:	(2)630.0 (µm)- 100.000(%)	:	(2)10.00 (%)- 0.0811(µm)
D10	: 0.08106(µm)	:	(3)200.0 (µm)- 100.000(%)	:	(3)20.00 (%)- 0.0989(µm)
D90	: 6.54926(µm)	:	(4)63.00 (µm)- 98.979(%)	:	(4)30.00 (%)- 0.1153(µm)
R-Parameter	: 4.9867E-2	:	(5)20.00 (µm)- 94.335(%)	:	(5)50.00 (%)- 0.1504(µm)
		:	(6)6.300 (µm)- 89.783(%)	:	(6)60.00 (%)- 0.1748(µm)
		:	(7)2.000 (µm)- 82.663(%)	:	(7)70.00 (%)- 0.2170(µm)
				:	(8)80.00 (%)- 1.2249(µm)
				:	(9)90.00 (%)- 6.5493(µm)
				:	(10)95.00 (%)- 23.9633(µm)

Datenbezeichnung Darstellung Datum
MW12   Freitag, 5. Februar 2016 12:34:24

Labor-Nr.   : 2016-1
Datenbezeichnung   : MW13
Arbeitsgruppe   : Prof Menz
Brechungsindex (R)   : 1.60-0.10i(1.33)[1.60-0.10(1.600 - 0.100i),1.33(1.333)]
Brechungsindex (B)   : 1.60-0.10i(1.33)[1.60-0.10(1.600 - 0.100i),1.33(1.333)]
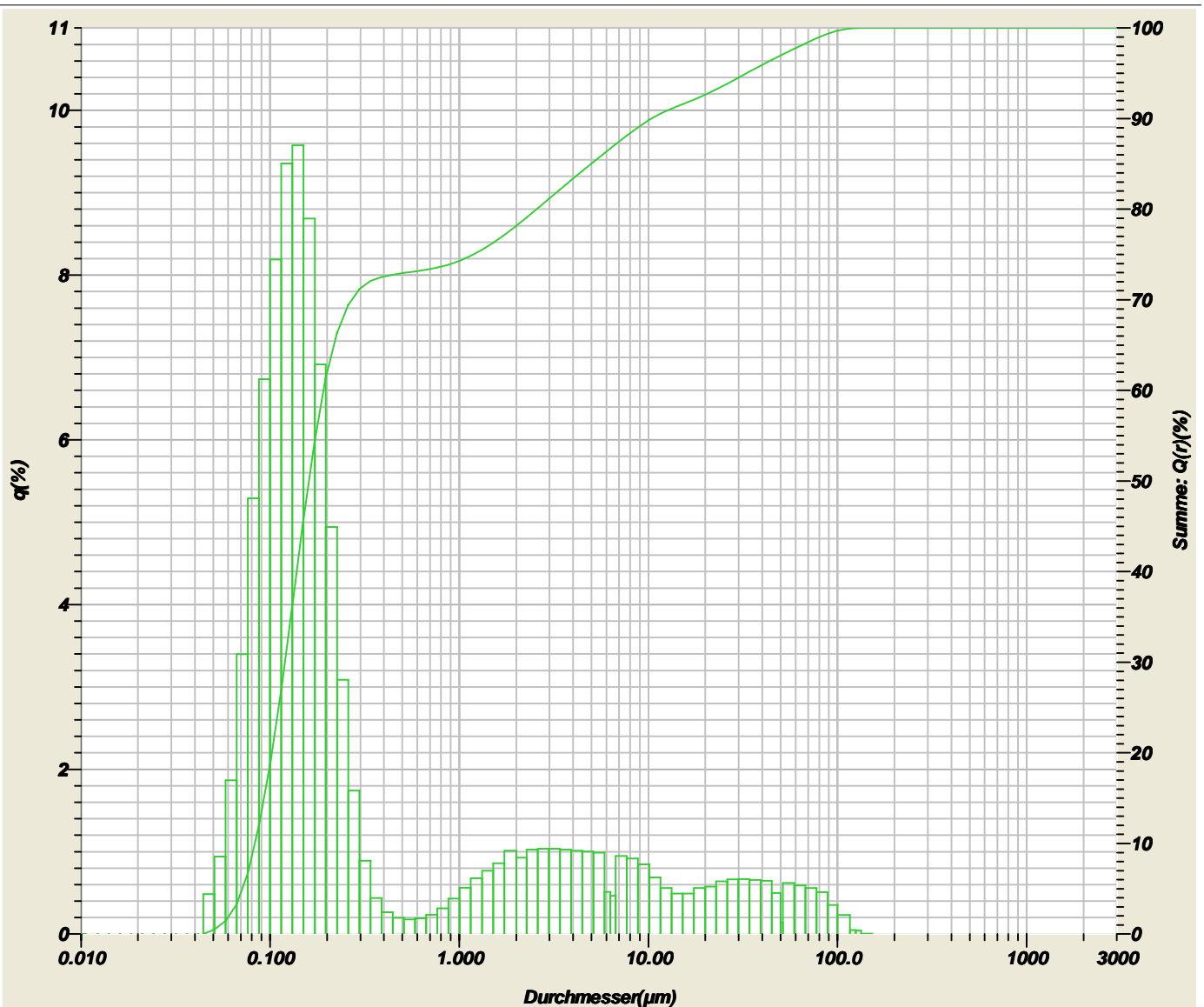Techniker/in   : Kuria

2016.02.05 10:01:08

Median	: 0.17260(µm)	Q(x)-Wert : (1)2000 (µm)- 100.000(%)	x(Q)-Wert : (1)5.000 (%)- 0.0697(µm)
Modalwert	: 0.1226(µm)	: (2)630.0 (µm)- 100.000(%)	: (2)10.00 (%)- 0.0808(µm)
D10	: 0.08077(µm)	: (3)200.0 (µm)- 99.135(%)	: (3)20.00 (%)- 0.0999(µm)
D90	: 34.85083(µm)	: (4)63.00 (µm)- 92.981(%)	: (4)30.00 (%)- 0.1190(µm)
R-Parameter	: 7.3593E-2	: (5)20.00 (µm)- 86.573(%)	: (5)50.00 (%)- 0.1726(µm)
		: (6)6.300 (µm)- 77.742(%)	: (6)60.00 (%)- 0.2877(µm)
		: (7)2.000 (µm)- 66.647(%)	: (7)70.00 (%)- 2.8614(µm)
			: (8)80.00 (%)- 7.9029(µm)
			: (9)90.00 (%)- 34.8508(µm)
			: (10)95.00 (%)- 91.0216(µm)

Datenbezeichnung Darstellung Datum
MW13   Freitag, 5. Februar 2016 10:01:08
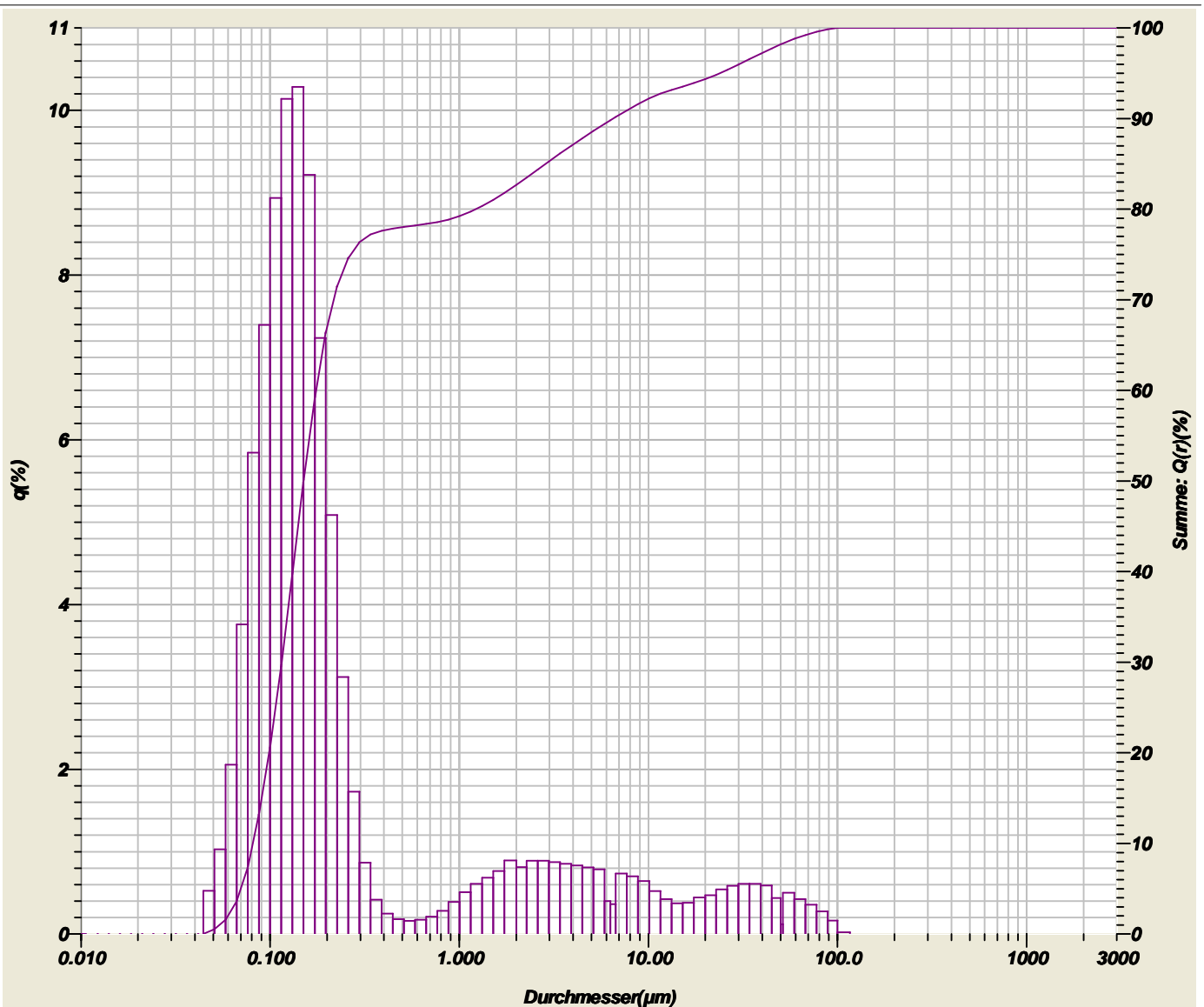
Labor-Nr.   : 2016-1
Datenbezeichnung   : MW14
Arbeitsgruppe   : Prof Menz
Brechungsindex (R)   : 1.60-0.10i(1.33)[1.60-0.10(1.600 - 0.100i),1.33(1.333)]
Brechungsindex (B)   : 1.60-0.10i(1.33)[1.60-0.10(1.600 - 0.100i),1.33(1.333)]
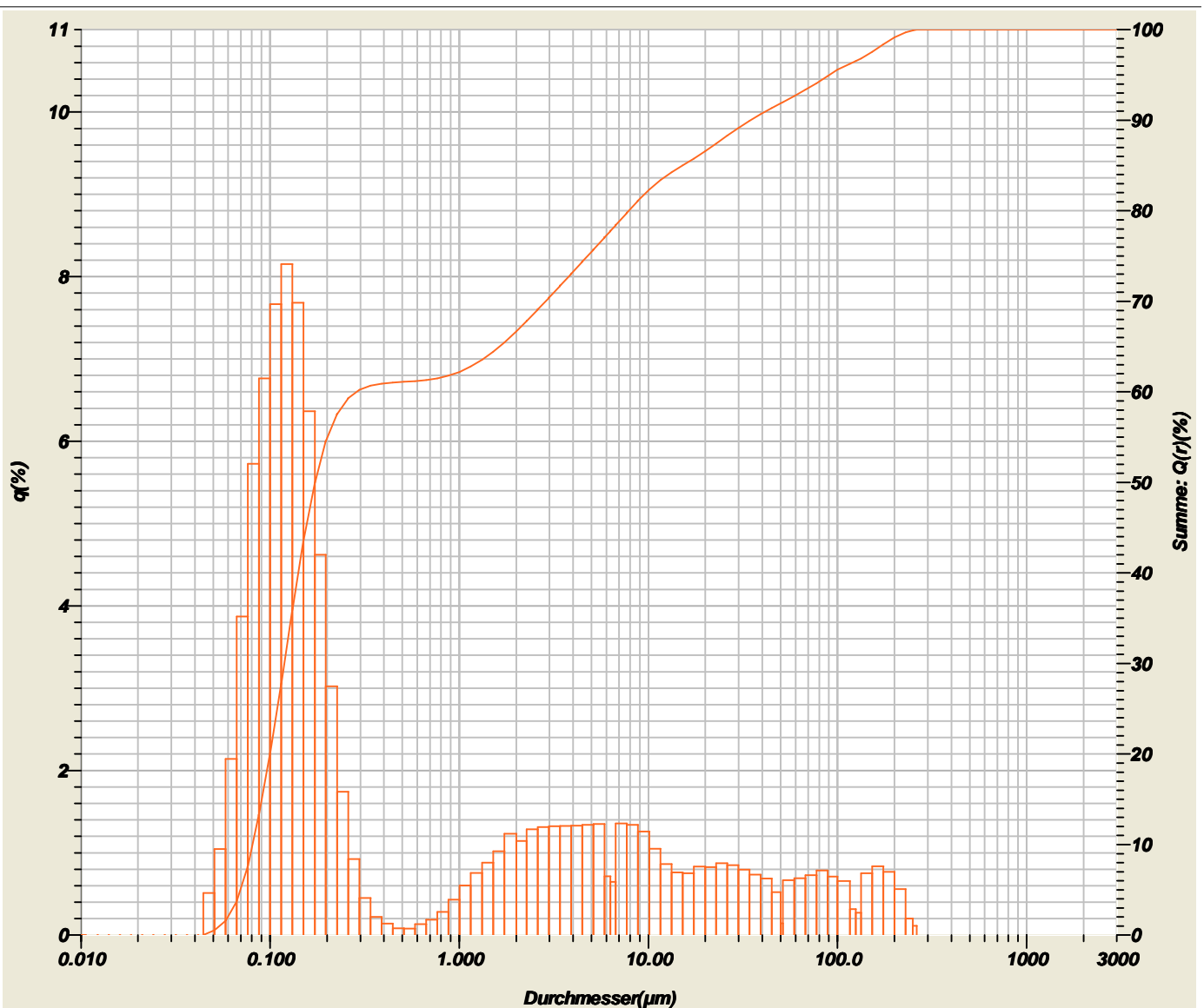Techniker/in   : Kuria

2016.02.05 10:22:41

Median	: 0.15118(µm)	Q(x)-Wert	: (1)2000 (µm)- 100.000(%)	x(Q)-Wert	: (1)5.000 (%)- 0.0675(µm)
Modalwert	: 0.1224(µm)		: (2)630.0 (µm)- 100.000(%)		: (2)10.00 (%)- 0.0778(µm)
D10	: 0.07784(µm)		: (3)200.0 (µm)- 99.944(%)		: (3)20.00 (%)- 0.0944(µm)
D90	: 16.96389(µm)		: (4)63.00 (µm)- 97.130(%)		: (4)30.00 (%)- 0.1111(µm)
R-Parameter	: 6.1333E-2		: (5)20.00 (µm)- 90.768(%)		: (5)50.00 (%)- 0.1512(µm)
			: (6)6.300 (µm)- 83.793(%)		: (6)60.00 (%)- 0.1885(µm)
			: (7)2.000 (µm)- 73.797(%)		: (7)70.00 (%)- 1.1446(µm)
					: (8)80.00 (%)- 4.0263(µm)
					: (9)90.00 (%)- 16.9639(µm)
					: (10)95.00 (%)- 42.0868(µm)

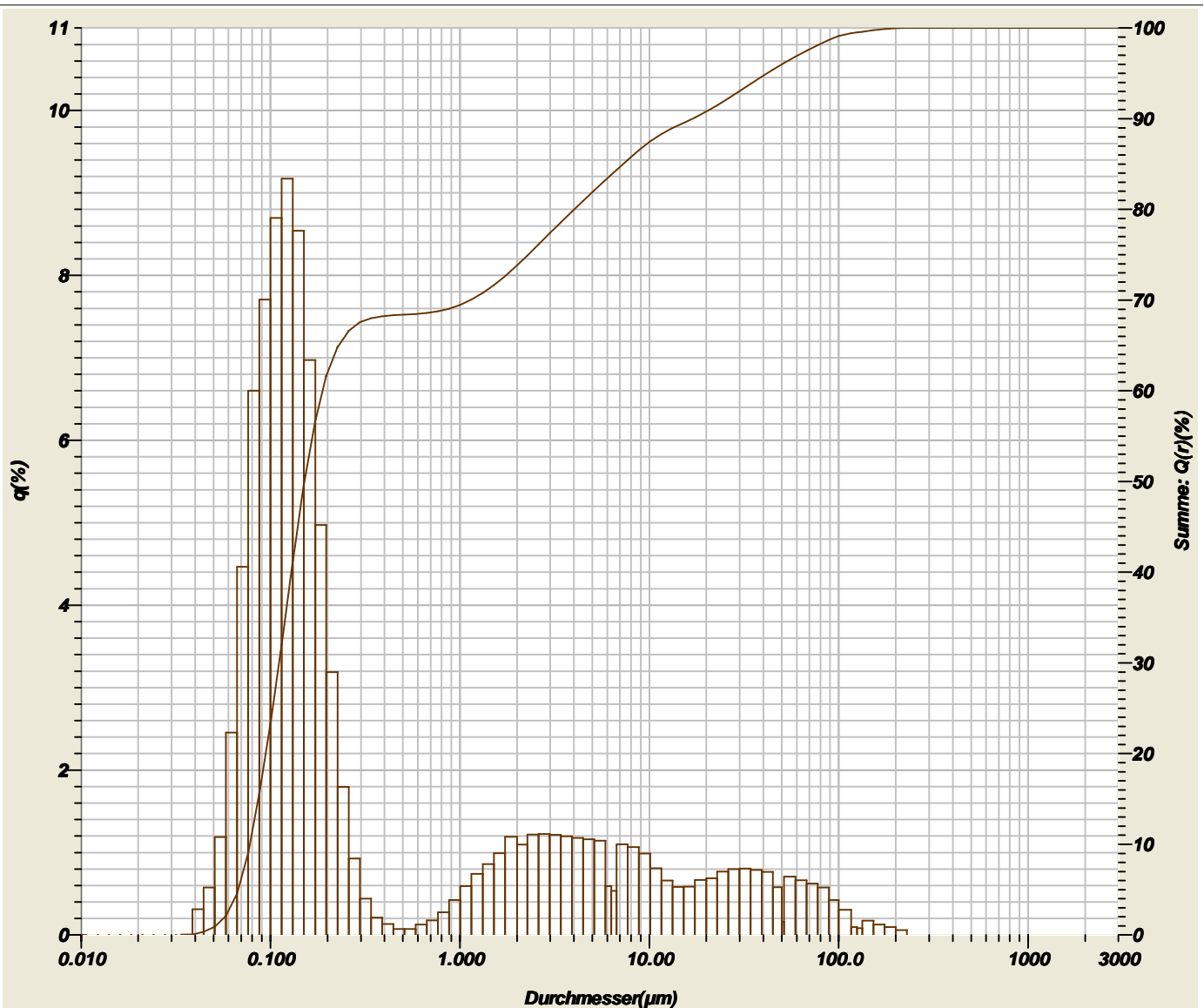| Labor-Nr. | : 2016-1 |
Datenbezeichnung	: MW15
Arbeitsgruppe	: Prof Menz
Brechungsindex (R)	: 1.60-0.10i(1.33)[1.60-0.10(1.600 - 0.100i),1.33(1.333)]
Brechungsindex (B)	: 1.60-0.10i(1.33)[1.60-0.10(1.600 - 0.100i),1.33(1.333)]
Techniker/in	: Kuria

2016.02.05 12:18:06

Median	: 0.16408(µm)	Q(x)-Wert	: (1)2000 (µm)- 100.000(%)	x(Q)-Wert	: (1)5.000 (%)- 0.0711(µm)
Modalwert	: 0.1395(µm)		: (2)630.0 (µm)- 100.000(%)		: (2)10.00 (%)- 0.0828(µm)
D10	: 0.08280(µm)		: (3)200.0 (µm)- 100.000(%)		: (3)20.00 (%)- 0.1022(µm)
D90	: 15.42041(µm)		: (4)63.00 (µm)- 97.211(%)		: (4)30.00 (%)- 0.1204(µm)
R-Parameter	: 5.7555E-2		: (5)20.00 (µm)- 91.137(%)		: (5)50.00 (%)- 0.1641(µm)
			: (6)6.300 (µm)- 84.450(%)		: (6)60.00 (%)- 0.2017(µm)
			: (7)2.000 (µm)- 75.261(%)		: (7)70.00 (%)- 0.6310(µm)
					: (8)80.00 (%)- 3.6013(µm)
					: (9)90.00 (%)- 15.4204(µm)
					: (10)95.00 (%)- 41.0321(µm)

A.4 Weather data recorded in the study area for 2015 and 2016

2015			2016		
Date	Daily temperature	Daily rainfall	Date	Daily temperature	Daily rainfall
01/04/2015	20.1	1.4	01/04/2016	20.8	7.4
02/04/2015	19.4	0.2	02/04/2016	18.3	1.8
03/04/2015	20.3	0.8	03/04/2016	19.5	16.2
04/04/2015	20	11.8	04/04/2016	18.1	19.6
05/04/2015	17	42.2	05/04/2016	20.9	4.6
06/04/2015	18.1	35	06/04/2016	20.8	0.8
07/04/2015	18.8	38.6	07/04/2016	21.1	4.6
08/04/2015	18.3	8.4	08/04/2016	21.7	0
09/04/2015	18.1	12.6	09/04/2016	21.1	0.8
10/04/2015	19	0	10/04/2016	20.4	52.6
11/04/2015	19.5	0	11/04/2016	20.6	3.4
12/04/2015	20.1	0.4	12/04/2016	21.4	0.6
13/04/2015	19.5	1.8	13/04/2016	21.7	18
14/04/2015	20.3	0	14/04/2016	19.4	13.8
15/04/2015	20.1	0	15/04/2016	21.6	10.8
16/04/2015	19.6	22.8	16/04/2016	21.4	1.4
17/04/2015	19	1.2	17/04/2016	21.1	1.2
18/04/2015	18.1	7.4	18/04/2016	20.7	17.8
19/04/2015	18.7	6.4	19/04/2016	18.9	43.2
20/04/2015	17.9	0.6	20/04/2016	20.6	0.2
21/04/2015	18.8	0.8	21/04/2016	20.7	0
22/04/2015	18.9	5	22/04/2016	22.4	0
23/04/2015	19.3	0	23/04/2016	21.6	0
24/04/2015	18.9	1	24/04/2016	20.6	4.2
25/04/2015	19.7	0	25/04/2016	20.6	17.6
26/04/2015	19.5	0.6	26/04/2016	19.5	5.2
27/04/2015	18.5	2	27/04/2016	20.8	6.8
28/04/2015	18.1	4.2	28/04/2016	18.3	5.4
29/04/2015	17.9	0	29/04/2016	19.7	10
30/04/2015	18.9	0	30/04/2016	20.1	63
01/05/2015	18.7	0	01/05/2016	18.4	12.4
02/05/2015	19.4	9	02/05/2016	18.9	32
03/05/2015	18.3	7.2	03/05/2016	20.5	0.2
04/05/2015	18.7	17.8	04/05/2016	20.6	9.4
05/05/2015	18.5	0	05/05/2016	20.3	0
06/05/2015	19.6	1.8	06/05/2016	18.2	38.2
07/05/2015	19.1	3.2	07/05/2016	18.1	7
08/05/2015	17.9	0.4	08/05/2016	19.5	5.2
09/05/2015	16.5	17.2	09/05/2016	19.5	11.8
10/05/2015	18.5	12	10/05/2016	18.9	20.4
11/05/2015	18.6	1.8	11/05/2016	19	8.2
12/05/2015	19.6	0.4	12/05/2016	19.1	0
13/05/2015	19.4	0	13/05/2016	18.5	8.4
14/05/2015	19.3	0.6	14/05/2016	19.3	5
15/05/2015	20.1	0	15/05/2016	20.8	0
16/05/2015	20.6	0	16/05/2016	20	0
17/05/2015	20.2	0	17/05/2016	19.5	27.8
18/05/2015	18.9	2.2	18/05/2016	18.4	7.4
19/05/2015	19.2	30.8	19/05/2016	18	36.2
20/05/2015	19.1	0.8	20/05/2016	19.7	0
21/05/2015	20.2	0	21/05/2016	19.8	6.4
22/05/2015	20	0	22/05/2016	19.9	0.4
23/05/2015	18.8	8.6	23/05/2016	19.5	0
24/05/2015	19.4	0	24/05/2016	20.1	0
25/05/2015	19	0.2	25/05/2016	19.2	0
26/05/2015	20.1	3.2	26/05/2016	20.3	0
27/05/2015	18.4	0.8	27/05/2016	20.4	0
28/05/2015	18.3	8.4	28/05/2016	20.3	0
29/05/2015	19	6.8	29/05/2016	20.2	0
30/05/2015	18.8	2.8	30/05/2016	20.2	0
31/05/2015	18.2	4.2	31/05/2016	20.6	0
01/06/2015	17.5	70.2	01/06/2016	20.3	0
02/06/2015	17.8	19.4	02/06/2016	20.8	0
03/06/2015	17.5	5.4	03/06/2016	20.3	0
04/06/2015	18.6	0	04/06/2016	20.5	0
05/06/2015	17	45.8	05/06/2016	20.4	0
06/06/2015	18.3	0.2	06/06/2016	20.6	0
07/06/2015	17.4	3.6	07/06/2016	20.8	0
08/06/2015	18.2	0	08/06/2016	20.6	0
09/06/2015	17.1	6.4	09/06/2016	20.5	0
10/06/2015	18	0	10/06/2016	20.2	0
11/06/2015	18.6	0.4	11/06/2016	20.3	0
12/06/2015	18.2	1.6	12/06/2016	20.5	0
13/06/2015	18.5	0.8	13/06/2016	20.1	0
14/06/2015	18	0	14/06/2016	19.8	0
15/06/2015	16.7	0.2	15/06/2016	18	2.2
16/06/2015	17.7	0	16/06/2016	18.7	19
17/06/2015	17	1.6	17/06/2016	17.8	1.2
18/06/2015	16.5	5.2	18/06/2016	17.1	0
19/06/2015	16.2	2.6	19/06/2016	18	0
20/06/2015	17.7	0.8	20/06/2016	17.7	19.2
21/06/2015	17.3	0.2	21/06/2016	16.8	41.2
22/06/2015	18	0	22/06/2016	16.4	14.4
23/06/2015	18	0	23/06/2016	18.5	8.4
24/06/2015	16.9	0	24/06/2016	17.6	9.2
25/06/2015	16.4	6.6	25/06/2016	18.5	3.6
26/06/2015	16.7	6	26/06/2016	18.4	4.8
27/06/2015	16.1	18	27/06/2016	16.9	16.8
28/06/2015	17.6	5.8	28/06/2016	18.1	2.4
29/06/2015	18.2	0	29/06/2016	17.9	0.2

2015			2016		
Date	Daily temperature	Daily rainfall	Date	Daily temperature	Daily rainfall
30/06/2015	18.1	0	30/06/2016	17.4	10.8
01/07/2015	18.2	0.2	01/07/2016	17.2	12.4
02/07/2015	17.8	0	02/07/2016	18.5	0
03/07/2015	18.1	0	03/07/2016	18.4	0
04/07/2015	18.5	0	04/07/2016	18.6	1.8
05/07/2015	18.1	0	05/07/2016	17.1	5
06/07/2015	18.2	0	06/07/2016	19.4	0
07/07/2015	19.1	0	07/07/2016	17.3	1.8
08/07/2015	18.1	0	08/07/2016	17.9	0.2
09/07/2015	17.6	0	09/07/2016	18	2
10/07/2015	18.1	0	10/07/2016	18.7	4
11/07/2015	18.2	0	11/07/2016	18	0.2
12/07/2015	18	0	12/07/2016	17.2	5.2
13/07/2015	18	0	13/07/2016	18.8	0.4
14/07/2015	18.1	0	14/07/2016	18.6	0
15/07/2015	18.1	0	15/07/2016	19.2	0
16/07/2015	18.5	0	16/07/2016	19.3	0
17/07/2015	18.8	0	17/07/2016	18.4	0
18/07/2015	18.2	0	18/07/2016	17.6	7.8
19/07/2015	17.7	8.6	19/07/2016	18.1	0
20/07/2015	17.2	0.8	20/07/2016	17.2	3.4
21/07/2015	16.8	1.4	21/07/2016	17.6	0
22/07/2015	16.8	8.6	22/07/2016	19.1	0
23/07/2015	15.6	25.2	23/07/2016	18.3	0
24/07/2015	15.4	23.4	24/07/2016	18	25.2
25/07/2015	17.6	1.2	25/07/2016	18.7	0
26/07/2015	15.9	13.2	26/07/2016	18	9.8
27/07/2015	17.1	11.6	27/07/2016	16.6	17.4
28/07/2015	18.2	0	28/07/2016	17.2	15.6
29/07/2015	17.2	3.6	29/07/2016	17.9	0.4
30/07/2015	17	3.6	30/07/2016	16.1	8
31/07/2015	17.2	19.5	31/07/2016	17.8	0.2
01/08/2015	17	3.7	01/08/2016	17.7	0
02/08/2015	16.6	22.8	02/08/2016	18.8	0
03/08/2015	16.9	4.8	03/08/2016	18.7	3.6
04/08/2015	18.1	0	04/08/2016	17.1	8.8
05/08/2015	17.5	0	05/08/2016	17.3	45
06/08/2015	17.3	0	06/08/2016	18.6	7.8
07/08/2015	16.9	5	07/08/2016	18.5	0
08/08/2015	17	0	08/08/2016	17	18.2
09/08/2015	16.9	5	09/08/2016	17.2	2.2
10/08/2015	17.7	0.2	10/08/2016	17.7	0.6
11/08/2015	18.2	0	11/08/2016	19.2	0
12/08/2015	18.3	0	12/08/2016	17.4	0.2
13/08/2015	19.2	0	13/08/2016	19.2	0
14/08/2015	18.4	0	14/08/2016	18.9	0
15/08/2015	18.2	0	15/08/2016	19.7	0
16/08/2015	18.1	0	16/08/2016	18.4	19.4
17/08/2015	18.5	0	17/08/2016	18.9	0
18/08/2015	18	0	18/08/2016	19.9	0
19/08/2015	17.9	0.8	19/08/2016	19	28.8
20/08/2015	18.1	0	20/08/2016	19.4	0
21/08/2015	17	2.8	21/08/2016	17.7	18.6
22/08/2015	19.4	0	22/08/2016	18.7	2.4
23/08/2015	16.8	17.6	23/08/2016	17.7	1.6
24/08/2015	17.7	0.6	24/08/2016	20.4	1.6
25/08/2015	18	0	25/08/2016	23.5	0
26/08/2015	18	0	26/08/2016	23.5	0
27/08/2015	17.9	0	27/08/2016	28	0
28/08/2015	18.9	0	28/08/2016	27.2	0
29/08/2015	17.9	0	29/08/2016	22.5	0
30/08/2015	18.1	0	30/08/2016	30.3	0
31/08/2015	16.8	25	31/08/2016	30.3	0
01/09/2015	18.8	0	01/09/2016	30.8	0
02/09/2015	17.4	9	02/09/2016	18.9	0.2
03/09/2015	17.8	1.8	03/09/2016	19.2	2.2
04/09/2015	17.3	1	04/09/2016	18	1.2
05/09/2015	16.3	4.6	05/09/2016	19.4	0
06/09/2015	18.6	0	06/09/2016	18.9	3.4
07/09/2015	16.7	10.8	07/09/2016	20.3	0
08/09/2015	18	0.2	08/09/2016	18.3	0
09/09/2015	17.9	0	09/09/2016	18.1	0.6
10/09/2015	17.4	25.6	10/09/2016	19	0
11/09/2015	17.8	5	11/09/2016	18.3	4
12/09/2015	19.3	0	12/09/2016	18.3	0
13/09/2015	18.2	0	13/09/2016	20.3	0
14/09/2015	18.3	1.8	14/09/2016	18.1	9.2
15/09/2015	18.8	0.2	15/09/2016	18.2	0
16/09/2015	18.6	0.2	16/09/2016	19.5	0
17/09/2015	17.8	0.2	17/09/2016	19.5	0
18/09/2015	18.5	0	18/09/2016	18.3	0
19/09/2015	17.8	3.2	19/09/2016	16.9	16.8
20/09/2015	18.6	9.6	20/09/2016	17.2	2.6
21/09/2015	18.6	1.4	21/09/2016	18.1	0.8
22/09/2015	18.8	0.8	22/09/2016	18.6	0.4
23/09/2015	15.9	1.6	23/09/2016	19.3	0
24/09/2015	17.9	0	24/09/2016	19.3	0
25/09/2015	17.4	7.4	25/09/2016	19.8	0
26/09/2015	17.3	16	26/09/2016	18	0.6
27/09/2015	18.3	0	27/09/2016	18.2	13.4
28/09/2015	18.3	0	28/09/2016	19.1	1.6
29/09/2015	18.2	1.4	29/09/2016	19.1	0
30/09/2015	19.4	0	30/09/2016	19.3	0

Curriculum Vitae

PERSONAL INFORMATION	
Name	Kuria, Bartholomew Thiong'o
Email Address	tbkuria@yahoo.com
	Bartholomew.Kuria@ruhr-uni-bochum.de
Date of Birth	03/07/1983
Nationality	Kenyan

WORK EXPERIENCE	
March 2012 - Date	Assistant Lecturer, Institute of Geomatics, GIS and Remote Sensing Dedan Kimathi University of Technology (DKUT), Nyeri, www.dkut.ac.ke
June 2011 – January 2012	GIS Consultant Ingenieurbüro für Luftbildauswertung und Vermessung (ILV), Germany, www.ilv-fernerkundung.de
February 2009 - May 2009	GIS Specialist, Kenya Roads Board roads digitization project Gath Consulting Engineers, Muthangari drive, Nairobi
August 2008 - December 2008	Data Analyst, Forest Inventory project Kenya Forest Service (KFS), Nairobi, www.kenyaforestservice.org
May 2007 - July 2007	Intern Kenya Forest Service (KFS), Nairobi, www.kenyaforestservice.org
May 2006 – June 2006	Intern Kenya Institute of Surveying and Mapping (KISM), P.O. Box 64005-00620, Nairobi
June 2002 – March 2003	Mathematics and Physics tutor St. Elizabeth Secondary School, Karen, P.O.Box 313-00502, Karen

EDUCATION AND TRAINING	
October 2017 - Date	Doctoral (PhD.) studies in Remote Sensing Ruhr-University Bochum, Germany
October 2014 – September 2017	Doctoral (PhD.) studies in Remote Sensing University of Bonn, Germany
September 2009 – May 2011	Master of Science (MSc.) Geomatic Engineering (GEOENGINE) Stuttgart University, Stuttgart, Germany
May 2003 – April 2008	Bachelor of Science (BSc.) Geomatic Engineering Jomo Kenyatta University of Agriculture and Technology (JKUAT), Thika, Kenya
1998 - 2001	Kenya Certificate of Secondary Education (K.C.S.E) Alliance High School, Kikuyu, Kenya
1994 - 1997	Kenya Certificate of Primary Education (K.C.P.E) St. Martins Boys Primary School, Murang'a, Kenya